

**PHYSICS CALCULATIONS FOR THE
CLINCH RIVER BREEDER REACTOR**

by

**Kalimullah, P. H. Kier,
and H. H. Hummel**



U of C-AUA-USERDA

ARGONNE NATIONAL LABORATORY, ARGONNE, ILLINOIS

Operated for the U. S. ENERGY RESEARCH

AND DEVELOPMENT ADMINISTRATION

under Contract W-31-109-Eng-38

The facilities of Argonne National Laboratory are owned by the United States Government. Under the terms of a contract (W-31-109-Eng-38) between the U. S. Energy Research and Development Administration, Argonne Universities Association and The University of Chicago, the University employs the staff and operates the Laboratory in accordance with policies and programs formulated, approved and reviewed by the Association.

MEMBERS OF ARGONNE UNIVERSITIES ASSOCIATION

The University of Arizona	Kansas State University	The Ohio State University
Carnegie-Mellon University	The University of Kansas	Ohio University
Case Western Reserve University	Loyola University	The Pennsylvania State University
The University of Chicago	Marquette University	Purdue University
University of Cincinnati	Michigan State University	Saint Louis University
Illinois Institute of Technology	The University of Michigan	Southern Illinois University
University of Illinois	University of Minnesota	The University of Texas at Austin
Indiana University	University of Missouri	Washington University
Iowa State University	Northwestern University	Wayne State University
The University of Iowa	University of Notre Dame	The University of Wisconsin

NOTICE

This report was prepared as an account of work sponsored by the United States Government. Neither the United States nor the United States Energy Research and Development Administration, nor any of their employees, nor any of their contractors, subcontractors, or their employees, makes any warranty, express or implied, or assumes any legal liability or responsibility for the accuracy, completeness or usefulness of any information, apparatus, product or process disclosed, or represents that its use would not infringe privately-owned rights. Mention of commercial products, their manufacturers, or their suppliers in this publication does not imply or connote approval or disapproval of the product by Argonne National Laboratory or the U. S. Energy Research and Development Administration.

Printed in the United States of America
Available from
National Technical Information Service
U. S. Department of Commerce
5285 Port Royal Road
Springfield, Virginia 22161
Price: Printed Copy \$9.00; Microfiche \$3.00

ANL-77-27

ARGONNE NATIONAL LABORATORY
9700 South Cass Avenue
Argonne, Illinois 60439

PHYSICS CALCULATIONS FOR THE
CLINCH RIVER BREEDER REACTOR

by

Kalimullah, P. H. Kier,
and H. H. Hummel

Applied Physics Division

June 1977

Prepared for the
Division of Reactor Safety Research
U. S. Nuclear Regulatory Commission

TABLE OF CONTENTS

	<u>Page</u>
ABSTRACT.	1
I. INTRODUCTION	2
II. CALCULATION OF POWER AND REACTIVITY COEFFICIENT DISTRIBUTIONS FOR THE LIGHT WATER REACTOR DISCHARGE PLUTONIUM-FUELED CRBR AT THE BEGINNING OF LIFE	3
A. Calculation of Power Distribution at the Beginning of Life.	3
B. Calculation of Sodium Void Worth Distribution at BOL Using an R-Z Model.	4
C. Calculation of Unvoided and Voided Doppler Coefficient Distributions at BOL Using an R-Z Model	5
D. Calculation of Steel Worth Distribution at BOL Using an R-Z Model.	7
E. Calculation of Fuel Worth Distribution at BOL Using an R-Z Model.	8
III. CALCULATION OF POWER AND REACTIVITY COEFFICIENT DISTRIBUTIONS FOR THE FAST FLUX TEST FACILITY GRADE PLUTONIUM-FUELED CRBR AT BOL	9
IV. EQUILIBRIUM CYCLE BURNUP CALCULATION USING LWR-Pu FUEL	11
A. Burnup Pattern of Initial Cycles.	11
B. Equilibrium Cycle Calculation and Results	11
C. Improved Equilibrium Cycle Calculations With More Detailed Radial Blanket Fuel Management Model.	13
V. CALCULATION OF POWER AND REACTIVITY COEFFICIENT DISTRIBUTIONS FOR THE BOEC 14 STATE.	15
A. Calculation of B ₄ C Absorber Concentrations for the Three Primary Control Banks and Power Distribution at BOEC 14	15
B. Effect of Isotopic Fission and Capture Energies on Subassembly Power Factors in the CRBR at the Beginning of Equilibrium Cycle 14	17
C. Calculation of Sodium Void Worth Distribution at BOEC 14 Using R-Z Model and Version III Cross-Sections.	19
D. Calculation of Unvoided and Voided Doppler Coefficient Distributions at BOEC 14 Using R-Z Model and Version III Cross-Sections.	20

E.	Calculation of Steel Worth Distribution at BOEC 14 Using R-Z Model and Version III Cross-Sections.	21
F.	Calculation of Core Fuel Worth Distribution at BOEC 14 Using R-Z Model and Version III Cross-Sections.	22
VI.	POWER DISTRIBUTION IN THE LWR-Pu-FUELED CLINCH RIVER BREEDER REACTOR AT THE END OF EQUILIBRIUM CYCLE 17	23
VII.	CALCULATION OF REACTIVITY COEFFICIENTS FOR THE LWR-Pu-FUELED CRBR AT EOEC 17 USING R-Z GEOMETRY AND TWO CROSS SECTION LIBRARIES.	25
A.	Methods and Cross Sections.	25
B.	Sodium Void Reactivity.	26
C.	Unvoided and Voided Doppler Coefficient	27
D.	Steel Worth	28
E.	Core Fuel Worths.	29
VIII.	COMPARISON OF R-Z GEOMETRY AND TRIANGULAR MESH CALCULATIONS OF REACTIVITY COEFFICIENTS USING ENDF/B-III CROSS SECTIONS	30
A.	Reactivity Coefficients at BOEC 14.	30
B.	Reactivity Coefficients at EOEC 17.	31
IX.	EVALUATION OF ERRORS AND UNCERTAINTIES IN REACTIVITY COEFFICIENT CALCULATIONS BECAUSE OF CROSS SECTIONS AND GEOMETRIC REPRESENTATION	32
A.	Cross-Sections.	32
1.	Sodium Void Worth.	32
2.	Doppler Coefficient.	32
3.	Steel Worth.	33
4.	Fuel Worth	33
B.	Geometric Effects	34
1.	Sodium Void Worth.	34
2.	Doppler Coefficient.	34
3.	Steel Worth.	34
4.	Fuel Worth	35
APPENDIX A	36
ACKNOWLEDGMENT	38
REFERENCES	39

LIST OF FIGURES

<u>No.</u>	<u>Title</u>	<u>Page</u>
II-1	Clinch River Breeder Reactor Layout	41
II-2	R-Z Model of the Hot Full Power Clinch River Breeder Reactor at the Beginning of Life. CONO is a collection of spatially disconnected control regions from which the control rod is out (sodium and steel 90.56 and 9.44 v/o). CONI, CON3F and CON3C are regions representing the central rod (two-thirds inserted), the six rods at flats (two-thirds inserted) and the other six rods at corners (completely withdrawn) of Row 7.	42
II-3	Axial Distribution of Power in the LWR-Grade Plutonium Fueled Clinch River Breeder Reactor Core at the Beginning of Life	43
II-4	Axial Distribution of Power in the LWR-Grade Plutonium Fueled Clinch River Breeder Reactor Lower Axial Blanket at the Beginning of Life	43
II-5	Axial Distribution of Power in the LWR-Grade Plutonium Fueled Clinch River Breeder Reactor Upper Axial Blanket at the Beginning of Life	44
II-6	Axial Distribution of Power in the LWR-Grade Plutonium Fueled Clinch River Breeder Reactor Blanket at the Beginning of Life	44
II-7	Axial Distribution of Power in the LWR-Grade Plutonium Fueled Clinch River Breeder Reactor Core & Blankets at the Beginning of Life	45
II-8	Radial Distribution of Power in the LWR-Grade Plutonium Fueled Clinch River Breeder Reactor Core & Blankets at the Beginning of Life	45
II-9	Subassembly Power Factors for the LWR-Grade Plutonium Fueled Clinch River Breeder Reactor at the Beginning of Life	46
II-10	Subassembly Peak-To-Average Power Density Ratios for the LWR-Grade Plutonium Fueled Clinch River Breeder Reactor at the Beginning of Life	46
II-11	Subassembly Peak Power Factors for the LWR-Grade Plutonium Fueled Clinch River Breeder Reactor at the Beginning of Life	46
II-12	Comparison of Void Worth Distributions in Core Between Normal and Core-and-Blanket-Voided LWR-Pu-Fueled CRBR at the Beginning of Life	47

LIST OF FIGURES (Contd)

<u>No.</u>	<u>Title</u>	<u>Page</u>
II-13	Comparison of Void Worth Distributions in Upper Blanket Between Normal and Core-and-Blanket-Voided LWR-Pu-Fueled CRBR at the Beginning of Life	47
II-14	Comparison of Void Worth Distributions in Radial Blanket Between Normal and Core-and Blanket-Voided LWR-Pu-Fueled CRBR at the Beginning of Life	48
II-15	Distribution of Sodium Void Worth in Core in the LWR-Grade Plutonium Fueled Clinch River Breeder Reactor at the Beginning of Life	48
II-16	Distribution of Sodium Void Worth in Lower Blanket in the LWR-Grade Plutonium Fueled Clinch River Breeder Reactor at the Beginning of Life	49
II-17	Distribution of Sodium Void Worth in Upper Blanket in the LWR-Grade Plutonium Fueled Clinch River Breeder Reactor at the Beginning of Life	49
II-18	Distribution of Sodium Void Worth in Radial Blanket in the LWR-Grade Plutonium Fueled Clinch River Breeder Reactor at the Beginning of Life	50
II-19	Distribution of Sodium Void Worth in Core and Blankets in the LWR-Grade Plutonium Fueled Clinch River Breeder Reactor at the Beginning of Life	50
II-20	Comparison of Doppler Coefficients over 2200-4400K in Unvoided Core Computed from Fluxes at Both Temperatures for LWR-Pu-Fueled CRBR at BOL	51
II-21	Comparison of Doppler Coefficients over 2200-4400K in Unvoided Upper Blanket Computed from Fluxes at Both Temperatures for LWR-Pu-Fueled CRBR at BOL	51
II-22	Comparison of Doppler Coefficients over 2200-4400K in Unvoided Radial Blanket Computed from Fluxes at Both Temperatures for LWR-Pu-Fueled CRBR at BOL	52
II-23	Doppler Coefficient over 2200-4400K in Unvoided Core of the LWR-Pu-Fueled CRBR at the Beginning of Life	52
II-24	Doppler Coefficient over 2200-4400K in Unvoided Lower Blanket of the LWR-Pu-Fueled CRBR at the Beginning of Life	53

LIST OF FIGURES (Contd)

<u>No.</u>	<u>Title</u>	<u>Page</u>
II-25	Doppler Coefficient over 2200-4400K in Unvoided Upper Blanket of the LWR-Pu-Fueled CRBR at the Beginning of Life	53
II-26	Doppler Coefficient over 2200-4400K in Unvoided Radial Blanket of the LWR-Pu-Fueled CRBR at the Beginning of Life	54
II-27	Doppler Coefficient over 2200-4400K in Unvoided Core and Blankets of the LWR-Pu-Fueled CRBR at the Beginning of Life	54
II-28	Comparison of Doppler Coefficients over 2200-4400K in Totally Voided Core Computed from Fluxes at Both Temperatures for LWR-Pu-Fueled CRBR at BOL	55
II-29	Comparison of Doppler Coefficients over 2200-4400K in Totally Voided Upper Blanket Computed from Fluxes at Both Temperatures for LWR-Pu-Fueled CRBR at BOL	55
II-30	Comparison of Doppler Coefficients over 2200-4400K in Totally Voided Radial Blanket Computed from Fluxes at Both Temperatures for LWR-Pu-Fueled CRBR at BOL	56
II-31	Doppler Coefficient over 2200-4400K in Totally Voided Core of the LWR-Pu-Fueled CRBR at the Beginning of Life	56
II-32	Doppler Coefficient over 2200-4400K in Totally Voided Core and Blankets of the LWR-Pu-Fueled CRBR at the Beginning of Life	57
II-33	Comparison of Steel Worth Distributions in Core Between Normal and Core-and-Blanket-Voided LWR-Pu-Fueled CRBR at the Beginning of Life	57
II-34	Comparison of Steel Worth Distributions in Upper Blanket Between Normal and Core-and-Blanket-Voided LWR-Pu-Fueled CRBR at the Beginning of Life	58
II-35	Comparison of Steel Worth Distributions in Radial Blanket Between Normal and Core-and-Blanket-Voided LWR-Pu-Fueled CRBR at the Beginning of Life	58
II-36	Axial Distribution of Steel Worth in Core in the LWR-Grade Plutonium Fueled Clinch River Breeder Reactor at the Beginning of Life.	59

LIST OF FIGURES (Contd)

<u>No.</u>	<u>Title</u>	<u>Page</u>
II-37	Axial Distribution of Steel Worth in Radial Blanket in the LWR-Grade Plutonium Fueled Clinch River Breeder Reactor at the Beginning of Life	59
II-38	Axial Distribution of Steel Worth in Core and Blankets in the LWR-Grade Plutonium Fueled Clinch River Breeder Reactor at the Beginning of Life	60
II-39	Axial Distribution of Core Fuel Worth in Core in the LWR-Grade Plutonium Fueled Clinch River Breeder Reactor at the Beginning of Life	60
II-40	Axial Distribution of Core Fuel Worth in Lower Blanket in the LWR-Grade Plutonium Fueled Clinch River Breeder Reactor at the Beginning of Life	61
II-41	Axial Distribution of Core Fuel Worth in Upper Blanket in the LWR-Grade Plutonium Fueled Clinch River Breeder Reactor at the Beginning of Life	61
II-42	Axial Distribution of Radial Blanket Fuel Worth in the LWR-Grade Plutonium Fueled Clinch River Breeder Reactor at the Beginning of Life.	62
II-43	Axial Distribution of Core and Radial Blanket Fuel Worths in the LWR-Grade Plutonium Fueled Clinch River Breeder Reactor at the Beginning of Life	62
III-1	Subassembly Power Factors for the FFTF Plutonium Fueled Clinch River Breeder Reactor at the Beginning of Life	63
III-2	Subassembly Peak-to-Average Power Density Ratios for the FFTF Plutonium Fueled Clinch River Breeder Reactor at the Beginning of Life	63
III-3	Subassembly Peak Power Factors for the FFTF Plutonium Fueled Clinch River Breeder Reactor at the Beginning of Life	63
III-4	Axial Distribution of Power in the FFTF-Plutonium Fueled Clinch River Breeder Reactor Core at the Beginning of Life	64
III-5	Axial Distribution of Power in the FFTF-Plutonium Fueled Clinch River Breeder Reactor Radial Blanket at the Beginning of Life	64

LIST OF FIGURES (Contd)

<u>No.</u>	<u>Title</u>	<u>Page</u>
III-6	Axial Distribution of Power in the FFTF-Plutonium Fueled Clinch River Breeder Reactor Core & Blanket at the Beginning of Life	65
III-7	Radial Distribution of Power in the FFTF-Plutonium Fueled Clinch River Breeder Reactor Core & Blanket at the Beginning of Life	65
III-8	Distribution of Sodium Void Worth in Core in the FFTF-Plutonium Fueled Clinch River Breeder Reactor at the Beginning of Life	66
III-9	Distribution of Sodium Void Worth in Core and Blankets in the FFTF-Plutonium Fueled Clinch River Breeder Reactor at the Beginning of Life	66
III-10	Comparison of Void Worth Distributions in Core Between LWR-Pu-Fueled and FFTF-Pu-Fueled CRBR at the Beginning of Life	67
III-11	Comparison of Void Worth Distributions in Upper Blanket Between LWR-Pu-Fueled and FFTF-Pu-Fueled CRBR at the Beginning of Life	67
III-12	Comparison of Void Worth Distributions in Radial Blanket Between LWR-Pu-Fueled and FFTF-Pu-Fueled CRBR at the Beginning of Life	68
III-13	Axial Distribution of Steel Worth in Core in the FFTF-Plutonium Fueled Clinch River Breeder Reactor at the Beginning of Life	68
III-14	Axial Distribution of Steel Worth in Core and Blankets in the FFTF-Plutonium Fueled Clinch River Breeder Reactor at the Beginning of Life	69
III-15	Comparison of Steel Worth Distributions in Core Between LWR-Pu-Fueled and FFTF-Pu-Fueled CRBR at the Beginning of Life	69
III-16	Comparison of Steel Worth Distributions in Upper Blanket Between LWR-Pu-Fueled and FFTF-Pu-Fueled CRBR at the Beginning of Life	70
III-17	Comparison of Steel Worth Distributions in Radial Blanket Between LWR-Pu-Fueled and FFTF-Pu-Fueled CRBR at the Beginning of Life	70
III-18	Doppler Coefficient over 2200-4400K in Unvoided Core of the FFTF-Pu-Fueled CRBR at the Beginning of Life	71

LIST OF FIGURES (Contd)

<u>No.</u>	<u>Title</u>	<u>Page</u>
III-19	Doppler Coefficient over 2200-4400K in Unvoided Core and Blankets of the FFTF-Pu-Fueled CRBR at the Beginning of Life	71
III-20	Doppler Coefficient over 2200-4400K in Totally Voided Core of the FFTF-Pu-Fueled CRBR at the Beginning of Life . . .	72
III-21	Doppler Coefficient over 2200-4400K in Totally Voided Core and Blankets of the FFTF-Pu-Fueled CRBR at the Beginning of Life	72
III-22	Comparison of Doppler Coefficients over 2200-4400K in Unvoided Core Between LWR-Pu-Fueled and FFTF-Pu-Fueled CRBR at BOL	73
III-23	Comparison of Doppler Coefficients over 2200-4400K in Unvoided Upper Blanket Between LWR-Pu-Fueled and FFTF-Pu-Fueled CRBR at BOL	73
III-24	Comparison of Doppler Coefficients over 2200-4400K in Unvoided Radial Blanket Between LWR-Pu-Fueled and FFTF-Pu-Fueled CRBR at BOL	74
III-25	Comparison of Doppler Coefficients over 2200-4400K in Totally Voided Core Between LWR-Pu-Fueled and FFTF-Pu-Fueled CRBR at BOL	74
III-26	Comparison of Doppler Coefficients over 2200-4400K in Totally Voided Upper Blanket Between LWR-Pu-Fueled and FFTF-Pu-Fueled CRBR at BOL	75
III-27	Comparison of Doppler Coefficients over 2200-4400K in Totally Voided Radial Blanket Between LWR-Pu-Fueled and FFTF-Pu-Fueled CRBR at BOL	75
III-28	Axial Distribution of Core Fuel Worth in Core in the FFTF-Plutonium Fueled Clinch River Breeder Reactor at the Beginning of Life	76
III-29	Axial Distribution of Core Fuel Worth in Lower Blanket in the FFTF-Plutonium Fueled Clinch River Breeder Reactor at the Beginning of Life	76
III-30	Axial Distribution of Core Fuel Worth in Upper Blanket in the FFTF-Plutonium Fueled Clinch River Breeder Reactor at the Beginning of Life	77
III-31	Axial Distribution of Radial Blanket Fuel Worth in the FFTF-Plutonium Fueled Clinch River Breeder Reactor at the Beginning of Life	77

LIST OF FIGURES (Contd)

<u>No.</u>	<u>Title</u>	<u>Page</u>
IV-1	R-Z Model of the Lower Half of the Hot Full Power Clinch River Breeder Reactor Used for Equilibrium Cycle Calculations. The two-digit numbers shown in the regions are region names.	78
IV-2	Radial Split of the Radial Blanket of the Hot Full Power CRBR showing its Detailed Fuel Management Used for the Improved Equilibrium Cycle Calculations. The arrows indicate the charging, shuffling and discharging of the subassemblies. Axially there are six regions in the radial blanket and the rest of the R-Z model is the same as that shown in Fig. IV-1. Regions 71 and 91 each consist of two annuli	79
V-1	Subassembly Power Factors for the LWR-Grade Plutonium Fueled Clinch River Breeder Reactor at the Beginning of Equilibrium Cycle 14	80
V-2	Subassembly Peak-To-Average Power Density Ratio for the LWR-Grade Plutonium Fueled Clinch River Breeder Reactor at the Beginning of Equilibrium Cycle 14	80
V-3	Subassembly Peak Power Factors for the LWR-Grade Plutonium Fueled Clinch River Breeder Reactor at the Beginning of Equilibrium Cycle 14	81
V-4	Axial Distribution of Power in Core of the LWR-Pu-Fueled CRBR at the Beginning of Equilibrium Cycle 14.	81
V-5	Axial Distribution of Power in Lower Blanket of the LWR-Pu-Fueled CRBR at the Beginning of Equilibrium Cycle 14	82
V-6	Axial Distribution of Power in Upper Blanket of the LWR-Pu-Fueled CRBR at the Beginning of Equilibrium Cycle 14	82
V-7	Comparison of Power Distributions in Radial Blanket of the LWR-Pu-Fueled CRBR Between the BOEC 14 and EOEC 17	83
V-8	Subassembly Power Factors for the LWR-Grade Plutonium Fueled Clinch River Breeder Reactor at the Beginning of Equilibrium Cycle 14 Without Capture Energy with an Average Energy/Fission Based on Version IV Cross-Section Set 2	83

LIST OF FIGURES (Contd)

<u>No.</u>	<u>Title</u>	<u>Page</u>
V-9	Subassembly Peak-to-Average Power Density Ratios for the LWR-Grade Plutonium Fueled Clinch River Breeder Reactor at the Beginning of Equilibrium Cycle 14 without Capture Energy with an Average Energy/Fission Based on Version IV Cross-Section Set 2	84
V-10	Subassembly Peak Power Factors for the LWR-Grade Plutonium Fueled Clinch River Breeder Reactor at the Beginning of Equilibrium Cycle 14 without Capture Energy with an Average Energy/ Fission Based on Version IV Cross-Section Set 2	84
V-11	Subassembly Power Factors for the LWR-Grade Plutonium Fueled Clinch River Breeder Reactor at the Beginning of Equilibrium Cycle 14 with Isotopic Capture and Fission Energies Based on Version IV Cross-Section Set 2	85
V-12	Subassembly Peak-to-Average Power Density Ratios for the LWR-Grade Plutonium Fueled Clinch River Breeder Reactor at the Beginning of Equilibrium Cycle 14 with Isotopic Capture and Fission Energies Based on Version IV Cross-Section Set 2	85
V-13	Subassembly Peak Power Factors for the LWR-Grade Plutonium Fueled Clinch River Breeder Reactor at the Beginning of Equilibrium Cycle 14 with Isotopic Capture and Fission Energies Based on Version IV Cross-Section Set 2	86
V-14	Subassembly Average Power Densities for the LWR-Grade Plutonium Fueled Clinch River Breeder Reactor at the Beginning of Equilibrium Cycle 14 with Isotopic Capture and Fission Energies Based on Version IV Cross-Section Set 2	86
V-15	Distribution of Sodium Void Worth in Core of the LWR-Pu-Fueled CRBR at the Beginning of Equilibrium Cycle 14	87
V-16	Distribution of Sodium Void Worth in Lower Blanket of the LWR-Pu-Fueled CRBR at the Beginning of Equilibrium Cycle 14	87
V-17	Distribution of Sodium Void Worth in Upper Blanket of the LWR-Pu-Fueled CRBR at the Beginning of Equilibrium Cycle 14	88

LIST OF FIGURES (Contd)

<u>No.</u>	<u>Title</u>	<u>Page</u>
V-18	Distribution of Sodium Void Worth in Core and Blankets of the LWR-Pu-Fueled CRBR at the Beginning of Equilibrium Cycle 14	88
V-19	Comparison of Void Worth Distributions in Radial Blanket of the LWR-Pu-Fueled CRBR Between the BOEC 14 and EOEC 17	89
V-20	Doppler Coefficient over 2200-4400K in Unvoided Core of the LWR-Pu-Fueled CRBR at the Beginning of Equilibrium Cycle 14	89
V-21	Doppler Coefficient over 2200-4400K in Unvoided Core and Blankets of the LWR-Pu-Fueled CRBR at the Beginning of Equilibrium Cycle 14	90
V-22	Comparison of Doppler Coefficients over 2200-4400K in Unvoided Radial Blanket of the LWR-Pu-Fueled CRBR Between the BOEC 14 and EOEC 17	90
V-23	Doppler Coefficient over 2200-4400K in Totally Voided Core of the LWR-Pu-Fueled CRBR at the Beginning of Equilibrium Cycle 14	91
V-24	Doppler Coefficient over 2200-4400K in Totally Voided Core and Blankets of the LWR-Pu-Fueled CRBR at the Beginning of Equilibrium Cycle 14	91
V-25	Comparison of Doppler Coefficients over 2200-4400K in Voided Radial Blanket of the LWR-Pu-Fueled CRBR Between the BOEC 14 and EOEC 17	92
V-26	Axial Distribution of Steel Worth in Core of the LWR-Pu-Fueled CRBR at the Beginning of Equilibrium Cycle 14	92
V-27	Axial Distribution of Steel Worth in Core and Blankets of the LWR-Pu-Fueled CRBR at the Beginning of Equilibrium Cycle 14	93
V-28	Comparison of Steel Worth Distributions in Radial Blanket of the LWR-Pu-Fueled CRBR Between the BOEC 14 and EOEC 17	93
V-29	Distribution of Core Fuel Worth in Core of the LWR-Pu-Fueled CRBR at the Beginning of Equilibrium Cycle 14	94
V-30	Distribution of Core Fuel Worth in Core and Blankets of the LWR-Pu-Fueled CRBR at the Beginning of Equilibrium Cycle 14	94

LIST OF FIGURES (Contd)

<u>No.</u>	<u>Title</u>	<u>Page</u>
VI-1	Subassembly Power Factors for the LWR-Pu-Fueled CRBR at the End of Equilibrium Cycle 17, Unimproved Radial Blanket Compositions	95
VI-2	Subassembly Peak-to-Average Power Density Ratios for the LWR-Pu-Fueled CRBR at the End of Equilibrium Cycle 17, Unimproved Radial Blanket Compositions	95
VI-3	Subassembly Peak Power Factors for the LWR-Pu-Fueled CRBR at the End of Equilibrium Cycle 17, Unimproved Radial Blanket Compositions	96
VI-4	Subassembly Power Factors for the LWR-Grade Plutonium Fueled Clinch River Breeder Reactor at the End of Equilibrium Cycle 17 with Improved Radial Blanket Compositions	96
VI-5	Subassembly Peak-to-Average Power Density Ratios for the LWR-Grade Plutonium Fueled Clinch River Breeder Reactor at the End of Equilibrium Cycle 17 with Improved Radial Blanket Compositions	97
VI-6	Subassembly Peak Power Factors for the LWR-Grade Plutonium Fueled Clinch River Breeder Reactor at the End of Equilibrium Cycle 17 Improved Radial Blanket Compositions	97
VI-7	Axial Distribution of Power in Core of the LWR-Pu-Fueled CRBR at the End of Equilibrium Cycle 17	98
VI-8	Axial Distribution of Power in Lower Blanket of the LWR-Pu-Fueled CRBR at the End of Equilibrium Cycle 17	98
VI-9	Axial Distribution of Power in Upper Blanket of the LWR-Pu-Fueled CRBR at the End of Equilibrium Cycle 17	99
VII-1	Distribution of Sodium Void Worth in Core of the LWR-Pu-Fueled CRBR at the End of Equilibrium Cycle 17	100
VII-2	Distribution of Sodium Void Worth in Core and Blankets of the LWR-Pu-Fueled CRBR at the End of Equilibrium Cycle 17	100

LIST OF FIGURES (Contd)

<u>No.</u>	<u>Title</u>	<u>Page</u>
VII-3	Comparison of Void Worth Distribution in Core of the LWR-Pu-Fueled CRBR Between the BOEC 14 and EOEC 17	101
VII-4	Doppler Coefficient over 2200-4400K in Unvoided Core of the LWR-Pu-Fueled CRBR at the End of Equilibrium Cycle 17.	101
VII-5	Doppler Coefficient over 2200-4400K in Unvoided Core and Blankets of the LWR-Pu-Fueled CRBR at the End of Equilibrium Cycle 17	102
VII-6	Doppler Coefficient over 2200-4400K in Totally Voided Core of the LWR-Pu-Fueled CRBR at the End of Equilibrium Cycle 17	102
VII-7	Doppler Coefficient Over 2200-4400K in Totally Voided Core and Blankets of the LWR-Pu-Fueled CRBR at the End of Equilibrium Cycle 17	103
VII-8	Comparison of Doppler Coefficients over 2200-4400K in Unvoided Core of the LWR-Pu-Fueled CRBR Between the BOEC 14 and EOEC 17	103
VII-9	Comparison of Doppler Coefficients over 2200-4400K in Voided Core of the LWR-Pu-Fueled CRBR Between the BOEC 17 and EOEC 17	104
VII-10	Axial Distribution of Steel Worth in Core of the LWR-Pu-Fueled CRBR at the End of Equilibrium Cycle 17	104
VII-11	Axial Distribution of Steel Worth in Core and Blankets of the LWR-Pu-Fueled CRBR at the End of Equilibrium Cycle 17	105
VII-12	Comparison of Steel Worth Distributions in Core of the LWR-Pu-Fueled CRBR Between tje BOEC 14 and EOEC 17	105
VII-13	Distribution of Core Fuel Worth in Core of the LWR-Pu-Fueled CRBR at the End of Equilibrium Cycle 17	106
VII-14	Distribution of Core Fuel Worth in Core and Blankets of the LWR-Pu-Fueled CRBR at the End of Equilibrium Cycle 17 . . .	106
VII-15	Comparison of Core Fuel Worths in Core of the LWR-Pu-Fueled CRBR Between the BOEC 14 and EOEC 17	107

LIST OF TABLES

<u>No.</u>	<u>Title</u>	<u>Page</u>
II-1	Clinch River Breeder Reactor Full Power Parameters at Beginning of Life	108
II-2	Steady State Coolant Temperature Used for Estimating Its Axial Density Variation in Core Subassemblies	109
II-3	Power and Reactivities by Region in the LWR-Pu-Fueled CRBR at the Beginning of Life	109
II-4	Sodium Void Worth, $1.0E3 \cdot \Delta k/k$ by Region in LWR-Pu- Fueled CRBR at BOL by Different Methods	110
II-5	Rough Percentage of Reactivity Components in CRBR Material Worths at Beginning of Life	111
II-6	Channel Definition for the Clinch River Breeder Reactor at the Beginning of Life	112
II-7	Reactivity Worths Totalled by Channel in the LWR- Pu-Fueled Clinch River Breeder Reactor at the Beginning of Life	113
II-8	Unvoided Doppler Coefficient, $-T \frac{dk}{dT} \times 10^4$ by Region Over Different Temperature Ranges in LWR-Pu-Fueled CRBR at the Beginning of Life	114
II-9	Voided ^a Doppler Coefficient, $-T \frac{dk}{dT} \times 10^4$ by Region Over Different Temperature Ranges in LWR-Pu-Fueled CRBR at the Beginning of Life	115
II-10	Doppler Coefficient Averaged Over 1100-4400°K, $-1.0E4 \cdot T \frac{dk}{dT}$ in LWR-Pu-Fueled CRBR at BOL for Different Stages of Voiding	115
II-11	Steel Worth, $1.0E3 \cdot \Delta k/k$ by Region in LWR-PU-Fueled CRBR at BOL by Different Methods	116
III-1	Comparison of Power and Reactivities by Region Between LWR-Pu-Fueled and FFTF-Pu-Fueled CRBR at the Beginning of Life	117
III-2	Reactivity Worths Totalled by Channel in the FFTF-Pu- Fueled Clinch River Breeder Reactor at the Beginning of Life	118
IV-1a	Number of Cycles of Burnup at the End of Cycles 1 to 7 for Core and Radial Blanket Subassembly Locations	119

LIST OF TABLES (Contd)

<u>No.</u>	<u>Title</u>	<u>Page</u>
IV-1b	Number of Cycles of Burnup at the End ^a of Cycles 8 to 13 for Core and Radial Blanket Subassembly Locations	120
IV-2	Radial Blanket Shuffling and Refueling Scheme	121
IV-3	Basic Input to Equilibrium Cycle Burnup Calculations	121
IV-4	Nuclear Reactions Considered in Burnup Calculations	122
IV-5	Fission Product Yields and Atomic Weights Used in the Equilibrium Cycle Calculations	122
IV-6	Required Enrichments of the Fresh Charges, and Breeding Ratios in the Equilibrium Cycle of the LWR-Pu-Fueled CRBR	123
IV-7	Heavy Metal Mass (kg) Inventory in the Equilibrium Cycle of the LWR-Pu-Fueled Clinch River Breeder Reactor	124
IV-8	Comparison with PSAR Calculation of Heavy Metal Mass (kg) Inventory at the Beginning of Equilibrium Cycle for the LWR-Pu-Fueled CRBR	125
IV-9	Plutonium Isotopic Composition (Weight Percent) in the Equilibrium Cycle of the LWR-Pu-Fueled CRBR	125
IV-10	Comparison with PSAR Calculation of Plutonium Buildup (kg) in the Equilibrium Cycle of the LWR-Pu-Fueled CRBR	126
IV-11	Isotopic Composition and Total Mass of Plutonium in the Discharged Subassemblies at the End of an Average* Equilibrium Cycle for the LWR-Pu-Fueled CRBR	126
IV-12	Subassembly Burnup in the Equilibrium Cycle of the LWR-Pu-Fueled CRBR	127
IV-13	Required Enrichments of the Fresh Charges, and Breeding Ratios Obtained in the Improved Equilibrium Cycle Calcula- tions of the LWR-Pu-Fueled CRBR	127
IV-14	Heavy Metal Mass (kg) Inventory in the Radial Blanket of the LWR-Pu-Fueled CRBR for the Improved* Equilibrium Cycle Calculation	128
IV-15	Isotopic Composition and Total Mass of Plutonium in the Subassemblies Discharged from the Radial Blanket for the Improved Equilibrium Cycle Calculation of the LWR-Pu-Fueled CRBR	129

LIST OF TABLES (Contd)

<u>No.</u>	<u>Title</u>	<u>Page</u>
IV-16	Axial Maximum Burnup of the Radial Blanket Subassemblies for the Improved Equilibrium Cycle Calculation of the LWR-Pu-Fueled CRBR	129
V-1	Radial Structure of the R-Z Model of the Hot Full Power LWR-Pu-Fueled CRBR at BOEC 14 Used for Power and Reactivity Coefficient Distribution Calculations	130
V-2	Power by Reactor Region, MWt in the LWR-Pu-Fueled CRBR at the Beginning of Equilibrium Cycle 14 by Different Methods	133
V-3	Summary of K-Effective of the LWR-Pu-Fueled CRBR at BOEC 14 Based on the R-Z Model and Version III Cross-Sections	133
V-4	Definition of SAS Channels at the Beginning and End of the Equilibrium Cycle	134
V-5	Reactivity Worths Totalled by Channel in the LWR-Pu-Fueled Clinch River Breeder Reactor at BOEC 14	135
V-6	Sodium Void Worth, $\frac{\Delta k}{k} \times 10^3$ by Region in LWR-Pu-Fueled CRBR at BOEC 14 by Different Methods	136
V-7	Unvoided Doppler Coefficient, $-T \frac{dk}{dT} \times 10^4$ by Region Over Different Temperature Ranges in LWR-Pu-Fueled CRBR at BOEC 14	136
V-8	Voided ^a Doppler Coefficient, $-T \frac{dk}{dT} \times 10^4$ by Region Over Different Temperature Ranges in LWR-Pu-Fueled CRBR at BOEC 14	137
V-9	Steel Worth, $\frac{\Delta k}{k} \times 10^3$ by Region in LWR-Pu-Fueled CRBR at BOEC 14 by Different Methods	138
V-10	Core Fuel* Worth, $\frac{\Delta k}{k} \times 10^3$ by Region in LWR-Pu-Fueled CRBR at Boec 14 by Different Methods	138
VI-1	Power Distribution by Region (MW) in the LWR-Pu-Fueled Clinch River Breeder Reactor at EOC 17 by Different Methods	139
VII-1	Sodium Void Worth, $\frac{\Delta k}{k} \times 10^3$ by Region in LWR-Pu-Fueled CRBR at EOC 17 by Different Methods	140
VII-2	Unvoided Doppler Coefficient, $-T \frac{dk}{dT} \times 10^4$ by Region Over Different Temperature Ranges in LWR-Pu-Fueled CRBR at EOC 17	141

LIST OF TABLES (Contd)

<u>No.</u>	<u>Title</u>	<u>Page</u>
VII-3	Voided Doppler Coefficient, $-T \frac{dk}{dT} \times 10^4$ by Region Over Different Temperature Ranges in LWR-Pu-Fueled CRBR at EOEC 17	142
VII-4	Steel Worth, $\frac{\Delta k}{k} \times 10^3$ by Region in LWR-Pu-Fueled CRBR at EOEC 17 by Different Methods	143
VII-5	Core Fuel ^a Worth, $\frac{\Delta k}{k} \times 10^3$ by Region in LWR-Pu-Fueled CRBR at EOEC 17 by Different Methods	144
VII-6	Contribution to Differences in Sodium Void Worth for Two Subassemblies in the Inner Core	145
VII-7	Comparison of Peak Reactivity Coefficients by PSAR Channel ($10^{-5} \frac{\Delta k}{k}$ per kg).	145
VII-8	Effect on the Sodium Voiding Reactivity in the Inner Core of CRBR at EOEC of Changing from ENDF/B-III data to ENDF/B-IV for Selected Materials (One-Dimensional Model)	146
VII-9	A More General Fit for the Temperature Dependence of the Doppler Effect in the LWR-Pu-Fueled Clinch River Breeder Reactor at EOEC 17, $\frac{1}{k} \frac{dk}{dT} = -\alpha T - \gamma$	146
VII-10	Comparison of Doppler Coefficients with the Preliminary Safety Analysis Reprot (PSAR) for the LWR-Pu-Fueled Clinch River Breeder Reactor at EOEC 17	147
VII-11	Comparison of Doppler Coefficients by Channel for the LWR-Pu-Fueled CRBR at EOEC 17	147
IIIX-1	Comparison of Reactivity Coefficients for Full Core Height, by Channel, for LWR-Pu-Fueled CRBR at BOEC 14 as Obtained from 2-D Triangular-Mesh and R-Z Perturbation Calculations, $\Delta k/k^2 \times 10^3$	148
IIIX-2	Comparison of the Sodium Void Worth by Channel and Component over Full Core Height as Obtained from 2-D Triangular-Mesh and R-Z Perturbation Calculations for LWR-Pu-Fueled CRBR at BOEC 14 (Normalized to 100 for the total worth from R-Z Calculations)	149
IIIX-3	Comparison of Reactivity Coefficients for a 5.752 cm thick Slice about the Midplane, by Channel, for LWR-Pu-Fueled CRBR with Normal Sodium at EOEC 17 as Obtained from 2-D Triangular-Mesh and R-Z Perturbation Calculation, $\Delta k/k^2 \times 10^4$	150

LIST OF TABLES (Contd)

<u>No.</u>	<u>Title</u>	<u>Page</u>
IIX-4	Comparison of Reactivity Coefficients for a 5.752 cm Thick Slice about the Midplane, by Channel for LWR-Pu-Fueled CRBR with Sodium Voided at EOEC 17 as Obtained from 2-D Triangular-Mesh and R-Z Perturbation Calculations, $\Delta k/k^2 \times 10^4$	151
A.1	The ANL-27 and WARD-9 Broad Group Energy Structures	152
A.2	Description of Cells Used to Compute Cross Sections Using Integral Transport Theory Capability of MC ² -2 Code	153
A.3	CRBR Configuration & Compositions Used in SDX Code to Collapse to 27 Groups	154

PHYSICS CALCULATIONS FOR THE
CLINCH RIVER BREEDER REACTOR

by

Kalimullah, P. H. Kier,
and H. H. Hummel

ABSTRACT

Calculations of distributions of power and sodium void reactivity, unvoided and voided Doppler coefficients and steel and fuel worths have been performed using diffusion theory and first-order perturbation theory for the LWR discharge Pu-fueled CRBR at BOL, the FFTF-grade Pu-fueled CRBR at BOL and for the beginning and end of equilibrium cycle of the LWR-Pu-fueled CRBR. The results of the burnup and breeding ratio calculations performed for obtaining the reactor compositions during the equilibrium cycle are also reported. Effects of sodium and steel contents on the distributions of sodium void reactivity and steel worth have also been studied. Errors and uncertainties in the reactivity coefficients due to cross-sections and the two-dimensional geometric representations of the reactor used in the calculations have also been estimated. Comparisons of the results with those in the CRBR PSAR are also discussed.

I. INTRODUCTION

This report describes physics calculations for the beginning of life (BOL) state, for which some preliminary results were reported in Ref. 1, and the beginning and end of equilibrium cycle (BOEC and EOEC) states of the Clinch River Breeder Reactor (CRBR),² undertaken to provide power and reactivity coefficient distributions for use in accident studies mostly performed at Brookhaven National Laboratory (BNL) in support of the CRBR Preliminary Safety Analysis Report (PSAR) review by Advanced Reactors Division of Reactor Licensing. As a decision was made later to employ Fast Flux Test Facility (FFTF) grade plutonium fuel in the first core and subsequent two reloads of the CRBR due to unavailability of Light Water Reactor (LWR) discharge plutonium, power and reactivity coefficient distributions for the FFTF-Pu-fueled CRBR at BOL have also been reported here. The SAS3A channel definitions at BOL, BOEC and EOEC used in this work are those used at BNL for accident studies. The results of the burnup calculations performed for obtaining reactor compositions during the equilibrium cycle are also reported here.

Four cross-section libraries were generated from the ENDF/B Versions III and IV data for use in these calculations. Comparisons of R-Z geometry and 2-D triangular mesh calculations of reactivity coefficients using ENDF/B-III cross-sections were made to get an estimate of the uncertainty due to geometric representation. The reactivity coefficients at EOEC were calculated using two cross-section sets, one based on the ENDF/B-III data and the other based on the ENDF/B-IV data, to get an estimate of the uncertainties due to cross-sections.

II. CALCULATION OF POWER AND REACTIVITY COEFFICIENT DISTRIBUTIONS FOR THE LIGHT WATER REACTOR GRADE PLUTONIUM-FUELED CRBR AT THE BEGINNING OF LIFE

Figure II-1 shows the layout of the inner core, outer core, radial blanket and reflector regions in the Clinch River Breeder Reactor (CRBR), and also shows the identification numbers assigned to the subassemblies in the Preliminary Safety Analysis Report and the present report.

The present calculations of power and reactivity distributions are improved over those reported earlier¹ in that the revised fuel masses and hot full power volume fractions given in the Preliminary Safety Analysis Report (PSAR)² Table D4-1, and the hot full power axial dimensions in the PSAR Fig. D4-14 have been used in the present calculations. The hot full power subassembly pitch is 12.16 cm (4.788 in.). The 1 w/o of ^{238}Pu present in the Light Water Reactor (LWR) grade plutonium not accounted for in the earlier¹ analysis has also been included. All the dimensions, volume fractions and fuel masses used in the present analyses are put together in Table II-1 and the R-Z model shown in Fig. II-2. A 27-group temperature-dependent sodium present and voided cross-section set (Appendix A) generated from the ENDF/B version III data for four reactor regions (inner core, outer core, blanket and reflector) using the MC²-2 and SDX codes^{3,4} was employed in all of the calculations at the Beginning of Life (BOL) unless otherwise specified.

A. Calculations of Power Distribution at the Beginning of Life

The axial distribution of power and the radial power factors of the core and radial blanket subassemblies were calculated using the 2-D R-Z and 2-D triangular mesh diffusion theory capabilities⁵ of the Argonne Reactor Computations (ARC) System. Figure II-2 shows the R-Z model of the hot full power CRBR at the beginning of life. The central control rod and the six rods at flats of row 7 are two-thirds inserted, and all other rods are completely withdrawn. All the primary control rods contain B_4C absorber of natural enrichment (19.8 w/o ^{10}B) having 1.21 kg of ^{10}B per subassembly. The axial reflectors (steel and sodium 28.50 and 41.54 v/o) and the radial reflector (inconel X, steel and sodium 75.20, 13.65 and 11.15 v/o) are essentially of infinite thickness neutronically. The axial variation of sodium density in the core subassemblies was accounted for in the R-Z model by computing the steady state coolant temperature distribution using the SAS code⁶ and averaging the axial distributions of all the core subassemblies. The resulting average coolant temperature is shown in Table II-2.

Figures II-3 to II-7 show the axial variation of power at different typical locations in the core, lower and upper axial blankets and the radial blanket at BOL with the fuel assumed at a uniform temperature of 1100°K, and Fig. II-8 shows the radial distributions at core top and bottom and in the axial blankets at their interface with the core ends. Table II-3 summarizes total power produced in different reactor regions. The maximum (in row 7) and the minimum (in row 4) axial power shape skewness [(power density at core bottom)/(power density at core top) minus 1] are 31% and 16%, compared to 20% row-independent skewness reported in the PSAR Fig. 4.3-9. Calculations with all control rods out indicate that the axial variation of sodium density causes an insignificant skewness ($\sim 0.2\%$) in the axial power distribution.

Axial variation of fuel temperature is estimated to have a greater effect on the skewness of axial power distribution (3 to 4%). With the lower half of the reactor fuel at 300°K and the upper half at 2200°K, an upper limit of the skewness of power distribution caused by axial variation of fuel temperature was found to be about 10%.

For the 2-D triangular mesh model used for computing the radial power factors, a sodium density of 0.8426 gm/cm³ corresponding to an axially averaged coolant temperature of 722°K was used. By a buckling search, a half height of 64.744 cm was determined such that the k-effective with all the control rods completely withdrawn equaled that obtained from the R-Z model. Figures II-9, II-10, and II-11 show the subassembly power factors, the subassembly peak-to-average power density ratios and the subassembly peak power factors when the central control rod and the six rods at flats of row 7 are fully inserted, and all other control rods are completely withdrawn. Subassembly power factor is defined as the power produced in the subassembly divided by the average power per subassembly in the region (core or radial blanket). Subassembly peak-to-average power density ratio is defined as the power of the highest power pin in the subassembly divided by the average power per pin in the subassembly. Subassembly peak power factor is defined as the power of the highest power pin in the subassembly divided by the average power per pin in the region (core or radial blanket). The comparison of core subassembly power factors shown in Fig. II-9 with those in the PSAR Fig. 4.3-5 shows that the present calculation gives slightly higher (maximum difference 1% in row 2) values in rows 2-6, and lower (maximum difference 1% at corners of row 9) in rows 7-9. The maximum peak-to-average power density ratio at corners of row 9 is 1.173 based on the present calculation compared to 1.218 reported in the PSAR. It should be noted that the central control rod and the six rods at flats of row 7 are assumed to be fully inserted in the 2-D triangular mesh model although they are required to be actually inserted two-thirds.

B. Calculation of Sodium Void Worth Distribution at BOL Using RZ Model

Using the R-Z model of section II.A and the 2-D R-Z diffusion perturbation theory capability⁷ of the ARC System, studies have been made, at a uniform fuel temperature of 1100°K, of the distribution of sodium void reactivity and its resonance self-shielding part and the effects of steel and sodium content of the reactor on sodium void reactivity. Table II-4 summarizes sodium void worths totalled by reactor region computed by first order perturbation theory and by k-effective difference using three different cross-section sets, the standard Version III cross-section set and the Version IV cross-section set 1 (both generated using the narrow resonance approximation as described in Appendix A) and the Version IV cross-section set 2 (generated using the RABANL integral transport theory neutron slowing down³ over the resonance energy interval). Voided microscopic cross-sections were used for isotopes remaining in voided regions of the reactor. The control subassemblies were never voided. Table II-5 shows rough percentages of the different reactivity components obtained by first order perturbation calculations of sodium void and other reactivities, normalized to 100% for the total effect. These results show to what extent large compensating positive and negative effects occur, and give an idea of the uncertainty of the net total of the components (due to difference in methods of analysis or small changes in the state of the reactor) for sodium void reactivity in

core and blanket regions. Based on the channels defined in Table II-6, a comparison is shown in Table II-7 of sodium void worth distributions in the normal reactor and in the core-and-blankets-voided reactor, cases 1 and 2 of Table II-4, totalled by channel. The difference between the spatial distributions of cases 1 and 2 is quite significant as shown by Figs. II-12, II-13, and II-14 which compare the axial distributions of sodium void worth of cases 1 and 2 at some typical locations in the core, upper axial blanket and the radial blanket. Figures II-15 to II-19 show the axial distributions of sodium void worth obtained by averaging those in the normal reactor and the core-and-blankets-voided reactor, cases 1 and 2, for all the subassembly rows in the core, lower and upper axial blankets and radial blanket.

The regional totals of sodium void $\Delta k \times 10^3$ obtained by k-effective difference at a uniform fuel temperature of 1100°K, listed as case 3 of Table II-4, are (11.55, -2.70, -1.45, -0.92, -1.79, 4.69) compared to (9.89, -3.03, -0.91, -0.84, -1.53, 3.58) reported in the PSAR Table 4.3-10. Case 3 is also included in Table II-3 as the recommended regional totals of sodium void worth. A comparison of cases 4 and 5 of Table II-4 shows that the resonance self-shielding change accounts for about 16.5% of the total sodium void worth of the inner core. A comparison of cases 6 and 7 shows that the inner core void worth changes by only about 6% with steel content changing from 0.5 to 1.5 of normal. A study of cases 8 and 9 shows that the inner core specific sodium void worth changes by less than 5% with the sodium content changing from normal to zero.

Cases 10 and 11 show sodium void worth distributions computed by linearized leakage perturbation in a normal reactor using the Version IV cross-section sets 1 and 2, respectively. These void worths are more positive mainly due to higher ^{238}U capture cross-sections in the resonance energy interval, e.g. in Version IV cross-section set 2 the ^{238}U capture cross-section in groups 17-22, i.e. from 3.36 keV to 0.10 keV is from 2% to 29% higher than that in Version IV cross-section set 1. Increase in the ^{238}U capture cross-section below about 67 keV causes an increase in sodium void worth. Cases 12 and 13 give total inner core void worths computed by k-effective difference using the Version IV cross-section sets 1 and 2, compared to the worth obtained in case 3 by the same method using the standard Version III cross-section set. Case 14 and 15 show total inner core void worths without the resonance self-shielding part computed by k-effective difference using the Version IV cross-section sets 1 and 2, compared to that obtained in case 4 using the Version III cross-section set. Comparison of cases 12 to 15 shows that the resonance self-shielding accounts for about 18.2% of the total inner core void worth based on the Version IV cross-section sets.

C. Calculation of Unvoided and Voided Doppler Coefficient Distributions at BOL Using R-Z Model

Table II-8 summarizes Doppler coefficient distributions in the unvoided reactor totalled by region over different temperature ranges, computed by first order perturbation theory and k-effective difference. Cases 1 and 2 are Doppler coefficient calculations over the temperature range 2200-4400°K by diffusion perturbation theory, considering the reactor fuel to be initially at a uniform temperature of 2200°K and then to be heated to 4400°K during perturbation in case 1. The reverse is assumed in case 2, i.e. the reactor is considered to be initially at 4400°K and then to be cooled to 2200°K

during perturbation. The resonant isotopes whose capture and fission cross-sections were considered temperature-dependent are ^{235}U , ^{238}U , ^{238}Pu , ^{239}Pu , ^{240}Pu , ^{241}Pu , and ^{242}Pu . The difference between the spatial distribution of cases 1 and 2 is quite significant as shown by Figs. II-20, II-21, and II-23 in which are compared the axial distributions of unvoided Doppler coefficients of cases 1 and 2 at some typical locations in the core, upper axial blanket and the radial blanket. Case 3 which is the average of cases 1 and 2 represents a more accurate unvoided Doppler coefficient distribution over the temperature range 2200-4400°K, and the total of the core and blankets in case 3 agrees more closely to the exact total in case 4 obtained by k-effective difference. Figures II-23 to II-27 show the axial distributions of the unvoided Doppler coefficient of case 3 for all the subassembly rows of the core, lower and upper axial blankets and radial blanket. Recommended regional totals of the unvoided Doppler coefficient over the range 2200-4400°K are also included for case 3 in Table II-3. Table II-7 shows the unvoided Doppler coefficient of case 3 by channel, and the total $T dk/dT \times 10^4$ of all channels is -62.30 compared to -62.50 reported in the PSAR Table D4-11.

Table II-8 case 5 gives unvoided Doppler coefficient distribution obtained by R-Z diffusion perturbation theory considering the reactor fuel to be initially at a uniform temperature of 1100°K and then to be heated to 2200°K during perturbation. Case 7 is obtained by normalizing case 5 to the total unvoided Doppler coefficient over 1100-2200°K computed by k-effective difference, shown as case 6. As shown by the comparison of cases 1 to 4, case 7 represents a more accurate unvoided Doppler coefficient distribution over the temperature range 1100-2200°K than case 5. Case 8 is an average value over the range 1100-4400°K and has been obtained by k-effective difference.

Cases 9 and 10 show the distributions of unvoided Doppler coefficient over 2200-4400°K computed by first order perturbation theory using the Version IV cross-section sets 1 and 2, compared to that obtained in case 5 by the same method using the standard Version III cross-section.

Table II-9 summarizes voided Doppler coefficients totalled by reactor region over different temperature ranges in the same order as Table II-8 summarizes unvoided Doppler coefficients. In the voided case, the core, lower and upper axial blankets and radial blanket of the reactor were completely voided including the sodium in the intersubassembly duct wall gap but excluding the control subassemblies. Figures II-28, II-29, and II-30 compare the axial distributions of the voided Doppler coefficients over the range 2200-4400°K of cases 1 and 2, computed by first order perturbation using fluxes at 2200°K and 4400°K respectively, at some typical locations in the core, upper axial blanket and the radial blanket. Figures II-31 and II-32 show the axial distributions of the voided Doppler coefficient over the range 2200-4400°K given by case 3 of Table II-9. Its distribution by channel is given in Table II-7 and case 3 is also included in Table II-3 as the recommended regional totals of voided Doppler coefficient over 2200-4400°K. The total $T dk/dT \times 10^4$ of all channels is -38.94 compared to -36.0 reported in the PSAR Table 4.3-9. Case 7 of Table II-9 gives the recommended regional totals of the voided Doppler coefficient over the temperature range 1100-2200°K.

Table II-10 summarizes Doppler coefficients averaged over the temperature range 1100-4400°K for different stages of sodium voiding. The comparison of cases 4 and 5 shows that the inner core Doppler coefficient of the core-and-blankets-voided reactor reduces by 20% when the control subassemblies are also voided. A study of the effect of reflector thickness shows that the inner core Doppler coefficient decreases by about 3% if the axial and the radial reflectors are reduced to 1/4 and 1/2 of their thicknesses.

D. Calculation of Steel Worth Distribution at BOL Using R-Z Model

Studies have been made of the steel worth distribution and of the effects of steel and sodium contents on this distribution. Table II-11 summarizes steel worth distributions totalled by reactor region computed by linearized leakage perturbation theory, exact leakage perturbation theory and k-effective difference at a uniform fuel temperature of 1100°K. The large values of rough percentages of leakage, spectral and capture components of steel worth in the outer core indicate the great uncertainty of the steel worth in the outer core with respect to small changes in the reactor and to different methods of analysis. This uncertainty is also clear from Table II-11. The worth of half of the total steel in cladding, wrapper wires and the subassembly duct in an unvoided reactor, at a uniform fuel temperature of 1100°K is given under case 1 of Table II-11. Case 2 is the same with the core, axial blankets and radial blanket completely voided including the sodium in the intersubassembly duct wall gap but not the control subassemblies. Figures II-33, II-34 and II-35 compare the axial distributions of steel worth of cases 1 and 2 at some typical locations in the core, upper axial blanket and radial blanket, and Table II-7 compares the totals by channel of these steel worth distributions. The difference between these two cases in the inner core is not small. Figures II-36, II-37, and II-38 show the axial distributions of steel worth obtained by averaging cases 1 and 2, for all the subassembly rows. The average steel worth is also included in Table II-3 as the recommended regional totals, and the spatial distribution of this average agrees with the PSAR Table D4-18 within 8%.

Case 3 of Table II-11 shows the steel worth distribution in the reactor with only the inner core voided. Cases 4 to 7 show the effect of the exact leakage component of reactivity, compared to the linearized value for the inner core voided and for the normal reactor. The steel worth distribution computed by the exact leakage perturbation with steel removal during perturbation is more positive than with steel addition during perturbation because of the larger (positive) leakage component of the reactivity. Cases 8 to 11 show inner core steel worths in the inner-core-voided and the normal reactors computed by k-effective difference for 50% steel removal from and addition to the inner core region. A study of cases 1 to 11 shows that the inner core steel worth decreases by less than 4.5% in magnitude when the inner core is completely voided. Cases 12 and 13 are respectively the worths of the first 10% and all the 100% of the normal amount of the inner core steel computed by k-effective difference for removing steel. A study of cases 8 to 13 indicates that the inner core steel worth changes by less than 3.7% when the steel content of the inner core changes by 0.5 of normal.

Cases 14 and 15 show steel worth distributions computed by first-order perturbation theory using the Version IV cross-section sets 1 and 2, com-

pared to that obtained in case 1 by the same method using the standard Version III cross-section set. The effect of using Version IV cross-section is not very significant on the steel worth distribution.

E. Calculation of Core Fuel Worth Distribution at BOL Using R-Z Model

Table II-3 shows regional totals of core fuel worth computed by first order perturbation theory in the reactor with the core, axial blankets and radial blanket completely voided (excluding the sodium in the control sub-assemblies) and with the fuel at a uniform temperature of 1100°K. In the axial blankets above and below the inner core zone, it is the inner core fuel whose worth was computed, and in the axial blankets above and below the outer core zone the worth of outer core fuel was computed. In the radial blanket the worth of radial blanket fuel was computed. This was done because in hypothetical core disruptive accidents only the core fuel may move and relocate during the initial phase of the accident which will be analyzed using these worth distributions. Figures II-39 to II-43 show the axial distributions of core fuel worth for all subassembly rows in the core, lower and upper axial blankets and radial blanket. Table II-7 shows the distribution of core fuel worth totalled by channel. The total of the inner and outer core fuel worths is nearly 6% higher than that reported in the PSAR Table D4-16. The skewness of the axial distribution of core fuel worth ranges from 22% to 37% due mainly to the partial insertion of the control rods.

III. CALCULATION OF POWER AND REACTIVITY COEFFICIENT DISTRIBUTIONS FOR THE FAST FLUX TEST FACILITY GRADE PLUTONIUM-FUELED CRBR AT BOL

The distributions of power and reactivity coefficients for the Fast Flux Test Facility (FFTF) grade plutonium-fueled CRBR at BOL was studied because of the recent decision to employ FFTF plutonium in the fresh fuel for the first core due to unavailability of the LWR plutonium. All these calculations were performed using the same methods and the R-Z model as those used in Section II for the calculation of power and reactivity worth distributions in the LWR-Pu-fueled CRBR, except that the R-Z model was modified to account for the changes in (a) the total heavy metal masses in the inner and outer cores, (b) the enrichments of the inner and outer core regions and (c) the isotopic composition of plutonium. The isotopic composition of the FFTF-grade plutonium, $^{238}\text{Pu}/^{239}\text{Pu}/^{240}\text{Pu}/^{241}\text{Pu}/^{242}\text{Pu}$ is 0.0/86.4/11.7/1.7/0.2 w/o compared to 1.0/67.3/19.2/10.1/2.4 w/o of the LWR discharge grade plutonium. With the FFTF-grade plutonium the required enrichments of the inner and outer core regions are 17.7 w/o and 25.6 w/o Pu/(U+Pu) compared to 18.7 w/o and 27.1 w/o Pu/(U+Pu) for the LWR-grade plutonium fuel as reported in the PSAR Chapter 4.3. The total heavy metal masses (including plutonium and uranium but excluding oxygen) in the inner and outer cores of the FFTF-Pu-fueled CRBR at BOL as reported in the PSAR Table 4.3-32 are 3561 kg and 2981 kg. Control rod insertions were the same as those used in the case of the LWR-grade plutonium-fueled CRBR at BOL, and the standard Version III cross-section set was used in all the calculations.

Table III-1 summarizes the regional totals of power, sodium void worth, unvoided and voided Doppler coefficients, steel and core fuel worths both for the FFTF-grade and the LWR-grade plutonium fuels, the method of analysis being alike in each case. Table III-2 shows the totals by channel of the distributions of power and reactivity coefficients in the FFTF-Pu-fueled CRBR at BOL.

Figure III-1, III-2, and III-3 show the subassembly power factors, subassembly peak-to-average power density ratios and subassembly peak power factors obtained from a 2-D triangular mesh diffusion theory calculation with the central control rod and the six rods at flats of row 7 fully inserted. Figures III-4, III-5, and III-6 show the axial distributions of power in all the rows of the core and some typical locations in the radial blanket obtained from a 2-D R-Z diffusion theory calculation with the central control rod and the six rods at flats of row 7 inserted two-thirds into the core, and with the fuel assumed at a uniform temperature of 1100°K. Figure III-7 shows the radial distributions at core top and bottom and in the axial blankets at their interface with the core ends. Comparison of regional power totals, subassembly power factors, subassembly peak-to-average power density ratios and axial power profiles between the FFTF-grade and the LWR-grade plutonium fuels shows that the power distribution remains essentially unchanged.

The sodium void worth and steel worth distributions have been computed by 2-D R-Z linearized leakage diffusion perturbation theory using the real and adjoint fluxes generated in the normal reactor at a uniform fuel temperature of 1100°K. Figures III-8 and III-9 show the axial distributions of sodium void worth in all the rows of the core and some typical locations in the radial blanket, and Figs. III-10, III-11, and III-12 show comparisons of

typical axial distributions in the core, upper axial blanket and radial blanket of sodium void worth between the FFTF-grade and the LWR-grade plutonium fuels (obtained by precisely the same method of analysis). Figures III-13 and III-14 show the axial distributions of steel worth in all the rows of the core and some typical locations in the radial blanket, and Figs. III-15, III-16, and III-17 show comparisons of typical axial distributions in the core, upper axial blanket and radial blanket of steel worth between the FFTF-grade and the LWR-grade plutonium fuels. In the blanket regions the comparisons are closer than those in the core regions both for the sodium void and the steel worth distributions, and the comparisons for the steel worth distributions are in general closer than those for the sodium void worth distributions. When converted into dollars, (total effective delayed neutron fraction is 0.00335 using the FFTF fuel compared to 0.00365 using the LWR fuel as reported in the PSAR Table 4.3-33) the inner core sodium void worth with the FFTF-plutonium fuel is found about 18% larger than that with the LWR-plutonium fuel, whereas the corresponding comparison reported in the PSAR Table 4.3-35 shows an increase of about 24%. A similar comparison of the inner core steel worth shows an increase in magnitude of a little less than 11% only. Table III-2 shows the totals by channel of the steel worth distribution in the FFTF-plutonium-fueled CRBR when the core and the axial and radial blankets are completely voided (excluding the sodium in the control subassemblies).

The distributions of unvoided and totally voided (including the sodium in the intersubassembly duct wall gap of core and blanket regions but excluding the sodium in the control subassemblies) Doppler coefficients over the temperature range 2200-4400°K have been computed by 2-D R-Z diffusion perturbation theory using the pairs of real and adjoint fluxes at both ends of the temperature range and then taking the average of the distributions resulting from the perturbations at the two temperatures. Figures III-18 to III-21 show the axial distributions of the unvoided and voided Doppler coefficients in all the rows of the core and some typical locations in the radial blanket, and Figs. III-22 to III-27 show comparisons of their typical axial distributions in the core, upper axial blanket and radial blanket between the FFTF-grade and the LWR-grade plutonium fuels (obtained by precisely the same method of analysis). The unvoided Doppler coefficient for the FFTF-Pu-fueled CRBR is about 3.4% lower, and the voided Doppler coefficient about 4.0% lower than those for the LWR-Pu-fueled CRBR.

Figures III-28 to III-31 show the axial distributions of core fuel worth in all the rows of the core and axial blankets, and the axial distributions of radial blanket fuel worth at some typical locations in the radial blanket, computed by 2-D R-Z linearized leakage diffusion perturbation theory using the real and adjoint fluxes generated in the core-and-blanket-voided reactor at a uniform fuel temperature of 1100°K. Comparison of fuel worth distributions between the FFTF-plutonium and the LWR-plutonium-fueled CRBR shows that these are essentially the same in units of $\Delta k/k$ per kilogram. It should be pointed out that the FFTF-plutonium fuel is about 9% higher in specific reactivity worth in dollar units than the LWR-plutonium fuel because of the difference in the total delayed neutron fraction.

IV. EQUILIBRIUM CYCLE BURNUP CALCULATION USING LWR-Pu FUEL

A. Burnup Pattern of Initial Cycles

Based on the core and radial blanket fuel management indicated in the Preliminary Safety Analysis Report² (PSAR), Fig. 4.3-3 and described in some detail in Ref. 8, Table IV-1 gives the number of cycles of burnup at the end of cycles 1 to 13 (beginning of cycle 1 marks beginning of life) for core and radial blanket subassembly locations identified by the subassembly identification numbers defined in the PSAR, Fig. D4-6. While the inner and outer core fuel subassemblies remain fixed in their locations between charging and discharging for three cycles, Table IV-2 describes the shuffling paths of the radial blanket subassemblies during their six-cycle residence in the blanket. The first cycle is of 128 days, the second 200 days, and the third and succeeding are of 274 days.

It is clear from Table IV-1 that cycles 1 to 7 are non-equilibrium cycles, and cycle 8 is the earliest which appears to be an equilibrium cycle as far as the burnup of different subassemblies measured in number of cycles is concerned. The actual burnup and composition of the subassemblies must be different from the values calculated for an equilibrium cycle because all the burnt subassemblies in cycle 8 were exposed to non-equilibrium neutron flux and adjacent subassemblies for up to 5 cycles. In view of the 3-cycle residence time of subassemblies in core, cycle 11 should have a core composition close to that of the equilibrium cycle. As far as both the core and the radial blanket subassemblies are concerned, cycle 14 should be the earliest to have the equilibrium composition because the radial blanket subassemblies have a 6-cycle residence time. The present calculations of power and reactivity distributions have been done using the core and radial blanket subassembly compositions at the beginning of cycle 14.

B. Equilibrium Cycle Calculation and Results

The equilibrium cycle calculation was performed with the help of the REBUS-2 Code⁹ using the R-Z model shown in Fig. IV-1 and a 9-group cross-section set based on ENDF/B Version III data. In the R-Z model each two adjacent fuel subassembly rows, e.g. rows 2 and 3, were put in one radial burnup region because taken together the two rows contain an exactly equal number of burnup stage 1, 2, and 3 subassemblies as the REBUS-2 Code requires. Axially there are two regions in the axial blanket and four in the lower half of the core. The REBUS-2 Code is not capable of modelling the charging and shuffling shown in Tables IV-1 and IV-2 of subassemblies in the radial blanket because unequal numbers of subassemblies are charged at the beginning of the six different equilibrium cycles. In the present calculation the whole of the radial blanket was put in one radial burnup region (thus smearing all the shuffling) and one-sixth of the blanket was assumed to be charged at the beginning of each cycle. The core and axial blanket are refueled in thirds.

Table IV-3 shows some of the basic input to the equilibrium cycle calculations. The cycle length of 274 days was split into four equal burn-steps. The fuel cycle was assumed to be of the once-through type with no reprocessing and recycle of the burnt fuel. The isotopic compositions of plutonium and uranium required for fabricating fresh charge are the same as

those at the beginning of life. The full atom densities of the fresh charges for the inner core, outer core, axial blanket and radial blanket, and the ratio of outer core charge enrichment to inner core charge enrichment are also the same as those at the beginning of life. Keeping the ratio of outer core to inner core charge enrichments constant at 1.4500, the enrichments of the inner and outer cores were adjusted to obtain a k -effective of 1.002 ± 0.005 with all control rods withdrawn at the end of the equilibrium cycle.

At each of the five time nodes, control absorber concentration search was done for the central rod containing natural enrichment B_4C and the 12 rods at the flats and corners of row 7 containing 50 w/o enrichment B_4C to keep the reactor critical. The control absorber was assumed to be smeared over the full core height and all the 18 rods were assumed to move together as one bank. The six control rods at corners of row 4 were always out.

Table IV-4 shows all the nuclear reactions accounted for in the burnup calculations. Two sets of lumped fission products available in ENDF/B Version III data for ^{239}Pu and ^{235}U fissions were used, and isotopes beyond the tertiary ones were not accounted for. Table IV-5 summarizes the yields¹⁰ and atomic weights of all the fission products for ^{239}Pu and ^{238}U fissions. The atomic weights of RSFP (rapidly saturating lumped fission product) and SSFP (slowly saturating) were determined by averaging the atomic weights of the isotopes in each lumped group weighted by their isotopic yields, and the atomic weight of NSFP (non-saturating) was determined based on mass conservation during fission. The data for yields, atomic weights and cross-sections of the lumped fission products of ^{235}U fission were also used for the fissions of ^{238}U , ^{236}U , ^{237}Np , ^{241}Am , ^{243}Am , and ^{244}Cm , and the corresponding data for ^{239}Pu fission were also used for the fissions of ^{238}Pu , ^{240}Pu , ^{241}Pu , and ^{242}Pu .

Table IV-6 shows the enrichments of the fresh fuel subassemblies required for refueling the inner and outer cores such that a k -effective of 1.002 is obtained with all control rods withdrawn at the end of the cycle. These enrichments, 21.139 w/o for the inner core and 30.635 w/o for the outer core, are higher than those required at the beginning of life, 18.7 and 27.1 w/o respectively. Table IV-6 also shows the reactor breeding ratio with its regional split and regional conversion ratios as functions of time. It should be noted that ^{235}U destruction was not added to the denominator in computing these ratios. The reactor breeding ratio rises from 1.097 at BOEC to 1.140 at EOEC.

Table IV-7 shows the regional mass inventory at BOEC and EOEC of all the isotopes whose production and depletion was computed, and Table IV-8 compares the regional mass inventory at BOEC of some of the important isotopes with those reported in the PSAR,² Table 4.3-2. The total mass of fissile isotopes (^{239}Pu , ^{241}Pu , ^{235}U , and ^{242}Am) based on our calculations is 0.1% less in the inner core and 3.2% less in the outer core than that in the PSAR. The total mass of heavy metals including fission products based on our calculations is 0.6% more in the inner core and 0.4% more in the outer core than that in the PSAR. The total mass of heavy metals including fission products based on our calculations is 0.2% more in the axial blankets and 0.2% more in the radial blanket than that in the PSAR. The comparison also indicates that depleted uranium (nearly 0.2 w/o ^{235}U) has been used in the

fresh fuel for the core in the PSAR equilibrium cycle calculations whereas the use of natural uranium (nearly 0.7 w/o ^{235}U) in the fresh fuel for the core was continued from the beginning of life to the equilibrium cycle in our calculations. Table IV-9 shows the isotopic composition of the plutonium inventory at the beginning and end of the equilibrium cycle by reactor region, averaged over all the fuel in different burnup stages present in the region.

The difference of isotopic inventories (shown in Table IV-7) between EOEC and BOEC gives the net buildup of the isotope over an average equilibrium cycle. Table IV-10 shows the buildup of the different plutonium isotopes by reactor region and compares with those reported in the PSAR, Table 4.3-4. The negative sign for ^{239}Pu and ^{241}Pu buildup in the inner and outer cores indicates that there is a net depletion of fissile isotopes in the core because the conversion ratios of the inner and outer cores (shown in Table IV-6) are each less than one.

Table IV-11 shows the isotopic composition and the total mass of the plutonium present in the subassemblies discharged at the end of an average equilibrium cycle. The fissile content of the plutonium discharged from the axial and radial blankets is nearly 94 w/o compared to 68-69 w/o in the plutonium discharged from the inner and outer cores. Table IV-12 shows the cumulative burnup of core and radial blanket subassemblies with the number of cycles of residence. For the subassemblies in rows 2 to 9, the axial segments A and B are located in the core and the segments C and D in the axial blanket. The burnup of a subassembly averaged over the axial segment A gives an estimate of the maximum burnup for that subassembly.

The atom densities of all the 24 isotopes shown in Table IV-4 in the 30 regions containing these active isotopes (shown in Fig. IV-1) were also obtained from the equilibrium cycle calculations for fuels of different burnups (1 to 3 cycles of burnup for core and axial blanket regions and 1 to 6 cycles of burnup for radial blanket regions) for subsequent use in the calculation of subassembly power factors and reactivity worths.

C. Improved Equilibrium Cycle Calculations with More Detailed Radial Blanket Fuel Management Model

With a view to understand the differences between the calculations reported in the PSAR and our calculations of radial power distributions using the fuel compositions at BOEC and EOEC obtained by the above equilibrium cycle calculations, another equilibrium cycle calculation was performed with the improvement that the radial blanket was split into six annuli and the radial blanket fuel management scheme (given in Table IV-2) was modeled in an average sense as shown in Fig. IV-2. The averaging implies, for example, that 18 subassemblies are assumed to be charged each year in the annular region 71 of Fig. IV-2 although during actual fuel management 24 subassemblies (identifications 34, 35, 39, and 40) are charged at the beginning of one cycle and the remaining 12 subassemblies (identifications 33 and 41) at the beginning of the next cycle. Fig. IV-2 shows radial blanket only; axially there are six regions as before and the rest of the R-Z model is the same as that shown in Fig. IV-1. The rest of the calculational details are identical to those of the earlier (unimproved) equilibrium cycle calculation.

Table IV-13 shows the required enrichments of the fresh charges for refueling the inner and outer cores such that a k-effective of 1.002 is obtained with all control rods withdrawn at EOEC. Table IV-13 also shows the reactor breeding ratio with its regional split and regional conversion ratios as functions of time. A comparison of Table IV-6 showing the same quantities obtained by the earlier unimproved calculation with Table IV-13 shows no significant differences.

Table IV-14 shows the radial blanket heavy metal mass inventory at BOEC and EOEC obtained by the improved fuel management calculation and compares it with the heavy metal mass inventory at BOEC reported in the PSAR, Table 4.3-2. The improvements in the isotopic mass inventories of the inner core, outer core and axial blankets were insignificant. The ^{239}Pu mass inventory at BOEC has increased to 295.35 kg for the improved calculation from 250.49 kg for the unimproved calculation compared to 262.4 kg reported in the PSAR. Total fission products mass inventory at BOEC has increased to 64.86 kg from 49.39 kg compared to 46.0 kg reported in the PSAR. Table IV-15 shows the net buildup of the different isotopes of plutonium in the radial blanket over an average equilibrium cycle obtained by the improved calculation, and compares with the results obtained by the unimproved calculation and those reported in the PSAR, Table 4.3-4. The reason for the agreement between the plutonium buildups obtained by the improved and the unimproved calculations (with significant difference between the plutonium mass inventories) is that during earlier burnup stages in the inner annuli of the improved radial blanket model ^{239}Pu builds up faster due to higher (than the average over the whole radial blanket used for burnup in the unimproved calculation) neutron flux averaged over an inner annulus (inspite of lower conversion ratios). The conversion ratio decreases with increasing ^{239}Pu content. During later burnup stages in the outer annuli of the radial blanket ^{239}Pu builds up at a slower rate than that in the unimproved calculation due to lower (than the average over the whole radial blanket used for burnup in the unimproved calculation) neutron flux and lower conversion ratio. The result is that the plutonium content of six-cycle burnt subassemblies turns out to be about the same by either calculation although the improved calculation gives a higher plutonium content for less than six cycle burnt subassemblies present in the radial blanket.

Table IV-16 shows the axial maximum burnups of the radial blanket subassemblies obtained by the improved calculation. Subassembly identification 37 has a maximum burnup of 48.86 MWD/kg after six cycles of residence which is significantly different from a maximum of 18.49 MWD/kg (radially averaged over the radial blanket) obtained by the unimproved calculation. The burnups of core subassemblies obtained by these two calculations were not significantly different.

V. CALCULATION OF POWER AND REACTIVITY COEFFICIENT DISTRIBUTIONS FOR THE BOEC 14 STATE

The present calculations of power and reactivity distributions are based on the burnup calculation described in section IV.B as are all of the calculations at the end of the equilibrium cycle unless otherwise specified. The present calculations at BOEC 14 are an improvement over those reported earlier¹¹ in that the stagewise burnt up fuel compositions rather than the stage-homogenized atom densities have been employed in the core, axial blanket and radial blanket regions, and also that the skewness caused by partially inserted control rods has been studied. A 27-group temperature-dependent sodium present and voided cross-section set (Appendix A) generated from the ENDF/B Version III data for four reactor regions (inner core, outer core, blanket and reflector) using the MC²-2³ and SDX Codes⁴ was employed in all of the calculations at BOEC 14 unless otherwise specified.

A. Calculation of B₄C Absorber Concentrations for the Three Primary Control Banks and Power Distribution at BOEC 14

The radial power factors of the core and radial blanket subassemblies were calculated using the 2-D triangular mesh diffusion theory capability⁵ of the Argonne Reactor Computations (ARC) System. For the burnt subassemblies, the fuel compositions in four equal-height segments over the half core height and two equal segments over the axial blanket thickness were calculated but for the 2-D triangular mesh model the fuel compositions of the core and radial blanket subassemblies were axially averaged over the core height only and the two compositions over the axial blanket thickness were excluded from this averaging. The burnup pattern of the core and radial blanket subassemblies at BOEC 14 are shown in Table V-1. The half-height of 66.025 cm used in this 2-D model was calculated by doing a buckling search, with the control rods completely withdrawn from the system, i.e. no B₄C at all in the system, to obtain a multiplication factor of 1.0588, equal to the value obtained from a 2-D R-Z model described in a later paragraph. Following the technique outlined below, the volume fractions of natural enrichment B₄C in the central control rod (bank 1) and of 50% enriched B₄C in the six rods at flats (bank 2) and the other six at corners (bank 3) of row 7 were adjusted such that the reactivity worth of each control bank equals that of the actual partially inserted bank.

Using the 2-D triangular mesh model described, effective multiplication factors, with one of the three primary control banks individually inserted, were calculated and from their differences the worths of the three control banks (including extensions of their absorber compositions into the extrapolation thicknesses at the top and bottom of the core) were found to be 0.956, 6.157, and 4.508%Δk. Using the formula for the worth of a partially inserted control rod¹² (based on a sinusoidal axial flux variation)

$$\frac{\rho(Z)}{\rho(H)} = \frac{Z}{H} - \frac{1}{2\pi} \sin \frac{2\pi Z}{H}, \quad (1)$$

where Z = distance from the top of the reactor, H = extrapolated height of the reactor, and $\rho(Z)$ = worth of a control rod inserted to a distance Z the reactor, the worths of the central rod two-thirds inserted into the core,

control bank 2 inserted two-thirds and control bank 3 one-third (including their extensions into the upper extrapolation thickness) are 72.23%, 72.23%, and 27.77% of their full worths, i.e. 0.691, 4.447, and 1.252 Δk .

Since these calculated worths have small errors from a number of sources,¹³ and only the relative magnitudes of these worths rather than the absolute values are important in the calculation of power distribution, these values were normalized to a total equal to the excess reactivity at the beginning of the cycle, i.e. 5.88 Δk so that a critical system is obtained. The volume fractions of B_4C for each of the three control banks were adjusted to these normalized worths, i.e. 0.636, 4.093, and 1.152 Δk , by carrying out a separate concentration search for each control bank using the 2-D triangular mesh capability⁵ of the ARC System. The volume fractions of natural B_4C for the central rod and 50% enriched B_4C for control banks 2 and 3 were found to be 0.1888, 0.1649, and 0.0425. (The actual volume fraction of B_4C in primary control subassemblies is 0.3390.) These adjusted B_4C volume fractions are lower than the actual value mainly because of the partial insertion of the banks, and those for the first-two control banks, both two-thirds inserted, are different due to the difference in spatial self-shielding arising from their different enrichments.

Figure V-1 shows core subassembly power factors based on the power produced in an average core subassembly, and radial blanket subassembly power factors based on the power produced in an average radial blanket subassembly at BOEC 14, calculated for the critical reactor using the 2-D triangular mesh model with the B_4C volume fractions adjusted as just described. Figures V-2 and V-3 show the subassembly peak-to-average power density ratios and subassembly peak power factors obtained by the same calculation. Core subassembly power factors range from 3.2% higher to 4.5% lower than the values reported in the PSAR, Fig. 4.3-7, most of the larger differences being in the outer core subassemblies. Total radial blanket power has been found to be 57.6 MW (59.0 MW from the 2-D R-Z calculation described below) compared to 76.1 MW reported in the PSAR Table 4.3-7. These differences are due to (a) the inaccuracies in the unimproved radial blanket burnt fuel compositions arising from the use of only one region in the radial direction in the R-Z model used for burnup calculation, and (b) the use of an incorrect radial blanket subassembly-burnup pattern¹⁴ (different from any of the six patterns it takes during its equilibrium operation) for the calculation of the power factors reported in the PSAR Fig. 4.3-7. The power factors of core subassemblies are fairly sensitive to the detailed composition of the radial blanket. If the detailed stagewise burnup compositions used in the present calculations in the radial blanket were homogenized and used in all the blanket subassemblies, the radial blanket power would increase to about 72.0 MW, the power factors of subassemblies in row 2 of the inner core would decrease by about 4%, and those of outer core subassemblies increase by a few percent. The reason is that the fissile isotope content of the newer radial blanket subassemblies adjacent to the outer core is much lower than that of the older subassemblies in the outer rows of the blanket. Homogenization of those subassemblies is equivalent to moving fissile isotopes radially inwards, and this tilts the overall radial shape of the neutron flux (and hence power) such that it increases at larger core radii and decreases at smaller radii (as if a bank of absorber rods were withdrawn at the core-blanket interface).

In order to calculate the axial distribution of power a fairly detailed full-height R-Z model of the Clinch River Breeder Reactor (CRBR) whose radial structure is given in Table V-1 was constructed for the beginning of cycle 14. The core subassemblies were represented by 25 annuli, the radial blanket subassemblies by 3 and the control banks 2 and 3 were split respectively into 2 and 3 annuli such that the model maintains as far as practicable (a) the radial distances of subassemblies from the reactor axis, (b) the relative locations of fuel subassemblies of varying burnups, and (c) the relative location of fuel and control subassemblies. The axial variation of fuel composition in the burnt core and radial blanket subassemblies (determined for six axial segments over the half height of the reactor as described in Section IV.B) was taken into account in the model except that the compositions for the two segments nearest to the core midplane were homogenized. For these two compositions, the maximum difference between ^{239}Pu atom densities was about 1.2% for various core subassemblies (5.5% for various radial blanket subassemblies), the maximum difference between ^{238}U atom densities about 0.7% for core (0.5% for radial blanket), and the maximum difference between atom densities of fission products about 6% for core (13% for radial blanket). The axial and radial reflectors were of neutronically infinite thicknesses in the model. The central control rod (bank 1) and the six rods at the flats of row 7 (bank 2) were inserted two-thirds and the six rods at corners of row 7 (bank 3) one-third into the core, some portion of the absorber rods extending into the upper axial reflector. The volume fractions of B_4C for each of the three control banks were adjusted to the normalised worths discussed above, i.e., 0.636, 4.093 and 1.152% Δk , by carrying out a separate concentration search for each control bank using the R-Z diffusion theory capability⁵ of the ARC System. The volume fractions of natural B_4C for the central rod and 50% enriched B_4C for control banks 2 and 3 were found to be 0.2501, 0.1621 and 0.1243 compared to the actual volume fraction of 0.3390. These adjusted volume fractions of B_4C are lower than the actual value mainly because of (a) the reduction in spatial self-shielding arising from modeling discrete subassemblies into annuli, (b) the overestimation of central rod worths by R-Z geometry diffusion theory calculations.¹³

Figs. V-4 to V-7 show the axial distributions of power at different typical locations in the core, lower and upper axial blankets and the radial blanket at BOEC 14 calculated for the critical reactor using the R-Z model with the B_4C volume fractions adjusted in this way. The maximum (in row 7 subassemblies) and the minimum (in row 2 subassemblies) axial power shape skewness [(power density at core bottom)/(power density at core top) minus 1] are about 75% and 27%, compared to 20% subassembly-independent skewness reported in the PSAR Fig. 4.3-9. The skewness adjacent to the central control rod is nearly 46%. Table V-2 summarizes total powers produced in different reactor regions.

B. Effect of Isotopic Fission and Capture Energies on Subassembly Power Factors in the CRBR at the Beginning of Equilibrium Cycle 14

The subassembly power factors reported in Section V.A were calculated using our standard 27-group cross-section based on ENDF/B Version III data with an isotope-independent average energy per fission event. Isotopic fission and capture energy data was not used. Core subassembly power factors were found to differ from the values reported in the PSAR Fig. 4.3-7

by up to 3.2% higher to 4.5% lower, most of the larger differences being in the outer core subassemblies. With a view to investigate the reasons for these rather significant differences, the effect of using isotopic fission and capture energy data on subassembly power factors was analyzed.

In order to study the effect of isotopic fission and capture energies, another 27-group cross-section set based on ENDF/B Version IV data referred to as Version IV cross-section set 2 was used because the former cross-section set did not contain isotopic fission and capture energy data. This cross-section set was generated using the RABANL integral transport theory neutron slowing down capability over the resonance energy interval of the MC²-2 code and the SDX code for the specific composition and geometry of the CRBR. Using the Version IV cross-section set, two calculations of radial power distribution, one using an average energy per fission event and the other with isotopic fission and capture energies, were done. Figures V-8, V-9 and V-10 show the subassembly power factors, subassembly peak-to-average power density ratios, and subassembly peak power factors using an average energy per fission event, and Figs. V-11, V-12 and V-13 show the same using isotopic fission and capture energies. Figure V-14 shows the subassemblywise radially-averaged power densities at the midheight of the reactor core computed using isotopic fission and capture energies. It should be noted that when an average energy per fission event is used the energy per capture in a fissile isotope can still be accounted for in the analysis by lumping it with the energy per fission event. What is not accounted for is the energy per capture in coolant, structural and other isotopes, and the isotopic variation of energies per capture and per fission.

Comparison of subassembly peak-to-average power density ratios between calculations with and without isotopic fission and capture energies (done with the Version IV cross-section set 2) shows largest differences of about 4% in row 10 of the radial blanket. The differences in row 11 are smaller and those in the outermost row of the radial blanket (row 12) are not more than about two tenths of a percent. Subassembly peak-to-average power density ratios with isotopic fission and capture energies are smaller than those without, in row 10 and larger in row 12. The subassembly peak-to-average power density ratios shown in Fig. V-1 (calculated using the Version III cross-section set without isotopic fission and capture energies) are closer to the values obtained using the Version IV cross-section set 2 without isotopic fission and capture energies than those with, the values in Fig. V-1 being not more than a percent larger than the Version IV values (without isotopic energies) in row 10 of the radial blanket. In the core region the subassembly peak-to-average power density ratios obtained from all these three calculations differ by not more than a couple of tenths of a percent.

Core subassembly power factors calculated using the Version IV cross-section set 2 with isotopic fission and capture energies, shown in Fig. V-11 are up to 0.9% higher and up to 0.7% lower than those computed using the same cross-section set with an average energy per fission event, shown in Fig. V-8. Subassembly power factors calculated with isotopic fission and core region than those computed without. Comparison of Figs. V-8 and V-11 smaller power factors when isotopic fission and capture energies are accounted for, more so in the outer rows of the core. As far as the comparison of these two calculations of core subassembly power factors (using the Version IV cross-section set 2) shown in Figs. V-8 and V-11 with the values

reported in the PSAR Fig. 4.3-7 is concerned, the differences are larger for the computation with isotopic fission and capture energies.

The effect of considering isotopic fission and capture energies is significantly larger in the radial blanket because the capture power is a larger fraction of the fission power in the radial blanket. The power factors of fresh subassemblies of row 10 increase by up to 7.7% due to the additional capture energy. Strikingly, the power factor of the fresh subassembly identification number 51 in row 11 of the radial blanket increases by about 22.5% due to its low fission power (compared to other radial blanket subassemblies). The power factors of highly burnt subassemblies in the radial blanket decrease by up to 4.5%. It is irrelevant to compare radial blanket subassembly power factors with the values reported in the PSAR Fig. 4.3-7 because an incorrect radial blanket subassembly-burnup pattern, different from any of the six patterns it takes during its equilibrium operation, was used for the calculation of power factors reported in the PSAR.

This analysis indicates that the main reasons for the differences in the core subassembly power factors between our calculation reported in section V.A and PSAR Fig. 4.3-7 is not connected with the use of isotopic fission and capture energies, but are still believed to be the ones discussed in that section.

It is interesting to obtain from Fig. V-14 an estimate of the capture power in control subassemblies. The central control rod of natural enrichment B_4C , inserted 2/3 into the core, produces about 4% of the power of the fresh fuel subassembly in row 2 of the core. Each control rod at flats of row 7 containing 50% enriched B_4C and inserted 2/3 into the core produces about 7.6% of the power of the adjacent two-cycle burnt inner core fuel subassembly in the same row.

C. Calculation of Sodium Void Worth Distribution at BOEC 14 Using R-Z Model and Version III Cross-Sections

Six pairs of real and adjoint fluxes were computed by two-dimensional diffusion theory using the R-Z model of the CRBR at BOEC 14 with the B_4C volume fractions determined in Section V.A at uniform fuel temperatures of 1100°K, 2200°K and 4400°K with the normal amount of sodium present, and with core and blankets (including lower and upper axial blankets and the radial blanket but excluding the control subassemblies) completely voided. The resonant isotopes whose capture and fission cross-sections were considered temperature-dependent are ^{149}Sm , ^{235}U , ^{236}U , ^{238}U , ^{237}Np , ^{238}Pu , ^{239}Pu , ^{240}Pu , ^{241}Pu , ^{242}Pu , ^{241}Am , ^{243}Am , and ^{244}Cm . Table V-3 shows the values of k -effective obtained for these six cases. A two-dimensional R-Z first order perturbation calculation based on diffusion theory with linearized leakage component of reactivity was performed for sodium void worth distribution in the core and blanket with the fuel at a uniform temperature of 1100°K. Based on the results of sodium void worth calculations at BOL by different methods, only one perturbation calculation, i.e. the voiding of sodium from a normal reactor, was considered necessary. In the perturbed reactor with the core and blankets completely voided except for the control subassemblies, voided microscopic cross-sections were used for the fuel and structural isotopes and unvoided cross-sections for the control subassembly isotopes.

Figures V-15 to V-19 show the axial distributions of sodium void worth at different typical locations in the core, lower and upper axial blankets and the radial blanket at BOEC 14. The axial distributions for subassemblies 9 and 68 located adjacent to the partially inserted control rods at corners of row 7 have a wiggle at the tip of the control rods, one-third of the core height below the core top. The axial distribution of void worth for the subassembly 14 adjacent to the control rods at flats of row 7 has a wiggle at the tip of the rods, two-thirds of the core height below the core top. The axial maxima of void worth distributions for PSAR channels 1 and 2, defined in Table V-4 reported in the PSAR Fig. F6.2-19 are nearly 88% of those obtained by the present calculation. Table V-5 shows the total sodium void worth by channel including also the sodium in the intersubassembly duct wall gap. Table V-6 summarizes void worth totalled over reactor regions, and the total over core and blankets computed by k-effective difference agrees fairly well with that obtained by perturbation theory.

D. Calculation of Unvoided and Voided Doppler Coefficient Distributions at BOEC 14 Using R-Z Model and Version III Cross-Sections

Table V-7 summarizes unvoided Doppler coefficients totalled by reactor region over different temperature ranges computed by first order perturbation theory using the three pairs of real and adjoint fluxes (discussed in section V.C) for the unvoided reactor at fuel temperatures of 1100°K, 2200°K and 4400°K. Values of the total Doppler coefficient for the whole reactor, i.e. the core, axial blankets and radial blanket, over different temperature ranges computed by k-effective difference are also included in Table V-7. Cases 1 and 2 are Doppler coefficient calculations over the temperature range 2200-4400°K by R-Z diffusion perturbation theory, considering the reactor to be initially at 2200°K and then to be heated to 4400°K during perturbation in case 1, and the reverse in case 2, i.e. considering the reactor to be initially at 4400°K and then to be cooled to 2200°K during perturbation. Case 3 which is the arithmetic mean of cases 1 and 2 represents a more accurate unvoided Doppler coefficient distribution over the temperature range 2200-4400°K, and the total of the core and blankets in case 3 agrees more closely to the exact total in case 4 obtained by k-effective difference using Table V-3. Figures V-20, V-21, and V-22 show the axial distributions of the unvoided Doppler coefficient of case 3 at different typical locations in the core, axial blankets and the radial blanket. There is quite a significant amount of suppression of the Doppler coefficient due to the increased absorption by the control rods of neutrons in the resonance energy interval. Table V-5 shows the unvoided Doppler coefficient of case 3 by channel, and the total $T(dk/dT) \times 10^4$ of all channels is -49.60 compared to -52.26 reported in the PSAR Table F6.2-5. Since the temperature range for that Doppler coefficient is not reported in the PSAR, this comparison may not be significant.

Table V-7 case 5 gives the unvoided Doppler coefficient distribution obtained by R-Z diffusion perturbation theory considering the reactor to be initially at 1100°K and then to be heated to 2200°K during perturbation. Case 7 is obtained by normalizing case 5 to the total unvoided Doppler coefficient over 1100-2200°K computed by k-effective difference, shown as case 6. As shown by the comparison of cases 1 to 4, case 7 represents a more accurate unvoided Doppler coefficient distribution over 1100-2200°K than case 5. Case 8 is an average value over the temperature range 1100-4400°K and has been obtained by k-effective difference using Table V-3.

Table V-8 summarizes voided Doppler coefficients totalled by reactor region over different temperature ranges in the same order as Table V-7 for unvoided Doppler coefficients. In the voided case, the core and blankets of the reactor were completely voided including the sodium in the intersubassembly duct wall gap but excluding the control subassemblies. Figures V-23, V-24, and V-25 show the axial distributions of the voided Doppler coefficient over the temperature range 2200-4400°K given by case 3 of Table V-8, and the distribution by channel is given in Table V-5. The total $T(dk/dT) \times 10^4$ of all channels is -30.85 compared to -32.57 reported in the PSAR Table F6.2-5 (temperature range not specified in the PSAR). Case 7 of Table V-8 gives the recommended values of the voided Doppler coefficient over the temperature range 1100-2200°K.

E. Calculation of Steel Worth Distribution at BOEC 14 Using R-Z Model and Version III Cross-Sections

Table V-9 summarizes steel worth distributions totalled by reactor region for the unvoided and core-and-blankets voided reactor at uniform fuel temperatures of 1100°K and 2200°K, computed by first order diffusion perturbation theory with linearized leakage component of reactivity using the real and adjoint flux pairs discussed in section V.C. Case 1 gives the worth of all the steel, including cladding, wrapper wires and the subassembly duct, in a normal reactor at a uniform fuel temperature of 1100°K, and case 2 is the same with the core, axial blankets and radial blanket completely voided including the sodium in the intersubassembly duct wall gap but with the control subassemblies not voided. The difference between cases 1 and 2 is the net result of (a) increase in the leakage component of the steel worth due to reduced transport cross-sections of the voided reactor and (b) decrease in the magnitude of the capture component and an increase in the magnitude of the spectral component due to harder spectrum in the voided reactor. Figures V-26, V-27, and V-28 show the axial distributions of the steel worth obtained by averaging cases 1 and 2, at different typical locations in the core, axial blankets and the radial blanket. The axial distributions in subassemblies 1, 9, 14, and 68 which are adjacent to control rods show a wiggle at the tip of the control rods. The axial maxima of steel worth distributions for PSAR channels 1 and 2 reported in the PSAR Fig. F6.2-20 are about 2.5% lower than those obtained by averaging cases 1 and 2 of the present calculation. Table V-5 shows the steel worth distributions of cases 1 and 2 totalled by channel. The differences between the two cases are significant.

The only difference between cases 3 and 4 of Table V-9 and cases 1 and 2 is that the former two calculations were done at a uniform fuel temperature of 2200°K compared to a fuel temperature of 1100°K used in the latter two calculations. Comparison of these four calculations shows that the effect of fuel temperature on steel worth distribution is smaller than the effect of sodium voiding.

F. Calculation of Core Fuel Worth Distribution at BOEC 14 Using R-Z Model and Version III Cross-Sections

Since at any time during an equilibrium cycle the composition of the core fuel varies along the length of the subassembly due to burnup, in the present calculations the reactivity worth distribution of the burnt fuel compositions in the central quarter core height about the midplane, i.e. the regions 26, 36, 46, and 56 of the R-Z model used for equilibrium cycle calculations shown in Fig. IV-1, was computed. The core fuel whose worth was calculated also differs from one subassembly to another, and in each subassembly the worth of the fuel composition in its own central quarter height was obtained. The worths of the axial or radial blanket fuels were not computed. The worth of the core fuel itself was obtained in the lower and upper axial blankets because in hypothetical core disruptive accidents only the core fuel may move and relocate during the initial phase of the accident which will be analyzed using these worth distributions.

Table V-10 summarizes core fuel worth distributions totalled by reactor region for the normal and core-and-blankets voided reactor at uniform fuel temperatures of 1100°K and 2200°K, computed by first order diffusion perturbation theory with linearized leakage component of reactivity using the real and adjoint flux pairs discussed in section V-C. The totals in Table V-10 are worths of the central quarter core fuel whose volume equals the actual fuel volume in the region. Figures V-29 and V-30 show the axial distributions of the central quarter core fuel worth obtained by averaging cases 1 and 2, for a number of core subassemblies. The axial maxima of core fuel worth distributions for PSAR channels 1 and 2 reported in the PSAR Fig. F6.2-18 are 8% and 12% higher than those obtained by averaging cases 1 and 2 of the present calculation. Table V-5 shows the core fuel worth distributions of cases 1 and 2 totalled by channel. The differences between the two cases are significant.

The only difference between cases 3 and 4 of Table V-10 and cases 1 and 2 is that the former two calculations were done at a uniform fuel temperature of 2200°K compared to a fuel temperature of 1100°K used in the latter two calculations. Comparison of these four calculations shows that the effect of fuel temperature on core fuel worth distribution is smaller than the effect of sodium voiding.

VI. POWER DISTRIBUTION IN THE LWR-Pu-FUELED CLINCH RIVER BREEDER REACTOR AT THE END OF EQUILIBRIUM CYCLE 17

Power distribution for the CRBR at End of Equilibrium Cycle (EOEC) conditions have been computed using the triangular mesh and R-Z models and the same procedure described previously in the discussion of the power distribution for the beginning of an equilibrium cycle. The R-Z model used for EOEC 17 was the same as that used for BOEC 14 (given in Table V-1) except that the stage-homogenized fuel composition (obtained from the REBUS code) made up of equal amounts of the six burnup stages was used in the radial blanket. In the triangular mesh calculations EOEC 17 was chosen as it corresponds most closely to the configuration considered in the PSAR. In the course of performing the triangular mesh calculations, it was discovered that the power split (between core and radial blanket) and power factors for the subassemblies in the outer row of the core and in the radial blanket agreed poorly with the values in the PSAR. There were indications that too little power was being generated in the outer row of the core and the inner row of the radial blanket. We determined that the use of one region in the radial blanket in the (unimproved) equilibrium cycle burnup calculation would underestimate the buildup of plutonium in those radial blanket subassemblies that were not resident for the full six burnup cycles and would consequently underestimate the power generation in the radial blanket. Therefore, the burnup calculation was redone with the radial blanket divided into six regions as described in section IV.C and with the shuffling scheme shown in Table II-2 simulated. Significant improvements resulted.

Comparison of power splits between the radial blanket and the rest of the reactor are given in Table VI-1. It is seen that when subassembly compositions were computed with six regions in the radial blanket (the improved calculation), there was a vast improvement in the agreement with the PSAR with a difference of only 1% in the power generation in the radial blanket. Also included in the table are calculations made with the R-Z model with the ENDF/B-III and ENDF/B-IV cross section libraries. In the R-Z model, it was not feasible to use the compositions derived from the burnup calculations with six regions in the radial blanket because of storage limitations on the computer. Use of the ENDF/B-IV library resulted in a slight shift in the power distribution with approximately 2% more power being generated in the radial blanket.

The subassembly power factors, subassembly peak-to-average power density ratios and subassembly peak power factors for cases 1 and 2 of Table VI-1 are given in Figs. VI-1 through VI-6. It is seen for subassemblies in the core that the use of the improved subassembly compositions significantly improved the agreement with the values given in Table 4.3-8 of the PSAR as the root mean square deviation was reduced about 40%. With the improved power factors, the deviation from the PSAR values is less than 1% for most subassemblies. However, our results yield values in the outer row of the core that are systematically lower than the values in the PSAR by an average of 2.5%. For the subassemblies in the radial blanket, the agreement is much poorer, with the discrepancy in power factors for most subassemblies being between 10% and 30%. The use of the improved subassembly compositions did not make a significant improvement except in the outer row of the radial blanket. It is difficult to explain these large discrepancies except that it appears that the power factors given in Table 4.3-8 of the

PSAR for radial blanket subassemblies resulted from a non-standard fuel burnup pattern.

Axial distributions of power in the core and axial blankets for some typical subassemblies, calculated using the R-Z model and the Version III crosssection set (case 3 of Table VI-1) are shown in Figs. VI-7 to VI-9. Some typical axial power distributions in the radial blanket are given in Fig. V-7.

VII. CALCULATION OF REACTIVITY COEFFICIENTS FOR THE LWR-Pu-FUELED CLINCH RIVER BREEDER REACTOR AT THE END OF AN EQUILIBRIUM CYCLE (EOEC) USING R-Z MODEL AND TWO CROSS SECTION LIBRARIES

A. Methods and Cross Sections

Distributions of sodium void, steel, Doppler and core fuel reactivities have been computed using first-order diffusion perturbation theory in the R-Z model discussed in section VI and have been processed by channel and axial slice for input to the accident analysis code, SAS-3A. Subassembly compositions were obtained from the burnup calculation in which there was one region in the radial blanket. The calculations were originally run with the 27-group cross section library based on ENDF/B-III data used in the BOL and BOEC calculations. A new cross section library based on ENDF/B-IV data (Version IV cross section set 2) and incorporating the refinements in the model afforded by the additional capabilities in the MC²-2 code was also created. These refinements are the elimination of the narrow resonance approximation at low energies, temperature dependence of resonance absorption in structural materials and temperature dependence of resonance scattering. A detailed description of the procedure used to generate the new library is given in Appendix A. To assess the effect of the newer data and the refinements in the model on the reactivity coefficients, they were recomputed using the ENDF/B-IV library.

For calculating the reactivity coefficients, real and adjoint flux distributions were computed using two-dimensional diffusion theory for uniform fuel temperatures of 1100, 2200, and 4400°K with sodium present and with sodium voided in the core, axial blankets and radial blanket except for the control rods. In the ENDF/B-III library, the resonant isotopes, i.e. the isotopes with temperature-dependent cross-sections, are ¹⁴⁹Sm, ²³⁵U, ²³⁶U, ²³⁸U, ²³⁷Np, ²³⁸Pu, ²³⁹Pu, ²⁴⁰Pu, ²⁴¹Pu, ²⁴²Pu, ²⁴¹Am, ²⁴³Am, and ²⁴⁴Cm. The ENDF/B-IV library has five additional resonant isotopes: Cr, Fe, Ni, ⁵⁵Mn, and Mo. In the generation of the fluxes with the ENDF/B-IV library, the temperature of steel was taken to be that of the fuel.

These two-dimensional, R-Z model, real and adjoint fluxes were used in first-order perturbation theory computations of the reactivity coefficients. Distributions of sodium void reactivity were obtained by voiding all of sodium (except for the control rods) and by replacing isotopes whose cross-sections were derived with sodium present in the coolant channels by isotopes whose cross sections were derived with sodium voided from these channels. The sodium void perturbations were made with the fuel at 1100°K using the fluxes computed with sodium present. Distributions of steel worth were obtained from perturbations in which the steel concentration was totally removed. Four cases were considered. For sodium either present or voided, the fuel was either at 1100, or at 2200 with the steel at 1100°K. These calculations were done with both ENDF/B-III cross-sections and the Version IV cross-section set 2. Additional cases were run with the ENDF/B-IV library with both the fuel and the steel at 2200°K. The distribution of Doppler reactivities were obtained from perturbations in which the temperature of the fuel was doubled from a base temperature of either 1100 or 2200°K. Doppler coefficients were also calculated for fluxes derived for 4400°K and a temperature change from 2200 to 4400°K. Additional cases were run with the Version-IV cross-section set 2 in which the temperature of steel was also

doubled. The distribution of core fuel reactivity was obtained from perturbations in which the fuel composition at the midplane of the core was added to all regions in the core and the axial blankets except the control rods. These core fuel worths were calculated for the same cases as were the steel removal worths. The results of these calculations are summarized in Tables VII-1 through VII-5, where the reactivity coefficients have been integrated over the regions inner core, outer core, lower axial blanket, upper axial blanket, and radial blanket.

Note that all sodium is voided from the core in these calculations except from control rods. In some accident situations it is more appropriate to assume that the sodium between the subassembly cans is not voided. In this case the sodium void worth given here and the difference of the Doppler coefficient between the unvoided and voided states would be divided by approximately 1.22.

B. Sodium Void Reactivity

Table VII-1 gives the results of the sodium void worth calculations. Axial distributions of sodium void worth for EOEC 17 calculated with ENDF/B-III cross-section at 1100°K (case 1 of Table VII-1) are given in Figs. VII-1 and VII-2. Comparisons of void worths calculated with ENDF/B-III cross sections between BOEC 14 (case 1 of Table V-6) and EOEC 17 (case 1 of Table VII-1) are given in Figs. VII-3 and V-19. From Table VII-1 it is seen that the computed sodium void worth is quite sensitive to the basic cross-section data. A change from the ENDF/B-III library to the ENDF/B-IV library resulted in an increase of about 14% for the inner core region. In the inner core, the net scattering, or spectrum, term provides the major contribution to the sodium void reactivity worth. An analysis of the reactivity components for two subassemblies in the inner core, indicates that the calculated differences in the sodium void worths arises primarily from differences in the net scattering reactivity term. The results of this analysis are summarized in Table VII-6. In this table, we have tabulated the contributions to the difference in sodium void reactivity arising from the change in the cross section library and we have normalized the total difference to 100. From the table it is seen that the contribution from the other terms for all cases is relatively small.

A partial comparison of the calculation of the sodium void reactivity worth distribution, made with the ENDF/B-III library, with the results given in Appendix F of the PSAR has been made. In Table VII-7, the peak sodium void reactivity by channel for the PSAR channel selection is given. From the table it is seen that except for channel 9 our computation yields peak sodium voiding reactivities that are larger than those in Appendix F. For channels 1 through 9, our peak values average 8% greater than those in Appendix F.

A study was made to determine where the difference in the sodium void worth associated with changing from ENDF/B-III to ENDF/B-IV cross sections arises. As discussed previously, we know that the net scattering term is the main one affected. Now we want to know what isotopes are responsible for the changes. Since the net scattering term is very sensitive to changes in the real and the adjoint flux spectra, the indirect effect of the changes in cross sections upon the flux spectra as well as the direct effect of the

changes in cross sections in the perturbation theory equation for reactivity should be considered. We used a one-dimensional representation in which only the radial configuration of the R-Z model discussed in section VI was mocked up. In the reference diffusion theory and perturbation theory calculations, ENDF/B-III cross sections were assigned to all isotopes in all regions of the reactor. The diffusion and the perturbation calculations were redone with ENDF/B-IV cross sections substituted for ENDF/B-III cross sections for a specified isotope in the inner core. The difference between this perturbation theory reactivity and that in the reference problem is attributable to differences between ENDF/B-III and ENDF/B-IV cross sections for the specified isotope.

The results of this study for thirteen isotopes are summarized in Table VII-8. Because the model was one-dimensional, the core explicitly extended to the extrapolated height of the reactor. Since there are large flux gradients near the top and bottom of the reactor, beyond the actual location of the core, the contribution to reactivity from transverse leakage is grossly exaggerated. Therefore, the leakage component of reactivity was omitted from the values in the table. Earlier calculations of the contributions to the sodium void worth by component shown in Table VII-6 indicate that the leakage component accounts for about 10% of the discrepancy. From Table VII-8, it can be seen that the discrepancy arises predominantly from differences between ENDF/B-III and ENDF/B-IV cross sections for ^{238}U , ^{239}Pu , and ^{240}Pu .

C. Unvoided and Voided Doppler Coefficient

The results of the Doppler reactivity worth calculations are given, in terms of the Doppler coefficient (or constant) α for an assumed inverse temperature dependence, in Tables VII-2 and VII-3. Axial distributions of Doppler coefficients calculated with ENDF/B-III cross section, cases 7 of Tables VII-2 and VII-3, are given in Figs. VII-4 to VII-7 for EOEC 17, with comparisons between BOEC 14 and EOEC 17 given in Figs. VII-8, VII-9, V-22 and V-25. The Doppler coefficient is quite sensitive to the presence or absence of sodium, with the voided Doppler coefficients some 35 to 40% lower than the unvoided Doppler coefficients. There were slight increases in the fuel Doppler coefficients when computed with the ENDF/B-IV cross-section set 2. When the Doppler effect of the constituents of steel is included in the calculations, the Doppler coefficients are augmented by about 10%. It is doubtful, however, that heat can be transferred to the cladding rapidly enough for the Doppler effect of steel to fully contribute this 10% bonus in transient conditions.

For both unvoided and voided conditions, the Doppler constant, Tdk/dT exhibited a dependence on the temperature range covered. This constant was smaller for the temperature range from 2200 to 4400°K than for the range from 1100 to 2200°K, indicating that the assumption of an inverse temperature dependence underestimates the decrease in the Doppler effect with temperature. For the purpose of studying the deviation from the inverse temperature dependence, the following more general temperature dependence was assumed:

$$\frac{1}{k} \frac{dk}{dT} = -\alpha T^{-\gamma}, \quad (1)$$

where α and γ were obtained from least-square fit of the multiplication constants of the reactor at several temperatures as obtained from diffusion theory calculations. These parameters were computed both for the unvoided and voided systems using the multiplication constants at 1100, 2200, and 4400°K as obtained using the ENDF/B-III library. As cross sections for the unvoided system at 6600°K were available, the fit for the unvoided system was recalculated using the multiplication constant at 6600°K as the fourth data point.

The results are shown in Table VII-9. The γ 's are greater than unity which indicates that the inverse temperature correlation well underestimates the rate of reduction of the Doppler effect with temperature. That γ is greater for the voided system than for the unvoided system could be expected. The flux distribution is harder in the voided system so that the Doppler increase in cross sections at higher energies is more important for the voided system than for the unvoided system. Since the Doppler increase in cross sections saturates sooner at higher energies than at lower energies, the rate of reduction in the Doppler effect should be larger for the voided system than for the unvoided system. The fit for α and γ did not change significantly when the fourth temperature point was used; this indicates that there will not be great error in extrapolations to higher temperatures. For example, when Eq. (1) was integrated to predict k at 6600°K from the γ and α obtained with three temperature points, the resulting k differed from that obtained in a direct calculation by only 0.002%.

Tables VII-10 and VII-11 compare the Doppler coefficients computed in this work with those given in Appendix F of the PSAR for the various reactor regions and for the PSAR channel selection. Our Doppler coefficients in these tables were computed using first-order perturbation theory for the temperature range 2200 to 4400°K and the ENDF/B-III cross section library. The values in these tables are the averages of the coefficients computed with real and adjoint fluxes for the fuel at 2200°K and for the fuel at 4400°K. For the Doppler coefficient summed over channel, our computations yield results that are 9.3% lower for both the unvoided and voided situations. The discrepancies by channel are not uniform; for the channels near the center of the reactor, channels 1-4, the agreement is significantly better than for the outer channels.

D. Steel Worth

The results of the steel worth calculations are given in Table VII-4. From the table the following information can be discerned. The steel worths are only weakly dependent upon fuel and steel temperatures but have a stronger dependence upon the presence or absence of sodium. When fluxes derived for sodium voided system were used, the steel worth totalled over core and blankets was reduced by about 20% with the inner core value reducing only 4 to 5%. These should be more appropriate because steel melting would occur only after sodium voiding. Use of the ENDF/B-IV cross-section set 2 yielded

steel worths that were 5-8% larger than those computed with the ENDF/B-III cross sections. For those cases where the fuel was at 2200°K, there was an increase of only 1% in the steel worth when steel cross sections derived for 2200°K rather than 1100°K were used.

As for the sodium void worth distribution, the peak steel worths by PSAR channel are compared with the values given in Appendix F of the PSAR in Table VII-7. Here the agreement is quite good with discrepancies of less than 8% for all channels except channel 9.

Axial distributions of steel worth obtained by using ENDF/B-III cross sections and averaging cases 1 and 3 of Table VII-4 are given in Figs. VII-10 and VII-11 for EOEC 17, with comparisons of steel worths obtained by this method between BOEC 14 and EOEC 17 given in Figs. VII-12 and V-28.

E. Core Fuel Worth

The results of the core fuel reactivity worth calculations are summarized in Table VII-5. Axial distributions of core fuel worth calculated by using ENDF/B-III cross-section and averaging cases 1 and 3 of Table VII-5 are given in Figs. VII-13 and VII-14 for EOEC 17, with comparisons of core fuel worths obtained by this method between BOEC 14 and EOEC 17 given in Fig. VII-15. The fuel worths were insensitive to the cross section library used and they increased only slightly with temperature. However, they did increase by about 8% in going from an unvoided system to a voided system. The peak core fuel worths by PSAR channel are compared with the values given in Appendix F of the PSAR in Table VII-7. Our values are some 10 to 20% lower than those given in Appendix F. In view of the general insensitivity of core fuel worth to cross section library, temperature, and sodium content better agreement with the PSAR values was expected.

VIII. COMPARISON OF R-Z GEOMETRY AND TRIANGULAR MESH CALCULATIONS OF REACTIVITY COEFFICIENTS USING ENDF/B-III CROSS SECTIONS

A. Reactivity Coefficients at BOEC 14

Distribution of power and distributions of sodium void, unvoided and voided Doppler, fuel, and steel reactivities are computed using the R-Z model and are then processed by channel and axial segment into a format suitable for input to the accident analysis code, SAS-3A. To gain an insight into the uncertainties in these quantities, their sensitivity to the geometric representation of the reactor has been studied. Reactivity coefficients were computed for the same R-Z and triangular mesh representations of CRBR for which the power distributions were computed at BOEC 14. These two-dimensional perturbation calculations, for which the ENDF/B-III cross section library was used, were for the unvoided system at a uniform fuel temperature of 1100°K. The results, by channel, of this comparison are given in Table VIII-1. This comparison is not completely satisfactory because of the use of an extrapolated core height and fully inserted rods (with reduced absorber concentration) in the case of the triangular mesh, but should indicate the approximate size of the errors in the R-Z calculations. From the table, it can be seen that the comparison is excellent for the core fuel reactivity worth and is generally good for the Doppler worth. For the steel removal worth, the agreement was somewhat poorer, with the triangular-mesh results smaller for all channels. For the sodium void worth, there were significant discrepancies for most channels with the triangular mesh results being systematically smaller.

The sodium void worth comparison was studied further by decomposing the total reactivity into five components (radial leakage, axial leakage, absorption, fission source, and net scattering) and by looking at how the geometric representation affected these components. The results are given in Table VIII-2 with the normalization that for each channel the total reactivity computed with the R-Z model was taken as 100. The sodium void perturbation was defined by removing sodium and replacing unvoided isotopic cross sections by voided isotopic cross sections; hence there was a small fission source component.

From Table VIII-2 one can see that the radial leakage term, having the largest relative differences near the center of the core, is most sensitive to the geometric representation. However, near the center of the core, the spectrum effect dominates so that differences in the net scattering term account for much of the discrepancies. As one moves outward, both the radial and the axial leakage terms become sensitive to the geometric representation and gradients in the fluxes become more important relative to fluxes and the leakage terms begin to approach the net scattering term in magnitude. For such a situation, where the net effect is the difference between several large terms, small errors in the individual terms will lead to large uncertainties in the net effect. In giving the results by channel, a partial averaging over somewhat larger discrepancies per subassembly has been made. However, since the reactivity coefficients are input to the accident analysis code by channel, it is felt that this is the proper level of aggregation to study the geometric effect.

For BOEC conditions, control rods are partly inserted and this makes the configuration fully three-dimensional. This study indicates that attempts to represent a fully three-dimensional configuration in two dimensions will introduce significant uncertainties in the calculation of the distribution of sodium void reactivity. It also indicates that two-dimensional representations are adequate for the calculation of reactivity worths dominated by absorptive reactions, such as the Doppler worth and the fuel worth.

B. Reactivity Coefficients at EOEC 17

Distributions of sodium void, Doppler, fuel and steel reactivities computed using the two-dimensional triangular-mesh and the R-Z models have been compared also for EOEC 17 conditions. Here the control rods are withdrawn from the core so that it is meaningful to make the comparison for a specified axial height centered about the midplane of the reactor core. For these comparisons, the four reactivity coefficients were computed using the ENDF/B-III cross section library for the reactor at a uniform fuel temperature of 1100°K with normal sodium and with sodium voided.

The results of these comparisons for the unvoided and voided cases are given in Tables VIII-3 and VIII-4 respectively. As for the BOEC 14 case, there was excellent agreement for the Doppler and fuel worths. For these reactivity coefficients, the discrepancies for individual subassemblies appeared to be random rather than systematic. For the steel removal and sodium void worths, the discrepancies were somewhat larger and the triangular-mesh results were systematically smaller. It should be noted, however, that the discrepancies in the steel removal and the sodium void worths were significantly smaller than those obtained for the BOEC 14 condition. Comparison of Tables VIII-3 and VIII-4 shows that the spectrum changes associated with voiding of sodium do not alter the character of the results. The agreements for the EOEC 17 case would have been even better if the only difference had been the geometric representation. The triangular-mesh calculations used subassembly compositions obtained from the improved burnup calculations in which there were (radially) six regions in the radial blanket whereas the R-Z calculations, because of limitations on computer storage capacity, used subassembly compositions obtained from the burnup calculations with (radially) one region in the radial blanket.

For the EOEC 17 case, the major difference between the triangular-mesh and the R-Z configuration was the representation of hexagonal subassemblies as annuli. For the BOEC 14 case, there were the additional differences associated with representing partly inserted hexagonal control rods in two dimensions (see the discussion of the power distribution at BOEC 14). Comparison of EOEC 17 and BOEC 14 results indicates that difficulties in representing partly inserted control rods in two dimensions contributes more to the discrepancies in reactivity coefficients between triangular-mesh and R-Z calculations than does the annularization of hexagonal subassemblies.

IX. EVALUATION OF ERRORS AND UNCERTAINTIES IN REACTIVITY COEFFICIENT CALCULATIONS BECAUSE OF CROSS SECTIONS AND GEOMETRIC REPRESENTATION

A. Cross Sections

1. Sodium Void Worth

The comparison of sodium void worths as calculated by ENDF/B-III and IV data gives an idea of the uncertainty in this quantity because of cross sections. The increase found in the inner core value only because of the cross section change from Version III to IV at BOL is 12.6% according to Table II-4, with another 7.2% added if the more accurate resonance energy-interval calculation is used in MC²-2, presumably a more accurate result. Comparison with critical experiments¹⁵ has indicated that Version IV without this correction gives a C/E ratio that averages to about 1.20 over the core of a CRBR mockup. If, as Bohn et al¹⁶ contend, this discrepancy is due to cross section error and not to an error in the reactivity scale, then the more accurate Version IV calculation yields values of the sodium void worth that are too positive by about 27%. However, the fact that C/E of the net sodium void worth is fairly consistent for various ratios of spectral to leakage component (corrected for neutron streaming by use of Benoist diffusion coefficients) suggests that at least part of the discrepancy results from an error in the reactivity scale, although it has been difficult to justify further reductions in delayed neutron parameters than that already given by the Version IV parameters. The C/E value for ²³⁹Pu central worth with Version IV is 1.13. If there is assumed to be a corresponding error in the reactivity scale, the transport-theory-corrected Version IV central sodium void worth would still be 14% too positive, so that it can be regarded as an extreme upper limit. A reasonable lower limit would correspond to agreement with the critical experiments; i.e. 27% lower than the corrected Version IV result.

2. Doppler Coefficient

A modest increase of about 5% was found in the Doppler coefficient in the core in going from Version III to IV for a temperature change from 1100 to 2200°K, for either the unvoided or the voided case according to Tables II-8, VII-2, and VII-3. This difference decreases at higher temperatures, indicating slightly larger values for the exponent γ for Version IV than those given in Table VII-9 based on the results with Version III data. Evaluation of the variation of the Doppler coefficient with temperature is a significant source of uncertainty in application of critical experiment results in accident analysis, where fuel temperatures in the neighborhood of 5000°K may be of interest. The exponent γ has an effective calculated value in the neighborhood of 1.0 for ²³⁸U in the energy range of interest for fast reactor operation,¹⁷ which is the reason the Doppler coefficient is usually quoted in terms of the "Doppler constant" $-Tdk/dT$. An exponent of 1.0 ± 0.2 was found to be consistent with the SEFOR experiments on mixed PuO₂-UO₂ fuel, which extended to about 1300°K.¹⁸ At higher energies the temperature exponent of the Doppler coefficient for ²³⁸U increases asymptotically to $-3/2$ in the absence of resonance self-overlap effects, so that hardening the spectrum increases the magnitude of the exponent. At higher temperatures (>1000°K-2000°K), and at energies above several keV, self-overlap in ²³⁸U has an important effect on γ .¹⁹ Since this is in the unresolved resonance

region there is some uncertainty in calculating the self-overlap effect because of uncertainty in the distribution of resonance spacings,²⁰ which does not appear serious. With the presence of ^{238}U self-overlap, γ for ^{238}U is in the range 1.3-1.6 for temperatures 2000°K-4000°K and energies above 5 keV, which appears to be the reason that γ in Table VII-9 was found to be 1.12 for the CRBR for the unvoided case and 1.17 for a voided core. A still higher value of γ would be expected in the absence of steel; the Doppler coefficient itself would also in this case be smaller because of the reduction in low energy flux. Note that γ is not truly constant; Malloy and Ott²¹ have suggested that a more satisfactory fit is obtained by the assumption

$$d\rho/dT = \frac{A}{T + BT^{3/2}} \cdot$$

Another source of uncertainty in evaluating γ is the contribution to the Doppler coefficient of fissile material, the calculation of which is rather uncertain because it depends on unresolved resonance parameters. Typically the fissile contribution is calculated to be positive and about 10% of the negative fertile material contribution. If the effective value of γ for fissile material is about 1.5^{19,20} and if the actual Doppler coefficient of fissile material is essentially zero, as critical experiments suggest,²² then calculated values of γ for the mixture would be too small by about 0.05, which would cause only a few percent error in extrapolating critical experiment measurements to high temperatures. For the LWR-Pu-fueled CRBR at BOL, ^{239}Pu contribution was computed to be 2% positive. This suggests that the fissile material contribution should not cause a serious error in computing γ . The overall error in this extrapolation is difficult to estimate without sensitivity studies but probably does not exceed 10%.

Comparison between critical experiments²² and SEFOR results and calculations indicate that uncertainty in calculation of the Doppler coefficient in the range of the experiments is ± 10 to $\pm 15\%$. The question of the reactivity scale enters here also. Normalization of ZPPR ^{238}U Doppler coefficient results to central ^{239}Pu worth gives C/E from 0.85 to 0.90 with ENDF/B-III data, whereas without such normalization C/E is between 1.04 and 1.08.²² It appears from the available information that assumption of a maximum error of $\pm 20\%$ in the calculated Doppler coefficient using ENDF/B-IV data would be sufficiently conservative for accident calculations.

3. Steel Worth

As with sodium worth, steel worth was found to be slightly larger with ENDF/B-IV data than with ENDF/B-III data. It was concluded from comparison with critical experiments that there is perhaps a 20% uncertainty in steel worth calculations,²² which is acceptable considering the great uncertainty in calculation of the motion of molten steel in a reactor accident.

4. Fuel Worth

There was practically no change in calculated fuel worth given in Table VII-5 in going from Version III data to Version IV data. Bohn et al¹⁶

found a 7% reduction in C/E for ^{239}Pu central worth and an 11% reduction in C/E for ^{238}U (^{238}U central worth is negative), so that there was some compensation between these changes. Five percent of the reduction was due in each case to a change in delayed neutron parameters. C/E for ^{239}Pu with ENDF/B-IV data is still 1.13¹⁶ which may be the result of cross section errors as suggested in Ref. 16 or of a reactivity scale error or both. In any case the possible errors in fuel worth calculations from cross section errors seem to be unimportant compared to the uncertainty in calculating fuel motion.

B. Geometrical Effects

1. Sodium Void Worth

The work in Section VIII indicates that the errors in the R-Z model compared to the triangular mesh model for the EOEC state, in which the control rods are withdrawn, are locally of the order of 10 to 20%. If a 2-D triangular mesh model is used for the BOEC state, greater discrepancies (of the order of 20 to 40%) in local sodium void worth are likely to be encountered because of the axial symmetry assumed in the 2-D triangular mesh calculation besides the inadequate geometrical modeling in the radial direction of the R-Z model. The most serious errors are in calculation of the leakage component. A triangular mesh model is much to be preferred if it is feasible to use it.

Analysis of critical assemblies has shown that the presence of control rods or channels causes a spread of $\pm 6\%$ in C/E values for sodium voiding when an X-Y model appropriate for the experiments is used in the calculations,²² indicating that the effect of these perturbations is being described reasonably well with this model. The same would presumably be true of a triangular mesh for power reactor calculations.

2. Doppler Coefficient

Local errors in the Doppler coefficient with an R-Z model are relatively less than for the total sodium void effect, being a maximum of about 5% for the EOEC state according to Table VIII-3. The discrepancies for the BOEC state are generally 10 to 20% according to the results in Table VIII-1 because of the same two reasons of section IX.B-1. This is still undesirably large, and use of triangular mesh models for these calculations is to be preferred if feasible. Comparison of calculations with Doppler effect experiments²⁴ in a mockup of an X-Y model of the CRBR indicated discrepancies of 10% or less in accounting for local perturbations from control rods and sodium-filled channels. Similar errors would presumably be encountered in power reactor calculations of control-rod effects on the local Doppler coefficient.

3. Steel Worth

As in the case of the sodium void worth, rather substantial local errors occur in steel worth calculations using an R-Z model according to the results in Tables VIII-1, VIII-3 and VIII-4, and triangular mesh calculations are desirable. Because of uncertainty in the motion of molten steel in an accident analysis, however, even errors this large may not be too significant for the available methods of accident analysis.

4. Fuel Worth

The R-Z model is adequate for calculating fuel worths in an undistorted core. The problem of greatest interest in this case is to account properly for flux distortion and streaming effects when large masses of fuel are moved. The analysis of ZPPR-5 and ZEBRA experiments indicated that transport theory could adequately account for such situations.²² However, there is a question about whether streaming effects due to void regions which are neither interior to the core nor well-reflected, can be properly described with current techniques.²⁵

APPENDIX A

CROSS SECTION LIBRARIES USED IN THE CLINCH RIVER BREEDER REACTOR ANALYSIS

The computation presented in this report was performed with four broad group cross section libraries: a 27-group library of ANL-27 energy structure based on ENDF/B-III data, a 9-group library of WARD-9 energy structure based on ENDF/B-III data, a 27-group library of ANL-27 energy structure based on ENDF/B-IV data (Version IV cross-section set 1), and another 27-group library of ANL-27 energy structure generated from ENDF/B-IV data using a more accurate resonance energy-interval calculation (Version IV cross-section set 2). These energy structures are given in Table A.1. Each library except the last one was generated based on the narrow resonance approximation using the MC²-2 and SDX codes; however, the Version IV cross-section set 2 used a more refined model based on the integral transport theory calculation of resonance absorption in MC²-2 that was not available when the other libraries were constructed. The two models that were used to generate the libraries are described below.

Model Used to Construct All the Libraries Except Version IV Cross-Section Set 2

212-group base cross section sets with the USS212 energy structure, the standard group structure adopted by CSEWG, were generated using MC²-2 Code³ for sodium unvoided and for voided conditions. The inner core composition of the LWR-Pu-fueled CRBR at BOL was assumed for the mixture from which the spectrum is determined. All isotopes were assumed to be at 1100°K and those not actually present in the inner core at BOL were taken to be infinitely dilute. In this way, 212-group cross sections were obtained for the following 33 isotopes:

²³⁸Pu, ²³⁹Pu, ²⁴⁰Pu, ²⁴¹Pu, ²⁴²Pu, ²³⁵U, ²³⁸U, ¹⁶O, Fe, Cr, Ni, Mo,
⁵⁵Mn, ²³Na, ¹⁰B, ¹¹B, ¹²C, ²⁷Al, ¹³⁵Xe, ¹³⁵Cs, ¹⁴⁹Sm, ¹⁵⁰Sm,
U5FP1, U5FP2, U5FP3, P9FP1, P9FP2, P9FP3, ²³⁶U, ²³⁷Np, ²⁴¹Am,
²⁴³Am and ²⁴⁴Cm.

Resonance scattering contributions were included in the base cross section set; however, for those isotopes (²³⁸Pu, ²³⁹Pu, ²⁴⁰Pu, ²⁴¹Pu, ²⁴²Pu, ²³⁸U, ²³⁵U, ¹⁴⁹Sm, ²³⁶U, ²³⁷Np, ²⁴¹Am, ²⁴³Am, and ²⁴⁴Cm) with separate resonance data files in the MC²-2 library, fission and capture resonance contributions were excluded.

Regionwise (inner core, outer core, radial blanket and radial reflector) spatially-averaged broad group cross sections for a given temperature and sodium condition were obtained from SDX Code⁴ used in the following way. Heterogeneous resonance cross sections for fission and capture, based on the narrow resonance approximation, were computed for unit cells (radii are given in Table A.2) for the inner core, outer core, and radial blanket regions and were added to the 212-group cross sections of those isotopes with resonance files (²³⁸Pu, ²³⁹Pu, ²⁴⁰Pu, ²⁴¹Pu, ²⁴²Pu, ²³⁵U, ²³⁶U, ²³⁸U, ²⁴¹Am, ²⁴³Am, ¹⁴⁹Sm, ²³⁷Np, ²⁴⁴Cm). Then unit cell homogenizations were performed using the perturbation method of Storrer.²⁶ Finally a 212-group, one-dimensional neutronics calculation was performed to generate flux for the four-region configuration given in Table A.3. The broad group cross sections were obtained by collapsing the base set cross sections over this flux. Broad group

radial reflector cross sections were also obtained by collapsing the base set cross sections over the flux in the radial reflector region. The resulting cross-section datasets (having the same group structure and based on the same version of the basic data) for sodium unvoided and voided conditions and for different fuel temperatures were merged into one library.

Model Used to Construct ENDF/B-IV Cross-Section Set 2

The implementation of the integral transport theory treatment of resonance absorption in MC²-2 permitted several refinements in the computation of cross-sections. At energies below several hundred electron-volts, where the narrow resonance approximation is of dubious validity, use of integral transport theory should yield more accurate cross sections. Also, the constituents of stainless steel have non-narrow resonances in the energy range 1-60 keV for which there is non-trivial Doppler broadening. Thus the use of integral transport theory makes it possible to compute the Doppler effect of structural materials. In generating this library, cross sections of the principal resonant materials (²³⁹Pu, ²⁴⁰Pu, ²⁴¹Pu, ²³⁵U, ²³⁸U, Fe, Cr, Ni, Mo, ⁵⁵Mn) were computed with use of integral transport theory. As it was required to run MC²-2 with materials at several temperatures, temperature dependent resonance scattering cross sections were also computed.

Our cross section generation codes required that the following procedure be used to construct space-dependent, broad group cross sections based on integral transport theory. For a given region of the reactor (inner core, outer core or radial blanket) at a given temperature (1100, 2200 or 4400°K) and sodium condition, two MC²-2 problems are run. The first problem is a full heterogeneous run from which the heterogeneous unresolved cross section file and the output dataset with 212-group homogeneous cross sections are saved. The second MC²-2 problem performs only the integral transport theory calculation and creates a data file with integral transport theory computed resolved resonance cross-sections (for each region in the unit cell and cell-averaged) including contributions from the unresolved energy range computed in the first MC²-2 run. Because we wanted to include the structural materials, the integral transport calculations extended up to 52.5 keV. Next a second 212-group cross section set is created in which the homogeneous cross sections of the original set are replaced with the integral transport theory computed cross-sections for capture, fission and nu-fission. The three-region unit cells for the three reactor regions are described in Table A.2. Then for a specified temperature and sodium condition, the modified 212-group cross section sets for the three reactor regions are combined into a single dataset which is used in an SDX problem that performs a neutronics calculation and spatially collapses the cross sections to the ANL-27 energy structure.

Six such SDX problems were run (for 1100, 2200 and 4400°K with sodium either present or voided) and the resulting datasets were combined into a single ANL-27 library. To this library were added from ENDF/B-IV cross-section set 1 cross sections for materials whose low concentration in CRBR did not warrant their receiving the elaborate integral transport theory treatment.

ACKNOWLEDGMENT

The work of L. Jergens and T. Abrams, in neatly typing the report is highly appreciated.

REFERENCES

1. Kalimullah, *Preliminary Physics Calculations for the Clinch River Breeder Reactor*, RSA-TM-2, Applied Physics Division, Argonne National Laboratory (1975).
2. Preliminary safety analysis report, Clinch River Breeder Reactor Plant, Project Management Corporation.
3. H. Henryson, II, B. J. Toppel and C. G. Stenberg, *MC²-2: A Code to Calculate Fast Neutron Spectra and Multigroup Cross-sections*, ANL-8144, Argonne National Laboratory, Argonne, Illinois (1976).
4. W. M. Stacey, Jr. et al., *A New Space-Dependent Fast Neutron Multigroup Cross-Section Preparation Capability*, Trans. Am. Nucl. Soc. 15, 292 (1972).
5. T. A. Daly et al, *The ARC System Two-Dimensional Diffusion Theory Capability, DARC2D*, ANL-7716, Argonne National Laboratory, Argonne, Illinois (May 1972).
6. M. G. Stevenson et al, *Current Status and Experimental Basis of the SAS LMFBR Accident Analysis Code*, Proc. Fast Reactor Safety Meeting, Beverly Hills, California, April 2-4, 1974, CONF-740701, p. 1303.
7. T. A. Daly et al, *The ARC System Two-Dimensional Adjunct Calculations*, ANL-7720, Argonne National Laboratory, Argonne, Illinois (1972).
8. N. C. Paik, R. A. Doncals and J. A. Lake, *Fuel and Blanket Management for the Clinch River Breeder Reactor*, Advanced Reactors: Physics, Design and Economics, Proc. Intern. Conf. Atlanta, Georgia, Sept. 8-11, 1974, p. 677, Pergamon Press, New York (1975).
9. A. P. Olson, *A User's Manual for the Reactor Burnup System, REBUS-2*, FRA-TM-62, Internal Memorandum, Argonne National Laboratory, Argonne, Illinois (March 1974).
10. W. A. Wittkopf, *Lumped Fission Product Neutron Capture Cross-Sections for ENDF/B*, BAW-320, the Babcock and Wilcox Company, Lynchburg, Virginia, December 1966.
11. Physics of Reactor Safety, Quarterly Report, January-March 1975, ANL-75-31, Argonne National Laboratory, Argonne, Illinois, pp. 10-12.
12. J. R. Lamarsh, *Introduction to Nuclear Reactor Theory*, Addison-Wesley Publishing Company, Inc., Reading, Massachusetts (1966).
13. A. M. Broomfield et al, *The Mozart Control Rod Experiments and Their Interpretation*, Proc. Intern. Symp. on Physics of Fast Reactors, October 16-19, 1973, Volume 1, p. 312, Tokyo, Japan.
14. J. A. Lake, Westinghouse Advanced Reactors Division, Madison, Pennsylvania, private communication.

15. C. L. Beck et al, *On the Extrapolation of ZPR Sodium Void Measurements to the Power Reactor*, Proc. Intern. Meeting on Fast Reactor Safety and Related Physics, Chicago, Illinois, October 5-8, 1976, CONF761007.
16. E. M. Bohn et al, *The Status of the Central Worth Discrepancy*, in Chapter V, "The Reactor Physics of Safety," in "The Present Status of Fast Reactor Physics," to be published by the Nuclear Energy Agency Committee on Reactor Physics through the Organization for Economic Cooperation and Development.
17. H. H. Hummel and D. Okrent, *Reactivity Coefficients in Large Fast Power Reactors*, American Nuclear Society, Hinsdale, Illinois (1970).
18. D. D. Freeman et al, *SEFOR: Verification of the Doppler Transient Shutdown Capability of LMFBR's*, Proc. Nat'l. Topical Meeting on New Developments in Reactor Physics and Shielding, Kiamesha Lake, New York, September 12-15, 1972, CONF-720901, p. 986.
19. R. N. Hwang and K. Ott, *Comparison and Analysis of Theoretical Doppler Coefficient Results for Fast Reactors*, ANL-7269 (December 1966).
20. R. N. Hwang, *Some Recent Developments in Resonance and Doppler Theory*, loc. cit. (Ref. 18) p. 1166.
21. D. J. Malloy and K. O. Ott, *Neutronic Coupling of Feedback Effects*, Intern. Meeting on Fast Reactor Safety and Related Physics, October 6-8, 1976, Chicago, Illinois.
22. C. L. Beck et al, *Comparisons of Calculated Reactivity Coefficients with Critical Experiments*, loc. cit (Ref. 16).
23. D. D. Freeman, *SEFOR Experimental Results and Applications to LMFBR's*, EAP-13929, General Electric Company (1973).
24. R. E. Kaiser, J. M. Gasidlo and R. W. Goin, *Influence of Control Rods and Sodium-Filled Channels on the ^{238}U Doppler Effect*, Trans. Am. Nucl. Soc. 18, 310 (June 1974).
25. E. M. Gelbard and B. R. Reynolds, *Problems of Grossly Distorted Cores*, loc. cit (Ref. 16).
26. F. Storrer et al, *Heterogeneity Calculations for Fast Reactors by a Perturbation Method*, Nucl. Sci. Eng. 24, 33 (1966).



***ASSEMBLY NUMBER**
****ORIFICING ZONE**

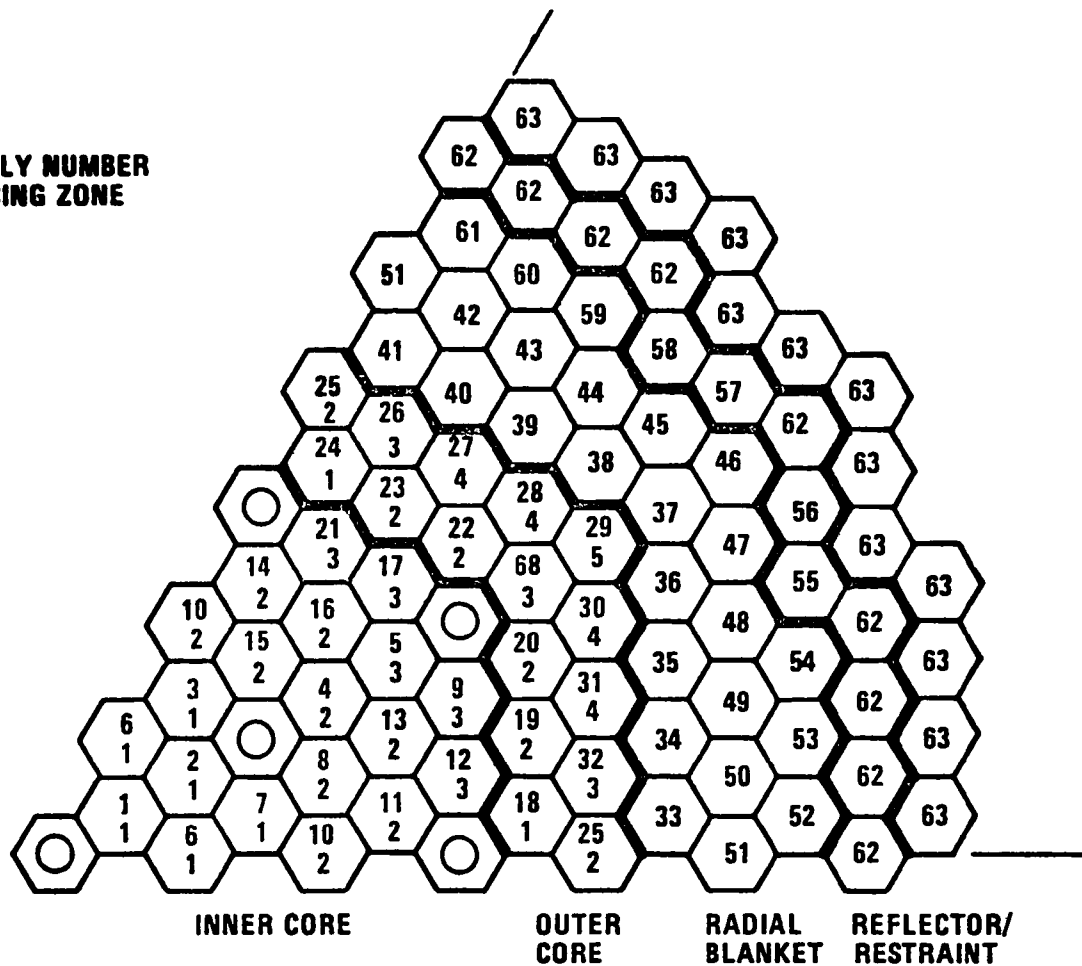


Fig. II-1. Clinch River Breeder Reactor Layout.
 ANL Neg. No. 116-77-699.

243.460	CONO	2J	21	2H	2G	2F	2E	2D	2C	2B	2A	29	28	27	26	25	24	23	22	21	CONO	ROW 1	40,000
185,605	CONO	2J	21	2H	2G	2F	2E	2D	2C	2B	2A	29	28	27	26	25	24	23	22	21	CONO	ROW 2	57,856
203,460	CONO	2J	21	2H	2G	2F	2E	2D	2C	2B	2A	29	28	27	26	25	24	23	22	21	CONO	ROW 3	167,749
185,605	CONO	2J	21	2H	2G	2F	2E	2D	2C	2B	2A	29	28	27	26	25	24	23	22	21	CONO	ROW 4	161,997
243.460	CONO	2J	21	2H	2G	2F	2E	2D	2C	2B	2A	29	28	27	26	25	24	23	22	21	CONO	ROW 5	156,244
185,605	CONO	2J	21	2H	2G	2F	2E	2D	2C	2B	2A	29	28	27	26	25	24	23	22	21	CONO	ROW 6	150,492
203,460	CONO	2J	21	2H	2G	2F	2E	2D	2C	2B	2A	29	28	27	26	25	24	23	22	21	CONO	ROW 7	144,739
185,605	CONO	2J	21	2H	2G	2F	2E	2D	2C	2B	2A	29	28	27	26	25	24	23	22	21	CONO	ROW 8	138,987
243.460	CONO	2J	21	2H	2G	2F	2E	2D	2C	2B	2A	29	28	27	26	25	24	23	22	21	CONO	ROW 9	133,235
185,605	CONO	2J	21	2H	2G	2F	2E	2D	2C	2B	2A	29	28	27	26	25	24	23	22	21	CONO	ROW 10	127,482
203,460	CONO	2J	21	2H	2G	2F	2E	2D	2C	2B	2A	29	28	27	26	25	24	23	22	21	CONO	ROW 11	121,730
185,605	CONO	2J	21	2H	2G	2F	2E	2D	2C	2B	2A	29	28	27	26	25	24	23	22	21	CONO	ROW 12	115,978
243.460	CONO	2J	21	2H	2G	2F	2E	2D	2C	2B	2A	29	28	27	26	25	24	23	22	21	CONO	ROW 13	110,225
185,605	CONO	2J	21	2H	2G	2F	2E	2D	2C	2B	2A	29	28	27	26	25	24	23	22	21	CONO	ROW 14	104,473
203,460	CONO	2J	21	2H	2G	2F	2E	2D	2C	2B	2A	29	28	27	26	25	24	23	22	21	CONO	ROW 15	98,721
185,605	CONO	2J	21	2H	2G	2F	2E	2D	2C	2B	2A	29	28	27	26	25	24	23	22	21	CONO	ROW 16	92,968
243.460	CONO	2J	21	2H	2G	2F	2E	2D	2C	2B	2A	29	28	27	26	25	24	23	22	21	CONO	ROW 17	87,216
185,605	CONO	2J	21	2H	2G	2F	2E	2D	2C	2B	2A	29	28	27	26	25	24	23	22	21	CONO	ROW 18	81,463
203,460	CONO	2J	21	2H	2G	2F	2E	2D	2C	2B	2A	29	28	27	26	25	24	23	22	21	CONO	ROW 19	75,711
185,605	CONO	2J	21	2H	2G	2F	2E	2D	2C	2B	2A	29	28	27	26	25	24	23	22	21	CONO	ROW 20	69,958
243.460	CONO	2J	21	2H	2G	2F	2E	2D	2C	2B	2A	29	28	27	26	25	24	23	22	21	CONO	ROW 21	64,205
185,605	CONO	2J	21	2H	2G	2F	2E	2D	2C	2B	2A	29	28	27	26	25	24	23	22	21	CONO	ROW 22	58,452
203,460	CONO	2J	21	2H	2G	2F	2E	2D	2C	2B	2A	29	28	27	26	25	24	23	22	21	CONO	ROW 23	52,699
185,605	CONO	2J	21	2H	2G	2F	2E	2D	2C	2B	2A	29	28	27	26	25	24	23	22	21	CONO	ROW 24	46,946
243.460	CONO	2J	21	2H	2G	2F	2E	2D	2C	2B	2A	29	28	27	26	25	24	23	22	21	CONO	ROW 25	41,193
185,605	CONO	2J	21	2H	2G	2F	2E	2D	2C	2B	2A	29	28	27	26	25	24	23	22	21	CONO	ROW 26	35,440
203,460	CONO	2J	21	2H	2G	2F	2E	2D	2C	2B	2A	29	28	27	26	25	24	23	22	21	CONO	ROW 27	29,687
185,605	CONO	2J	21	2H	2G	2F	2E	2D	2C	2B	2A	29	28	27	26	25	24	23	22	21	CONO	ROW 28	23,934
243.460	CONO	2J	21	2H	2G	2F	2E	2D	2C	2B	2A	29	28	27	26	25	24	23	22	21	CONO	ROW 29	18,181
185,605	CONO	2J	21	2H	2G	2F	2E	2D	2C	2B	2A	29	28	27	26	25	24	23	22	21	CONO	ROW 30	12,428
203,460	CONO	2J	21	2H	2G	2F	2E	2D	2C	2B	2A	29	28	27	26	25	24	23	22	21	CONO	ROW 31	6,675
185,605	CONO	2J	21	2H	2G	2F	2E	2D	2C	2B	2A	29	28	27	26	25	24	23	22	21	CONO	ROW 32	910

Fig. II-2. R-Z Model of the Hot Full Power Clinch River Breeder Reactor at the Beginning of Life. CONO is a collection of spatially disconnected control regions from which the control rod is out (sodium and steel 90.56 and 9.44 v/o). CON1, CON3F and CON3C are gions representing the central rod (two-thirds inserted), the six rods at flats (two-thirds inserted) and the other six rods at corners (completely withdrawn) of Row 7. ANL Neg. No. 116-77-695.

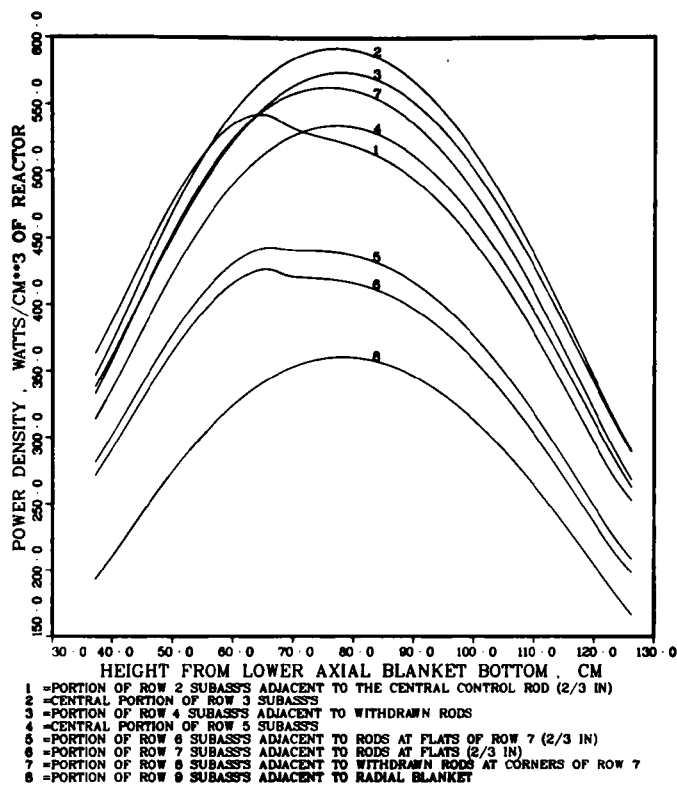
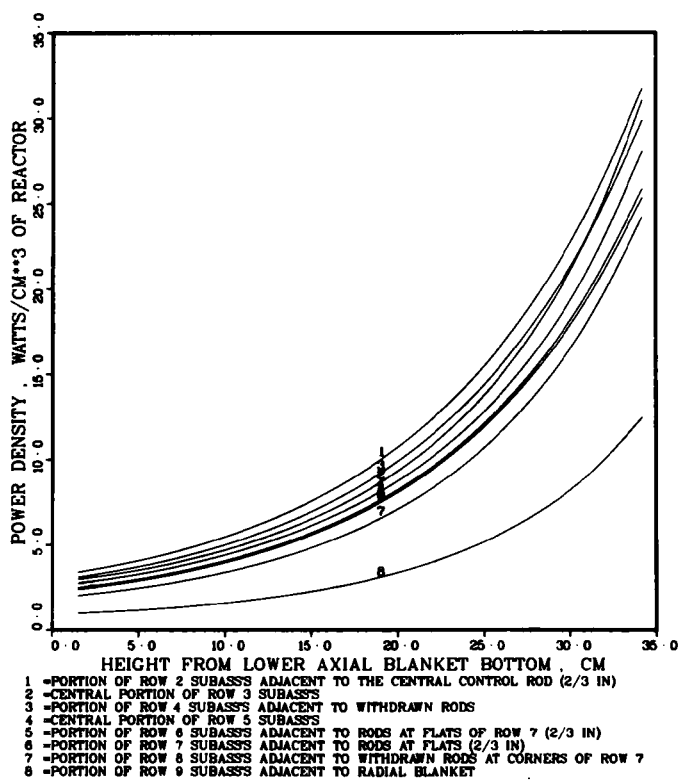


Fig. II-3.

Axial Distribution of Power in the LWR-Grade Plutonium Fueled Clinch River Breeder Reactor Core at the Beginning of Life. ANL Neg. No. 116-77-608.

Fig. II-4.
 Axial Distribution of Power in the LWR-Grade Plutonium Fueled Clinch River Breeder Reactor Lower Axial Blanket at the Beginning of Life. ANL Neg. No. 116-77-613.



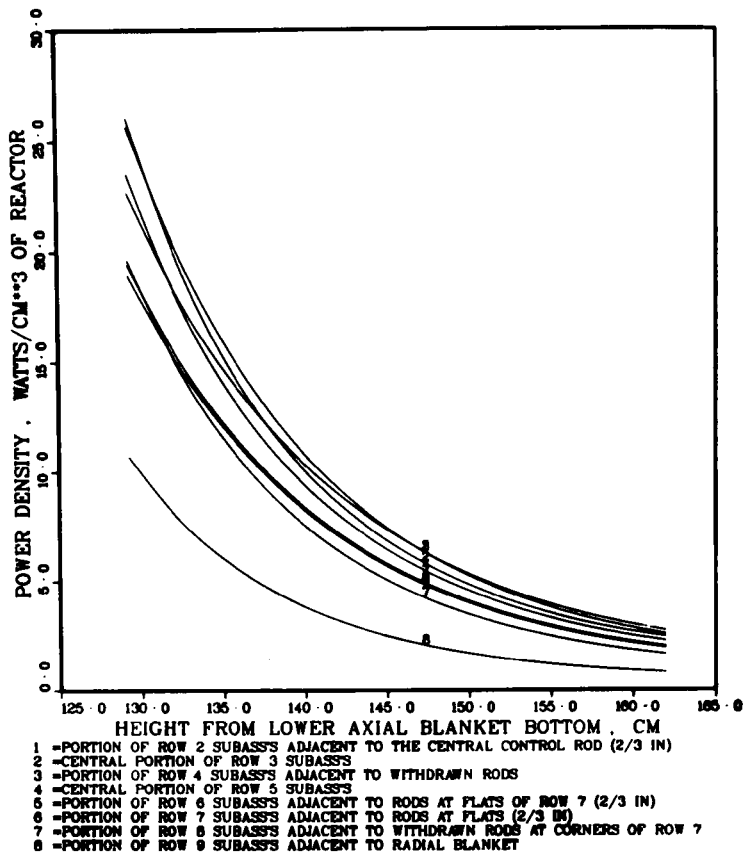
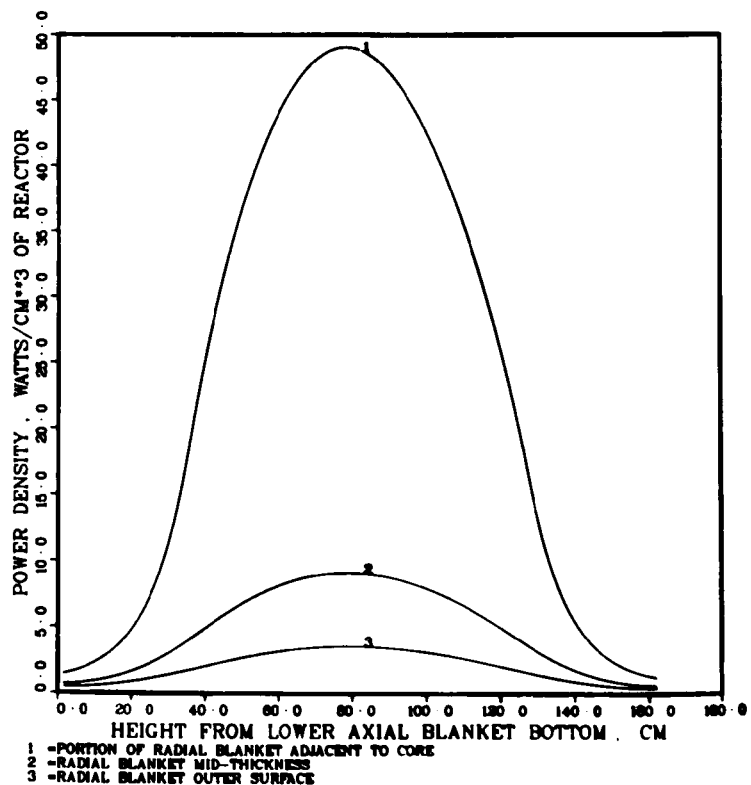


Fig. II-5.

Axial Distribution of Power in the LWR-Grade Plutonium Fueled Clinch River Breeder Reactor Upper Axial Blanket at the Beginning of Life. ANL Neg. No. 116-77-691.

Fig. II-6.
Axial Distribution of Power in the LWR-Grade Plutonium Fueled Clinch River Breeder Reactor Blanket at the Beginning of Life. ANL Neg. No. 116-77-690.



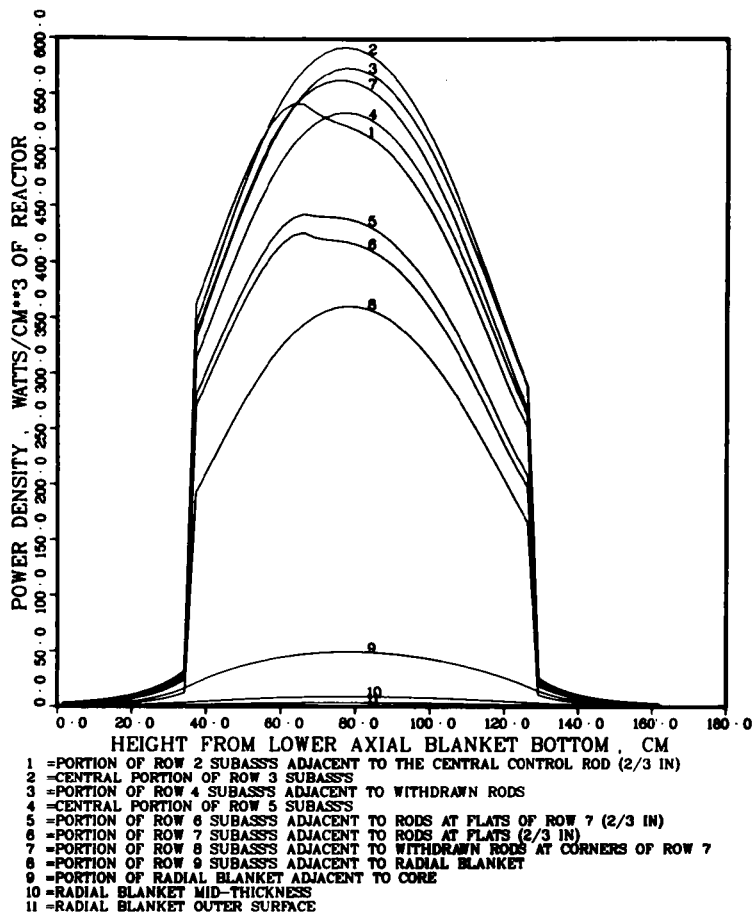


Fig. II-7.

Axial Distribution of Power in the LWR-Grade Plutonium Fueled Clinch River Breeder Reactor Core & Blankets at the Beginning of Life. ANL Neg. No. 116-77-591.

Fig. II-8.
 Radial Distribution of Power in the LWR-Grade Plutonium Fueled Clinch River Breeder Reactor Core & Blankets at the Beginning of Life. ANL Neg. No. 116-77-639.

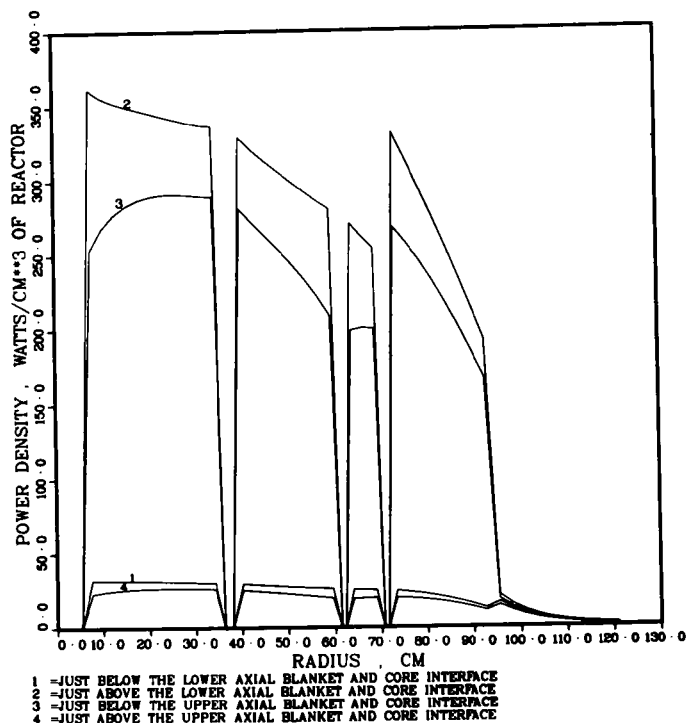


Fig. II-11. Subassembly Peak Power Factors for the LWR-Grade Plutonium Fueled Clinch River Breeder Reactor at the Beginning of Life. Neg. No. 116-77-631.

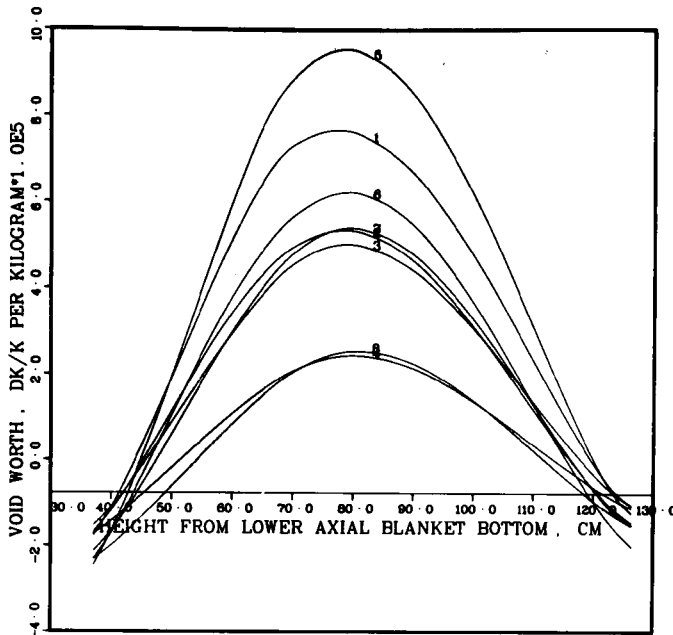


Fig. II-12.

Comparison of Void Worth Distributions in Core Between Normal and Core-and-Blanket-Voided LWR-Pu-Fueled CRBR at the Beginning of Life. ANL Neg. No. 116-77-605.

- 1 -NORMAL REACTOR. CENTRAL PORTION OF ROW 2 SUBASSS
- 2 -NORMAL REACTOR. CENTRAL PORTION OF ROW 4 SUBASSS
- 3 -NORMAL REACTOR. CENTRAL PORTION OF ROW 6 SUBASSS
- 4 -NORMAL REACTOR. CENTRAL PORTION OF ROW 8 SUBASSS
- 5 -VOIDED REACTOR. RADIAL POSITION SAME AS 1
- 6 -VOIDED REACTOR. RADIAL POSITION SAME AS 2
- 7 -VOIDED REACTOR. RADIAL POSITION SAME AS 3
- 8 -VOIDED REACTOR. RADIAL POSITION SAME AS 4

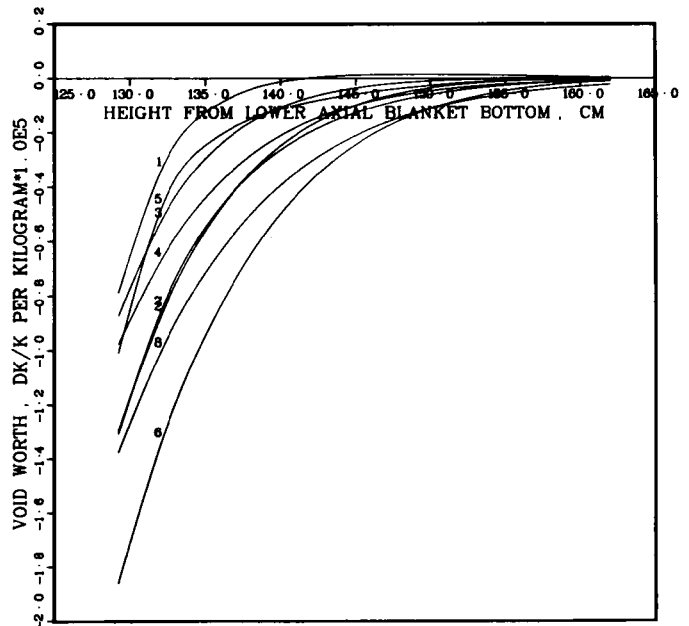


Fig. II-13.

Comparison of Void Worth Distributions in Upper Blanket Between Normal and Core-and-Blanket-Voided LWR-Pu-Fueled CRBR at the Beginning of Life. ANL Neg. No. 116-77-675.

- 1 -NORMAL REACTOR. CENTRAL PORTION OF ROW 2 SUBASSS
- 2 -NORMAL REACTOR. CENTRAL PORTION OF ROW 4 SUBASSS
- 3 -NORMAL REACTOR. CENTRAL PORTION OF ROW 6 SUBASSS
- 4 -NORMAL REACTOR. CENTRAL PORTION OF ROW 8 SUBASSS
- 5 -VOIDED REACTOR. RADIAL POSITION SAME AS 1
- 6 -VOIDED REACTOR. RADIAL POSITION SAME AS 2
- 7 -VOIDED REACTOR. RADIAL POSITION SAME AS 3
- 8 -VOIDED REACTOR. RADIAL POSITION SAME AS 4

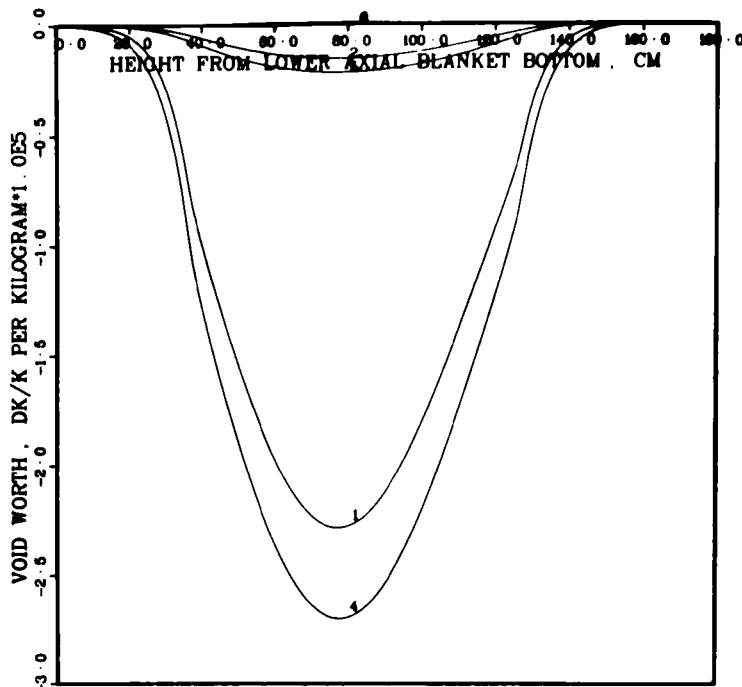


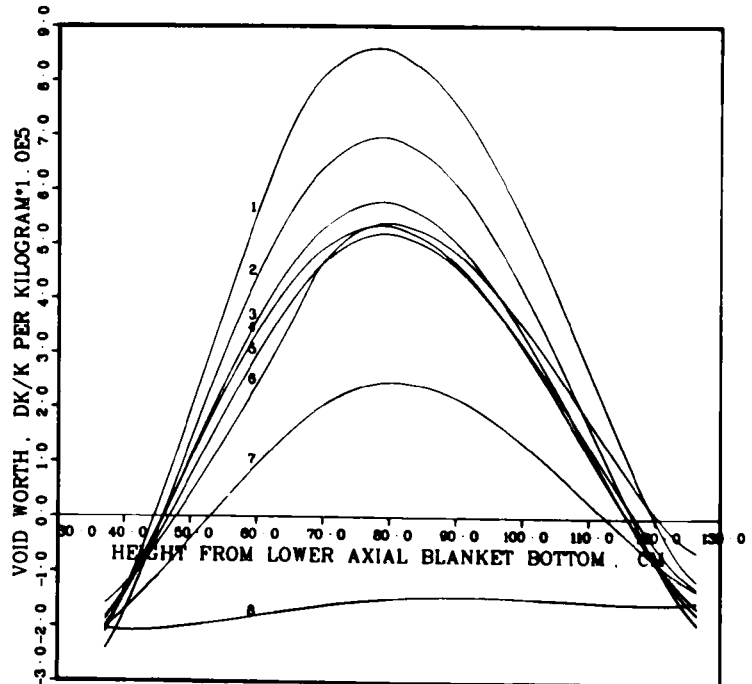
Fig. II-14.

Comparison of Void Worth Distributions in Radial Blanket Between Normal and Core-and Blanket-Voided LWR-Pu-Fueled CRBR at the Beginning of Life. ANL Neg. No. 116-77-589.

- 1 -NORMAL REACTOR. PORTION OF RADIAL BLANKET ADJACENT TO CORE
- 2 -NORMAL REACTOR. RADIAL BLANKET MID-THICKNESS
- 3 -NORMAL REACTOR. RADIAL BLANKET OUTER SURFACE
- 4 -VOIDED REACTOR. RADIAL POSITION SAME AS 1
- 5 -VOIDED REACTOR. RADIAL POSITION SAME AS 2
- 6 -VOIDED REACTOR. RADIAL POSITION SAME AS 3

Fig. II-15.

Distribution of Sodium Void Worth in Core in the LWR-Grade Plutonium Fueled Clinch River Breeder Reactor at the Beginning of Life. ANL Neg. No. 116-77-590.



- 1 -CENTRAL PORTION OF ROW 2 SUBASSEMBLY
- 2 -CENTRAL PORTION OF ROW 3 SUBASSEMBLY
- 3 -CENTRAL PORTION OF ROW 4 SUBASSEMBLY
- 4 -CENTRAL PORTION OF ROW 5 SUBASSEMBLY
- 5 -CENTRAL PORTION OF ROW 6 SUBASSEMBLY
- 6 -CENTRAL PORTION OF ROW 7 SUBASSEMBLY
- 7 -CENTRAL PORTION OF ROW 8 SUBASSEMBLY
- 8 -CENTRAL PORTION OF ROW 9 SUBASSEMBLY

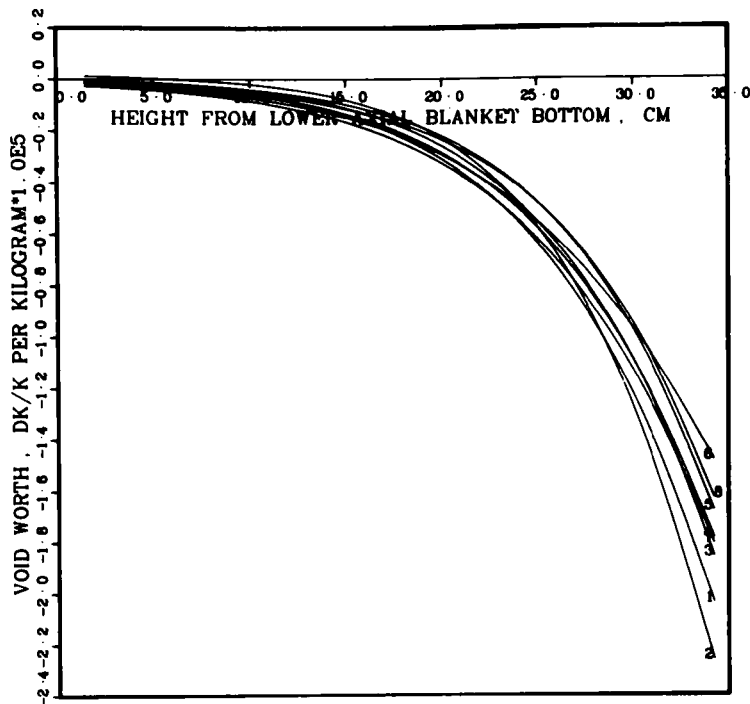


Fig. II-16.

Distribution of Sodium Void Worth in Lower Blanket in the LWR-Grade Plutonium Fueled Clinch River Breeder Reactor at the Beginning of Life. ANL Neg. No. 116-77-704.

- 1 = CENTRAL PORTION OF ROW 2 SUBASSES
- 2 = CENTRAL PORTION OF ROW 3 SUBASSES
- 3 = CENTRAL PORTION OF ROW 4 SUBASSES
- 4 = CENTRAL PORTION OF ROW 5 SUBASSES
- 5 = CENTRAL PORTION OF ROW 6 SUBASSES
- 6 = CENTRAL PORTION OF ROW 7 SUBASSES
- 7 = CENTRAL PORTION OF ROW 8 SUBASSES
- 8 = CENTRAL PORTION OF ROW 9 SUBASSES

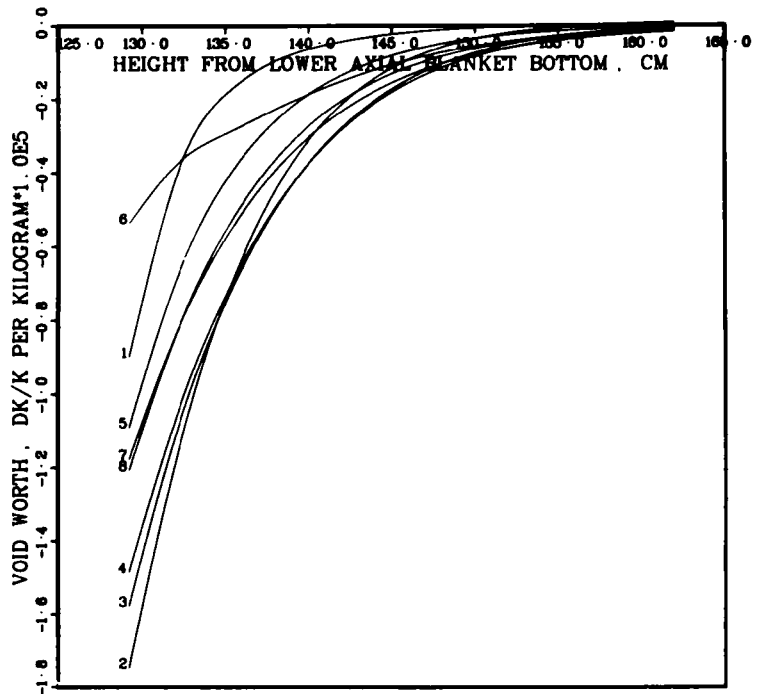


Fig. II-17.

Distribution of Sodium Void Worth in Upper Blanket in the LWR-Grade Plutonium Fueled Clinch River Breeder Reactor at the Beginning of Life. ANL Neg. No. 116-77-593.

- 1 = CENTRAL PORTION OF ROW 2 SUBASSES
- 2 = CENTRAL PORTION OF ROW 3 SUBASSES
- 3 = CENTRAL PORTION OF ROW 4 SUBASSES
- 4 = CENTRAL PORTION OF ROW 5 SUBASSES
- 5 = CENTRAL PORTION OF ROW 6 SUBASSES
- 6 = CENTRAL PORTION OF ROW 7 SUBASSES
- 7 = CENTRAL PORTION OF ROW 8 SUBASSES
- 8 = CENTRAL PORTION OF ROW 9 SUBASSES

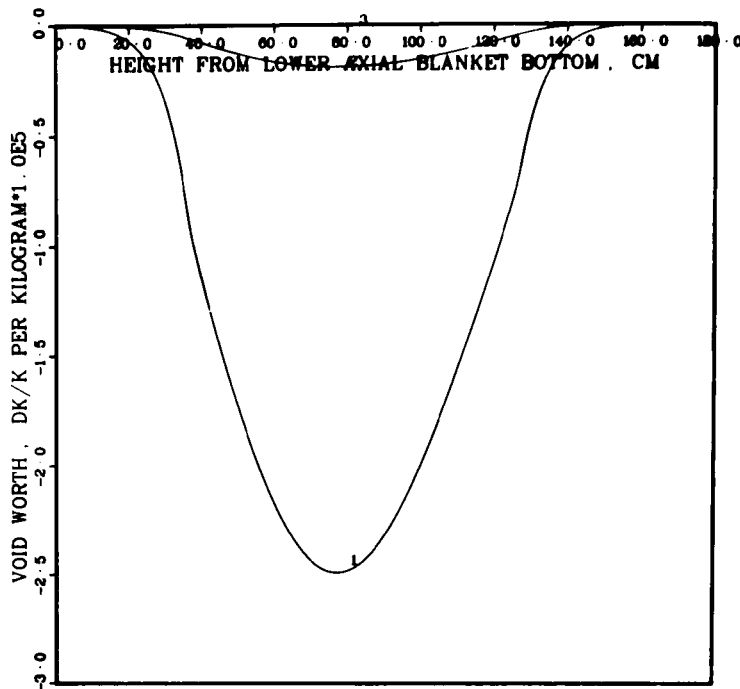


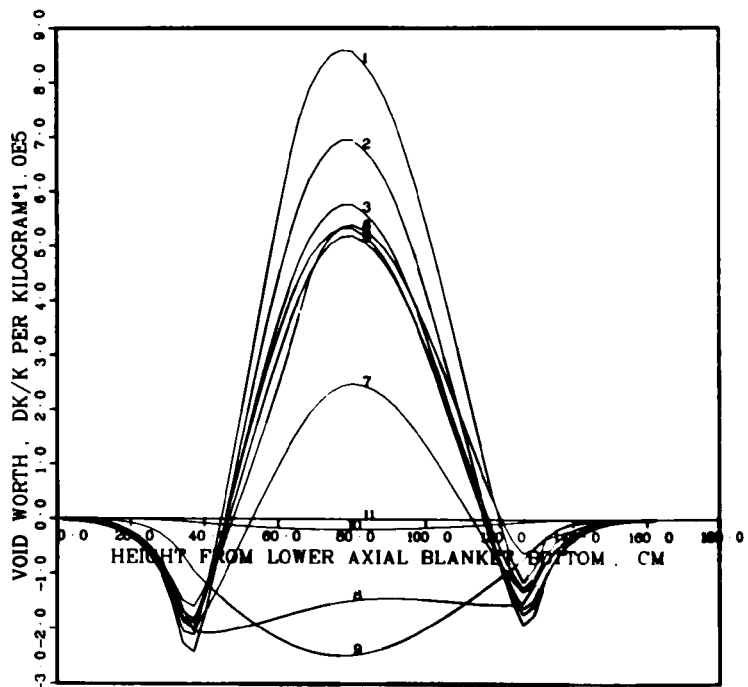
Fig. II-18.

Distribution of Sodium Void Worth in Radial Blanket in the LWR-Grade Plutonium Fueled Clinch River Breeder Reactor at the Beginning of Life. ANL Neg. No. 116-77-587.

- 1 -PORTION OF RADIAL BLANKET ADJACENT TO CORE
- 2 -RADIAL BLANKET MID-THICKNESS
- 3 -RADIAL BLANKET OUTER SURFACE

Fig. II-19.

Distribution of Sodium Void Worth in Core and Blankets in the LWR-Grade Plutonium Fueled Clinch River Breeder Reactor at the Beginning of Life. ANL Neg. No. 116-77-588.



- 1 -CENTRAL PORTION OF ROW 2 SUBASSES
- 2 -CENTRAL PORTION OF ROW 3 SUBASSES
- 3 -CENTRAL PORTION OF ROW 4 SUBASSES
- 4 -CENTRAL PORTION OF ROW 5 SUBASSES
- 5 -CENTRAL PORTION OF ROW 6 SUBASSES
- 6 -CENTRAL PORTION OF ROW 7 SUBASSES
- 7 -CENTRAL PORTION OF ROW 8 SUBASSES
- 8 -CENTRAL PORTION OF ROW 9 SUBASSES
- 9 -PORTION OF RADIAL BLANKET ADJACENT TO CORE
- 10 -RADIAL BLANKET MID-THICKNESS
- 11 -RADIAL BLANKET OUTER SURFACE

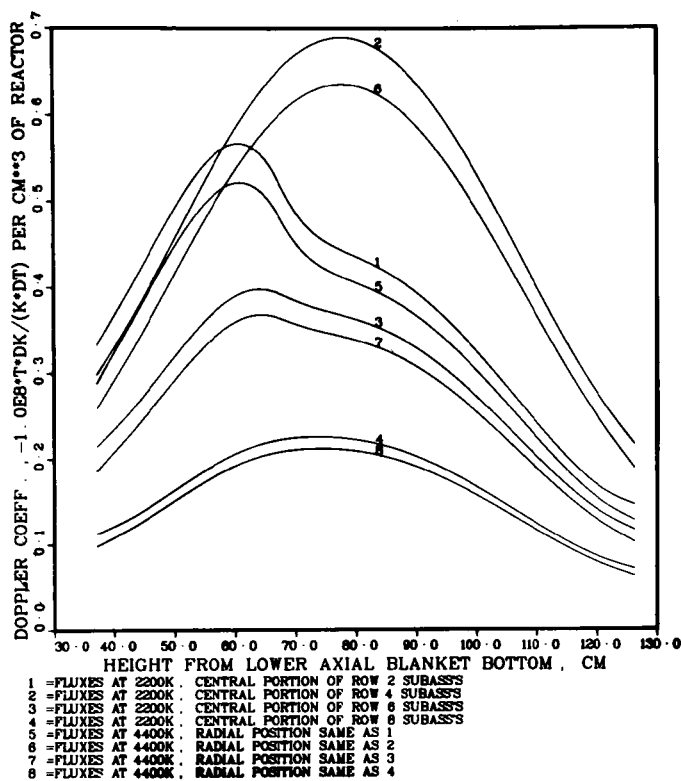
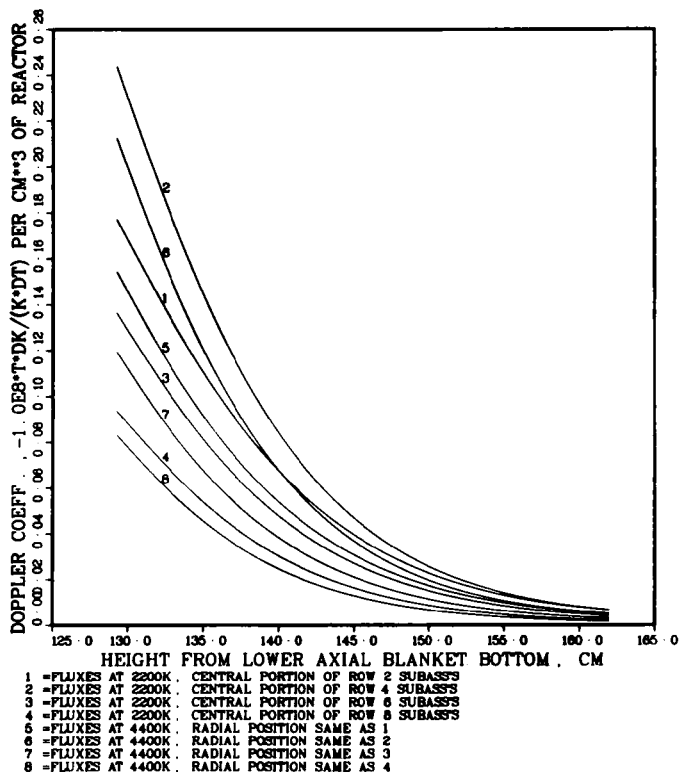


Fig. II-20.

Comparison of Doppler Coefficients over 2200-4400K in Unvoided Core Computed from Fluxes at Both Temperatures for LWR-Pu-Fueled CRBR at BOL. ANL Neg. No. 116-77-657.

Fig. II-21.

Comparison of Doppler Coefficients over 2200-4400K in Unvoided Upper Blanket Computed from Fluxes at Both Temperatures for LWR-Pu-Fueled CRBR at BOL. ANL Neg. No. 116-77-658



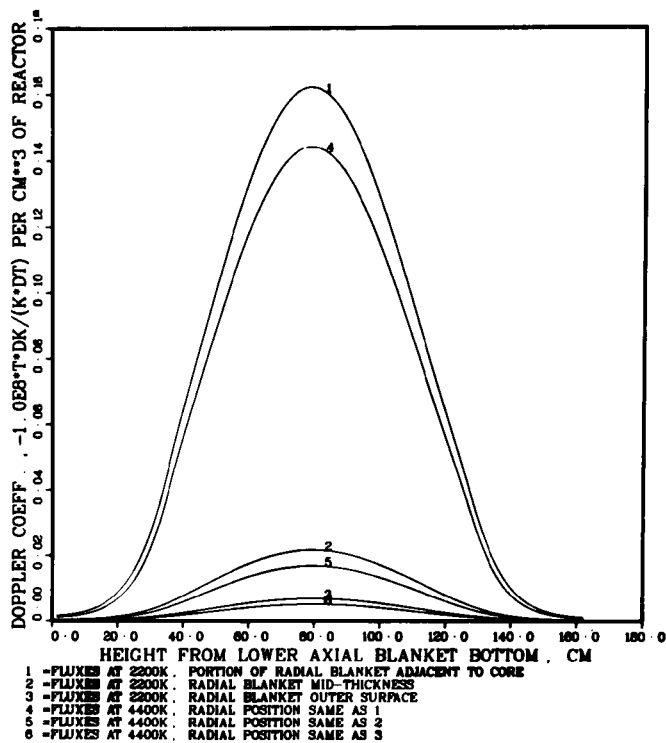
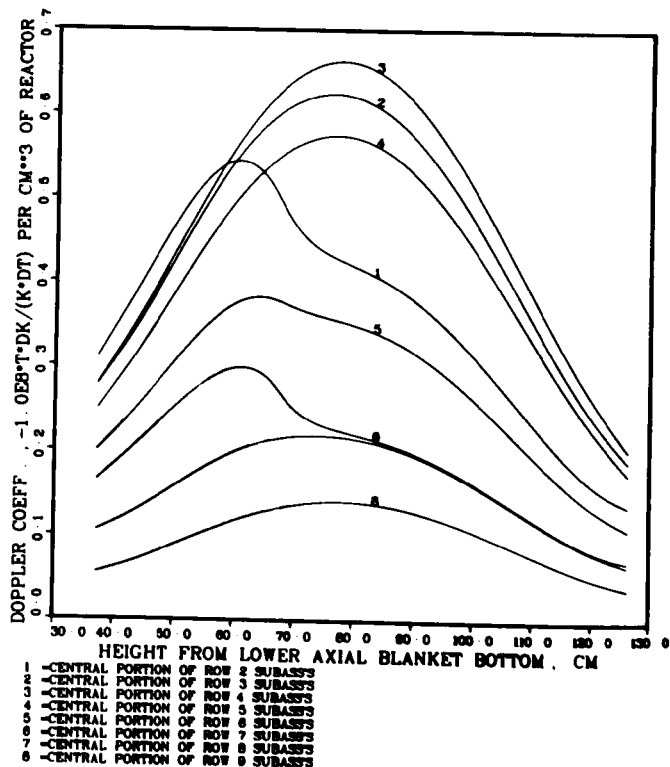


Fig. II-22.

Comparison of Doppler Coefficients over 2200-4400K in Unvoided Radial Blanket Computed from Fluxes at Both Temperatures for LWR-Pu-Fueled CRBR at BOL. ANL Neg. No. 116-77-622.

Fig. II-23.

Doppler Coefficient over 2200-4400K in Unvoided Core of the LWR-Pu-Fueled CRBR at the Beginning of Life. ANL Neg. No. 116-77-621.



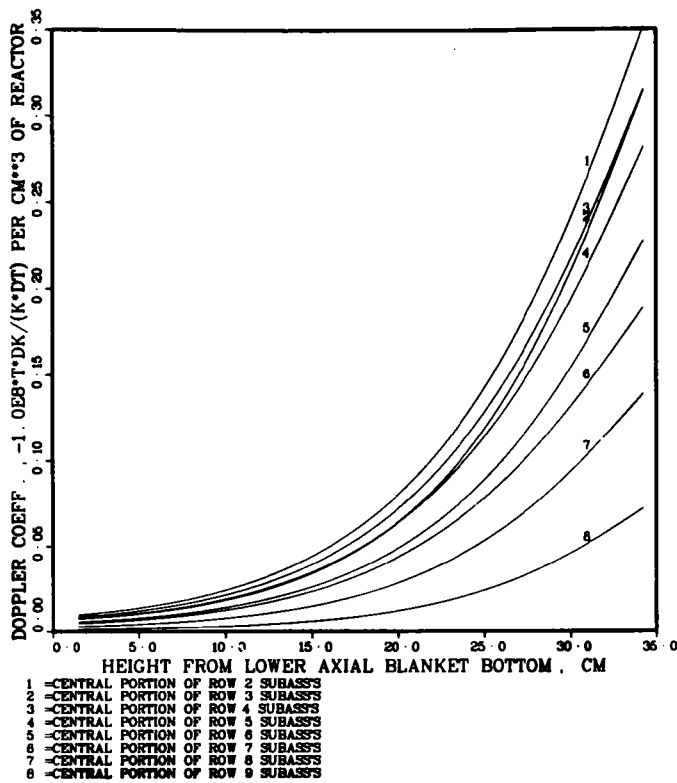
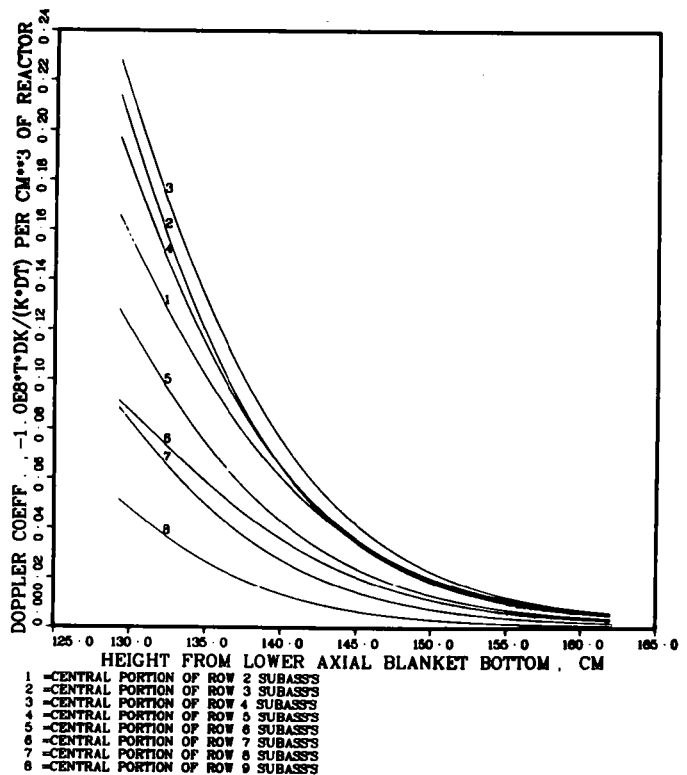


Fig. II-24.

Doppler Coefficient over 2200-4400K in Unvoided Lower Blanket of the LWR-Pu-Fueled CRBR at the Beginning of Life. ANL Neg. No. 116-77-645.

Fig. II-25.

Doppler Coefficient over 2200-4400K in Unvoided Upper Blanket of the LWR-Pu-Fueled CRBR at the Beginning of Life. ANL Neg. No. 116-77-644.



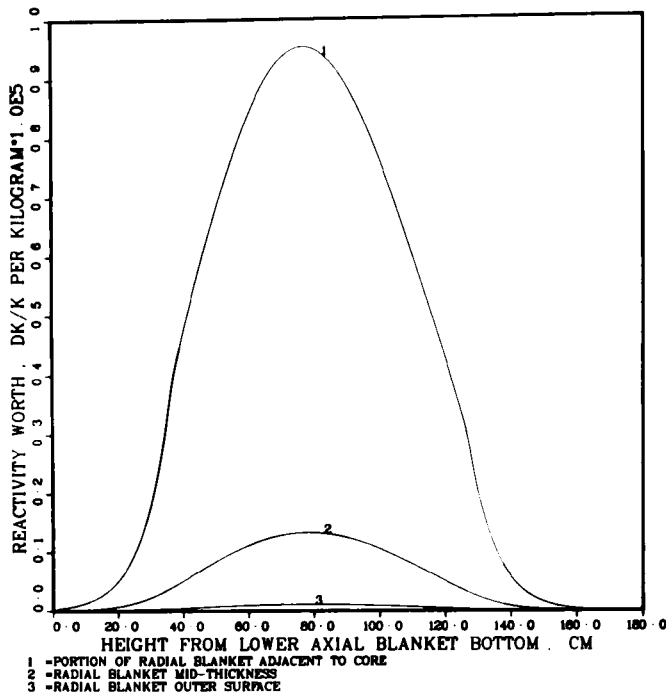
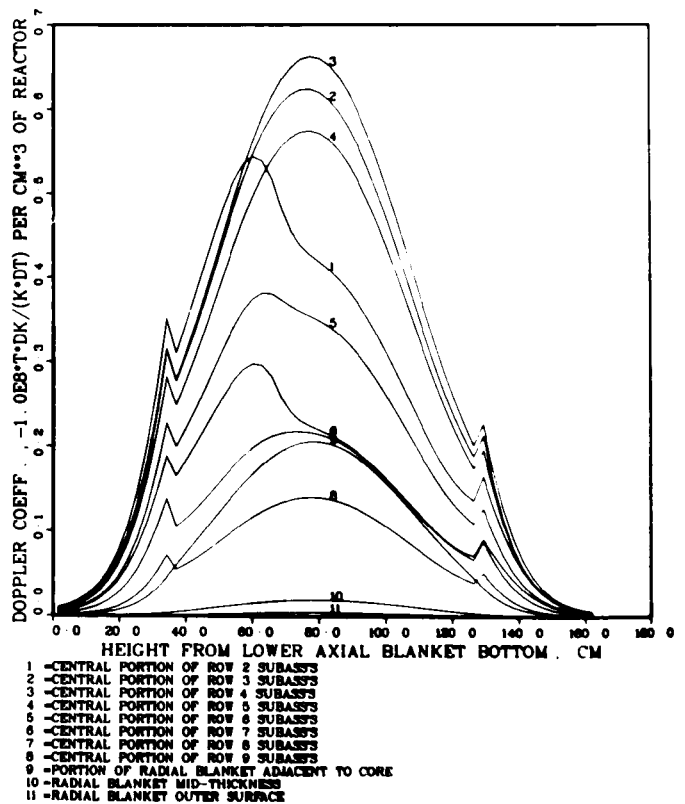


Fig. II-26.

Doppler Coefficient over 2200-4400K in Unvoided Radial Blanket of the LWR-Pu-Fueled CRBR at the Beginning of Life. ANL Neg. No. 116-77-676.

Fig. II-27.

Doppler Coefficient over 2200-4400K in Unvoided Core and Blankets of the LWR-Pu-Fueled CRBR at the Beginning of Life. ANL Neg. No. 116-77-677.



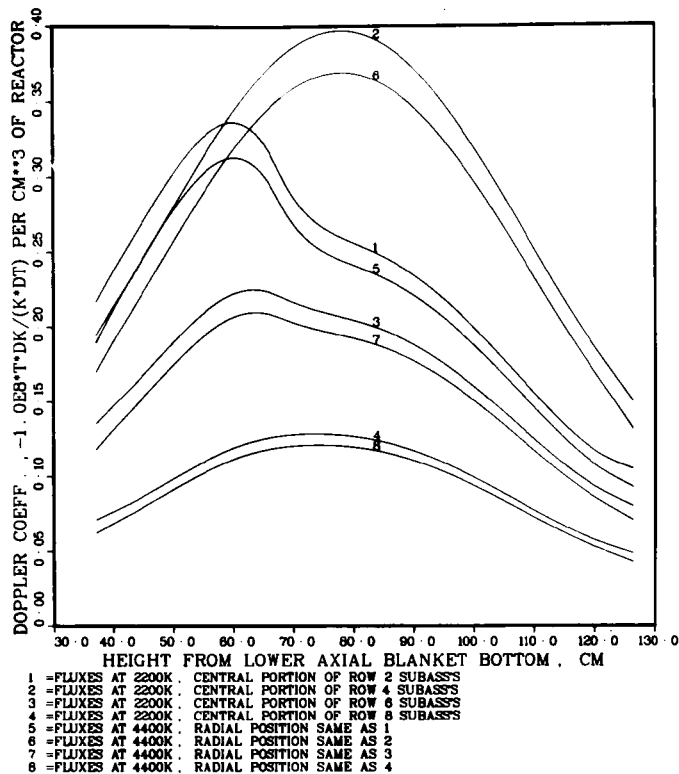
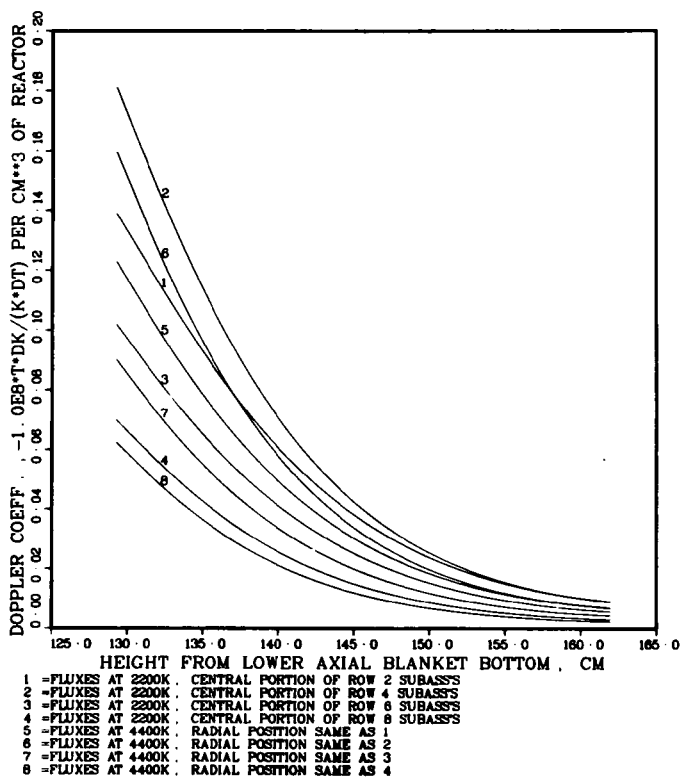


Fig. II-28.

Comparison of Doppler Coefficients over 2200-4400K in Totally Voided Core Computed from Fluxes at Both Temperatures for LWR-Pu-Fueled CRBR at BOL. ANL Neg. No. 116-77-633.

Fig. II-29.

Comparison of Doppler Coefficients over 2200-4400K in Totally Voided Upper Blanket Computed from Fluxes at Both Temperatures for LWR-Pu-Fueled CRBR at BOL. ANL Neg. No. 116-77-634.



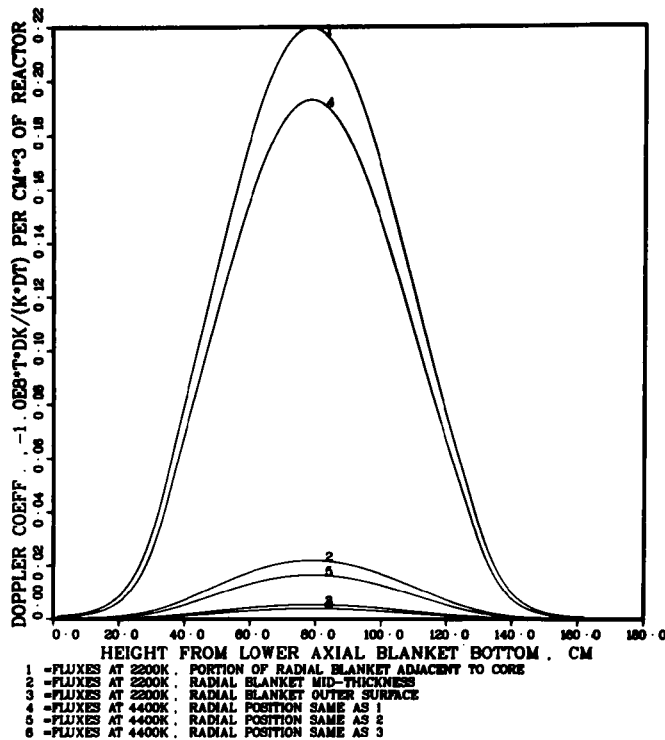
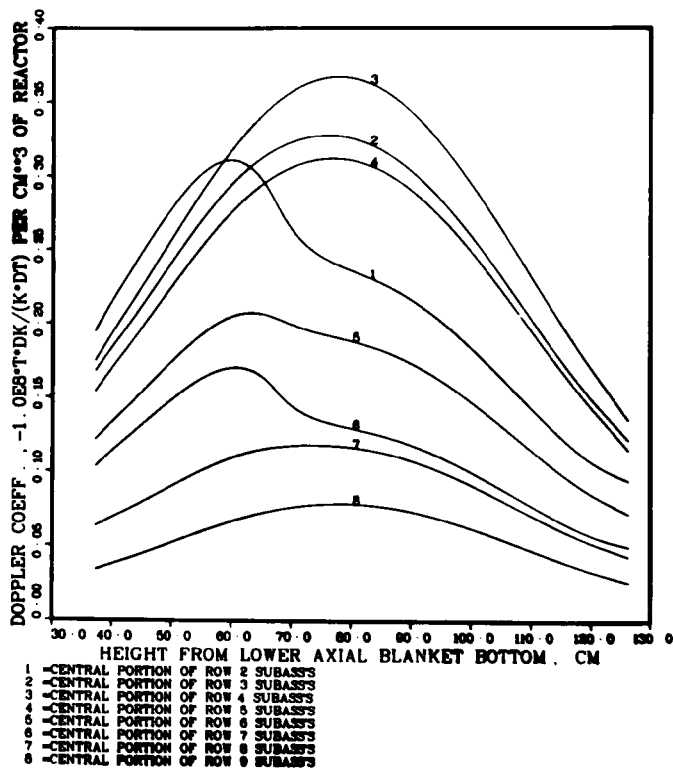


Fig. II-30.

Comparison of Doppler Coefficients over 2200-4400K in Totally Voided Radial Blanket Computed from Fluxes at Both Temperatures for LWR-Pu-Fueled CRBR at BOL. ANL Neg. No. 116-77-623.

Fig. II-31.

Doppler Coefficient over 2200-4400K in Totally Voided Core of the LWR-Pu-Fueled CRBR at the Beginning of Life. ANL Neg. No. 116-77-647.



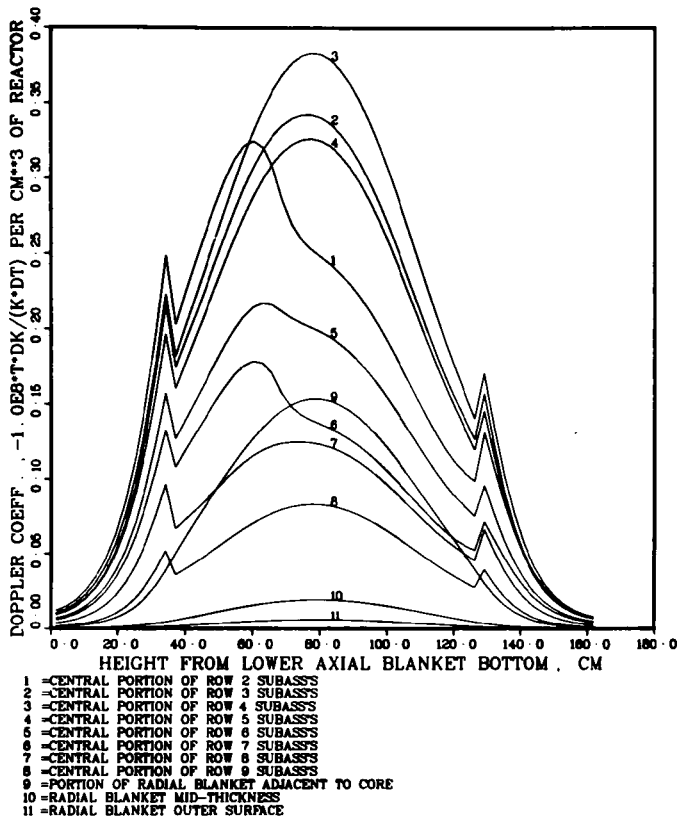


Fig. II-32.

Doppler Coefficient over 2200-4400K in Totally Voided Core and Blankets of the LWR-Pu-Fueled CRBR at the Beginning of Life. ANL Neg. No. 116-77-635.

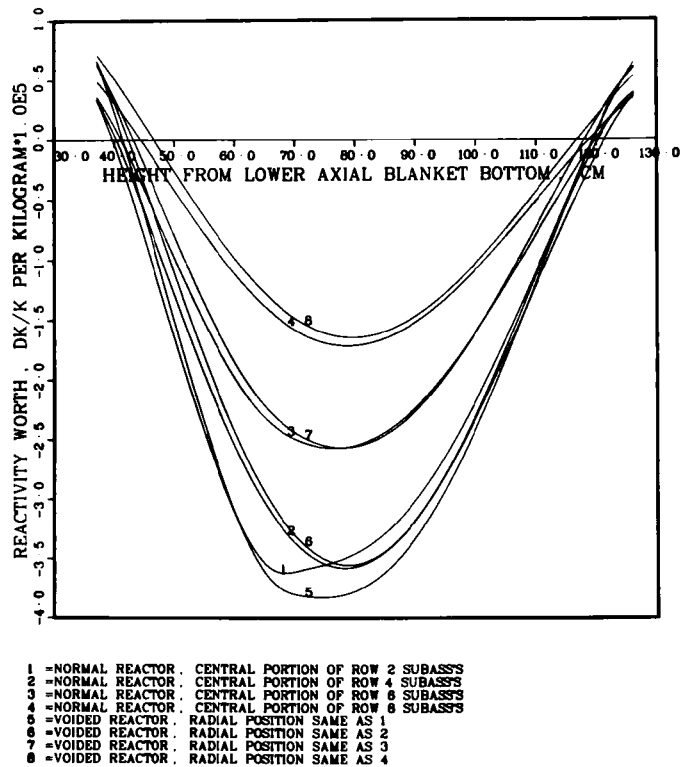


Fig. II-33.

Comparison of Steel Worth Distributions in Core Between Normal and Core-and-Blanket-Voided LWR-Pu-Fueled CRBR at the Beginning of Life. ANL Neg. No. 116-77-636.

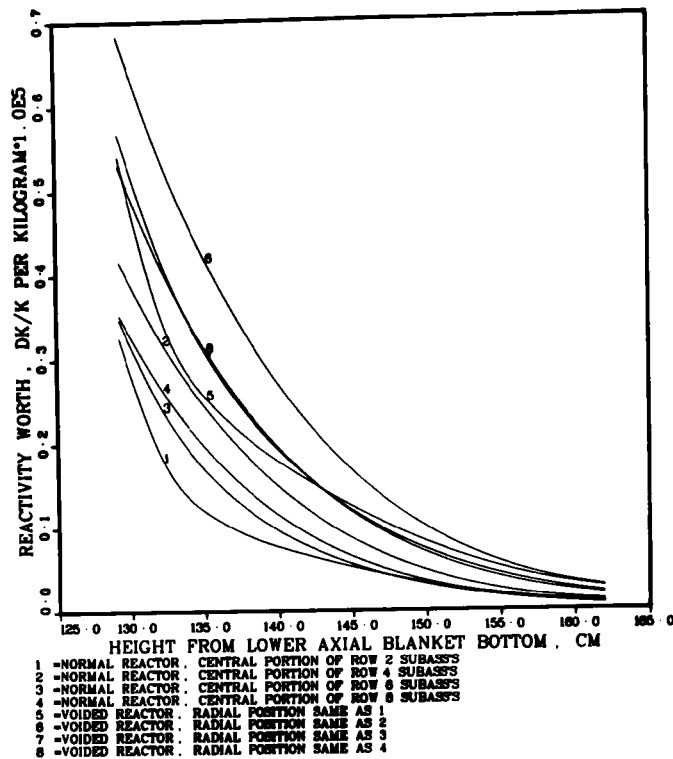
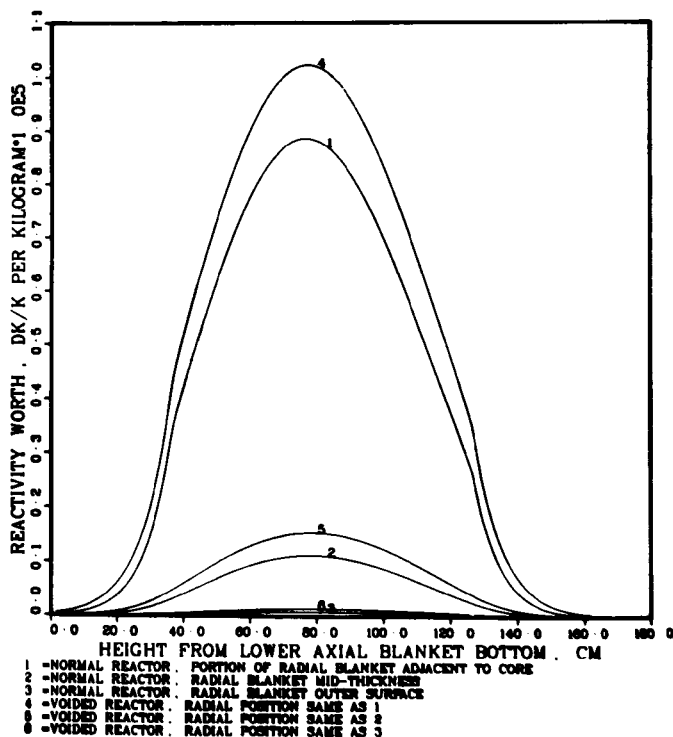
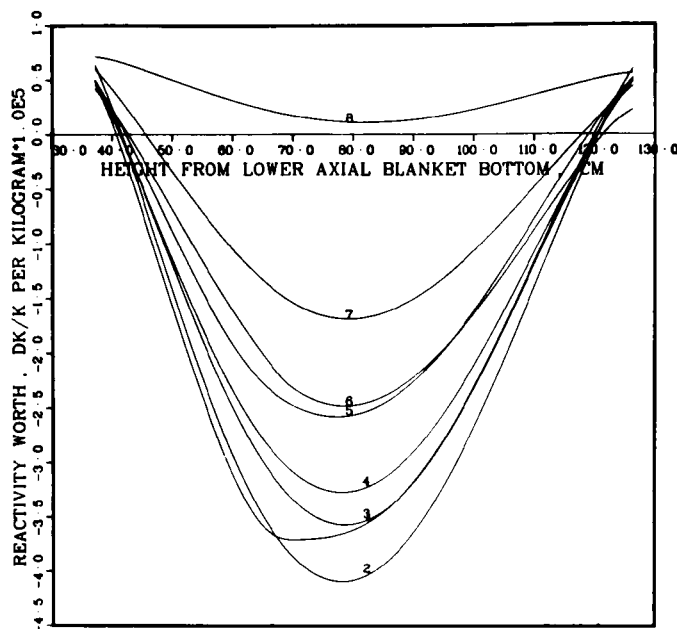


Fig. II-34.

Comparison of Steel Worth Distributions in Upper Blanket Between Normal and Core- and Blanket-Voided LWR-Pu-Fueled CRBR at the Beginning of Life. ANL Neg. No. 116-77-609.

Fig. II-35.
 Comparison of Steel Worth Distributions in Radial Blanket Between Normal and Core-and-Blanket-Voided LWR-Pu-Fueled CRBR at the Beginning of Life. ANL Neg. No. 116-77-606.



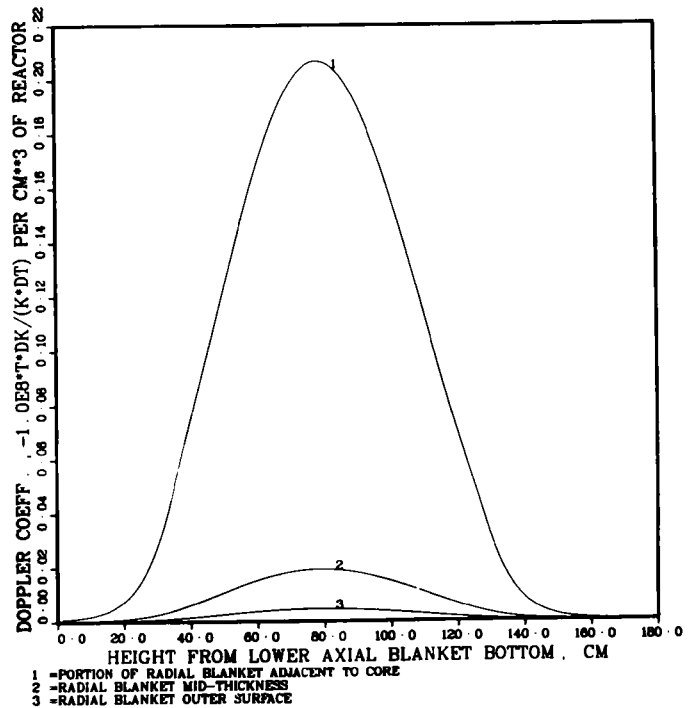


- 1 - CENTRAL PORTION OF ROW 2 SUBASSEMBLYS
- 2 - CENTRAL PORTION OF ROW 3 SUBASSEMBLYS
- 3 - CENTRAL PORTION OF ROW 4 SUBASSEMBLYS
- 4 - CENTRAL PORTION OF ROW 5 SUBASSEMBLYS
- 5 - CENTRAL PORTION OF ROW 6 SUBASSEMBLYS
- 6 - CENTRAL PORTION OF ROW 7 SUBASSEMBLYS
- 7 - CENTRAL PORTION OF ROW 8 SUBASSEMBLYS
- 8 - CENTRAL PORTION OF ROW 9 SUBASSEMBLYS

Fig. II-36.

Axial Distribution of Steel Worth in Core in the LWR-Grade Plutonium Fueled Clinch River Breeder Reactor at the Beginning of Life. ANL Neg. No. 116-77-697.

Fig. II-37.
Axial Distribution of Steel Worth in Radial Blanket in the LWR-Grade Plutonium Fueled Clinch River Breeder Reactor at the Beginning of Life. ANL Neg. No. 116-77-628.



- 1 - PORTION OF RADIAL BLANKET ADJACENT TO CORE
- 2 - RADIAL BLANKET MID-THICKNESS
- 3 - RADIAL BLANKET OUTER SURFACE

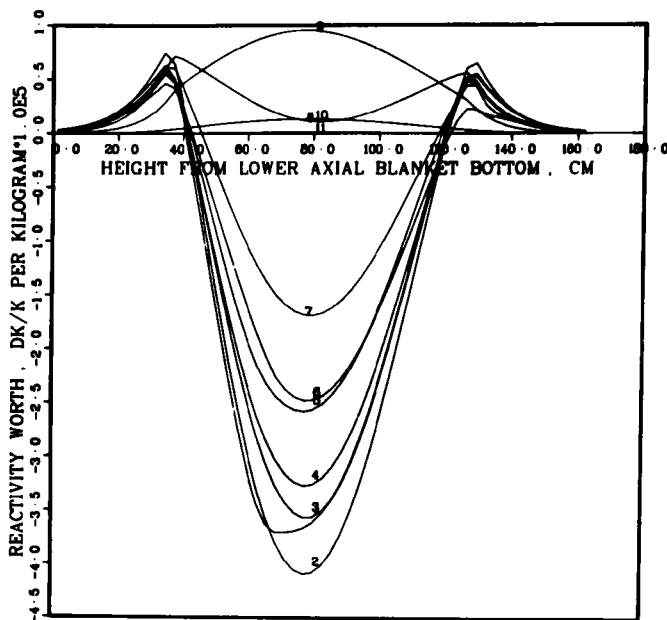


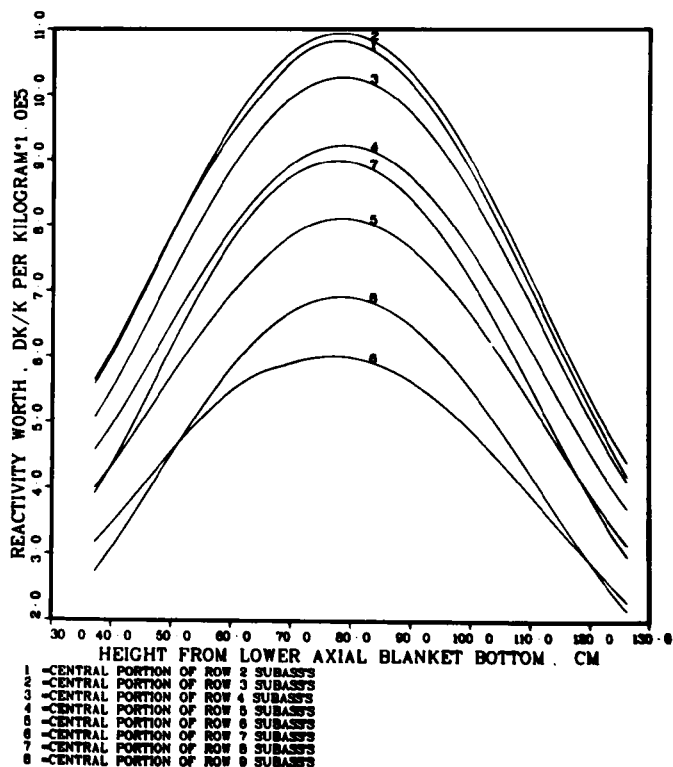
Fig. II-38.

Axial Distribution of Steel Worth in Core and Blankets in the LWR-Grade Plutonium Fueled Clinch River Breeder Reactor at the Beginning of Life. ANL Neg. No. 116-77-663.

- 1 - CENTRAL PORTION OF ROW 2 SUBASSEMBLY
- 2 - CENTRAL PORTION OF ROW 3 SUBASSEMBLY
- 3 - CENTRAL PORTION OF ROW 4 SUBASSEMBLY
- 4 - CENTRAL PORTION OF ROW 5 SUBASSEMBLY
- 5 - CENTRAL PORTION OF ROW 6 SUBASSEMBLY
- 6 - CENTRAL PORTION OF ROW 7 SUBASSEMBLY
- 7 - CENTRAL PORTION OF ROW 8 SUBASSEMBLY
- 8 - CENTRAL PORTION OF ROW 9 SUBASSEMBLY
- 9 - PORTION OF RADIAL BLANKET ADJACENT TO CORE
- 10 - RADIAL BLANKET MID-THICKNESS
- 11 - RADIAL BLANKET OUTER SURFACE

Fig. II-39.

Axial Distribution of Core Fuel Worth in Core in the LWR-Grade Plutonium Fueled Clinch River Breeder Reactor at the Beginning of Life. ANL Neg. No. 116-77-648.



- 1 - CENTRAL PORTION OF ROW 2 SUBASSEMBLY
- 2 - CENTRAL PORTION OF ROW 3 SUBASSEMBLY
- 3 - CENTRAL PORTION OF ROW 4 SUBASSEMBLY
- 4 - CENTRAL PORTION OF ROW 5 SUBASSEMBLY
- 5 - CENTRAL PORTION OF ROW 6 SUBASSEMBLY
- 6 - CENTRAL PORTION OF ROW 7 SUBASSEMBLY
- 7 - CENTRAL PORTION OF ROW 8 SUBASSEMBLY
- 8 - CENTRAL PORTION OF ROW 9 SUBASSEMBLY

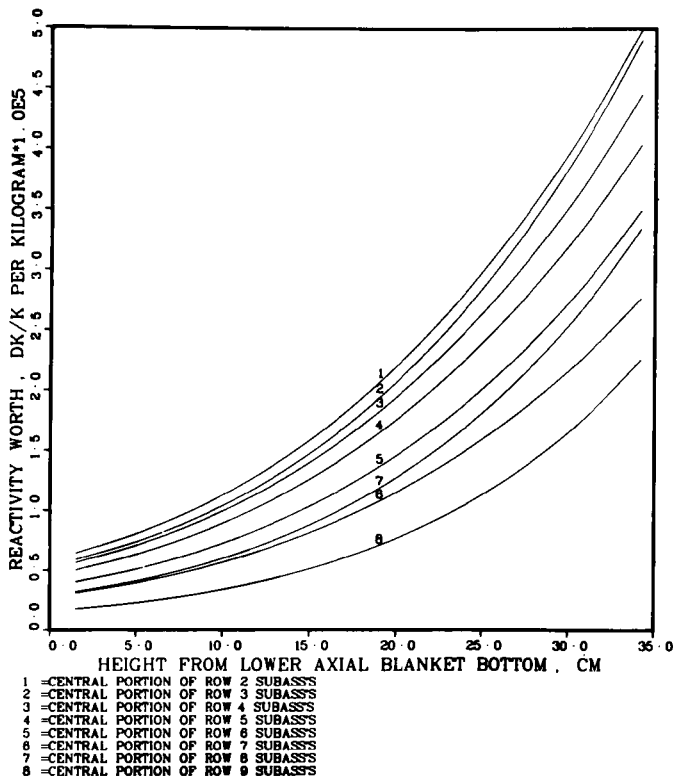
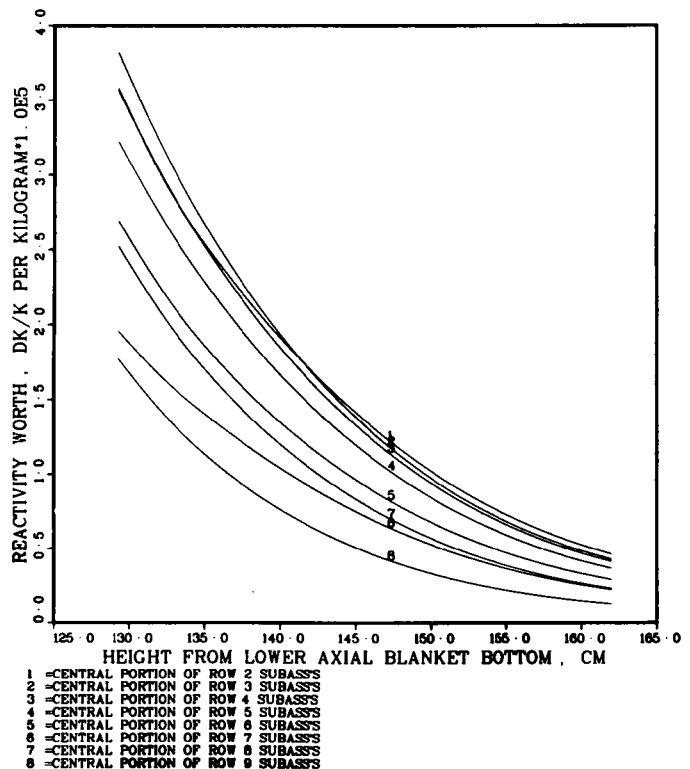
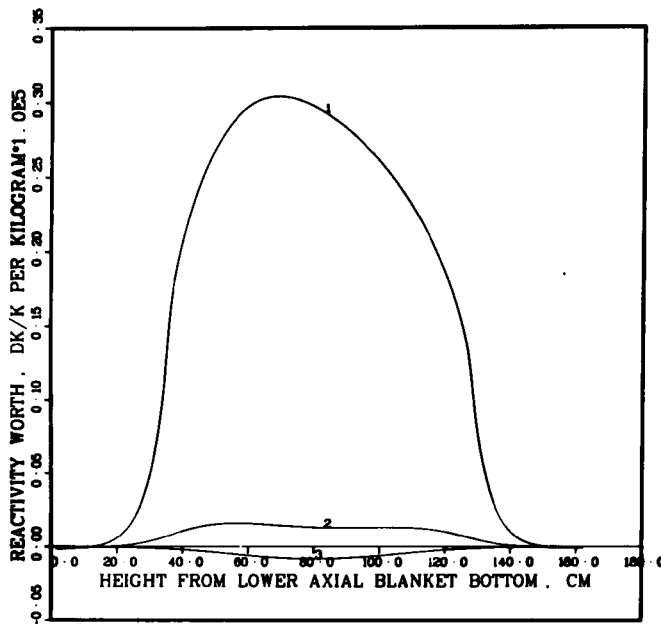


Fig. II-40.

Axial Distribution of Core Fuel Worth in Lower Blanket in the LWR-Grade Plutonium Fueled Clinch River Breeder Reactor at the Beginning of Life. ANL Neg. No. 116-77-660.

Fig. II-41.
 Axial Distribution of Core Fuel Worth in Upper Blanket in the LWR-Grade Plutonium Fueled Clinch River Breeder Reactor at the Beginning of Life. ANL Neg. No. 116-77-629.





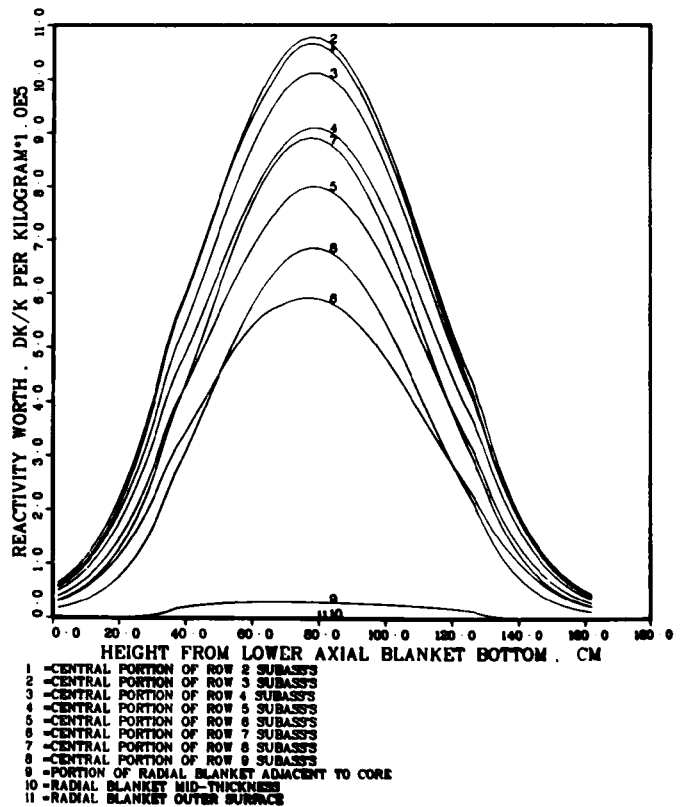
- 1 -PORTION OF RADIAL BLANKET ADJACENT TO CORE
- 2 -RADIAL BLANKET MID-THICKNESS
- 3 -RADIAL BLANKET OUTER SURFACE

Fig. II-42.

Axial Distribution of Radial Blanket Fuel Worth in the LWR-Grade Plutonium Fueled Clinch River Breeder Reactor at the Beginning of Life. ANL Neg. No. 116-77-616

Fig. II-43.

Axial Distribution of Core and Radial Blanket Fuel Worths in the LWR-Grade Plutonium Fueled Clinch River Breeder Reactor at the Beginning of Life. ANL Neg. No. 116-77-615.



- 1 -CENTRAL PORTION OF ROW 2 SUBASSES
- 2 -CENTRAL PORTION OF ROW 3 SUBASSES
- 3 -CENTRAL PORTION OF ROW 4 SUBASSES
- 4 -CENTRAL PORTION OF ROW 5 SUBASSES
- 5 -CENTRAL PORTION OF ROW 6 SUBASSES
- 6 -CENTRAL PORTION OF ROW 7 SUBASSES
- 7 -CENTRAL PORTION OF ROW 8 SUBASSES
- 8 -CENTRAL PORTION OF ROW 9 SUBASSES
- 9 -PORTION OF RADIAL BLANKET ADJACENT TO CORE
- 10 -RADIAL BLANKET MID-THICKNESS
- 11 -RADIAL BLANKET OUTER SURFACE

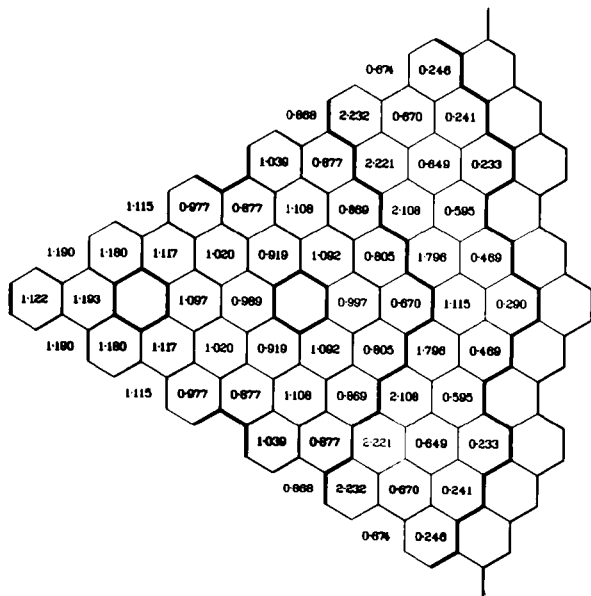


Fig. III-1.

Subassembly Power Factors for the FFTF Plutonium Fueled Clinch River Breeder Reactor at the Beginning of Life. ANL Neg. No. 116-77-661

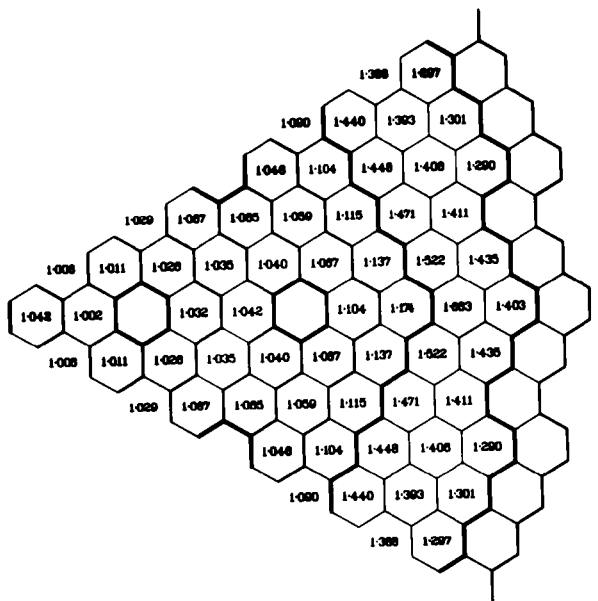


Fig. III-2.

Subassembly Peak-to-Average Power Density Ratios for the FFTF Plutonium Fueled Clinch River Breeder Reactor at the Beginning of Life. ANL Neg. No. 116-77-652

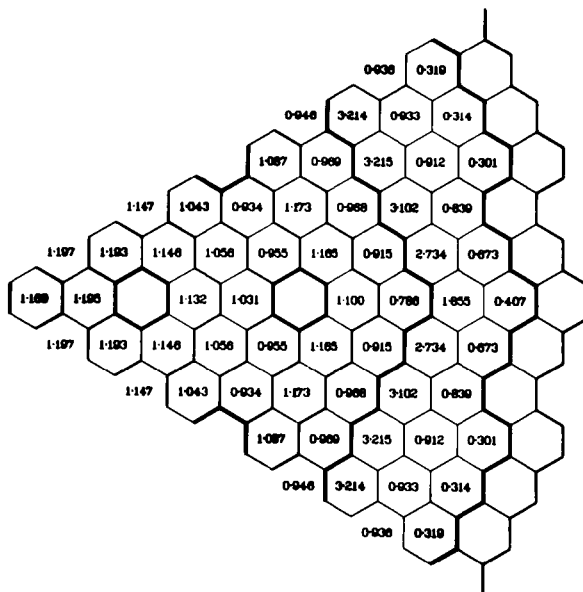


Fig. III-3.

Subassembly Peak Power Factors for the FFTF Plutonium Fueled Clinch River Breeder Reactor at the Beginning of Life. ANL Neg. No. 116-77-653

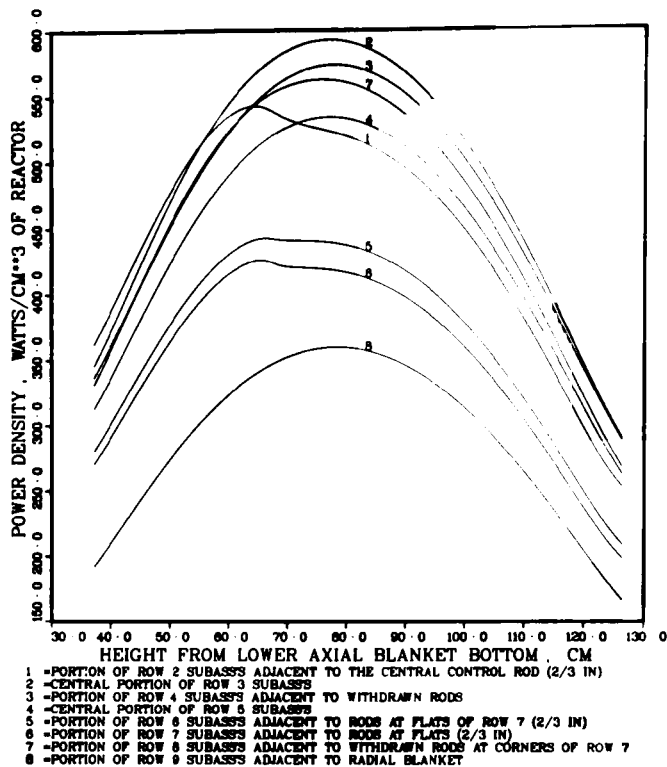
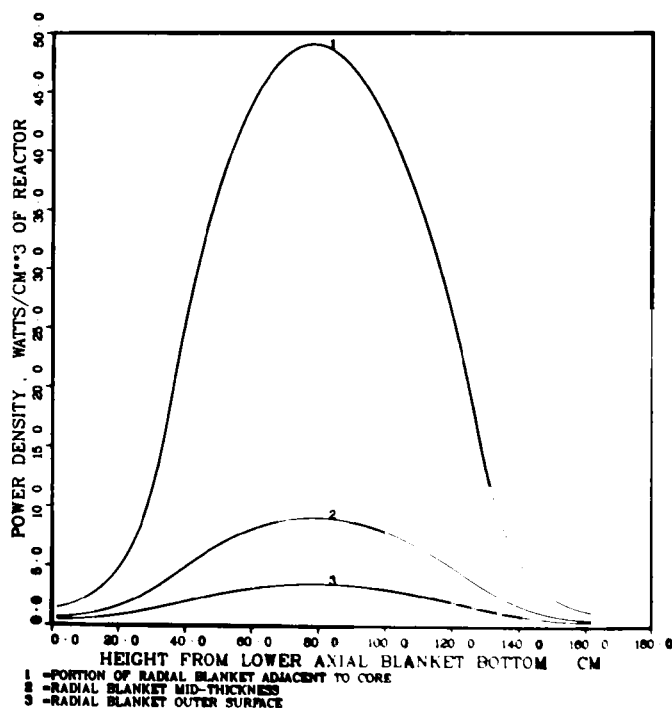


Fig. III-4.

Axial Distribution of Power in
the FFTF-Plutonium Fueled Clinch
River Breeder Reactor Core at
the Beginning of Life.
ANL Neg. No. 116-77-608

Fig. III-5.

Axial Distribution of Power in
the FFTF-Plutonium Fueled Clinch
River Breeder Reactor Radial
Blanket at the Beginning of
Life. ANL Neg. No. 116-77-665



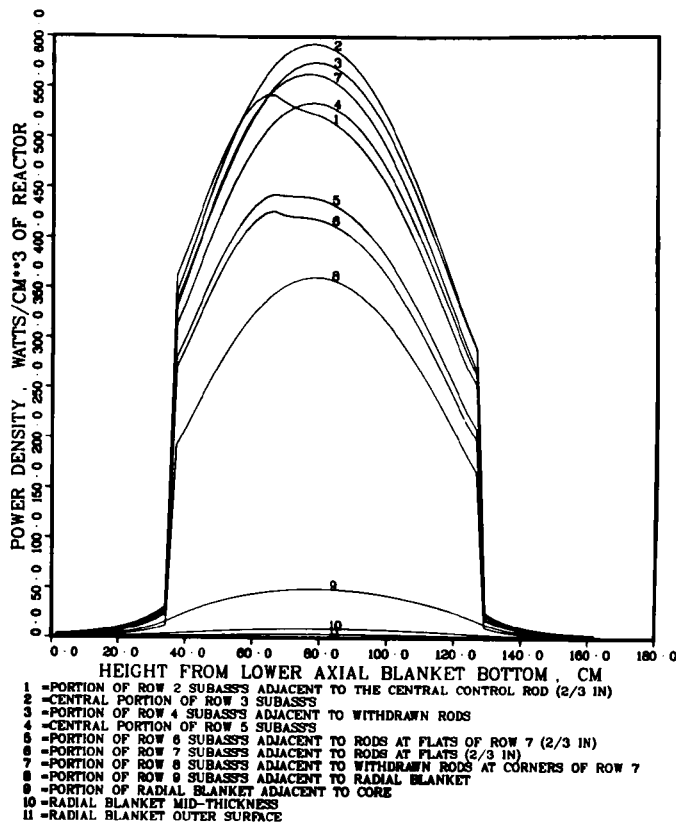
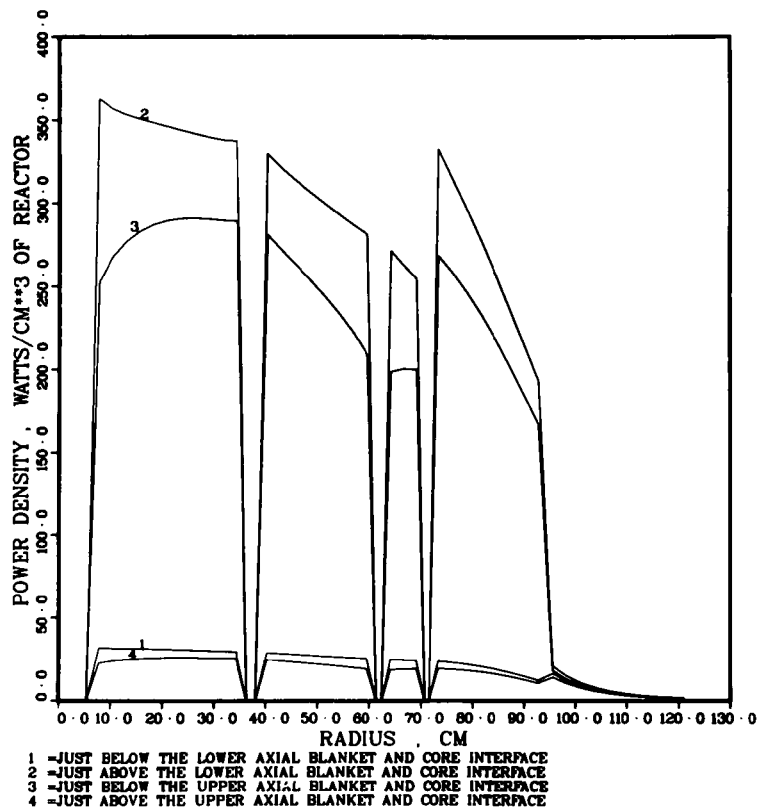


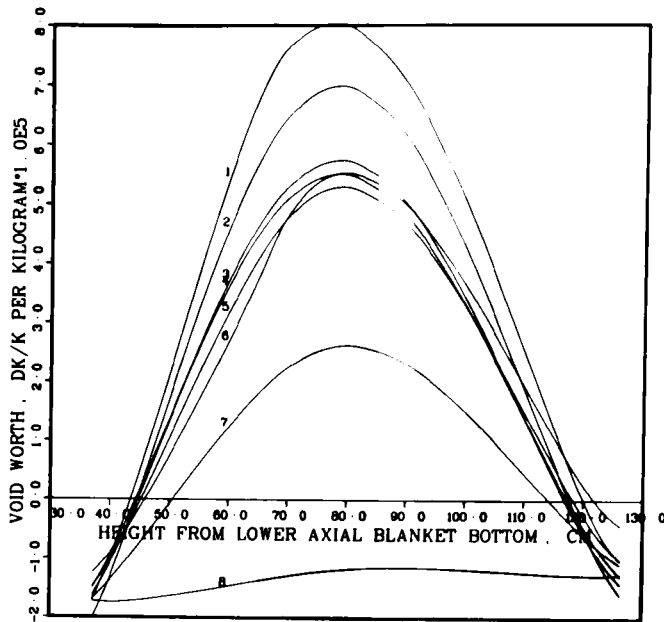
Fig. III-6.

Axial Distribution of Power in the FFTF-Plutonium Fueled Clinch River Breeder Reactor Core and Blanket at the Beginning of Life
ANL Neg. No. 116-77-664

Fig. III-7.

Radial Distribution of Power in the FFTF-Plutonium Fueled Clinch River Breeder Reactor Core and Blanket at the Beginning of Life.
ANL Neg. No. 116-77-572





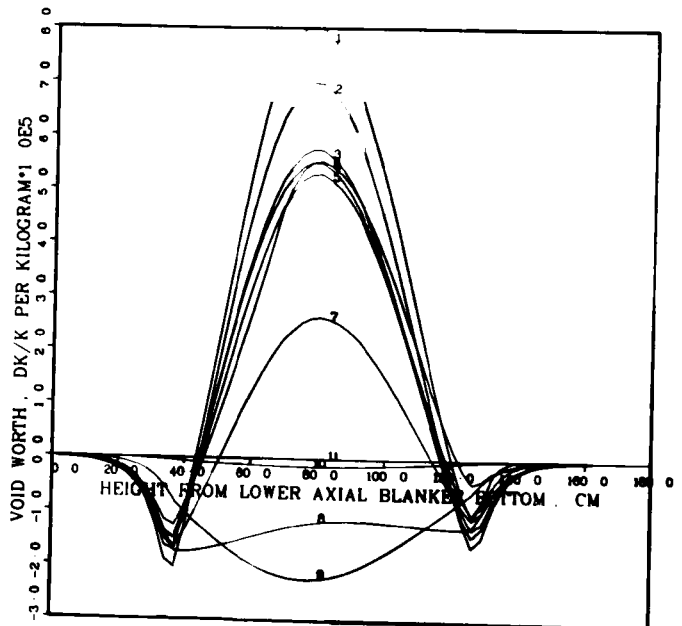
- 1 - CENTRAL PORTION OF ROW 2 SUBASSES
- 2 - CENTRAL PORTION OF ROW 3 SUBASSES
- 3 - CENTRAL PORTION OF ROW 4 SUBASSES
- 4 - CENTRAL PORTION OF ROW 5 SUBASSES
- 5 - CENTRAL PORTION OF ROW 6 SUBASSES
- 6 - CENTRAL PORTION OF ROW 7 SUBASSES
- 7 - CENTRAL PORTION OF ROW 8 SUBASSES
- 8 - CENTRAL PORTION OF ROW 9 SUBASSES

Fig. III-8.

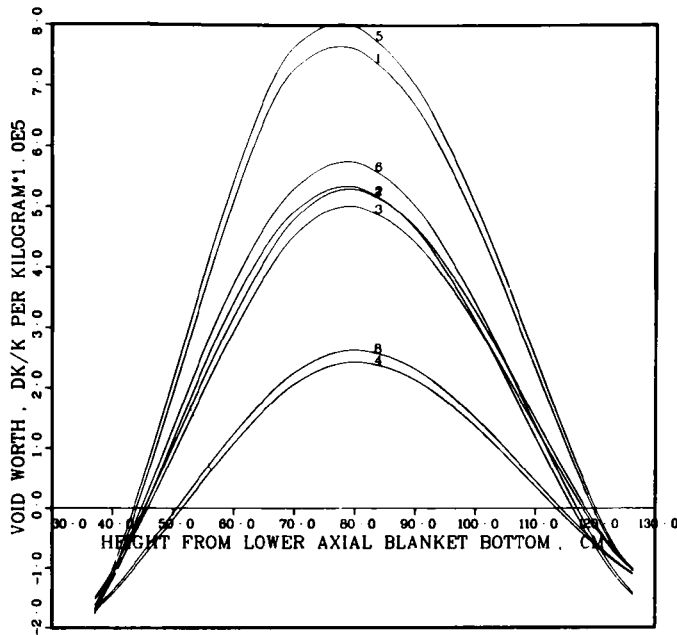
Distribution of Sodium Void Worth in Core in the FFTF-Plutonium Fueled Clinch River Breeder Reactor at the Beginning of Life. ANL Neg. No. 116-77-638.

Fig. III-9.

Distribution of Sodium Void Worth in Core and Blankets in the FFTF-Plutonium Fueled Clinch River Breeder Reactor at the Beginning of Life. ANL Neg. No. 116-77-655



- 1 - CENTRAL PORTION OF ROW 2 SUBASSES
- 2 - CENTRAL PORTION OF ROW 3 SUBASSES
- 3 - CENTRAL PORTION OF ROW 4 SUBASSES
- 4 - CENTRAL PORTION OF ROW 5 SUBASSES
- 5 - CENTRAL PORTION OF ROW 6 SUBASSES
- 6 - CENTRAL PORTION OF ROW 7 SUBASSES
- 7 - CENTRAL PORTION OF ROW 8 SUBASSES
- 8 - CENTRAL PORTION OF ROW 9 SUBASSES
- 9 - PORTION OF RADIAL BLANKET ADJACENT TO CORE
- 10 - RADIAL BLANKET MID-THICKNESS
- 11 - RADIAL BLANKET OUTER SURFACE



1 = LWR-Pu FUEL . CENTRAL PORTION OF ROW 2 SUBASSYS
 2 = LWR-Pu FUEL . CENTRAL PORTION OF ROW 4 SUBASSYS
 3 = LWR-Pu FUEL . CENTRAL PORTION OF ROW 6 SUBASSYS
 4 = LWR-Pu FUEL . CENTRAL PORTION OF ROW 8 SUBASSYS
 5 = FFTF-Pu FUEL . RADIAL POSITION SAME AS 1
 6 = FFTF-Pu FUEL . RADIAL POSITION SAME AS 2
 7 = FFTF-Pu FUEL . RADIAL POSITION SAME AS 3
 8 = FFTF-Pu FUEL . RADIAL POSITION SAME AS 4

Fig. III-10.

Comparison of Void Worth Distributions in Core Between LWR-Pu-Fueled and FFTF-Pu-Fueled CRBR at the Beginning of Life.
 ANL Neg. No. 116-77-671

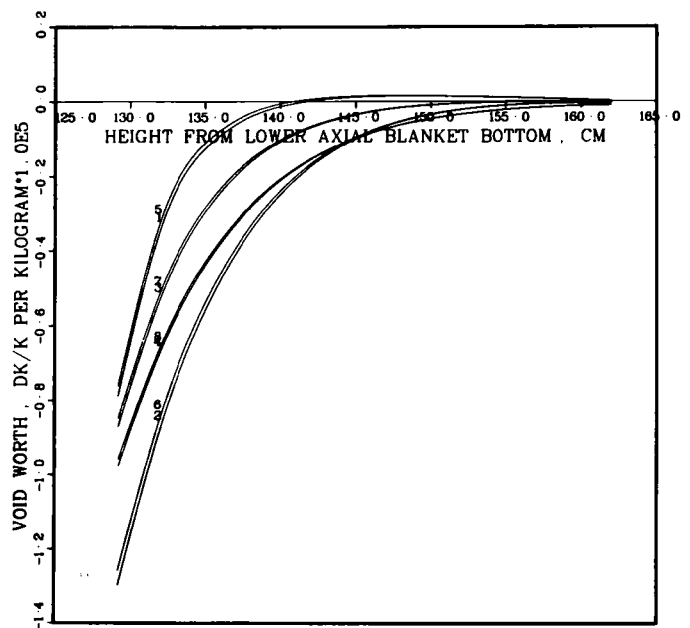


Fig. III-11.

Comparison of Void Worth Distributions in Upper Blanket Between LWR-Pu-Fueled and FFTF-Pu-Fueled CRBR at the Beginning of Life.
 ANL Neg. No. 116-77-672

1 = LWR-Pu FUEL . CENTRAL PORTION OF ROW 2 SUBASSYS
 2 = LWR-Pu FUEL . CENTRAL PORTION OF ROW 4 SUBASSYS
 3 = LWR-Pu FUEL . CENTRAL PORTION OF ROW 6 SUBASSYS
 4 = LWR-Pu FUEL . CENTRAL PORTION OF ROW 8 SUBASSYS
 5 = FFTF-Pu FUEL . RADIAL POSITION SAME AS 1
 6 = FFTF-Pu FUEL . RADIAL POSITION SAME AS 2
 7 = FFTF-Pu FUEL . RADIAL POSITION SAME AS 3
 8 = FFTF-Pu FUEL . RADIAL POSITION SAME AS 4

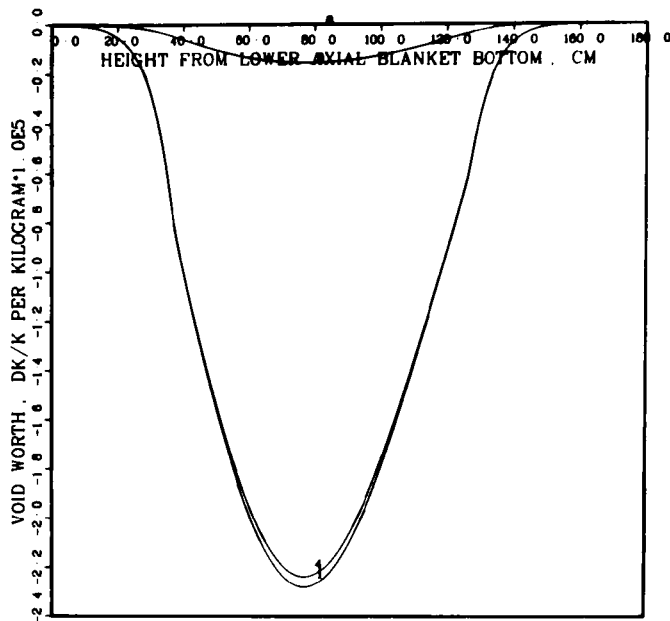


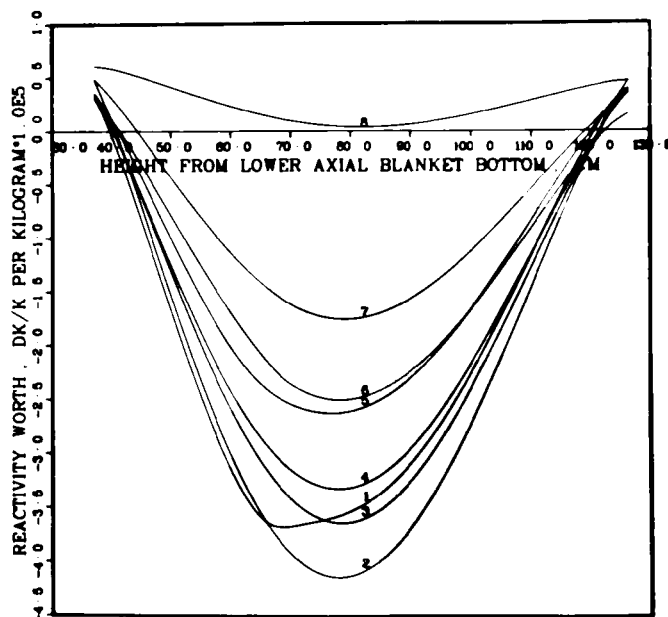
Fig. III-12.

Comparison of Void Worth Distributions in Radial Blanket Between LWR-Pu-Fueled and FFTF-Pu-Fueled CRBR at the Beginning of Life.
ANL Neg. No. 116-77-673.

- 1 = LWR-Pu FUEL . . . PORTION OF RADIAL BLANKET ADJACENT TO CORE
- 2 = LWR-Pu FUEL . . . RADIAL BLANKET MID-THICKNESS
- 3 = LWR-Pu FUEL . . . RADIAL BLANKET OUTER SURFACE
- 4 = FFTF-Pu FUEL . . . RADIAL POSITION SAME AS 1
- 5 = FFTF-Pu FUEL . . . RADIAL POSITION SAME AS 2
- 6 = FFTF-Pu FUEL . . . RADIAL POSITION SAME AS 3

Fig. III-13.

Axial Distribution of Steel Worth in Core in the FFTF-Plutonium Fueled Clinch River Breeder Reactor at the Beginning of Life. ANL Neg. No. 116-77-619



- 1 - CENTRAL PORTION OF ROW 2 SUBASSEMBLY
- 2 - CENTRAL PORTION OF ROW 3 SUBASSEMBLY
- 3 - CENTRAL PORTION OF ROW 4 SUBASSEMBLY
- 4 - CENTRAL PORTION OF ROW 5 SUBASSEMBLY
- 5 - CENTRAL PORTION OF ROW 6 SUBASSEMBLY
- 6 - CENTRAL PORTION OF ROW 7 SUBASSEMBLY
- 7 - CENTRAL PORTION OF ROW 8 SUBASSEMBLY
- 8 - CENTRAL PORTION OF ROW 9 SUBASSEMBLY

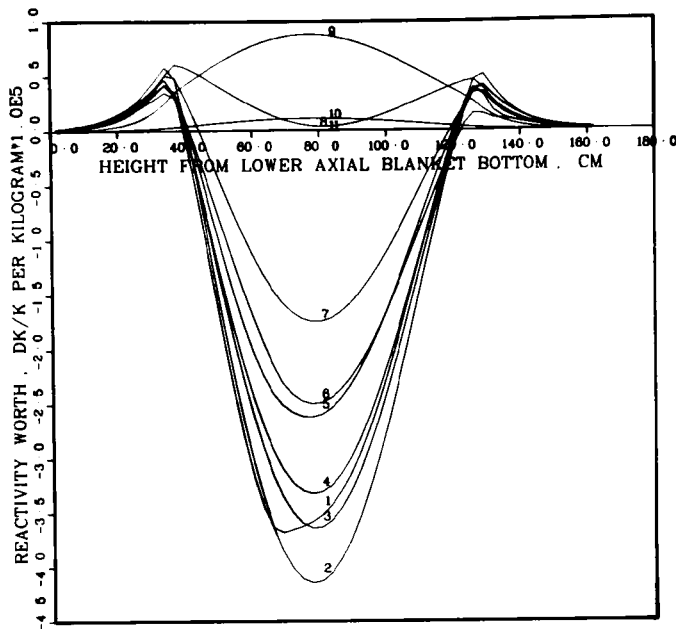


Fig. III-14.

Axial Distribution of Steel Worth in Core and Blankets in the FFTF-Plutonium Fueled Clinch River Breeder Reactor at the Beginning of Life.
ANL Neg. No. 116-77-620

- 1 = CENTRAL PORTION OF ROW 2 SUBASS'S
- 2 = CENTRAL PORTION OF ROW 3 SUBASS'S
- 3 = CENTRAL PORTION OF ROW 4 SUBASS'S
- 4 = CENTRAL PORTION OF ROW 5 SUBASS'S
- 5 = CENTRAL PORTION OF ROW 6 SUBASS'S
- 6 = CENTRAL PORTION OF ROW 7 SUBASS'S
- 7 = CENTRAL PORTION OF ROW 8 SUBASS'S
- 8 = CENTRAL PORTION OF ROW 9 SUBASS'S
- 9 = PORTION OF RADIAL BLANKET ADJACENT TO CORE
- 10 = RADIAL BLANKET MID-THICKNESS
- 11 = RADIAL BLANKET OUTER SURFACE

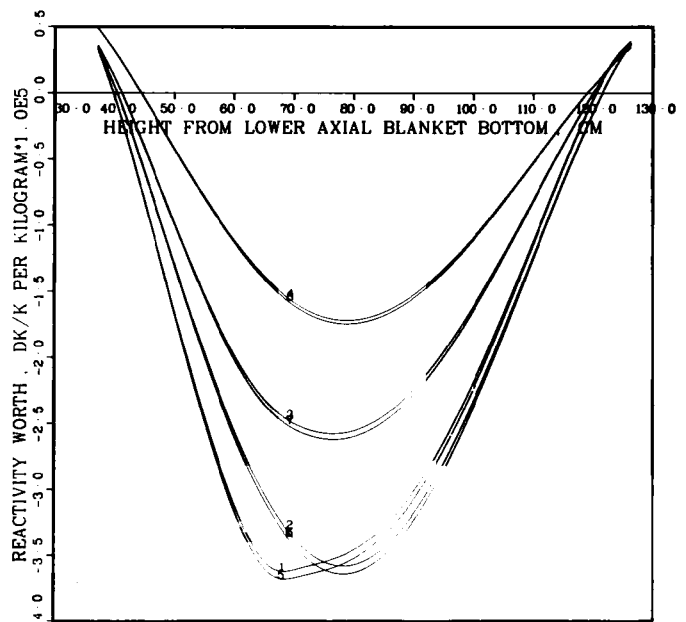


Fig. III-15.

Comparison of Steel Worth Distributions in Core Between LWR-Pu-Fueled and FFTF-Pu-Fueled CRBR at the Beginning of Life.
ANL Neg. No. 116-77-625

- 1 = LWR-PU FUEL CENTRAL PORTION OF ROW 2 SUBASS'S
- 2 = LWR-PU FUEL CENTRAL PORTION OF ROW 4 SUBASS'S
- 3 = LWR-PU FUEL CENTRAL PORTION OF ROW 6 SUBASS'S
- 4 = LWR-PU FUEL CENTRAL PORTION OF ROW 8 SUBASS'S
- 5 = FFTF-PU FUEL RADIAL POSITION SAME AS 1
- 6 = FFTF-PU FUEL RADIAL POSITION SAME AS 2
- 7 = FFTF-PU FUEL RADIAL POSITION SAME AS 3
- 8 = FFTF-PU FUEL RADIAL POSITION SAME AS 4

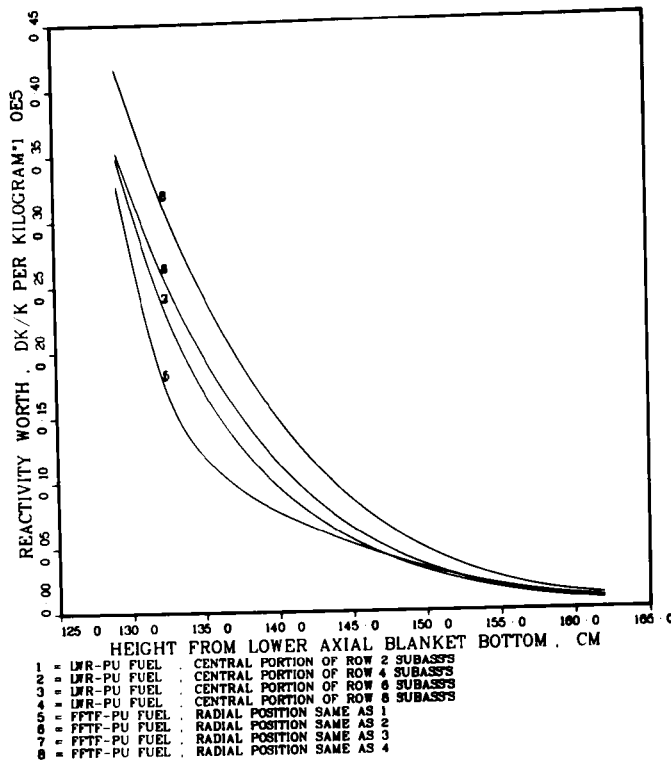
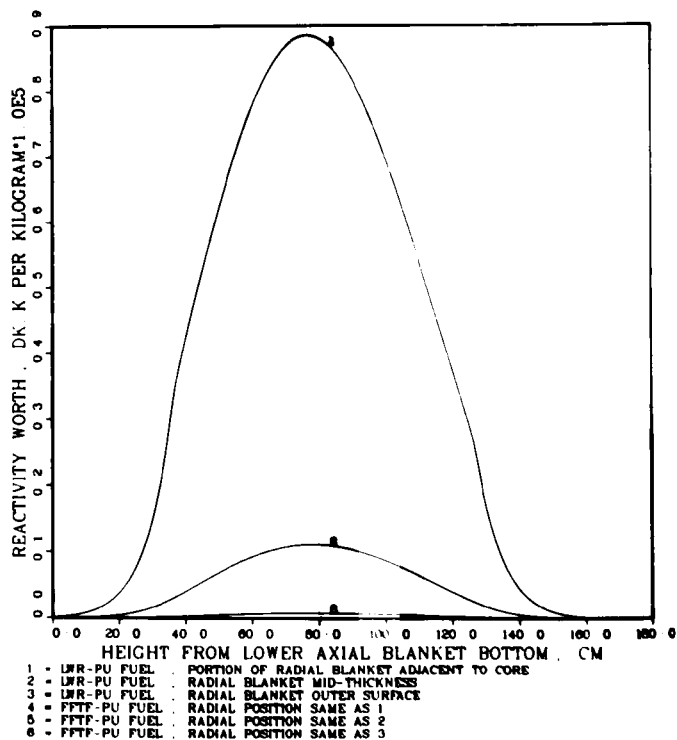


Fig. III-16.

Comparison of Steel Worth Distributions in Upper Blanket Between LWR-Pu-Fueled and FFTF-Pu-Fueled CRBR at the Beginning of Life.
 ANL Neg. No. 116-77-626.

Fig. III-17.

Comparison of Steel Worth Distributions in Radial Blanket Between LWR-Pu-Fueled and FFTF-Pu-Fueled CRBR at the Beginning of Life.
 ANL Neg. No. 116-77-682



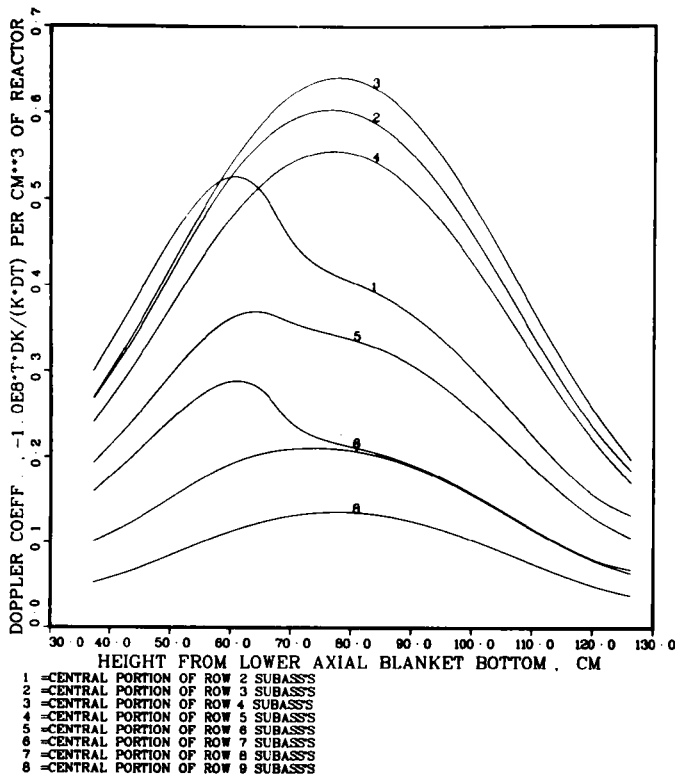
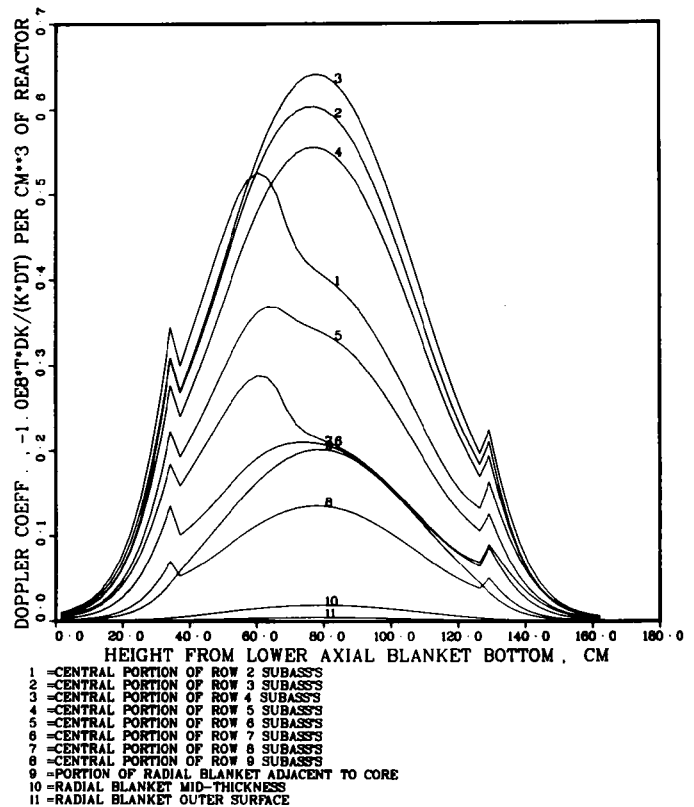


Fig. III-18.

Doppler Coefficient over 2200-4400K in Unvoided Core of the FFTF-Pu-Fueled CRBR at the Beginning of Life. ANL Neg. No. 116-77-683

Fig. III-19.

Doppler Coefficient over 2200-4400K in Unvoided Core and Blankets of the FFTF-Pu-Fueled CRBR at the Beginning of Life. ANL Neg. No. 116-77-646



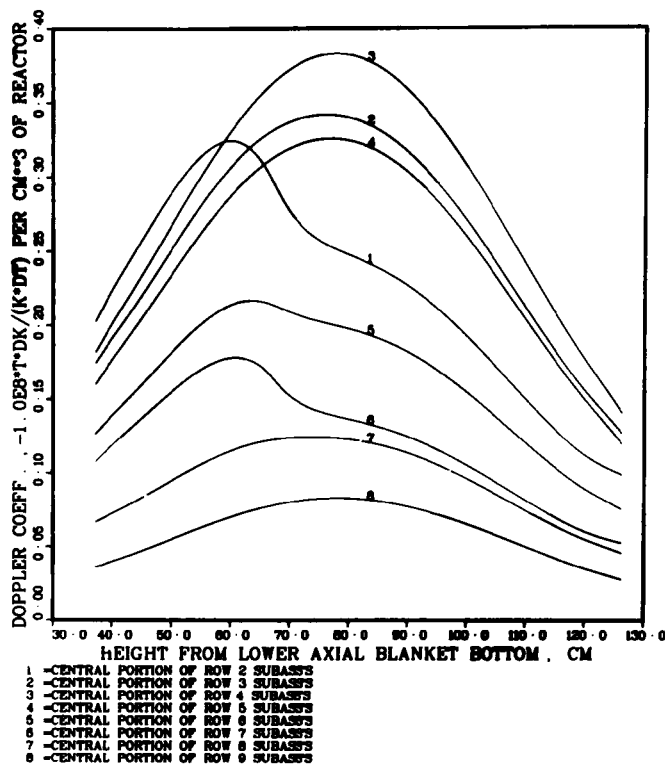
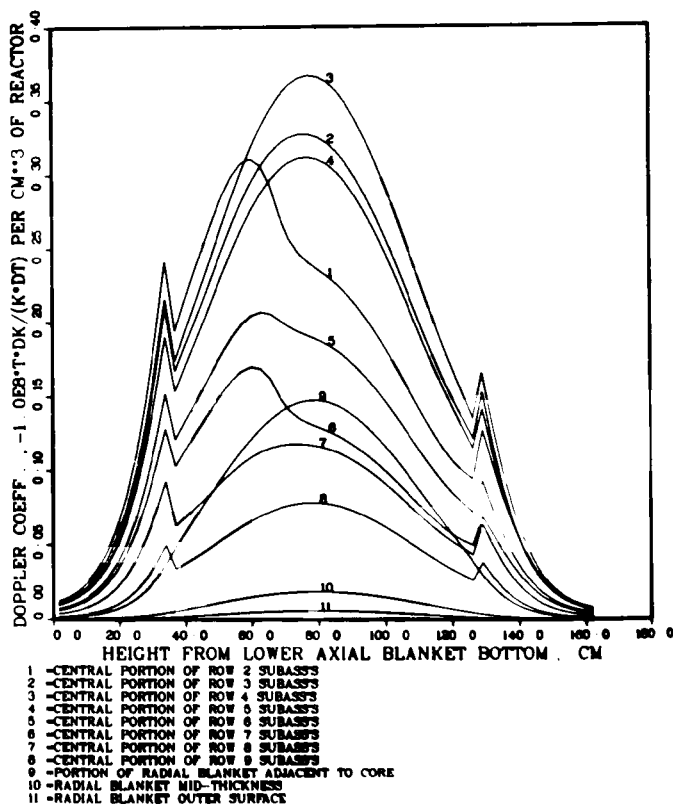


Fig. III-20.

Doppler Coefficient over 2200-4400K in Totally Voided Core of the FFTF-Pu-Fueled CRBR at the Beginning of Life.
ANL Neg. No. 116-77-624

Fig. III-21.

Doppler Coefficient over 2200-4400K in Totally Voided Core and Blankets of the FFTF-Pu-Fueled CRBR at the Beginning of Life. ANL Neg. No. 116-77-642



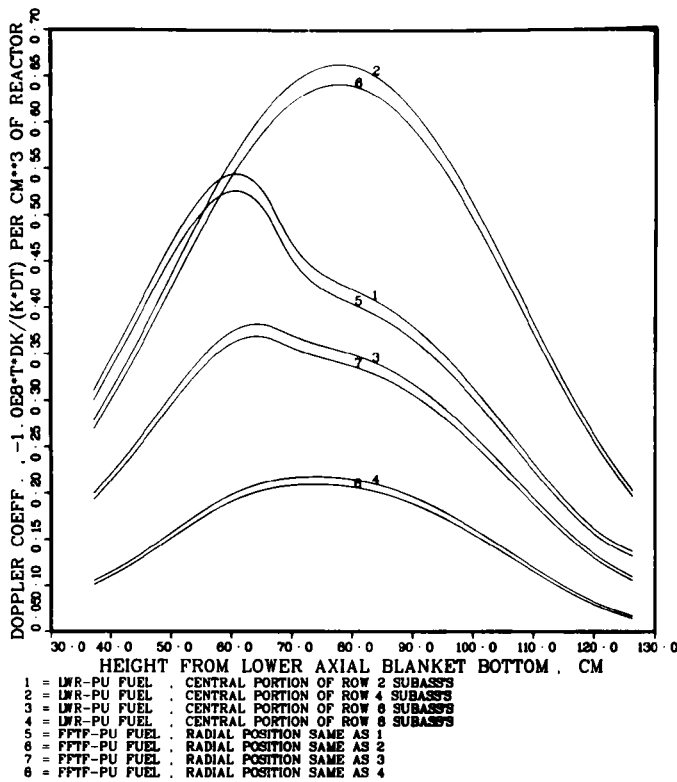
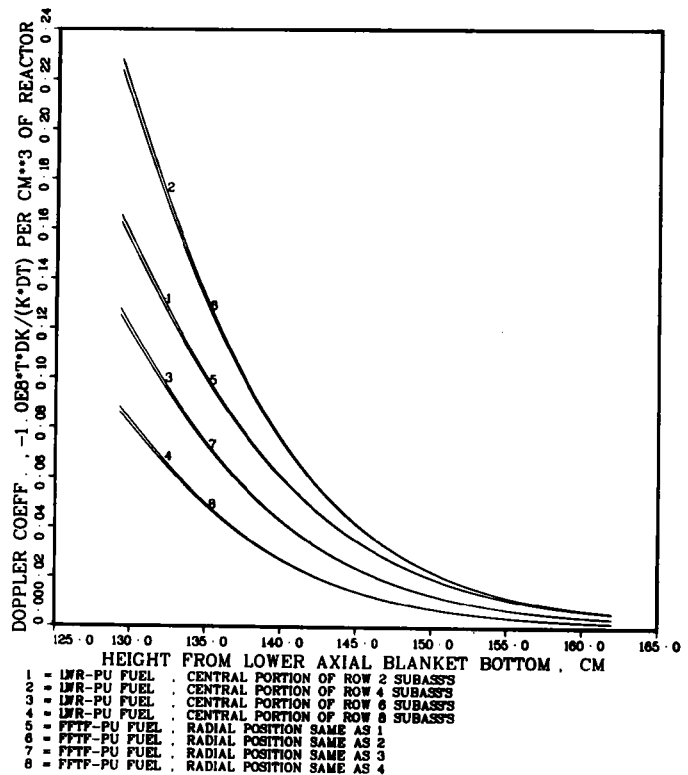


Fig. III-22.

Comparison of Doppler Coefficients over 2200-4400K in Unvoided Core Between LWR-Pu-Fueled and FFTF-Pu-Fueled CRBR at BOL. ANL Neg. No. 116-77-643

Fig. III-23.

Comparison of Doppler Coefficients over 2200-4400K in Unvoided Upper Blanket Between LWR-Pu-Fueled and FFTF-Pu-Fueled CRBR at BOL. ANL Neg. No. 116-77-641



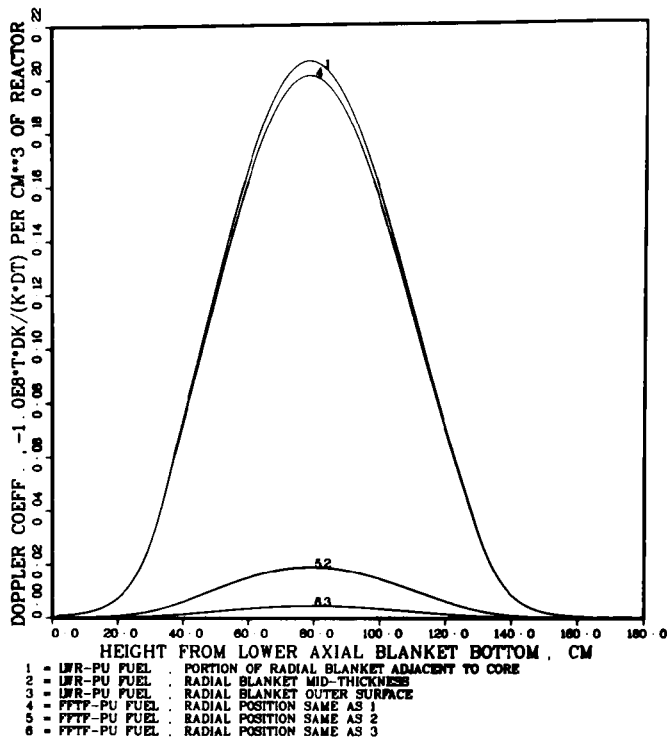
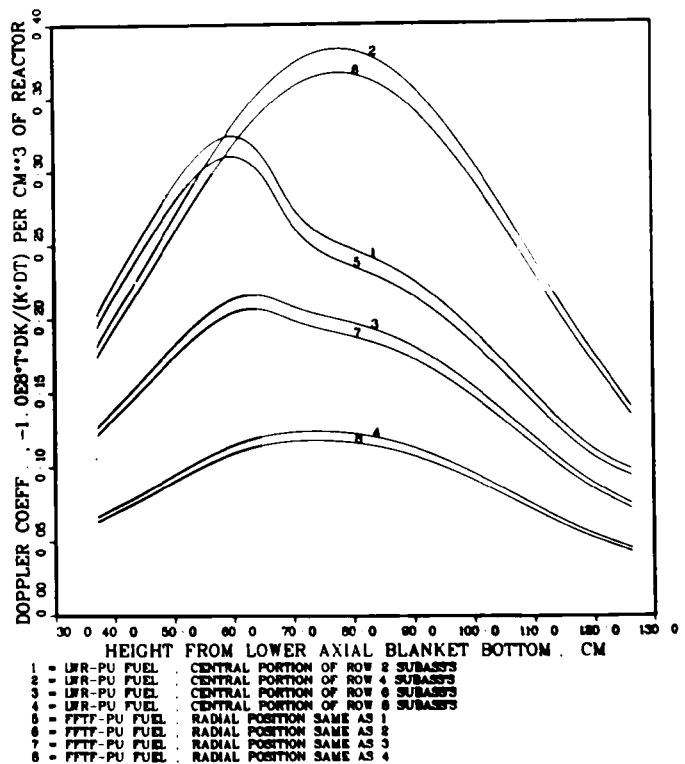


Fig. III-24.

Comparison of Doppler Coefficients over 2200-4400K in Unvoided Radial Blanket Between LWR-Pu-Fueled and FFTF-Pu-Fueled CRBR at BOL.
 ANL Neg. No. 116-77-640

Fig. III-25.

Comparison of Doppler Coefficients over 2200-4400K in Totally Voided Core Between LWR-Pu-Fueled and FFTF-Pu-Fueled CRBR at BOL.
 ANL Neg. No. 116-77-669



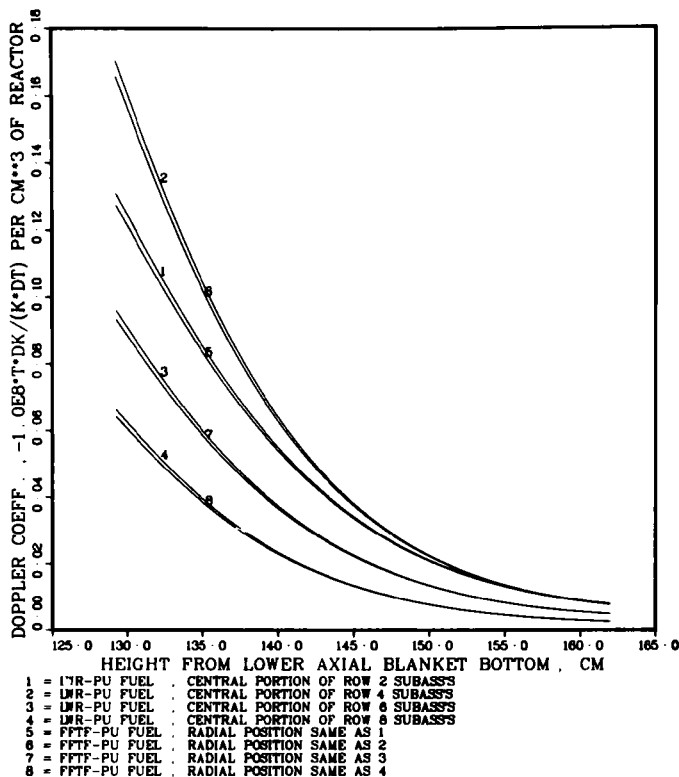
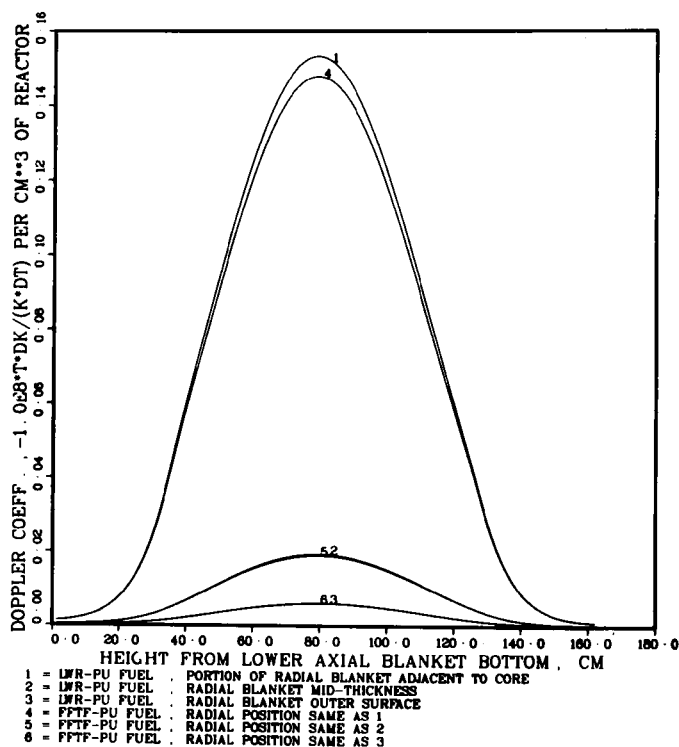


Fig. III-26.

Comparison of Doppler Coefficients over 2200-4400K in Totally Voided Upper Blanket Between LWR-Pu-Fueled and FFTF-Pu-Fueled CRBR at BOL.
 ANL Neg. No. 116-77-670

Fig. III-27.

Comparison of Doppler Coefficients over 2200-4400K in Totally Voided Radial Blanket Between LWR-Pu-Fueled and FFTF-Pu-Fueled CRBR at BOL.
 ANL Neg. No. 116-77-649



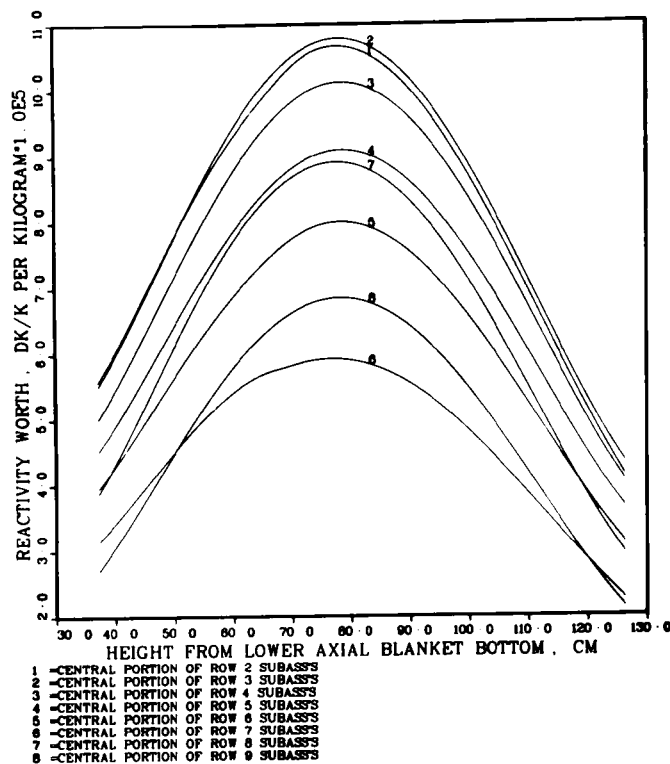
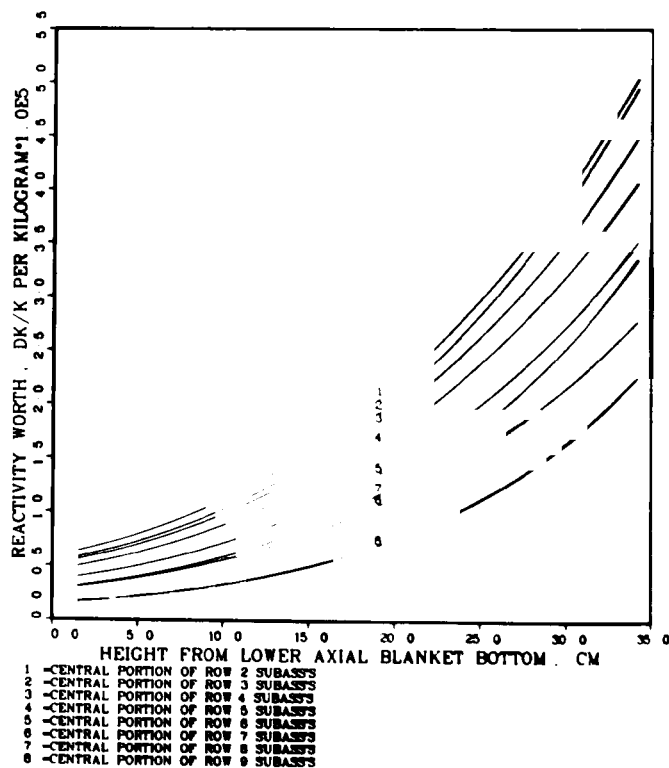


Fig. III-28.

Axial Distribution of Core Fuel Worth in Core in the FFTF-Plutonium Fueled Clinch River Breeder Reactor at the Beginning of Life.
ANL Neg. No. 116-77-668

Fig. III-29.

Axial Distribution of Core Fuel Worth in Lower Blanket in the FFTF-Plutonium Fueled Clinch River Breeder Reactor at the Beginning of Life.
ANL Neg. No. 116-77-630



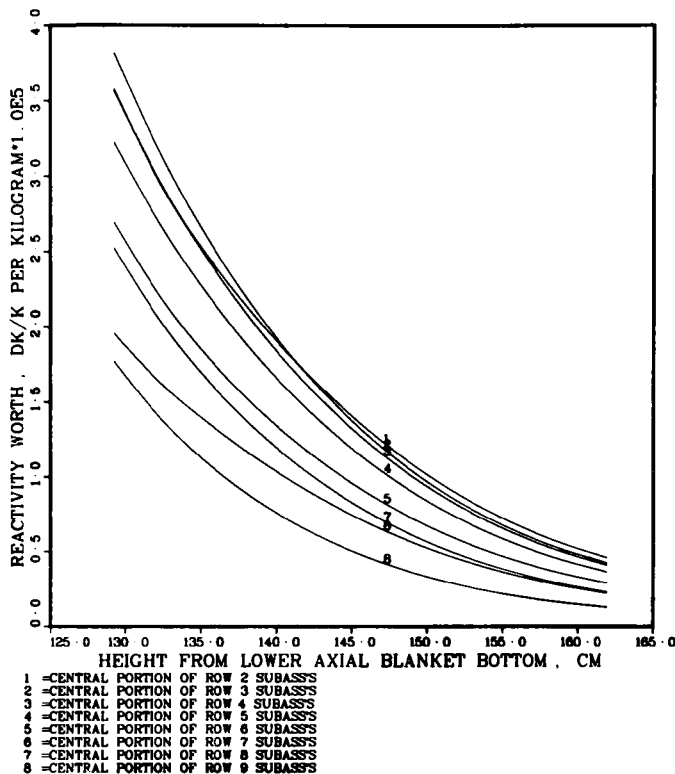
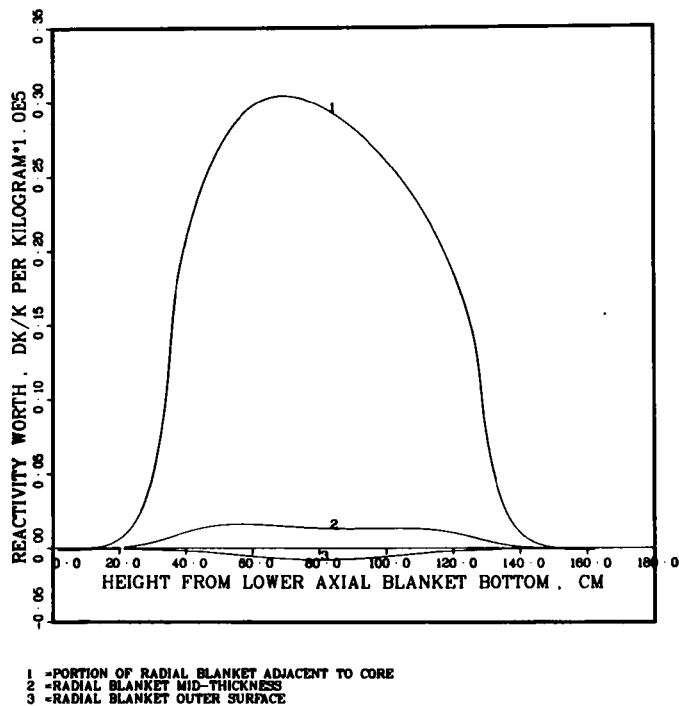


Fig. III-30.

Axial Distribution of Core Fuel Worth in Upper Blanket in the FFTF-Plutonium Fueled Clinch River Breeder Reactor at the Beginning of Life.
 ANL Neg. No. 116-77-659

Fig. III-31.

Axial Distribution of Radial Blanket Fuel Worth in the FFTF-Plutonium Fueled Clinch River Breeder Reactor at the Beginning of Life. ANL Neg. No. 116-77-674



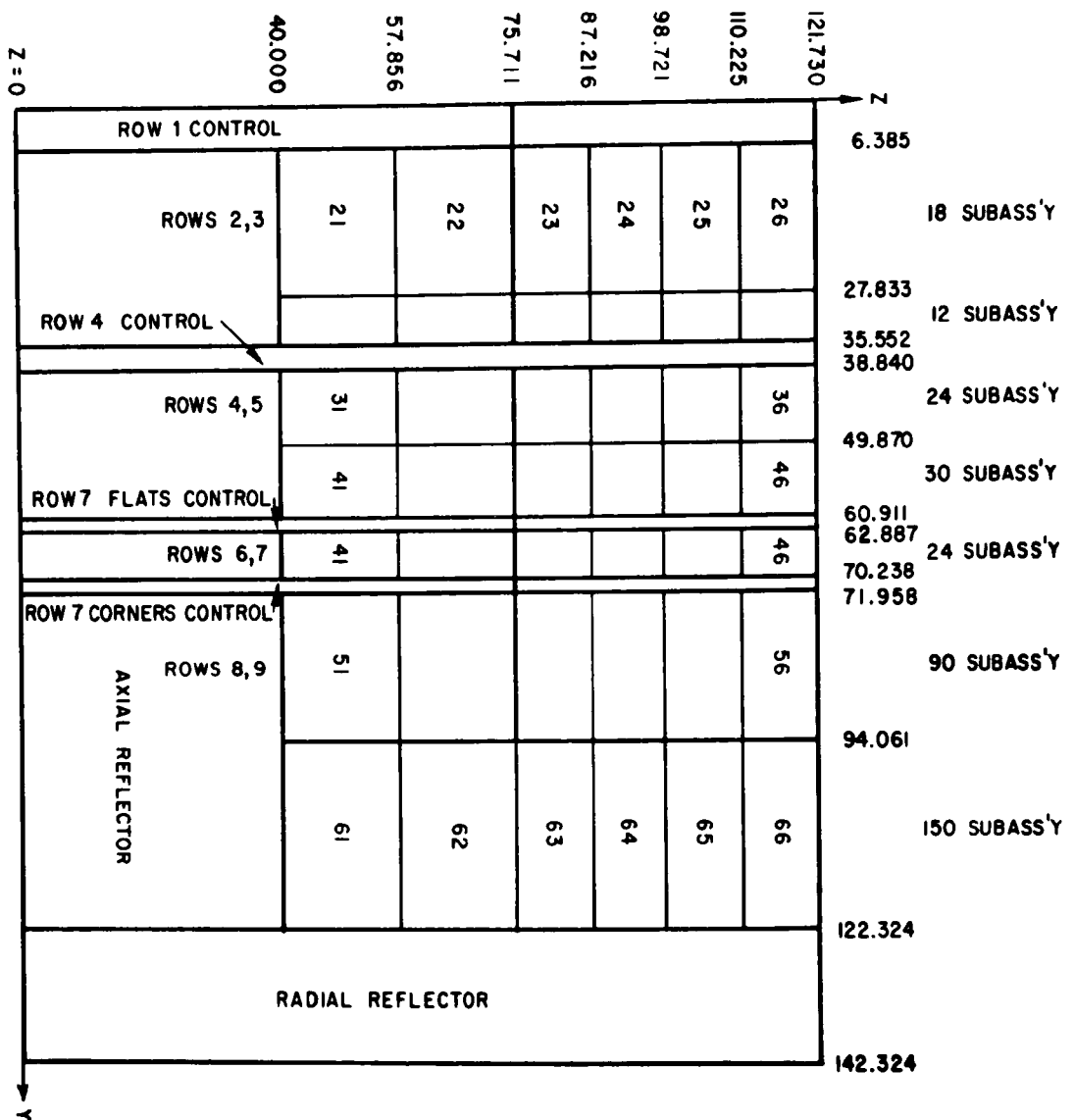


Fig. IV-1. R-Z Model of the Lower Half of the Hot Full Power Clinch River Breeder Reactor Used for Equilibrium Cycle Calculations. The two-digit numbers shown in the regions are region names. ANL Neg. No. 116-77-694

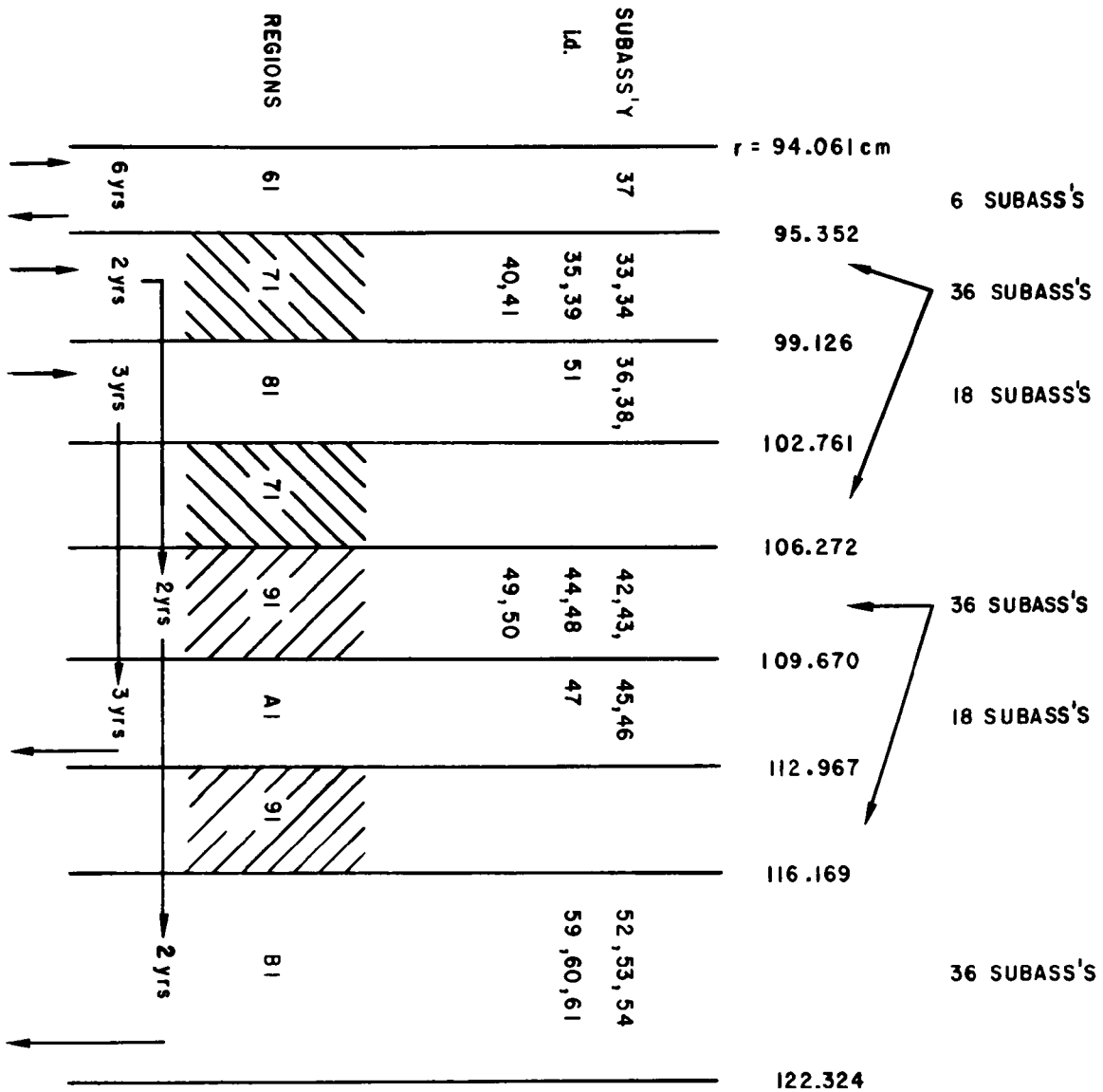


Fig. IV-2. Radial Split of the Radial Blanket of the Hot Full Power CRBR showing its Detailed Fuel Management Used for the Improved Equilibrium Cycle Calculations. The arrows indicate the charging, shuffling and discharging of the subassemblies. Axially there are six regions in the radial blanket and the rest of the R-Z model is the same as that shown in Fig. IV-1. Regions 7I and 9I each consist of two annuli. ANL Neg. No. 116-77-692.

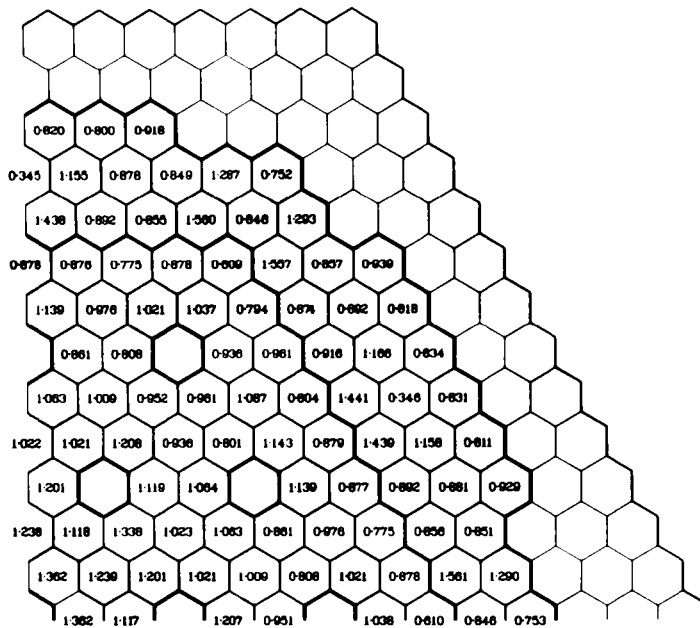
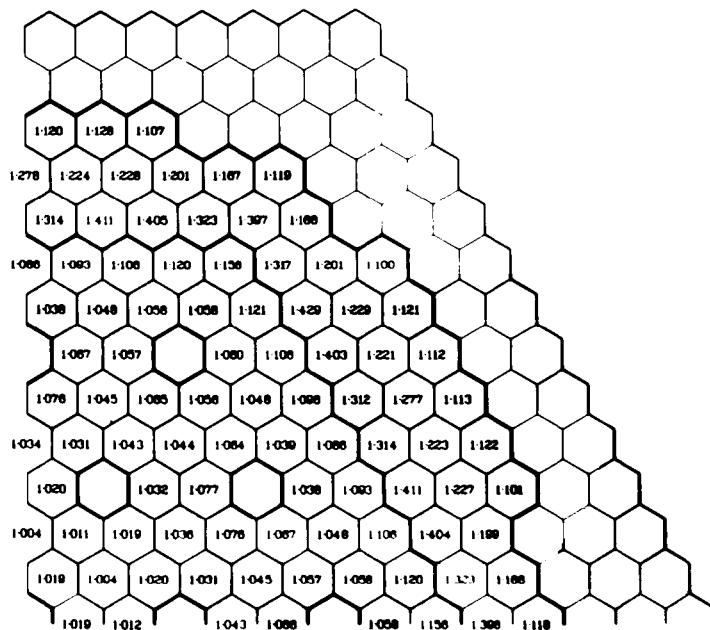


Fig. V-1

Subassembly Power Factors for
 the LWR-Grade Plutonium
 Fueled Clinch River Breeder
 Reactor at the Beginning of
 Equilibrium Cycle 14.
 ANL Neg. No. 116-77-618

Fig. V-2.

Subassembly Peak-To-Average
 Power Density Ratios for the
 LWR-Grade Plutonium Fueled
 Clinch River Breeder Reactor
 at the Beginning of Equilib-
 rium Cycle 14. ANL Neg. No.
 116-77-617



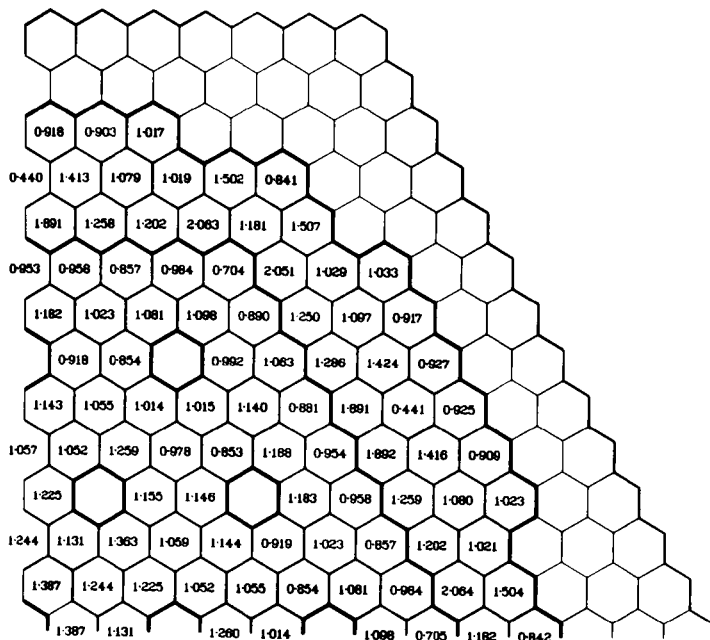
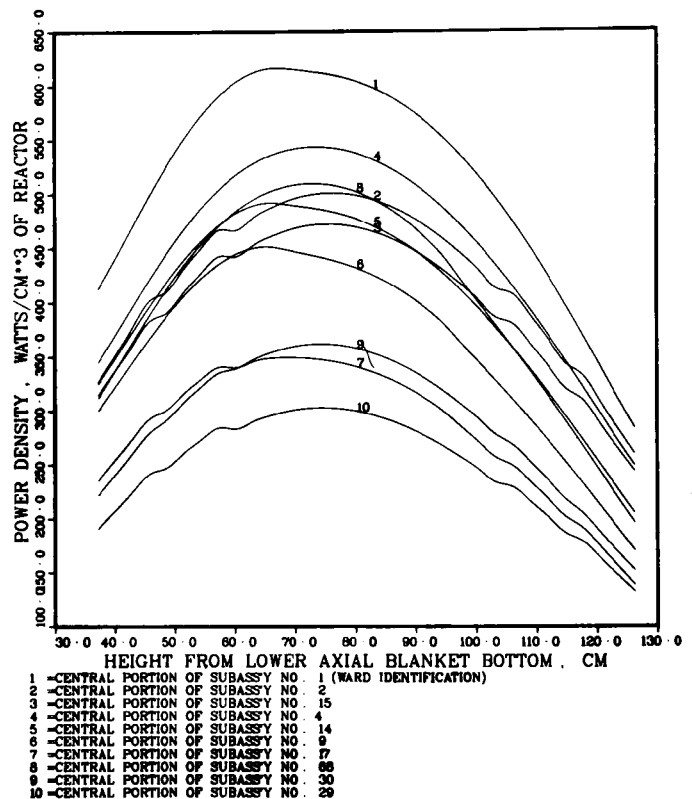


Fig. V-3.

Subassembly Peak Power
Factors for the LWR-Grade
Plutonium Fueled Clinch River
Breeder Reactor at the
Beginning of Equilibrium
Cycle 14. ANL Neg. No. 116-
77-656

Fig. V-4.

Axial Distribution of Power in
Core of the LWR-Pu-Fueled CRBR
at the Beginning of Equilibrium
Cycle 14. ANL Neg. No. 116-77-
598



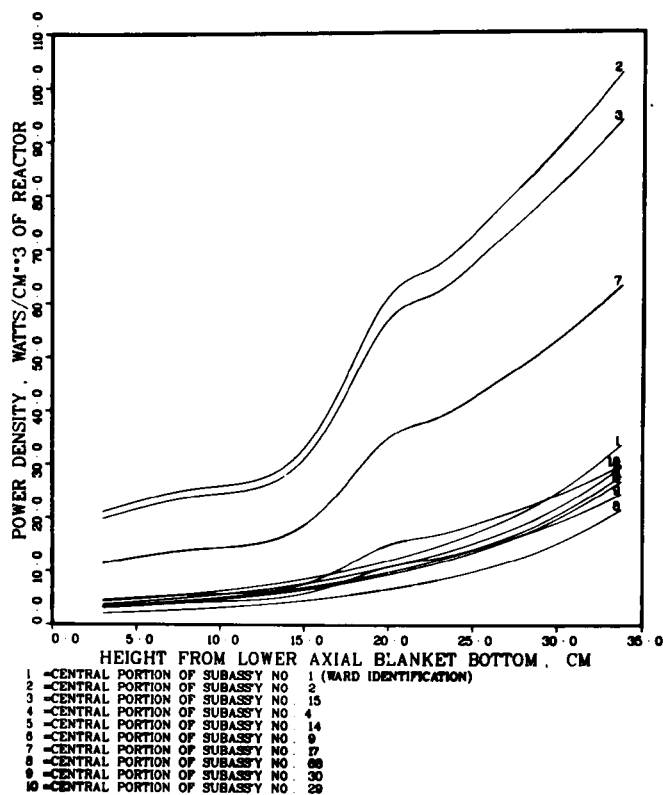
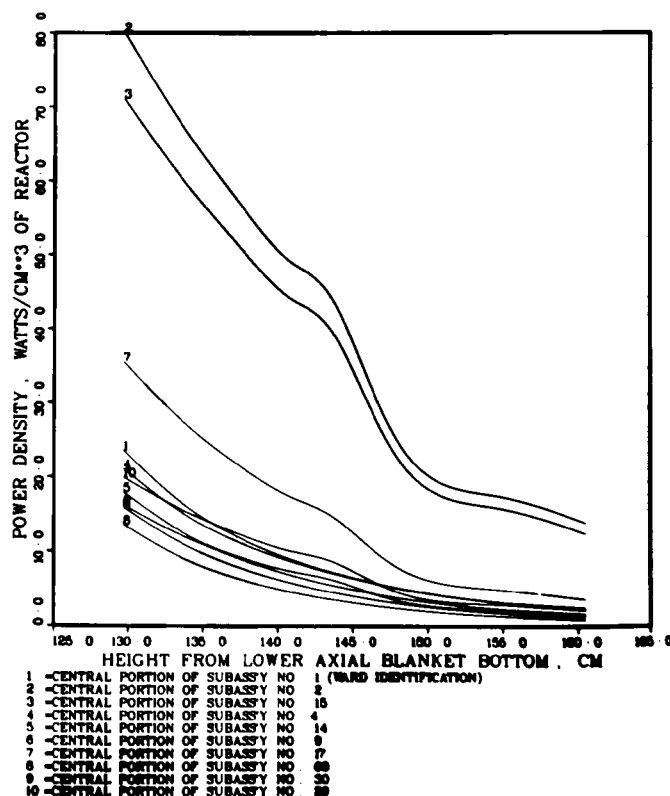


Fig. V-5.

Axial Distribution of Power in
Lower Blanket of the LWR-Pu-
Fueled CRBR at the Beginning of
Equilibrium Cycle 14.
ANL Neg. No. 116-77-611

Fig. V-6.

Axial Distribution of Power in
Upper Blanket of the LWR-Pu-
Fueled CRBR at the Beginning
of Equilibrium Cycle 14.
ANL Neg. No. 116-77-607



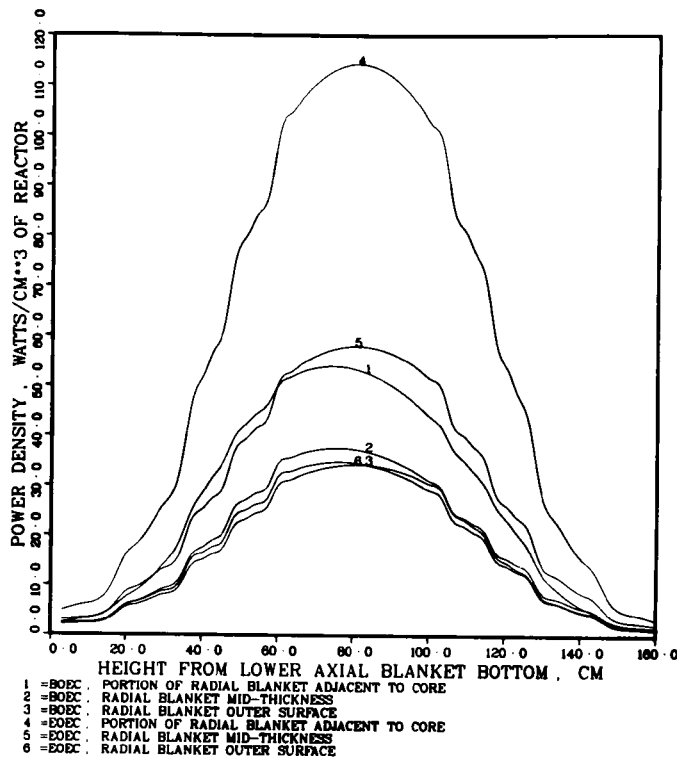
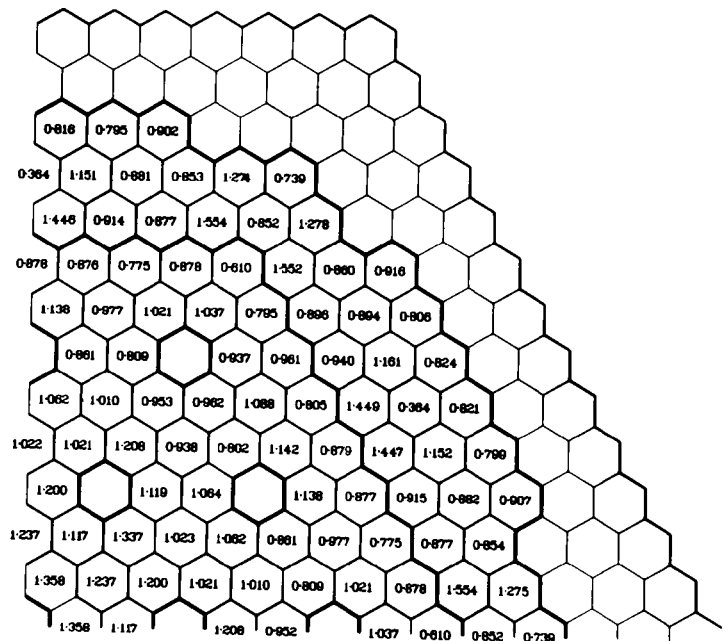


Fig. V-7.

Comparison of Power Distributions in Radial Blanket of the LWR-Pu-Fueled CRBR Between the BOEC 14 and EOEC 17. ANL Neg. No. 116-77-603

Fig. V-8.

Subassembly Power Factors for the LWR-Grade Plutonium Fueled Clinch River Breeder Reactor at the Beginning of Equilibrium Cycle 14 Without Capture Energy with an Average Energy/Fission Based on Version IV Cross-Section Set 2. ANL Neg. No. 116-77-654



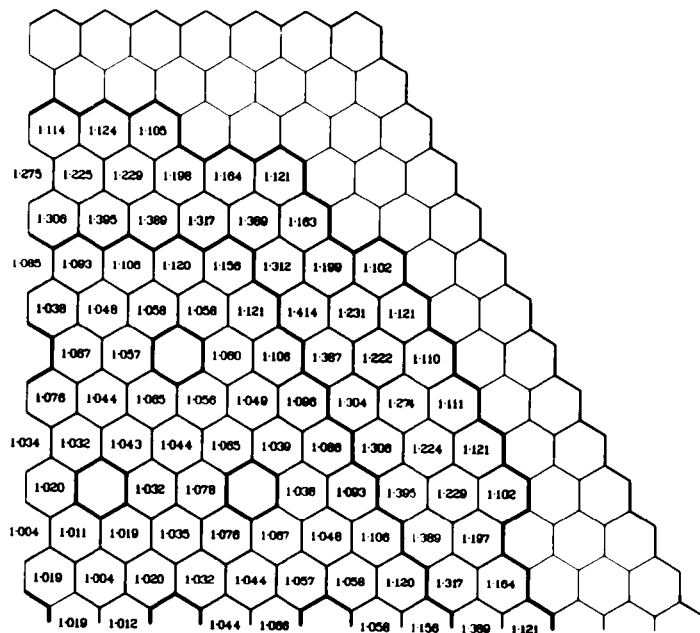
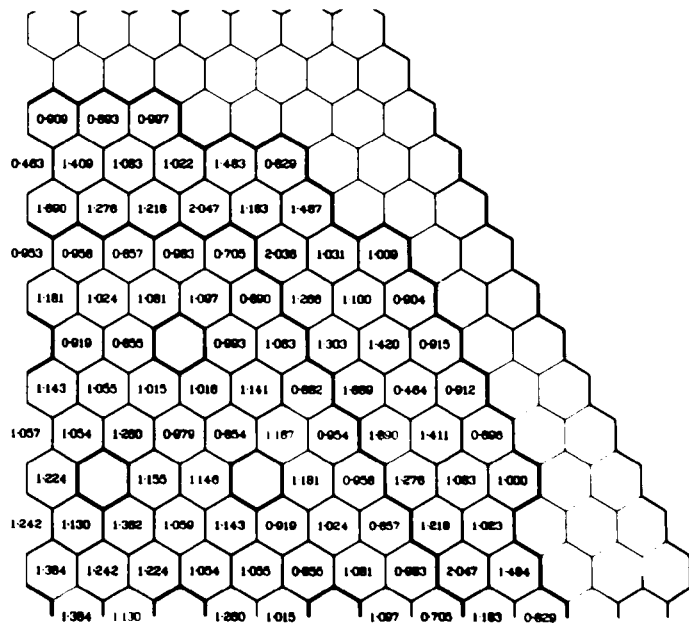


Fig. V-9.

Subassembly Peak-to-Average
Power Density Ratios for the
LWR-Grade Plutonium Fueled
Clinch River Breeder Reactor
at the Beginning of Equilibrium
Cycle 14 without Capture Energy
with an Average Energy/Fission
Based on Version IV Cross-
Section Set 2. ANL Neg. No.
116-77-678

Fig. V-10.

Subassembly Peak Power Factors
for the LWR-Grade Plutonium
Fueled Clinch River Breeder
Reactor at the Beginning of
Equilibrium Cycle 14 without
Capture Energy with an Average
Energy/ Fission Based on
Version IV Cross-Section Set 2.
ANL Neg. No. 116-77-679



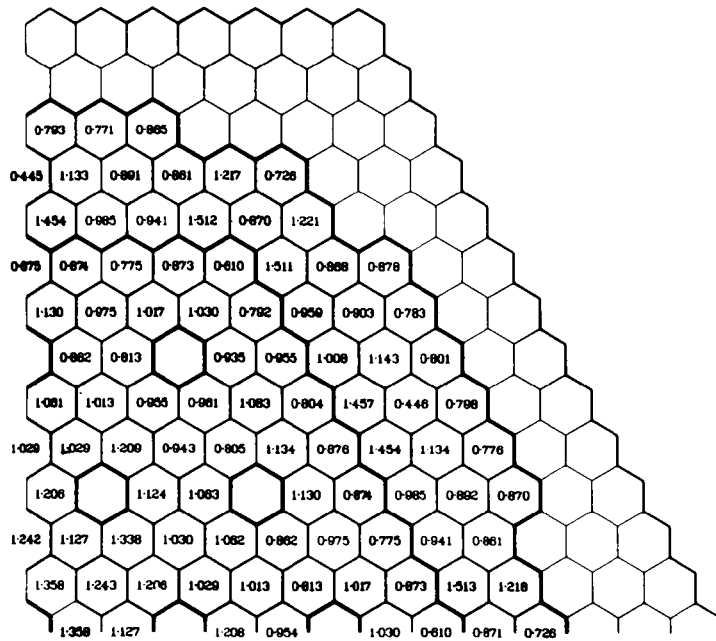


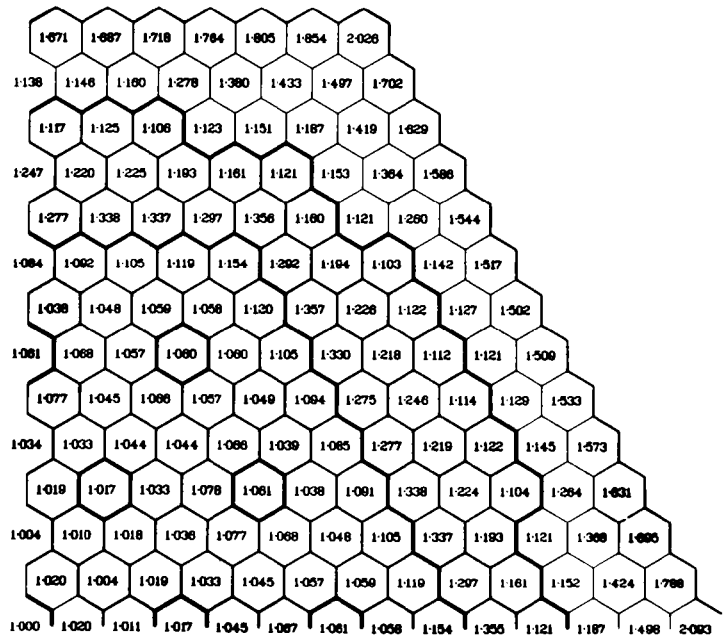
Fig. V-11.

Subassembly Power Factors for
 the LWR-Grade Plutonium
 Fueled Clinch River Breeder
 Reactor at the Beginning of
 Equilibrium Cycle 14 with
 Isotopic Capture and Fission
 Energies Based on Version IV
 Cross-Section Set 2.

ANL Neg. No. 116-77-604

Fig. V-12.

Subassembly Peak-to-Average
 Power Density Ratios for the
 LWR-Grade Plutonium Fueled
 Clinch River Breeder Reactor
 at the Beginning of Equilib-
 rium Cycle 14 with Isotopic
 Capture and Fission Energies
 Based on Version IV Cross-
 Section Set 2. ANL Neg. No.
 116-77-602



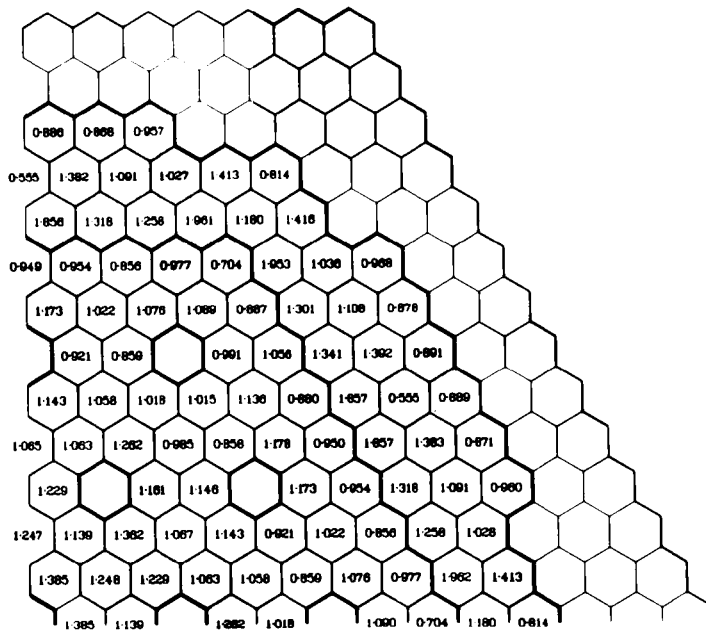
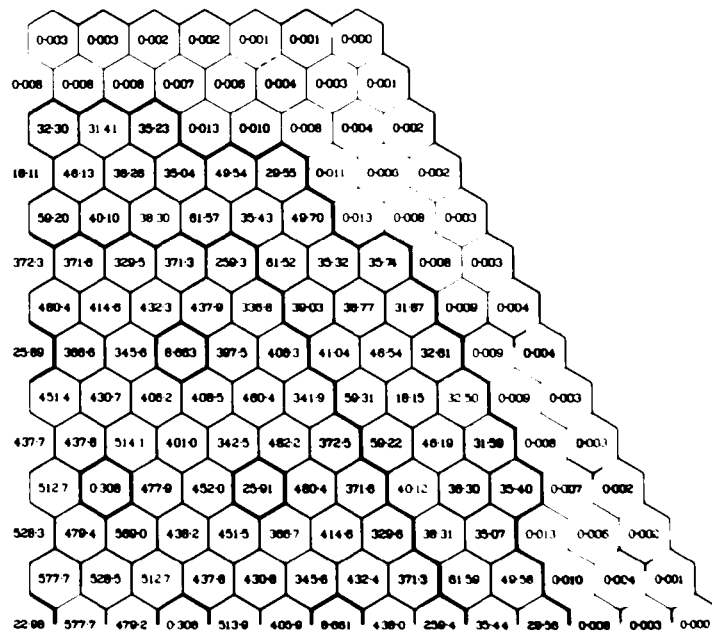


Fig. V-13.

Subassembly Peak Power Factors for the LWR-Grade Plutonium Fueled Clinch River Breeder Reactor at the Beginning of Equilibrium Cycle 14 with Isotopic Capture and Fission Energies Based on Version IV Cross-Section Set 2. ANL Neg. No. 116-77-666

Fig. V-14.

Subassembly Average Power Densities for the LWR-Grade Plutonium Fueled Clinch River Breeder Reactor at the Beginning of Equilibrium Cycle 14 with Isotopic Capture and Fission Energies Based on Version IV Cross-Section Set 2. ANL Neg. No. 116-77-693



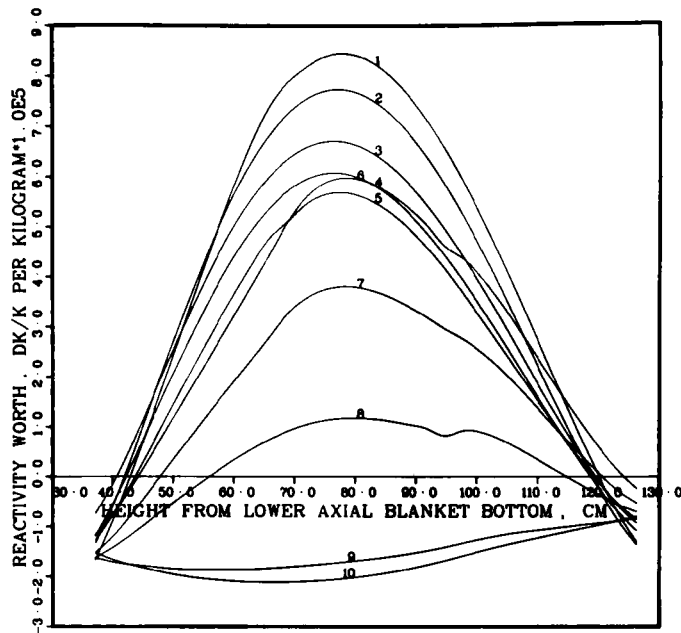


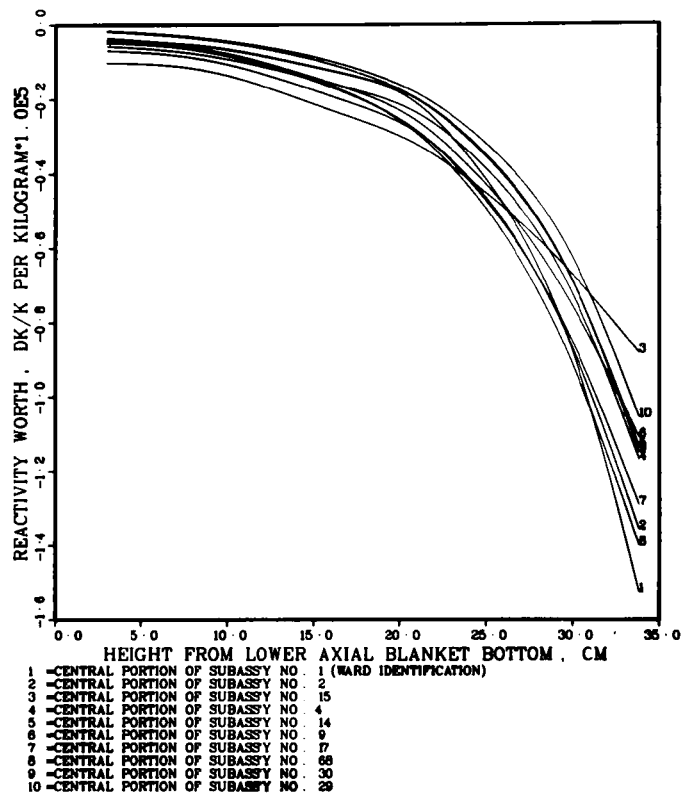
Fig. V-15.

Distribution of Sodium Void Worth in Core of the LWR-Pu-Fueled CRBR at the Beginning of Equilibrium Cycle 14.
ANL Neg. No. 116-77-581

1 - CENTRAL PORTION OF SUBASSY NO. 1 (WARD IDENTIFICATION)
2 - CENTRAL PORTION OF SUBASSY NO. 2
3 - CENTRAL PORTION OF SUBASSY NO. 15
4 - CENTRAL PORTION OF SUBASSY NO. 4
5 - CENTRAL PORTION OF SUBASSY NO. 14
6 - CENTRAL PORTION OF SUBASSY NO. 9
7 - CENTRAL PORTION OF SUBASSY NO. 17
8 - CENTRAL PORTION OF SUBASSY NO. 66
9 - CENTRAL PORTION OF SUBASSY NO. 30
10 - CENTRAL PORTION OF SUBASSY NO. 29

Fig. V-16.

Distribution of Sodium Void Worth in Lower Blanket of the LWR-Pu-Fueled CRBR at the Beginning of Equilibrium Cycle 14. ANL Neg. No. 116-77-580



1 - CENTRAL PORTION OF SUBASSY NO. 1 (WARD IDENTIFICATION)
2 - CENTRAL PORTION OF SUBASSY NO. 2
3 - CENTRAL PORTION OF SUBASSY NO. 15
4 - CENTRAL PORTION OF SUBASSY NO. 4
5 - CENTRAL PORTION OF SUBASSY NO. 14
6 - CENTRAL PORTION OF SUBASSY NO. 9
7 - CENTRAL PORTION OF SUBASSY NO. 17
8 - CENTRAL PORTION OF SUBASSY NO. 66
9 - CENTRAL PORTION OF SUBASSY NO. 30
10 - CENTRAL PORTION OF SUBASSY NO. 29

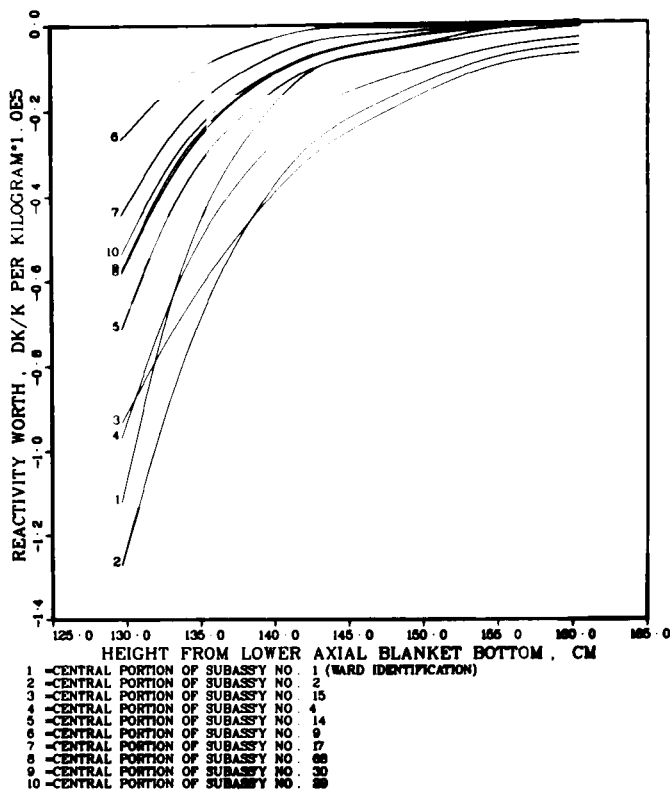
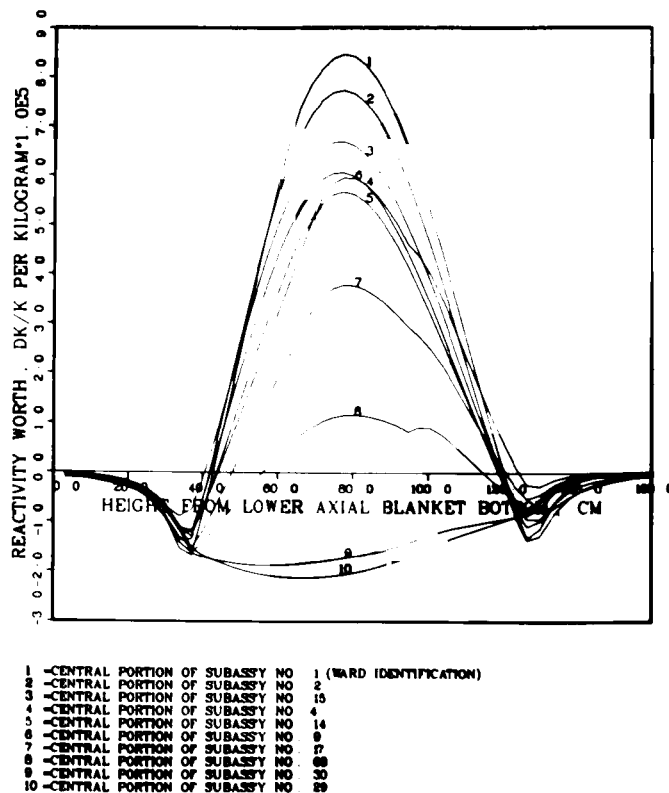


Fig. V-17.

Distribution of Sodium Void Worth in Upper Blanket of the LWR-Pu-Fueled CRBR at the Beginning of Equilibrium Cycle 14. ANL Neg. No. 116-77-584

Fig. V-18.

Distribution of Sodium Void Worth in Core and Blankets of the LWR-Pu-Fueled CRBR at the Beginning of Equilibrium Cycle 14. ANL Neg. No. 116-77-594



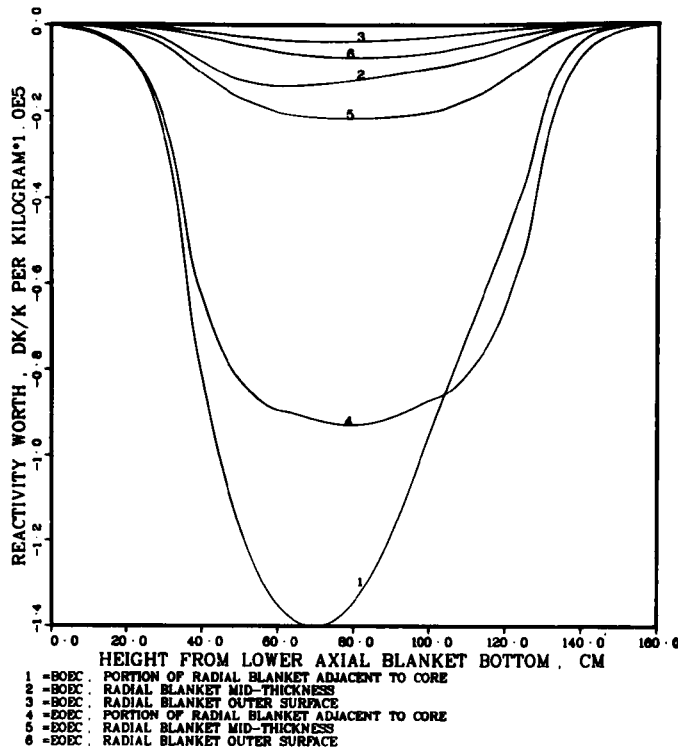
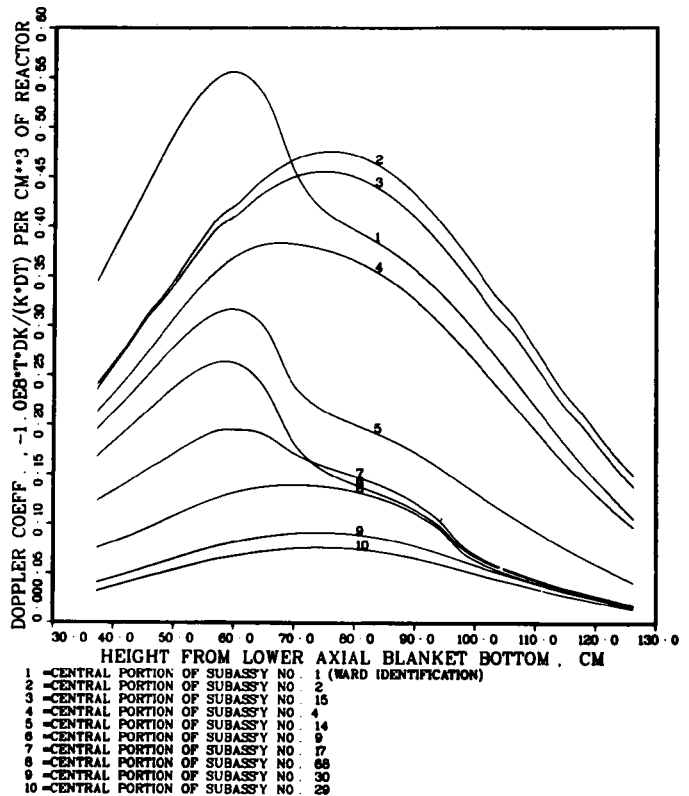


Fig. V-19.

Comparison of Void Worth Distributions in Radial Blanket of the LWR-Pu-Fueled CRBR Between the BOEC 14 and EOEC 17. ANL Neg. No. 116-77-705

Fig. V-20.

Doppler Coefficient over 2200-4400K in Unvoided Core of the LWR-Pu-Fueled CRBR at the Beginning of Equilibrium Cycle 14. ANL Neg. No. 116-77-707



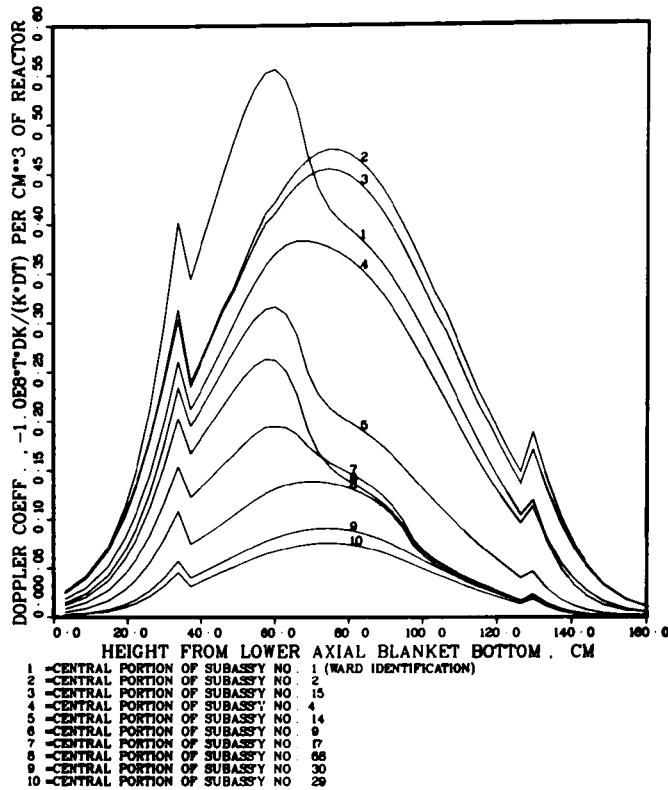
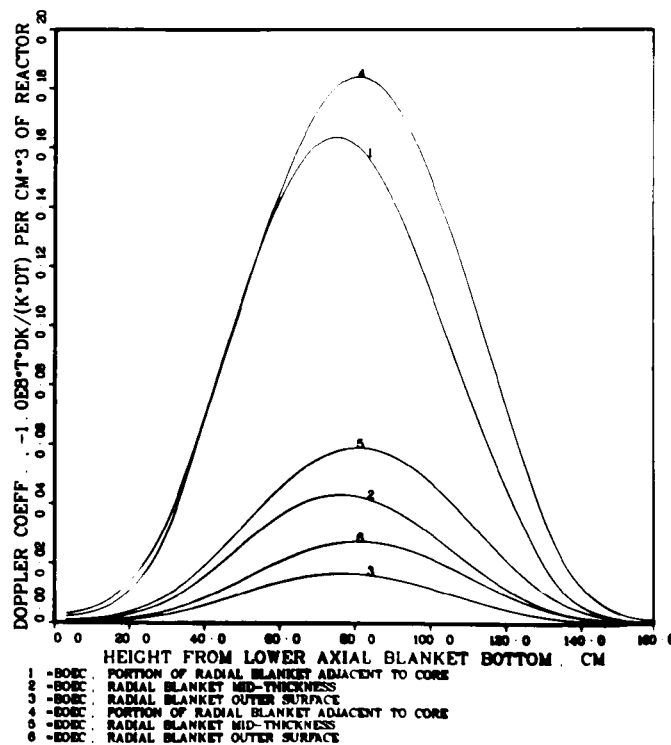


Fig. V-21.

Doppler Coefficient over 2200-4400K in Unvoided Core and Blankets of the LWR-Pu-Fueled CRBR at the Beginning of Equilibrium Cycle 14. ANL Neg. No. 116-77-708

Fig. V-22.

Comparison of Doppler Coefficients over 2200-4400K in Unvoided Radial Blanket of the LWR-Pu-Fueled CRBR Between the BOEC 14 and EOEC 17. ANL Neg. No. 116-77-706



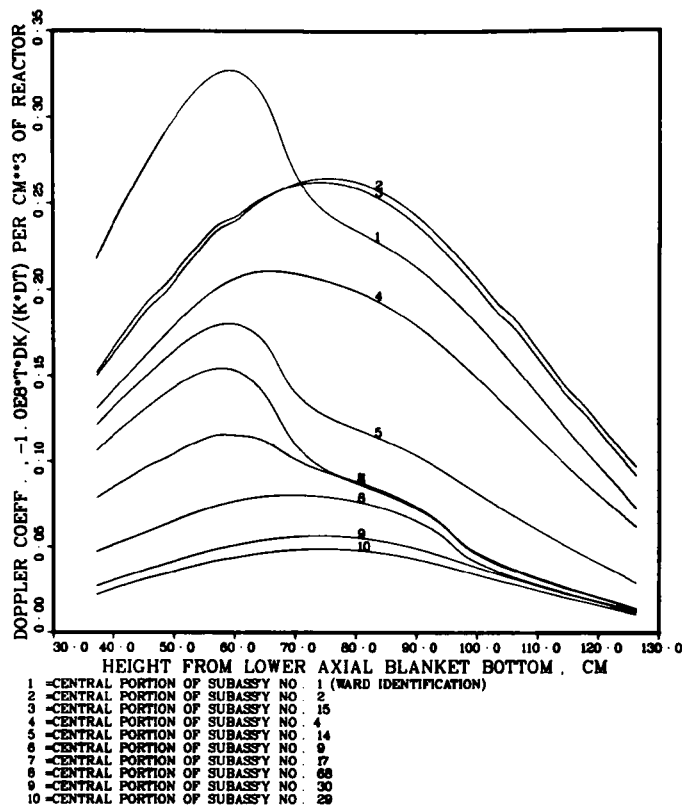
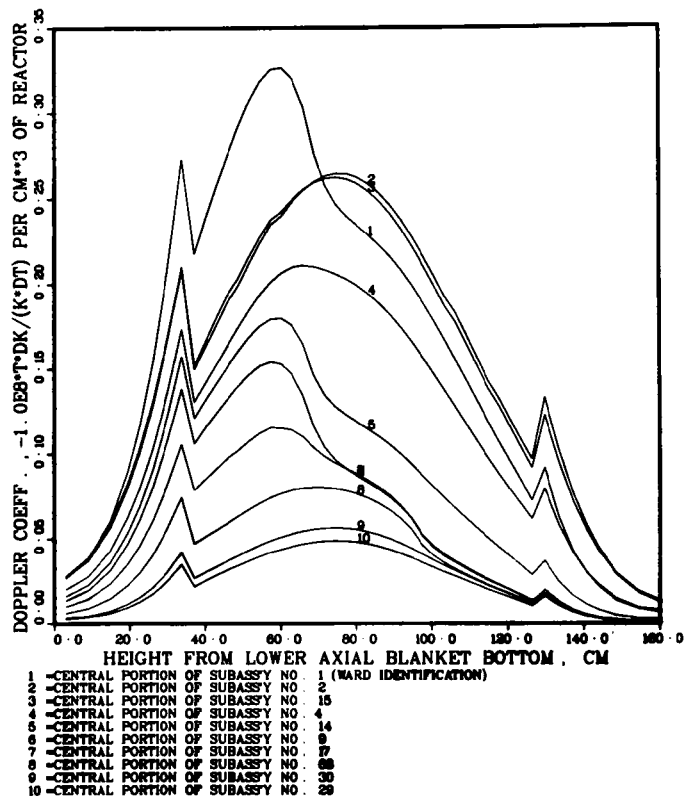


Fig. V-23.

Doppler Coefficient over 2200-4400K in Totally Voided Core of the LWR-Pu-Fueled CRBR at the Beginning of Equilibrium Cycle 14. ANL Neg. No. 116-77-685

Fig. V-24.

Doppler Coefficient over 2200-4400K in Totally Voided Core and Blankets of the LWR-Pu-Fueled CRBR at the Beginning of Equilibrium Cycle 14. ANL Neg. No. 116-77-684



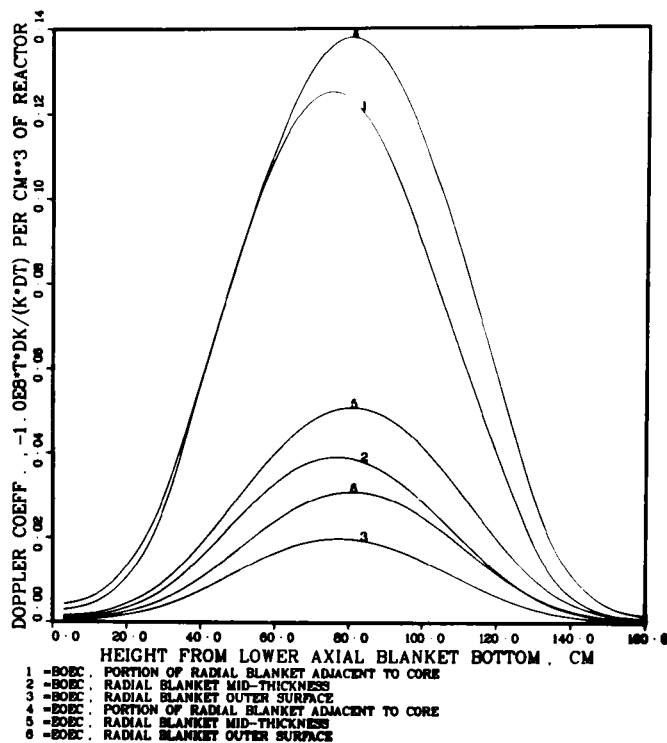


Fig. V-25.

Comparison of Doppler Coefficients over 2200-4400K in Voided Radial Blanket of the LWR-Pu-Fueled CRBR Between the BOEC 14 and EOEC 17. ANL Neg. No. 116-77-687

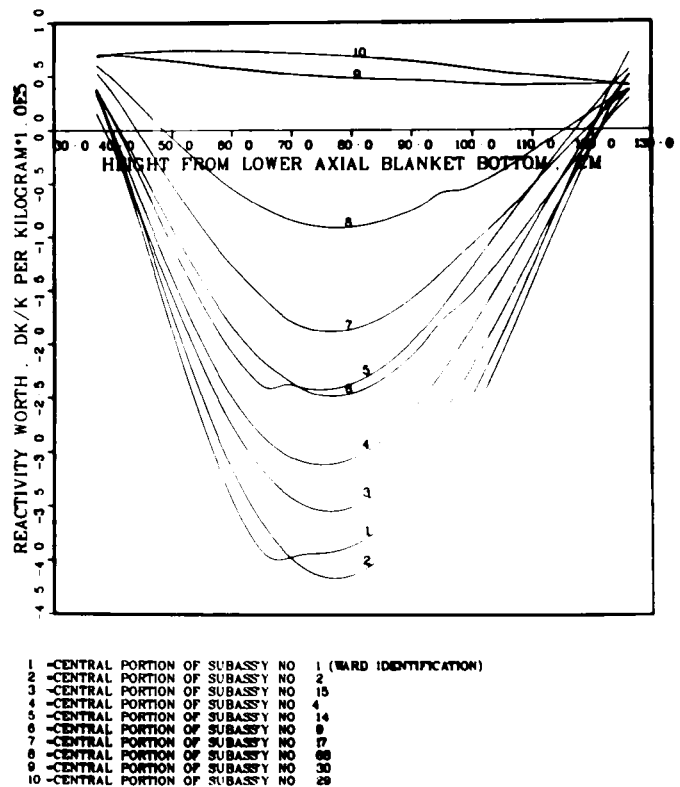


Fig. V-26.

Axial Distribution of Steel Worth in Core of the LWR-Pu-Fueled CRBR at the Beginning of Equilibrium Cycle 14. ANL Neg. No. 116-77-583

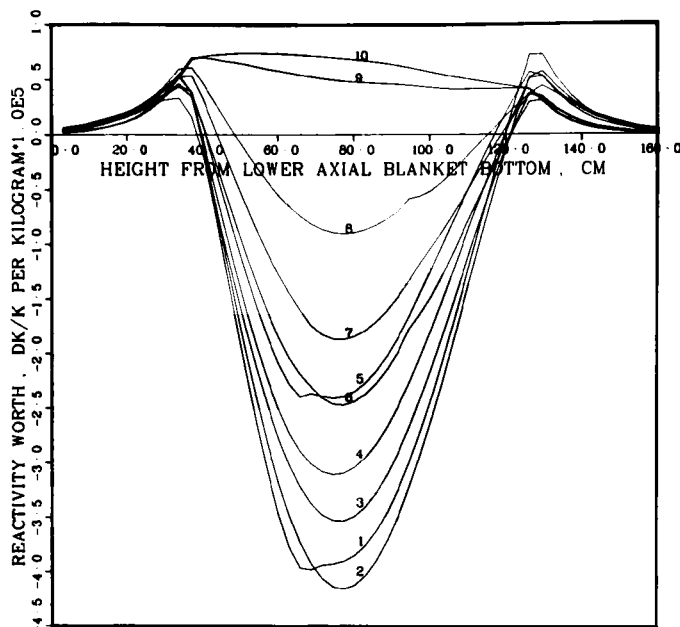


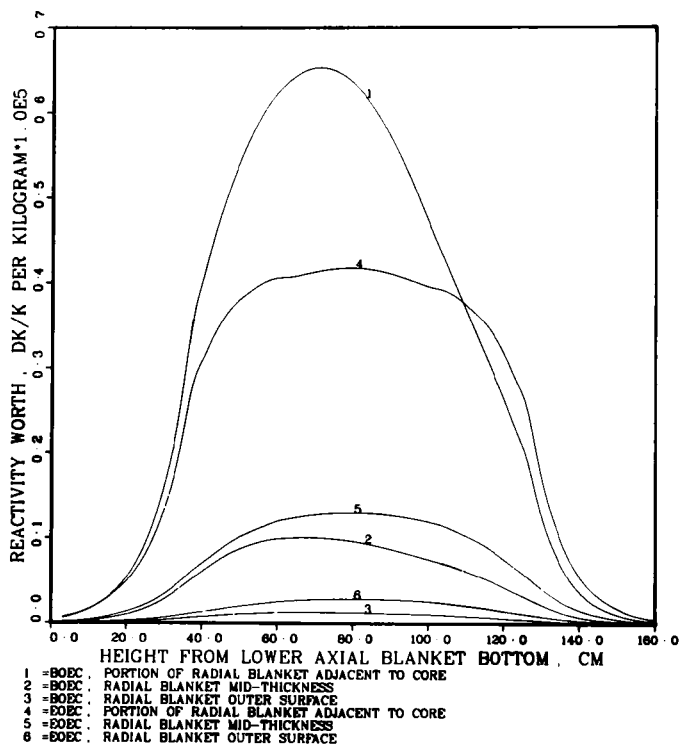
Fig. V-27.

Axial Distribution of Steel Worth in Core and Blankets of the LWR-Pu-Fueled CRBR at the Beginning of Equilibrium Cycle 14. ANL Neg. No. 116-77-600

1 = CENTRAL PORTION OF SUBASSY NO. 1 (WARD IDENTIFICATION)
 2 = CENTRAL PORTION OF SUBASSY NO. 2
 3 = CENTRAL PORTION OF SUBASSY NO. 15
 4 = CENTRAL PORTION OF SUBASSY NO. 4
 5 = CENTRAL PORTION OF SUBASSY NO. 14
 6 = CENTRAL PORTION OF SUBASSY NO. 9
 7 = CENTRAL PORTION OF SUBASSY NO. 17
 8 = CENTRAL PORTION OF SUBASSY NO. 68
 9 = CENTRAL PORTION OF SUBASSY NO. 30
 10 = CENTRAL PORTION OF SUBASSY NO. 29

Fig. V-28.

Comparison of Steel Worth Distributions in Radial Blanket of the LWR-Pu-Fueled CRBR Between the BOEC 14 and EOEC 17. ANL Neg. No. 116-77-601



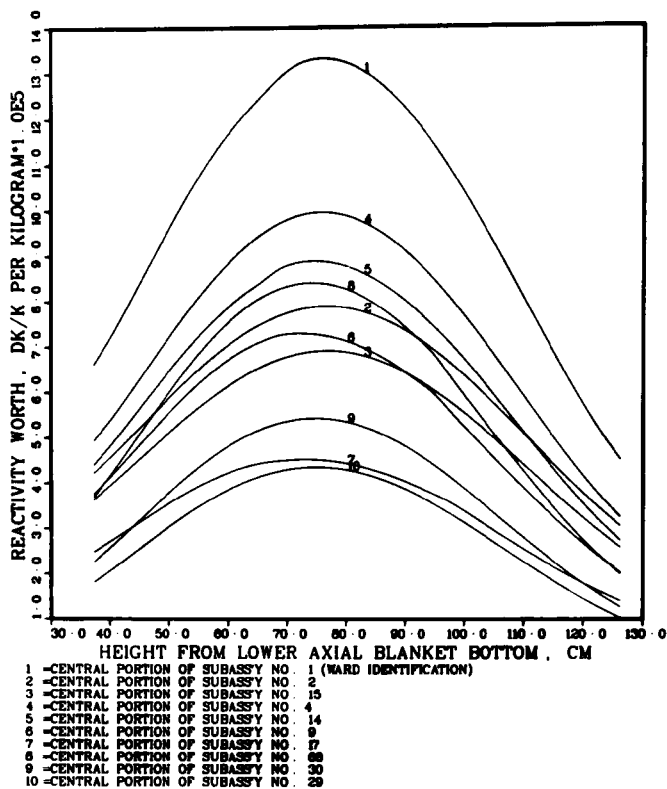
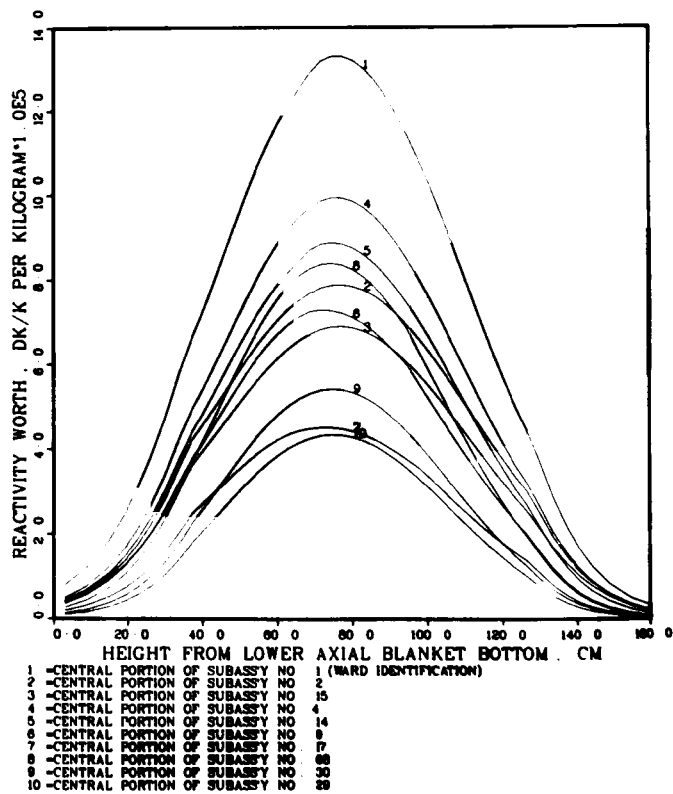


Fig. V-29.

Distribution of Core Fuel Worth in Core of the LWR-Pu-Fueled CRBR at the Beginning of Equilibrium Cycle 14. ANL Neg. No. 116-77-595

Fig. V-30.

Distribution of Core Fuel Worth in Core and Blankets of the LWR-Pu-Fueled CRBR at the Beginning of Equilibrium Cycle 14. ANL Neg. No. 116-77-597



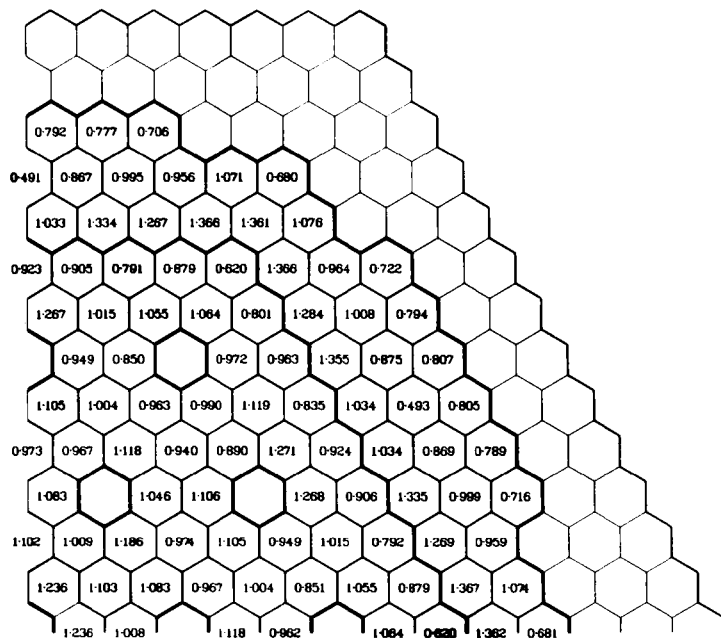
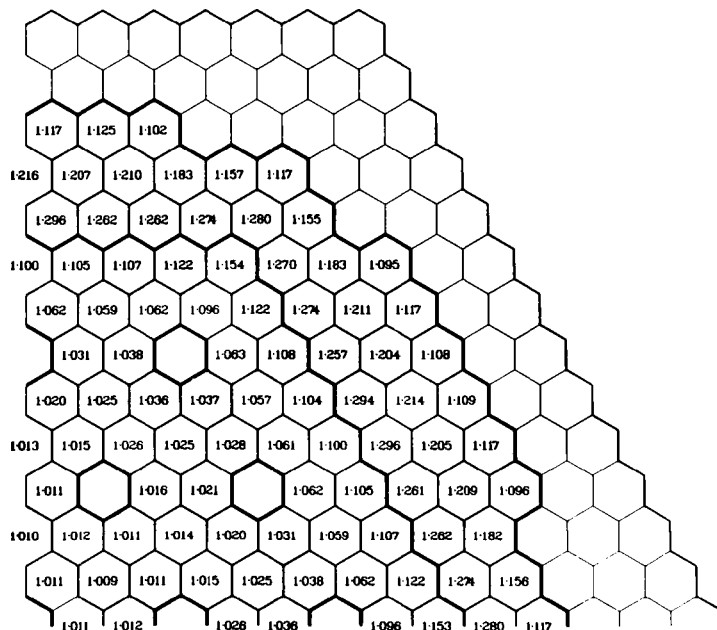


Fig. VI-1.

Subassembly Power Factors for
the LWP-Pu-Fueled CRBR at the
End of Equilibrium Cycle 17,
Unimproved Radial Blanket
Compositions. ANL Neg. No.
116-77-667

Fig. VI-2.

Subassembly Peak-to-Average
Power Density Ratios for the
LWR-Pu-Fueled CRBR at the
End of Equilibrium Cycle 17,
Unimproved Radial Blanket
Compositions. ANL Neg. No.
116-77-680



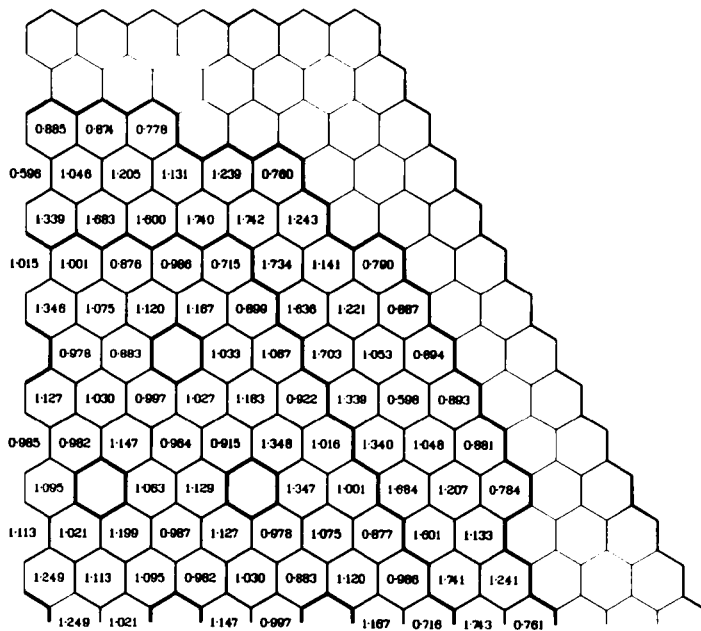
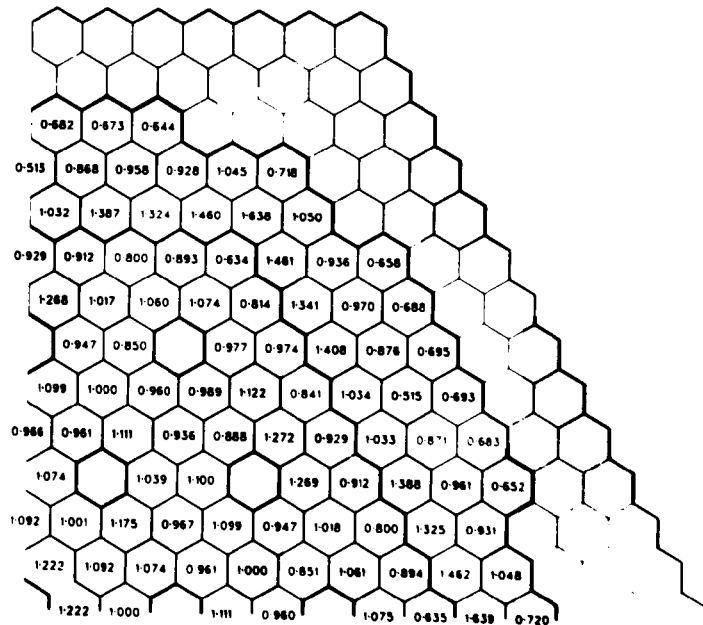


Fig. VI-3.

Subassembly Peak Power Factors
 for the LWR-Pu-Fueled CRBR at
 the End of Equilibrium Cycle
 17, Unimproved Radial Blanket
 Compositions. ANL Neg. No.
 116-77-681

Fig. VI-4.

Subassembly Power Factors for
 the LWR-Grade Plutonium Fueled
 Clinch River Breeder Reactor
 at the End of Equilibrium
 Cycle 17 with Improved Radial
 Blanket Compositions. ANL Neg.
 No. 116-77-651



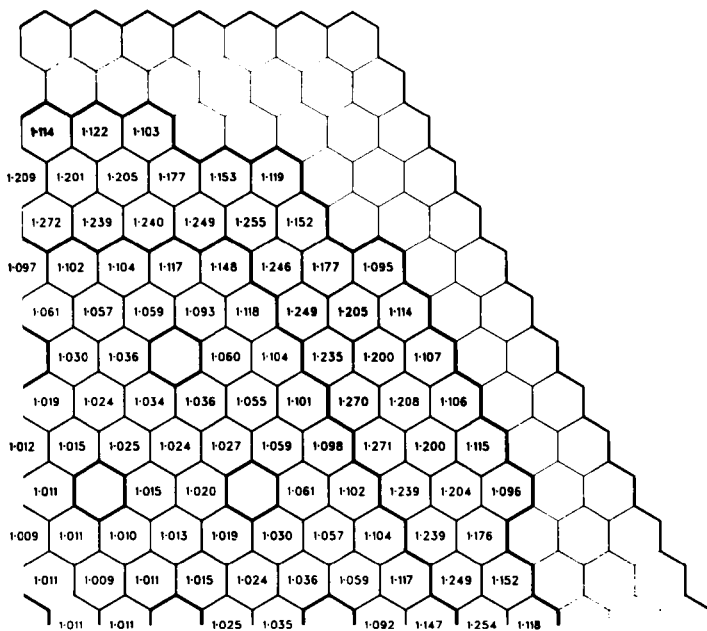
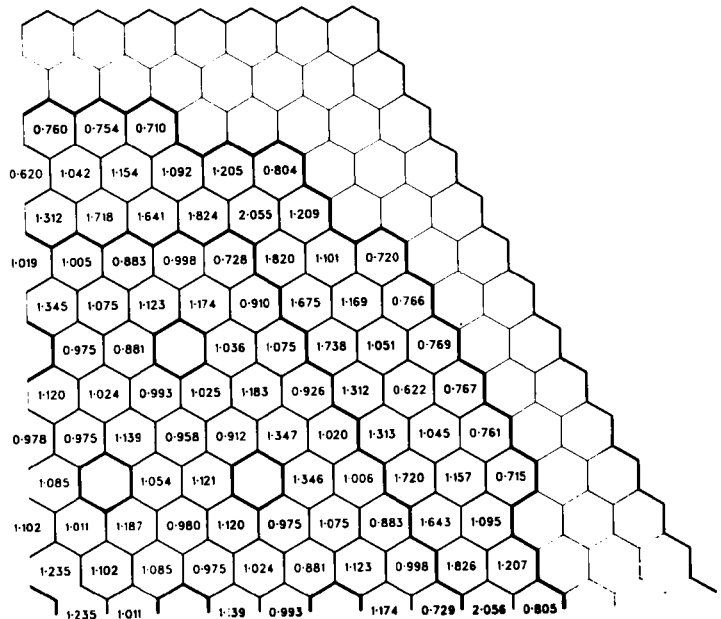


Fig. VI-5.

Subassembly Peak-to-Average
Power Density Ratios for the
LWR-Grade Plutonium Fueled
Clinch River Breeder Reactor
at the End of Equilibrium
Cycle 17 with Improved Radial
Blanket Compositions. ANL
Neg. No. 116-77-650

Fig. VI-6

Subassembly Peak Power Factors
for the LWR-Grade Plutonium
Fueled Clinch River Breeder
Reactor at the End of Equilib-
rium Cycle 17. ANL Neg. No.
116-77-632



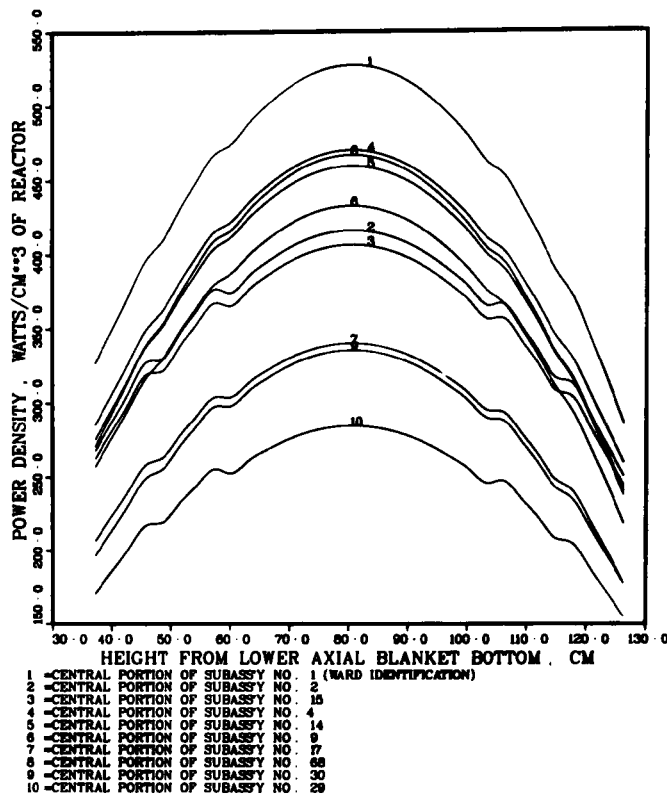
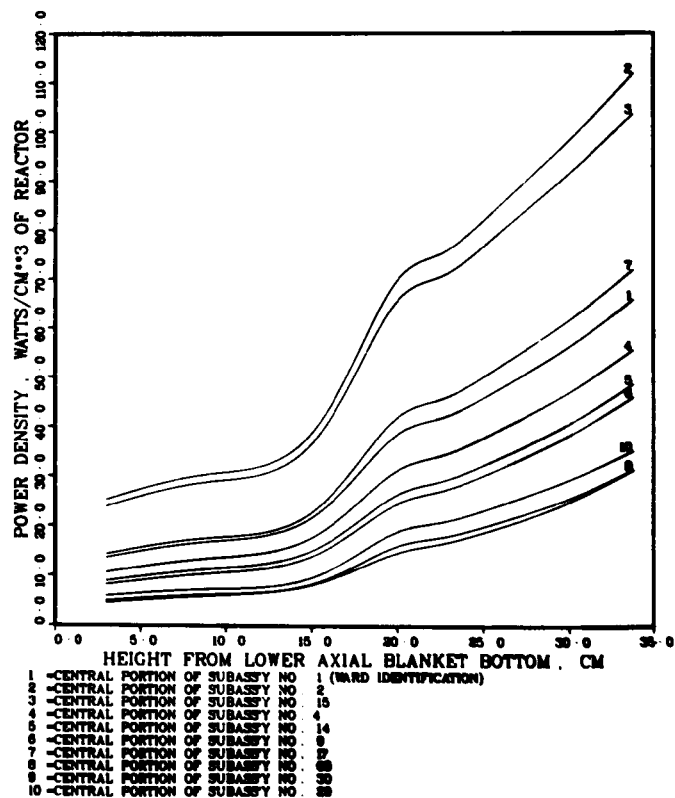


Fig. VI-7.

Axial Distribution of Power in
Core of the LWR-Pu-Fueled CRBR
at the End of Equilibrium
Cycle 17. ANL Neg. No. 116-
77-688

Fig. VI-8.

Axial Distribution of Power in
Lower Blanket of the LWR-Pu-
Fueled CRBR at the End of
Equilibrium Cycle 17. ANL
Neg. No. 116-77-582



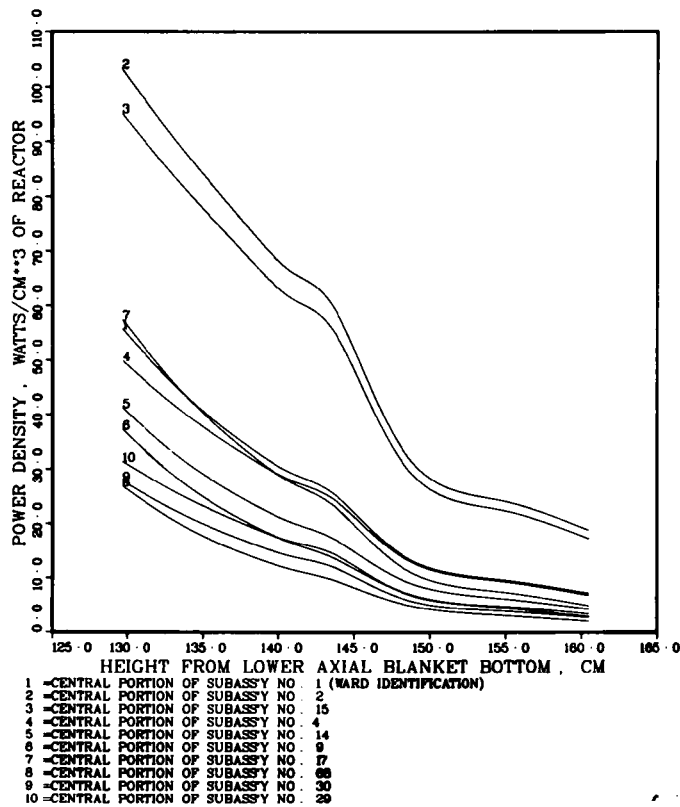


Fig. VI-9

Axial Distribution of Power in
 Upper Blanket of the LWR-Pu-
 Fueled CRBR at the End of
 Equilibrium Cycle 17. ANL Neg.
 No. 116-77-586

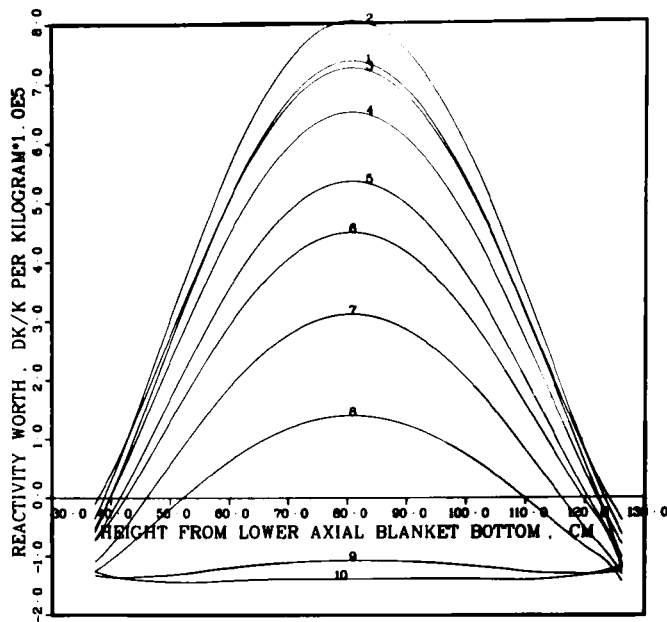


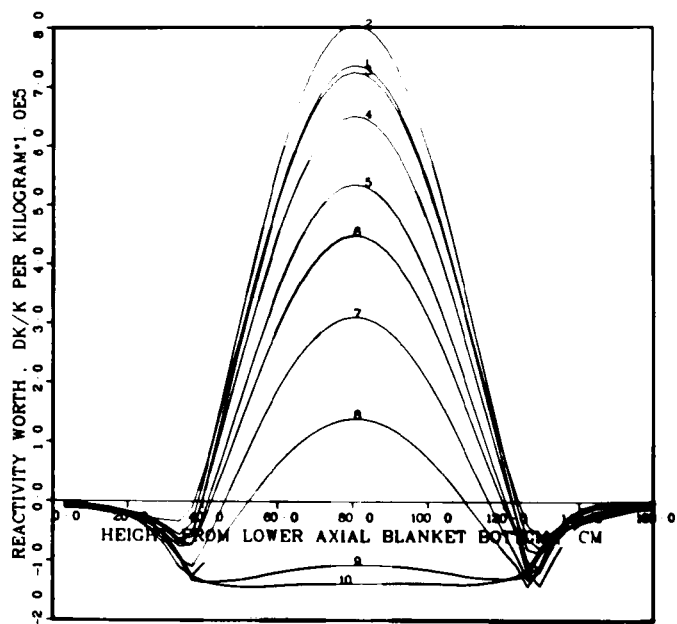
Fig. VII-1.

Distribution of Sodium Void Worth in Core of the LWR-Pu-Fueled CRBR at the End of Equilibrium Cycle 17. ANL Neg. No. 116-77-585

1 CENTRAL PORTION OF SUBASSY NO. 1 (WARD IDENTIFICATION)
 2 CENTRAL PORTION OF SUBASSY NO. 2
 3 CENTRAL PORTION OF SUBASSY NO. 15
 4 CENTRAL PORTION OF SUBASSY NO. 4
 5 CENTRAL PORTION OF SUBASSY NO. 14
 6 CENTRAL PORTION OF SUBASSY NO. 9
 7 CENTRAL PORTION OF SUBASSY NO. 7
 8 CENTRAL PORTION OF SUBASSY NO. 68
 9 CENTRAL PORTION OF SUBASSY NO. 36
 10 CENTRAL PORTION OF SUBASSY NO. 29

Fig. VII-2.

Distribution of Sodium Void Worth in Core and Blankets of the LWR-Pu-Fueled CRBR at the End of Equilibrium Cycle 17. ANL Neg. No. 116-77-686



1 CENTRAL PORTION OF SUBASSY NO. 1 (WARD IDENTIFICATION)
 2 CENTRAL PORTION OF SUBASSY NO. 2
 3 CENTRAL PORTION OF SUBASSY NO. 15
 4 CENTRAL PORTION OF SUBASSY NO. 4
 5 CENTRAL PORTION OF SUBASSY NO. 14
 6 CENTRAL PORTION OF SUBASSY NO. 9
 7 CENTRAL PORTION OF SUBASSY NO. 7
 8 CENTRAL PORTION OF SUBASSY NO. 68
 9 CENTRAL PORTION OF SUBASSY NO. 36
 10 CENTRAL PORTION OF SUBASSY NO. 29

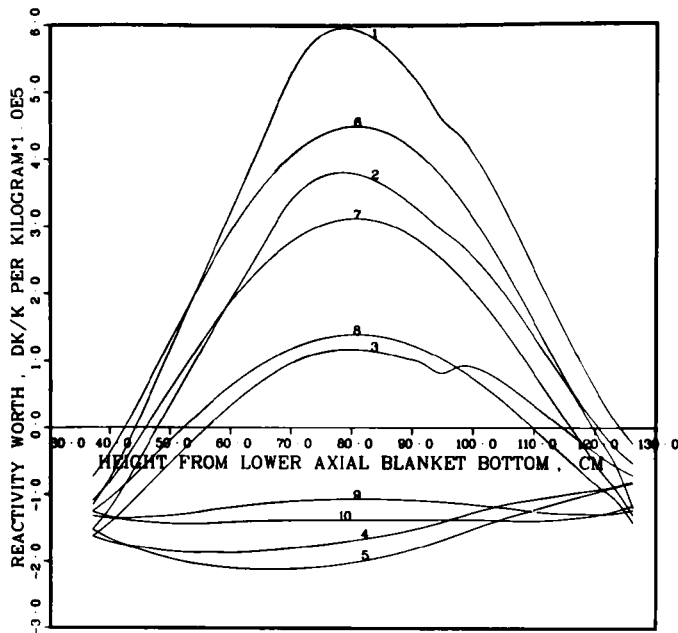


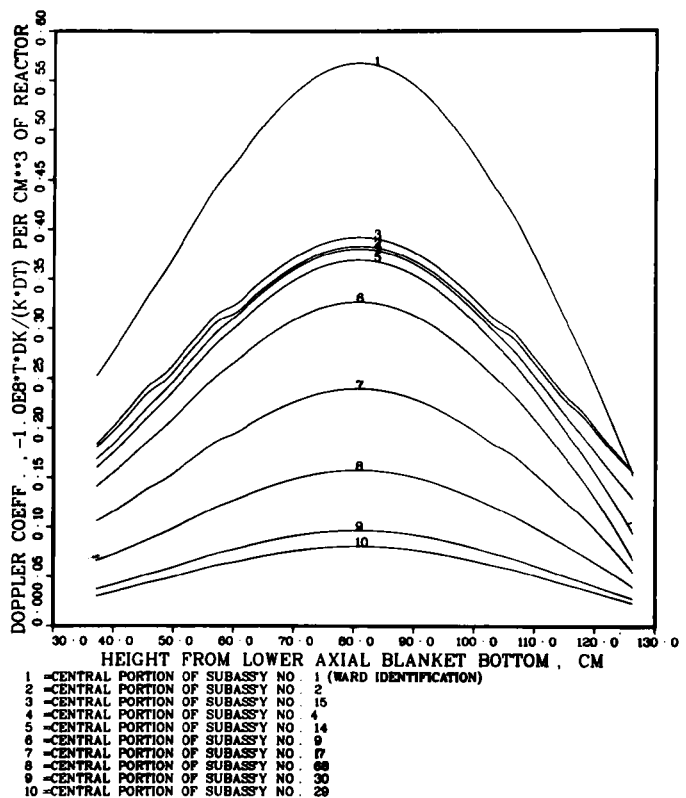
Fig. VII-3.

Comparison of Void Worth Distribution in Core of the LWR-Pu-Fueled CRBR Between the BOEC 14 and EOEC 17. ANL Neg. No. 116-77-689

1 = BOEC. CENTRAL PORTION OF SUBASSY NO. 9 (WARD IDENTIFICATION)
 2 = BOEC. CENTRAL PORTION OF SUBASSY NO. 17
 3 = BOEC. CENTRAL PORTION OF SUBASSY NO. 68
 4 = BOEC. CENTRAL PORTION OF SUBASSY NO. 30
 5 = BOEC. CENTRAL PORTION OF SUBASSY NO. 29
 6 = BOEC. CENTRAL PORTION OF SUBASSY NO. 9
 7 = BOEC. CENTRAL PORTION OF SUBASSY NO. 17
 8 = BOEC. CENTRAL PORTION OF SUBASSY NO. 68
 9 = BOEC. CENTRAL PORTION OF SUBASSY NO. 30
 10 = BOEC. CENTRAL PORTION OF SUBASSY NO. 29

Fig. VII-4.

Doppler Coefficient over 2200-4400K in Unvoided Core of the LWR-Pu-Fueled CRBR at the End of Equilibrium Cycle 17. ANL Neg. No. 116-77-677



1 = CENTRAL PORTION OF SUBASSY NO. 1 (WARD IDENTIFICATION)
 2 = CENTRAL PORTION OF SUBASSY NO. 2
 3 = CENTRAL PORTION OF SUBASSY NO. 15
 4 = CENTRAL PORTION OF SUBASSY NO. 14
 5 = CENTRAL PORTION OF SUBASSY NO. 14
 6 = CENTRAL PORTION OF SUBASSY NO. 9
 7 = CENTRAL PORTION OF SUBASSY NO. 17
 8 = CENTRAL PORTION OF SUBASSY NO. 68
 9 = CENTRAL PORTION OF SUBASSY NO. 30
 10 = CENTRAL PORTION OF SUBASSY NO. 29

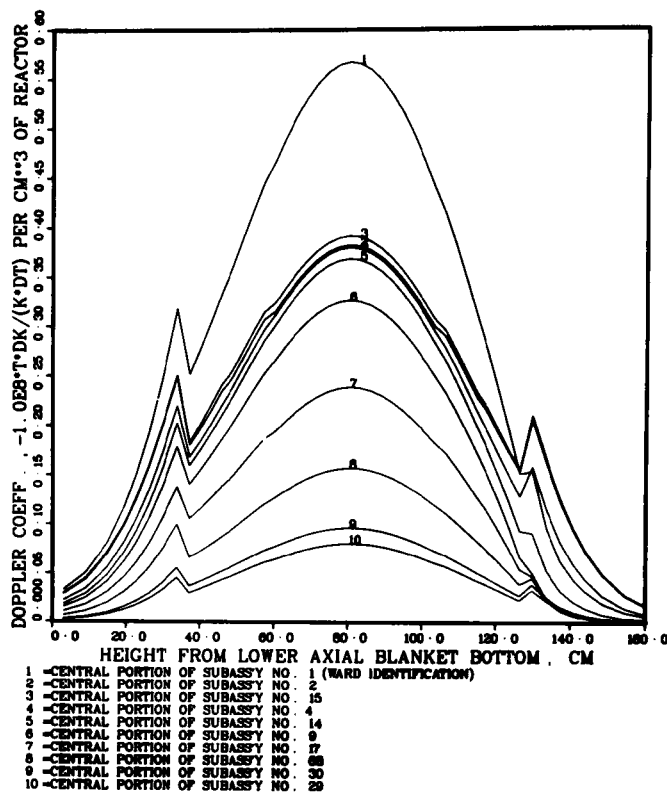
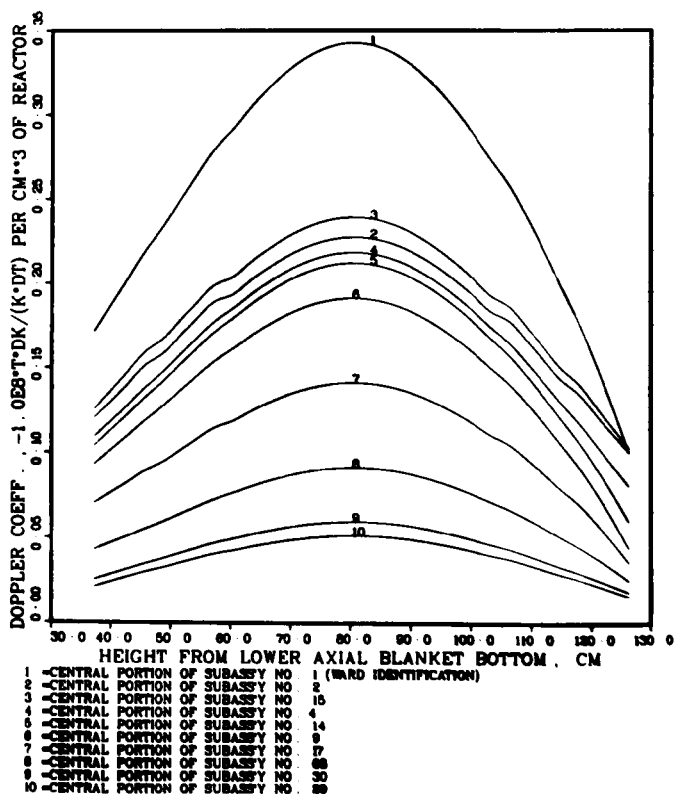


Fig. VII-5.

Doppler Coefficient over 2200-4400K in Unvoided Core and Blankets of the LWR-Pu-Fueled CRBR at the End of Equilibrium Cycle 17. ANL Neg. No. 116-77-698

Fig. VII-6.

Doppler Coefficient over 2200-4400K in Totally Voided Core of the LWR-Pu-Fueled CRBR at the End of Equilibrium Cycle 17. ANL Neg. No. 116-77-610



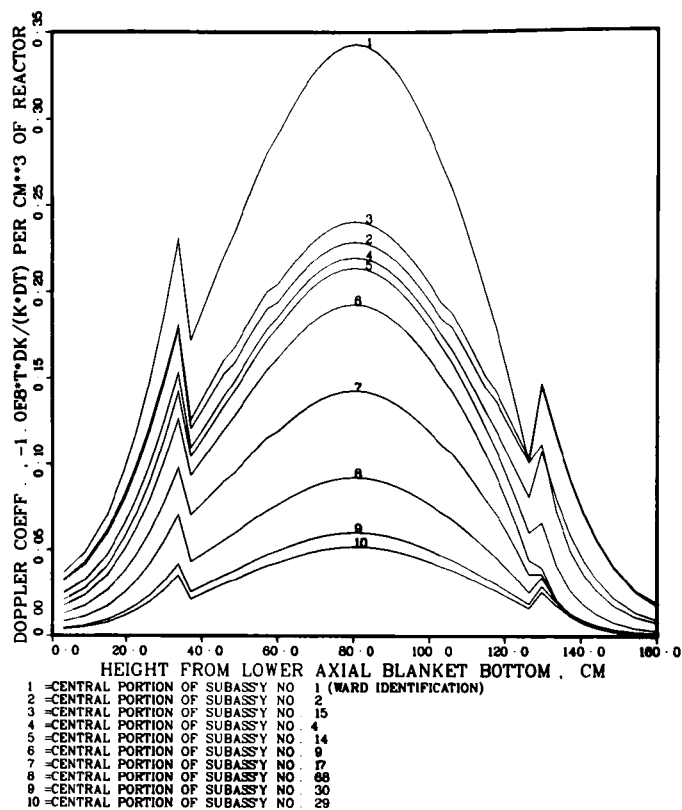
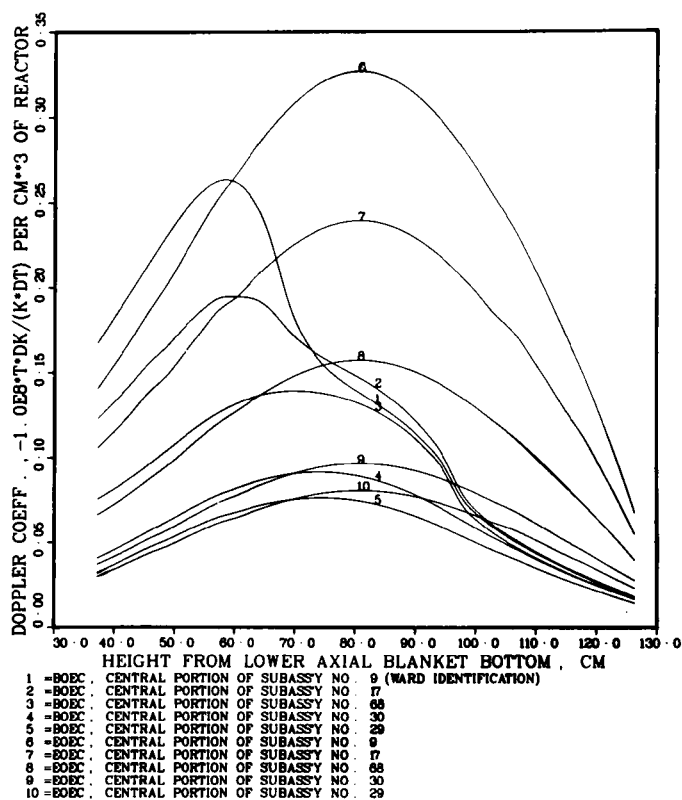


Fig. VII-7.

Doppler Coefficient Over 2200-4400K in Totally Voided Core and Blankets of the LWR-Pu-Fueled CRBR at the End of Equilibrium Cycle 17. ANL Neg. No. 116-77-596

Fig. VII-8.

Comparison of Doppler Coefficients over 2200-4400K in Unvoided Core of the LWR-Pu-Fueled CRBR Between the BOEC 14 and EOEC 17. ANL Neg. No. 116-77-579



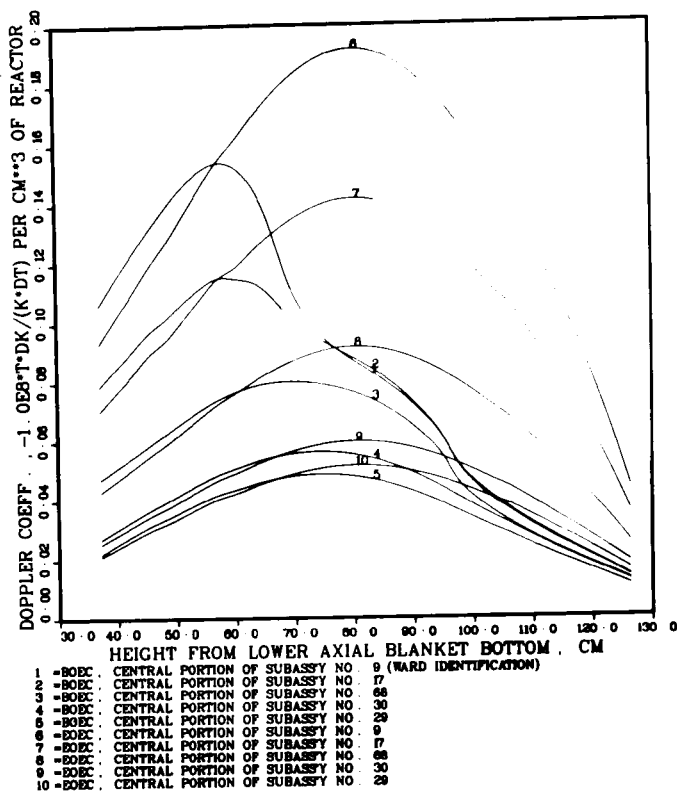


Fig. VII-9.

Comparison of Doppler Coefficients over 2200-4400K in Voided Core of the LWR-Pu-Fueled CRBR Between the BOEC 17 and EOEC 17. ANL Neg. No. 116-77-703

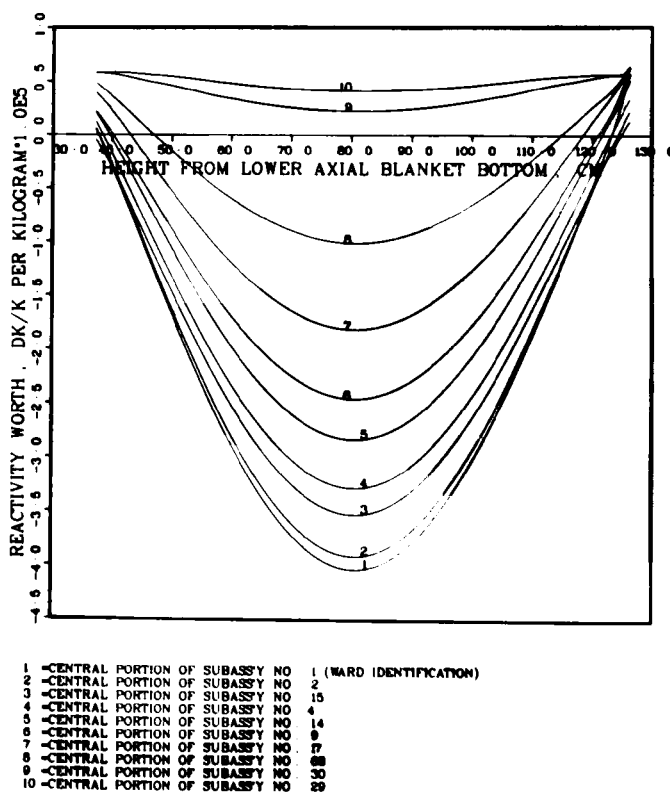


Fig. VII-10.

Axial Distribution of Steel Worth in Core of the LWR-Pu-Fueled CRBR at the End of Equilibrium Cycle 17. ANL Neg. No. 116-77-701

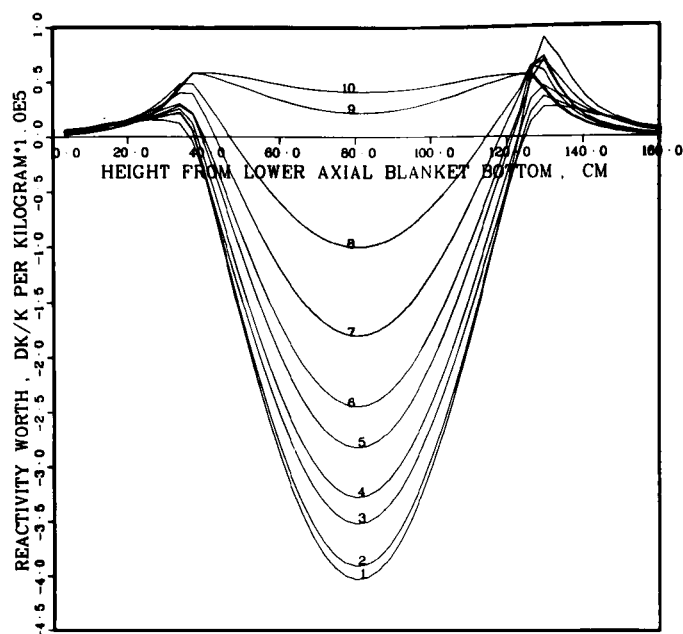


Fig. VII-11.

Axial Distribution of Steel Worth in Core and Blankets of the LWR-Pu-Fueled CRBR at the End of Equilibrium Cycle 17.
ANL Neg. No. 116-77-702

1 =CENTRAL PORTION OF SUBASSY NO. 1 (WARD IDENTIFICATION)
2 =CENTRAL PORTION OF SUBASSY NO. 2
3 =CENTRAL PORTION OF SUBASSY NO. 15
4 =CENTRAL PORTION OF SUBASSY NO. 4
5 =CENTRAL PORTION OF SUBASSY NO. 14
6 =CENTRAL PORTION OF SUBASSY NO. 9
7 =CENTRAL PORTION OF SUBASSY NO. 17
8 =CENTRAL PORTION OF SUBASSY NO. 88
9 =CENTRAL PORTION OF SUBASSY NO. 30
10 =CENTRAL PORTION OF SUBASSY NO. 29

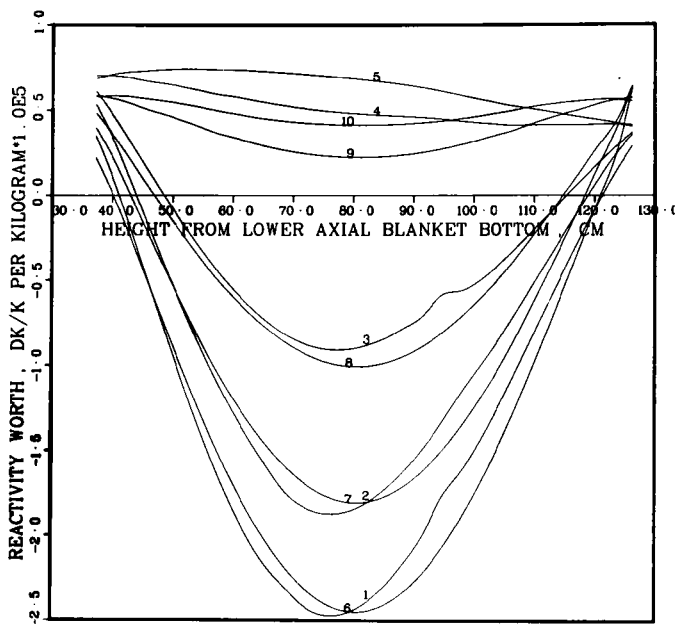


Fig. VII-12.

Comparison of Steel Worth Distributions in Core of the LWR-Pu-Fueled CRBR Between the BOEC 14 and EOEC 17. ANL Neg. No. 116-77-612

1 =BOEC, CENTRAL PORTION OF SUBASSY NO. 9 (WARD IDENTIFICATION)
2 =BOEC, CENTRAL PORTION OF SUBASSY NO. 17
3 =BOEC, CENTRAL PORTION OF SUBASSY NO. 88
4 =BOEC, CENTRAL PORTION OF SUBASSY NO. 30
5 =BOEC, CENTRAL PORTION OF SUBASSY NO. 29
6 =BOEC, CENTRAL PORTION OF SUBASSY NO. 9
7 =BOEC, CENTRAL PORTION OF SUBASSY NO. 17
8 =BOEC, CENTRAL PORTION OF SUBASSY NO. 88
9 =BOEC, CENTRAL PORTION OF SUBASSY NO. 30
10 =EOEC, CENTRAL PORTION OF SUBASSY NO. 29

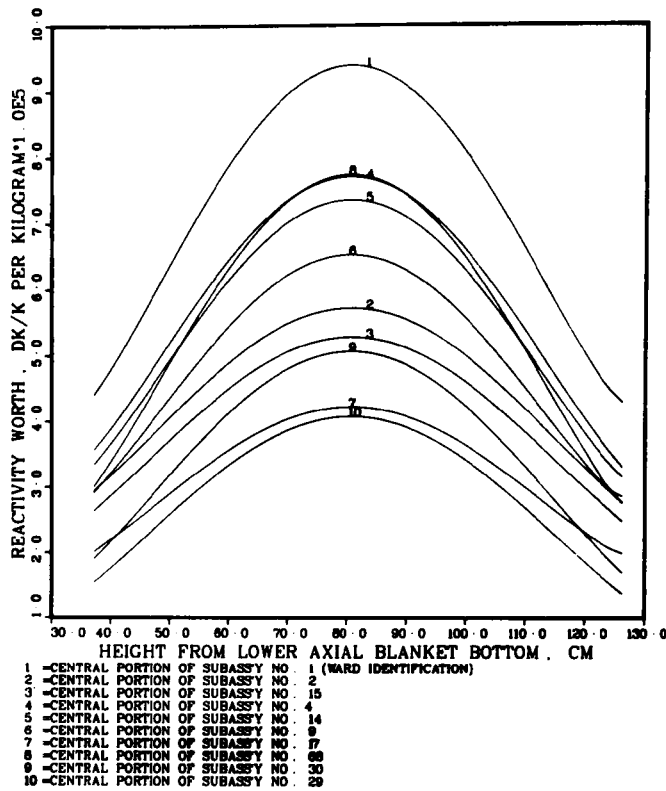
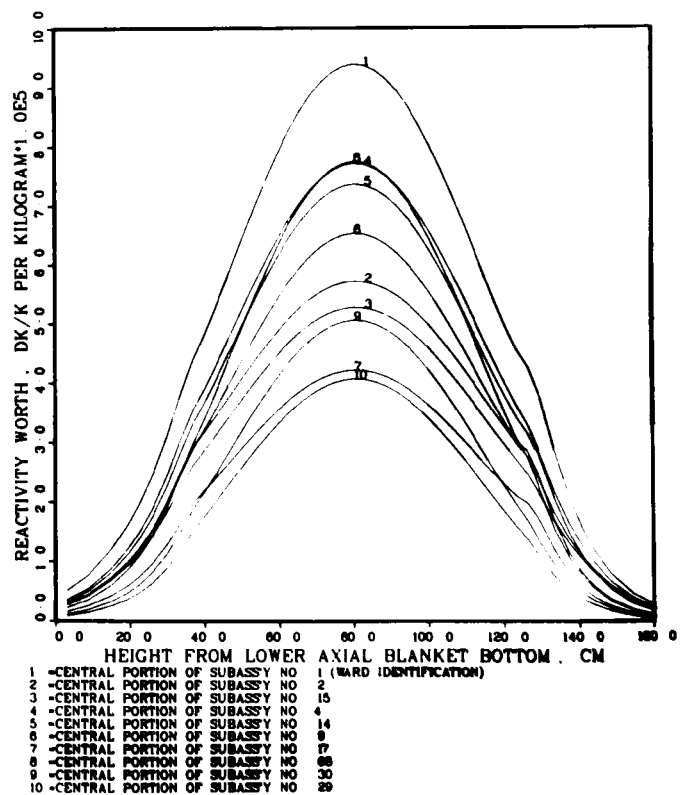


Fig. VII-13.

Distribution of Core Fuel Worth in Core of the LWR-Pu-Fueled CRBR at the End of Equilibrium Cycle 17. ANL Neg. No. 116-77-599

Fig. VII-14.

Distribution of Core Fuel Worth in Core and Blankets of the LWR-Pu-Fueled CRBR at the End of Equilibrium Cycle 17. ANL Neg. No. 116-77-700



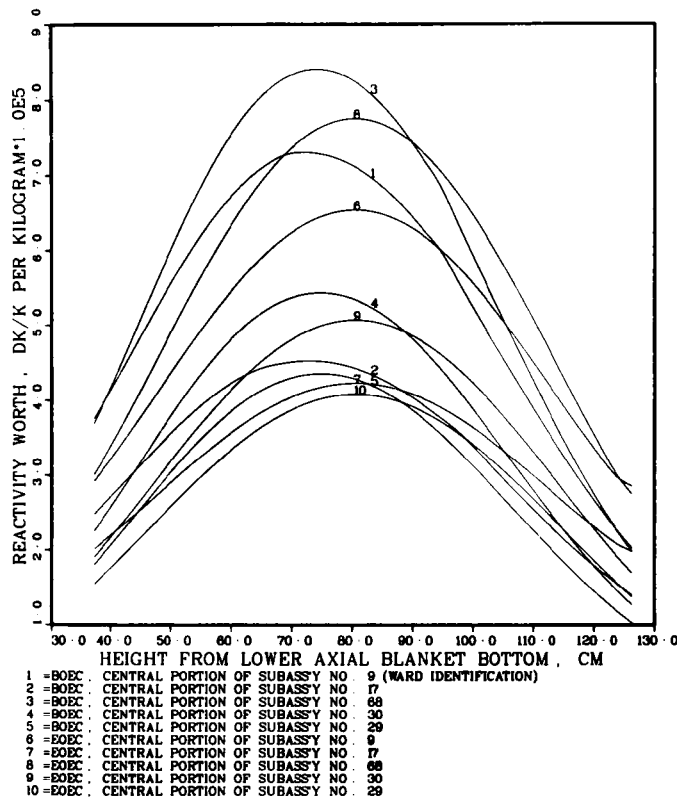


Fig. VII-15.

Comparison of Core Fuel Worths in Core of the LWR-Pu-Fueled CRBR Between the BOEC 14 and BOEC 17. ANL Neg. No. 116-77-696.

TABLE II-1. Clinch River Breeder Reactor Full Power Parameters at Beginning of Life

Thermal Power, MW	975.0				
Inlet Temperature, Degree F	710				
Outlet Temperature, Degree F	968				
Number of Subassemblies, Inner Core/Outer Core/Radial Blanket/ Primary Control/Secondary Control	108/90/150/15/4				
Subassembly Pitch, cm	12.1615				
Axial Height, cm, Core/Radial Blanket/Axial Blanket	92.038/163.460/35.711				
Plutonium Isotopic Composition, Weight %, $^{238}\text{Pu}/^{239}\text{Pu}/^{240}\text{Pu}/^{241}\text{Pu}/^{242}\text{Pu}$	1.0/67.3/19.2/10.1/2.4				
Stainless Steel Composition, Weight %, Fe/Cr/Ni/Mo/Mn	64.75/17.50/13.50/2.50/1.75				
Primary Control Volume Fractions, Boron Carbide/Steel/Sodium	0.3390/0.3287/0.3323				
Boron Isotopic Composition, Weight %, $^{10}\text{B}/^{11}\text{B}$	19.8/80.2				
Boron-10 Mass, kg/Subassembly	1.21				
<u>Parameter</u>	<u>Inner Core</u>	<u>Outer Core</u>	<u>Lower Blanket</u>	<u>Upper Blanket</u>	<u>Radial Blanket</u>
Mixed Oxide Fuel Mass, 1000 kg	4.066	3.401	3.076	3.076	18.503
Pu/(U + Pu), Weight %	18.7	27.1	0.0	0.0	0.0
Uranium Isotopic Composition, Weight %, ^{235}U	0.697	0.697	0.220	0.220	0.220
^{238}U	99.303	99.303	99.780	99.780	99.780
Volume Fractions					
Fuel + Gap	0.3488	0.3488	0.3475	0.3497	0.5872
Stainless Steel	0.2345	0.2345	0.2336	0.2553	0.1582
Sodium	0.4167	0.4167	0.4189	0.3950	0.2546

TABLE II-2. Steady State Coolant Temperature Used for Estimating Its Axial Density Variation in Core Subassemblies

Axial Position in the R-Z Model of Fig. II-2, cm	Coolant Temperature Averaged Over All Core Subassemblies, °K
40.000 to 75.711	650
75.711 to 87.216	656
87.216 to 98.721	672
98.721 to 110.225	689
110.225 to 121.730	711
121.730 to 133.235	733
133.235 to 144.739	755
144.739 to 156.244	772
156.244 to 167.749	789
167.749 to 203.460	794

TABLE II-3. Power and Reactivities by Region in the LWR-Pu-Fueled CRBR at the Beginning of Life

Power or Reactivity	Inner Core	Outer Core	Lower Blanket	Upper Blanket	Radial Blanket	Total
1. Power, MW (thermal)	531.2	404.8	7.7	6.3	25.0	975.0
2. Sodium Void Worth, $\Delta k \times 10^3$	11.55	-2.70	-1.45	-0.92	-1.79	4.69
3. Unvoided Doppler Coefficient Over the Temperature Range 2200-4400°K, $-T \frac{dk}{dT} \times 10^4$	41.59	12.64	4.97	3.10	6.60	68.90
4. Voided Doppler Coefficient Over the Temperature Range 2200-4400°K, $-T \frac{dk}{dT} \times 10^4$	24.91	7.65	3.81	2.57	5.70	44.63
5. Worth of Half Steel, $\frac{\Delta k}{k} \times 10^3$	17.89	-0.397	1.58	1.14	2.39	-13.18
6. Core Fuel Worth, $\frac{\Delta k}{k} \times 10^3$	262.0	187.3	39.79	29.74	5.93*	524.8

*Worth of radial blanket fuel in the radial blanket.

TABLE II-4. Sodium Void Worth, $1.0E3 \Delta k/k$ by Region in LWR-Pu-Fueled CRBR at BOL by Different Methods

Case	Inner Core	Outer Core	Lower Blanket	Upper Blanket	Radial Blanket	Total	Comments
1	10.93	-2.37	-1.06	-0.656	-1.51	5.34	Void worth in normal reactor by linearized leakage perturbation
2	11.31	-3.74	-1.75	-1.13	-1.96	2.73	Void worth in core-and-blanket-voided reactor by linearized leakage perturbation
3	11.55	-2.70	-1.45	-0.92	-1.79	4.69	By k-effective difference for removing sodium from normal reactor
4	9.65						By k-effective difference for removing sodium from normal reactor, without resonance self-shielding part
5	1.90						By k-effective difference for removing sodium from normal reactor, resonance self-shielding part only
6	11.18						Same as case 3 but only 50% of normal steel present in inner core
7	11.87						Same as case 3 but 150% of normal steel present in inner core
8	0.934						Void worth of first 10% sodium removed from normal reactor by k-effective difference, without resonance self-shielding part
9	0.971						Void worth of last 10% sodium by the same method as case 8
10	12.12	-1.65	-1.01	-0.624	-1.42	7.42	Same method as case 1 but using Version IV cross-section set 1
11	12.98	-1.42	-0.792	-0.492	-1.30	8.98	Same method as case 1 but using Version IV cross-section set 2
12	13.00						Same method as case 3 but using Version IV cross-section set 1
13	13.83						Same method as case 3 but using Version IV cross-section set 2
14	10.64						Same method as case 4 but using Version IV cross-section set 1
15	11.30						Same method as case 4 but using Version IV cross-section set 2

Note: The Version III cross-section set and the Version IV cross-section set 1 were generated using the narrow resonance approximation and the Version IV cross-section set 2 was generated using RABANL integral transport theory neutron slowing down over the resonance energy interval.

TABLE II-5. Rough Percentage of Reactivity Components in CRBR Material Worths at Beginning of Life

Material Worth	Reactivity Components					Total
	Leakage	Spectral	Capture	Fission Absorption	Fission Source	
Sodium Void						
Inner Core	-61	135	28	1	-3	100
Outer Core	-327	182	47	1	-3	-100
Radial Blanket	-204	93	11			-100
Steel Worth						
Inner Core	53	-89	-64			-100
Outer Core	4000	-2200	-1700			100
Radial Blanket	175	-53	-22			100
Unvoided and Voided Doppler Coeff.						
Inner Core			-110	-5	15	-100
Outer Core			-120	-10	30	-100
Blankets			-100			-100
Core Fuel Worth						
Inner Core	10	-25	-57	-73	245	100
Outer Core	17	-12	-32	-55	183	100
Lower Axial Blanket	31	-16	-28	-30	144	100
Radial Blanket Fuel Worth	631	-301	-333	-61	164	100
Axial Blanket Fuel Worth						
Inner Core	23	-59	-111	-29	76	-100
Outer Core	149	-119	-248	-74	192	-100
Lower Axial Blanket	983	-544	-720	-104	285	-100

TABLE II-6. Channel Definition for the Clinch
River Breeder Reactor at the
Beginning of Life

Subassembly Identification	Row	Channel Number	
		Present Work	PSAR
1	2	1	3
2	3	2	1
6	3	2	1
3	4	2	1
7	4	2	1
4	5	3	2
8	5	3	2
10	5	3	2
15	5	3	2
5	6	5	5
11	6	4	4
13	6	4	4
14	6	4	4
16	6	4	4
9	7	6	5
12	7	6	6
17	7	6	5
21	7	6	6
18	8	8	3
19	8	7	2
20	8	7	2
22	8	7	2
23	8	7	2
24	8	8	3
68	8	5	5
25	9	10	7
26	9	9	6
27	9	9	7
28	9	10	7
29	9	10	7
30	9	10	7
31	9	9	7
32	9	9	6

TABLE II-7. Reactivity Worths Totaled by Channel in the LWR-Pu-Fueled Clinch River Breeder Reactor at the Beginning of Life

Channel	Sodium void $\frac{\Delta k}{k} \times 10^4$ (a)		Unvoided Doppler coeff. $-T \frac{dk}{dT} \times 10^4$	Voided Doppler coeff. $-T \frac{dk}{dT} \times 10^4$	Steel worth $\frac{\Delta k}{k} \times 10^4$ (b)		Core fuel worth, ^c $\frac{\Delta k}{k} \times 10^3$
	Case 1	Case 2	Case 3	Case 3	Case 1	Case 2	
1	8.18	9.64	3.173	1.992	-24.48	-23.98	22.06
2	23.18	24.02	15.050	9.243	-97.73	-88.73	85.13
3	20.21	18.30	12.823	7.851	-81.37	-73.15	73.08
4	21.07	20.31	8.280	5.211	-62.08	-54.16	62.81
5	5.80	4.73	3.313	2.074	-22.80	-18.60	32.17
6	22.36	19.94	6.408	4.210	-62.59	-56.64	48.93
7	2.11	-1.41	4.970	3.083	-29.13	-20.24	65.86
8	1.05	-0.704	2.485	1.541	-14.57	-10.12	32.93
9	-17.72	-23.94	2.898	1.867	24.17	34.72	47.93
10	-17.72	-23.94	2.898	1.867	24.17	34.72	47.93
Total	68.53	46.94	62.298	38.939	-346.41	-276.19	518.83

^aIncludes the sodium in the intersubassembly duct wall gap also.

^bIncludes all the steel in cladding, wrapper wires and subassembly duct.

^cWorth computed in the core-and-blankets voided reactor by linearized leakage perturbation.

TABLE II-8. Unvoided Doppler Coefficient, $-T \frac{dk}{dT} \times 10^4$ by Region Over Different Temperature Ranges in LWR-Pu-Fueled CRBR at the Beginning of Life.

Case	Inner Core	Outer Core	Lower Blanket	Upper Blanket	Radial Blanket	Total	Comments
1	43.42	13.19	5.45	3.39	7.25	72.69	2200-4400°K, perturbation using fluxes at 2200°K.
2	39.76	12.10	4.49	2.81	5.95	65.11	2200-4400°K, perturbation using fluxes at 4400°K.
3	41.59	12.64	4.97	3.10	6.60	68.90	2200-4400°K, average of cases 1 and 2.
4						67.94	2200-4400°K, by k-effective difference.
5	47.46	14.72	5.80	3.59	8.24	79.81	1100-2200°K, perturbation using fluxes at 1100°K.
6						75.58	1100-2200°K, by k-effective difference.
7	44.94	13.95	5.49	3.40	7.80	75.58	1100-2200°K, case 5 normalized to case 6.
8						71.76	1100-4400°K, by k-effective difference.
9	46.82	14.64	5.94	3.70	8.72	79.82	1100-2200°K, same method as case 5 but using Version IV cross-section set 1.
10	49.87	15.46	5.45	3.38	7.92	82.08	1100-2200°K, same method as case 5 but using Version IV cross-section set 2.

TABLE II-9. Voided^a Doppler Coefficient, $-T \frac{dk}{dT} \times 10^4$ by Region Over Different Temperature Ranges in LWR-Pu-Fueled CRBR at the Beginning of Life.

Case	Inner Core	Outer Core	Lower Blanket	Upper Blanket	Radial Blanket	Total	Comments
1	25.89	7.97	4.15	2.80	6.21	47.02	2200-4400°K, perturbation using fluxes at 2200°K.
2	23.93	7.34	3.46	2.34	5.81	42.25	2200-4400°K, perturbation using fluxes at 4400°K.
3	24.91	7.65	3.81	2.57	5.70	44.63	2200-4400°K, average of cases 1 and 2.
4						44.32	2200-4400°K, by k-effective difference.
5	29.40	9.27	4.60	3.09	7.30	53.65	1100-2200°K, perturbation using fluxes at 1100°K.
6						51.19	1100-2200°K, by k-effective difference.
7	28.05	8.84	4.39	2.95	6.96	51.19	1100-2200°K, case 5 normalized to case 6.
8						47.75	1100-4400°K, by k-effective difference.

^aCompletely voided except for control subassemblies.

TABLE II-10. Doppler Coefficient Averaged Over 1100-4400°K, $-1.0E4 * T * dk/dT$ in LWR-Pu-Fueled CRBR at BOL for Different Stages of Voiding

Stage of Voiding	Total	Inner Core
(1) Unvoided, Sodium Volume Fraction = 0.4167	71.76	42.99
(2) Inside of Core Subassemblies Voided Over Core Height, Sodium Volume Fraction = 0.0870	56.54	
(3) Inside of Core and Radial Blanket Subassemblies Voided Over Core and Axial Blankets Height	53.03	29.56
(4) Core and Radial Blanket Subassemblies Totally Voided Over Core and Axial Blankets Height	47.75	26.15
(5) Core, Control, Radial Blanket and Restraint Subassemblies Totally Voided Over Core, Axial Blankets and Reflectors Height	41.98	20.93

TABLE II-11. Steel Worth, $1.0E3 \Delta k/k$ by Region in LWR-Pu-Fueled CRBR at BOL by Different Methods

Case	Inner Core	Outer Core	Lower Blanket	Upper Blanket	Radial Blanket	Total	Comments
1	-18.29	-1.05	1.18	0.832	2.09	-15.23	Worth of 50% steel in normal reactor by linearized leakage perturbation.
2	-17.50	0.257	1.98	1.45	2.68	-11.13	Worth of 50% steel in core-and-blanket-voided reactor by linearized leakage perturbation.
3	-17.71	-0.994	1.33	0.98	2.15	-14.24	Worth of 50% steel in inner-core-voided reactor by linearized leakage perturbation.
4	-15.42	0.84	1.99	1.46	2.57	-8.56	Worth of 50% steel (removed) in inner-core-voided reactor by exact leakage perturbation.
5	-19.21	-2.28	0.87	0.64	1.81	-18.16	Worth of 50% steel (added) in inner-core-voided reactor by exact leakage perturbation.
6	-16.66	0.735	1.79	1.25	2.50	-10.39	Worth of 50% steel (removed) in normal reactor by exact leakage perturbation.
7	-19.40	-2.29	0.761	0.537	1.76	-18.63	Worth of 50% steel (added) in normal reactor by exact leakage perturbation.
8	-18.583						Worth of 50% steel (removed) in normal reactor by k-effective difference.
9	-17.916						Worth of 50% steel (added) in normal reactor by k-effective difference.
10	-18.214						Worth of 50% steel (removed) in inner-core-voided reactor by k-effective difference.
11	-17.593						Worth of 50% steel (added) in inner-core-voided reactor by k-effective difference.
12	-3.591						Worth of 10% steel (removed) in inner-core-voided reactor by k-effective difference.
13	-37.098						Worth of 100% steel (removed) in inner-core-voided reactor by k-effective difference.
14	-19.58	-1.72	1.09	0.768	1.97	-17.48	Worth of 50% steel, same method as case (1) but using Version IV cross-section set 1.
15	-19.10	-1.20	1.22	0.854	2.22	-16.02	Worth of 50% steel, same method as case (1) but using Version IV cross-section set 2.

TABLE III-1. Comparison of Power and Reactivities by Region Between LWR-Pu-Fueled and FFTF-Pu-Fueled CRBR at the Beginning of Life

Power or Reactivity	Fuel Type	Inner Core	Outer Core	Lower Blanket	Upper Blanket	Radial Blanket	Total
Power, MWt	FFTF	531.5	404.5	7.7	6.3	25.0	975.0
	LWR	531.2	404.8	7.7	6.3	25.0	975.0
Sodium void worth in normal reactor, $\frac{\Delta k}{k} \times 10^3$	FFTF	11.83	-2.05	-1.03	-0.638	-1.49	6.63
	LWR	10.93	-2.37	-1.06	-0.656	-1.51	5.34
Unvoided Doppler coefficient ^a over 2200-4400°K, $-T \frac{dk}{dT} \times 10^4$	FFTF	40.18	12.16	4.87	3.04	6.45	66.70
	LWR	41.59	12.64	4.97	3.10	6.60	68.90
Voided Doppler coefficient ^a over 2200-4400°K, $-T \frac{dk}{dT} \times 10^4$	FFTF	23.89	7.30	3.72	2.51	5.54	42.96
	LWR	24.91	7.65	3.81	2.57	5.70	44.63
Worth of half steel in normal reactor, $\frac{\Delta k}{k} \times 10^3$	FFTF	-18.61	-1.15	1.18	0.829	2.08	-15.68
	LWR	-18.29	-1.05	1.18	0.832	2.09	-15.23
Core fuel worth in the core-and-blankets-voided reactor, $\frac{\Delta k}{k} \times 10^3$	FFTF	263.8	187.5	39.58	29.64	5.92 ^b	526.5
	LWR	262.0	187.3	39.79	29.74	5.93 ^b	524.8

^aAverage of perturbation calculations at both temperatures.

^bRadial blanket fuel in radial blanket.

TABLE III-2. Reactivity Worths Totalled by Channel in the FFTF-Pu-Fueled Clinch River Breeder Reactor at the Beginning of Life

Channel	Sodium ^a void in normal reactor, $\frac{\Delta k}{k} \times 10^4$	Unvoided Doppler coeff. ^b $-T \frac{dk}{dT} \times 10^4$	Voided Doppler coeff. ^b $-T \frac{dk}{dT} \times 10^4$	Steel ^c worth normal reactor	$\frac{\Delta k}{k} \times 10^4$ voided ^d reactor	Core fuel worth, ^d $\frac{\Delta k}{k} \times 10^3$
1	8.82	3.072	1.917	-24.98	-24.54	22.19
2	25.87	14.599	8.907	-99.64	-90.83	85.62
3	22.53	12.430	7.560	-83.03	-74.93	73.45
4	22.85	8.002	5.006	-63.33	-55.37	63.12
5	6.54	3.199	1.989	-23.31	-19.07	32.26
6	23.84	6.184	4.040	-63.51	-57.46	49.14
7	3.32	4.792	2.951	-29.92	-20.90	65.92
8	1.66	2.396	1.475	-14.96	-10.45	32.96
9	-17.13	2.791	1.784	23.79	34.43	47.95
10	-17.13	2.791	1.784	23.79	34.43	47.95
Total	81.16	60.255	37.414	-355.11	-284.70	520.53

^aIncludes sodium in the intersubassembly duct wall gap also.

^bOver the range 2200-4400°K and obtained by averaging perturbation calculations at both temperatures.

^cIncludes all the steel in cladding, wrapper wires and subassembly duct.

^dThe core and the axial and radial blankets are totally voided.

TABLE IV-1.a.Number of Cycles of Burnup at the End of Cycles 1 to 7
for Core and Radial Blanket Subassembly Locations

Subass'y I.D.	Burnup in Number of Cycles at the End of Cycles							Subass'y I.D.	Burnup in Number of Cycles at the End of Cycles							Subass'y I.D.	Burnup in Number of Cycles at the End of Cycles						
	1	2	3	4	5	6	7		1	2	3	4	5	6	7		1	2	3	4	5	6	7
1	1	1	2	1	2	1	2	21	1	2	1	2	1	2	1	39	1	2	3	1	2	1	2
2	1	1	2	1	2	1	2	22	1	2	1	2	1	2	1	40	1	2	3	1	2	1	2
3	1	2	1	2	1	2	1	23	1	1	2	1	2	1	2	41	1	2	1	2	1	2	1
4	1	2	1	2	1	2	3	24	1	1	2	1	2	1	2	42	1	2	3	4	3	4	3
5	1	2	1	2	1	2	1	25	1	2	1	2	1	2	1	43	1	2	3	4	5	3	4
6	1	2	1	2	1	2	1	26	1	2	1	2	1	2	1	44	1	2	3	4	5	3	4
7	1	2	1	2	1	2	3	27	1	1	2	1	2	1	2	45	1	2	3	4	5	4	5
8	1	2	1	2	1	2	1	28	1	1	2	1	2	1	2	46	1	2	3	4	5	6	7
9	1	1	2	1	2	1	2	29	1	1	2	1	2	1	2	47	1	2	3	4	5	4	5
10	1	1	2	1	2	1	2	30	1	1	1	2	1	2	1	48	1	2	3	4	5	3	4
11	1	1	2	1	2	1	2	31	1	2	1	2	1	2	3	49	1	2	3	4	5	3	4
12	1	1	2	1	2	1	2	32	1	1	2	1	2	1	2	50	1	2	3	4	3	4	3
13	1	1	2	1	2	1	2	68	1	2	1	2	1	2	3	51	1	2	3	4	1	2	3
14	1	2	1	2	1	2	3	33	1	2	1	2	1	2	1	52	1	2	3	4	5	6	7
15	1	1	2	1	2	1	2	34	1	2	3	1	2	1	2	53	1	2	3	4	5	6	7
16	1	2	1	2	1	2	1	35	1	2	3	1	2	1	2	54	1	2	3	4	5	6	5
17	1	1	2	1	2	1	2	36	1	2	1	2	3	1	2	59	1	2	3	4	5	6	5
18	1	2	1	2	1	2	3	37	1	2	3	4	5	6	1	60	1	2	3	4	5	6	7
19	1	2	1	2	1	2	1	38	1	2	1	2	3	1	2	61	1	2	3	4	5	6	7
20	1	1	2	1	2	1	2																

TABLE IV-1.b. Number of Cycles of Burnup at the End^a of Cycles 8^b to 13^c
for Core and Radial Blanket Subassembly Locations

Subass'y I.D.	Burnup in Number of Cycles at the End of Cycles						Subass'y I.D.	Burnup in Number of Cycles at the End of Cycles						Subass'y I.D.	Burnup in Number of Cycles at the End of Cycles					
	8	9	10	11	12	13		8	9	10	11	12	13		8	9	10	11	12	13
1	1	2	3	1	2	3	21	2	3	1	2	3	1	39	1	2	1	2	1	2
2	3	1	2	3	1	2	22	2	3	1	2	3	1	40	1	2	1	2	1	2
3	2	3	1	2	3	1	23	3	1	2	3	1	2	41	2	1	2	1	2	1
4	1	2	3	1	2	3	24	1	2	3	1	2	3	42	4	3	4	3	4	3
5	2	3	1	2	3	1	25	2	3	1	2	3	1	43	3	4	3	4	3	4
6	2	3	1	2	3	1	26	2	3	1	2	3	1	44	3	4	3	4	3	4
7	1	2	3	1	2	3	27	3	1	2	3	1	2	45	6	4	5	6	4	5
8	2	3	1	2	3	1	28	1	2	3	1	2	3	46	4	5	6	4	5	6
9	1	2	3	1	2	3	29	3	1	2	3	1	2	47	6	4	5	6	4	5
10	3	1	2	3	1	2	30	2	3	1	2	3	1	48	3	4	3	4	3	4
11	1	2	3	1	2	3	31	1	2	3	1	2	3	49	3	4	3	4	3	4
12	3	1	2	3	1	2	32	3	1	2	3	1	2	50	4	3	4	3	4	3
13	3	1	2	3	1	2	68	1	2	3	1	2	3	51	1	2	3	1	2	3
14	1	2	3	1	2	3	33	2	1	2	1	2	1	52	5	6	5	6	5	6
15	3	1	2	3	1	2	34	1	2	1	2	1	2	53	5	6	5	6	5	6
16	2	3	1	2	3	1	35	1	2	1	2	1	2	54	6	5	6	5	6	5
17	3	1	2	3	1	2	36	3	1	2	3	1	2	59	6	5	6	5	6	5
18	1	2	3	1	2	3	37	2	3	4	5	6	1	60	5	6	5	6	5	6
19	2	3	1	2	3	1	38	3	1	2	3	1	2	61	5	6	5	6	5	6
20	3	1	2	3	1	2														

^aNumber of cycles of burnup at the beginning of cycle is one less than the tabulated value.

^bCycle 8 is the first cycle to approach equilibrium as far as burnup in number of cycles is concerned.

^cCycle 14 is the same as cycle 8.

TABLE IV-2. Radial Blanket Shuffling and Refueling Scheme

Shuffling Path	Subassembly Location (No. of cycles of residence in the location)
1	+33(2)+50(2)+54(2)+
2	+34(2)+49(2)+53(2)+
3	+35(2)+48(2)+52(2)+
4	+36(3)+47(3)+
5	+37(6)+
6	+38(3)+45(3)+
7	+39(2)+44(2)+61(2)+
8	+40(2)+43(2)+60(2)+
9	+41(2)+42(2)+59(2)+
10	+51(3)+46(3)+

Note: An arrow on the left side of a subassembly location indicates charging of fresh fuel or loading of fuel burnt elsewhere into that location, and an arrow on the right indicates taking out for shuffling or discharging from the location.

TABLE IV-3. Basic Input to Equilibrium Cycle Burnup Calculations

Cycle length, days	274
K-effective at the end of cycle with all control rods withdrawn	1.002 ± 0.0005
Ratio of fresh charge enrichment of outer core, Pu-atoms/(U + Pu)-atoms, to that of inner core	1.4500
Isotopic composition of Pu-feed for core, $^{238}\text{Pu}/^{239}\text{Pu}/^{240}\text{Pu}/^{241}\text{Pu}/^{242}\text{Pu}$ a/o	1.006/67.428/19.156/ 10.035/2.375
Isotopic composition of U-feed for core, $^{235}\text{U}/^{238}\text{U}$ a/o	0.697/99.303
Isotopic composition of U-feed for axial and radial blankets, $^{235}\text{U}/^{238}\text{U}$ a/o	0.220/99.780
Full atom density of (U + Pu) of fresh charge, inner core/outer core/axial blanket/ radial blanket, 10^{23} atoms/cm ³	0.20394/0.20461/ 0.21791/0.22370
Volume fractions for primary control rods, $\text{B}_4\text{C}/\text{steel}/\text{sodium}$	0.3390/0.3287/0.3323
Boron isotopic composition, weight %, central control rod, B-10/B-11 control rods in row 7, B-10/B-11	19.8/80.2 50.0/50.0
Boron-10 mass, kg per control subassembly, central rod/row 7 control rod	1.21/3.07

TABLE IV-4. Nuclear Reactions Considered in Burnup Calculations

Reactions	Primary Isotopes							Secondary Isotopes										Tertiary Isotopes						
								²³⁹ Pu										²³⁵ U						
	²³⁸ Pu	²³⁹ Pu	²⁴⁰ Pu	²⁴¹ Pu	²⁴² Pu	²³⁵ U	²³⁸ U	²³⁶ U	²³⁷ Np	²⁴¹ Am	²⁴³ Am	¹³⁵ Xe	¹⁴⁹ Sm	RSFP	SSFP	NSFP	RSFP	SSFP	NSFP	²⁴² Am	²⁴⁴ Cm	¹³⁶ Xe	¹³⁵ Cs	¹⁵⁰ Sm
1. (n,γ)	X	X	X	X	X	X	X	X	X	X	X	X	X											
2. (n,f)	X	X	X	X	X	X	X	X	X	X	X										X			
3. (n,p)																								
4. (n,α)		X																						
5. (n,2n)		X	X	X	X		X	X																
6. β ⁻ -decay				X								X												
7. β ⁺ -decay																								
8. α-decay																					X			

X equals the specified reaction takes place.

TABLE IV-5. Fission Product Yields and Atomic Weights
Used in the Equilibrium Cycle Calculations

Fission Product	239Pu Fission		238U Fission	
	Yield	Atomic Weight	Yield	Atomic Weight
135Xe	0.0715	134.949	0.0645	134.949
149Sm	0.0130	148.965	0.0113	148.965
RSFP	0.0134	150.201	0.0050	150.534
SSFP	0.4010	122.739	0.3760	122.540
NSFP	1.5011	116.512	1.5432	116.302
Neutron	~2.878	1.009	~2.421	1.009

TABLE IV-6. Required Enrichments of the Fresh Charges, and Breeding Ratios in the Equilibrium Cycle of the LWR-Pu-Fueled CRBR

Fresh charge enrichment, Pu/(U+Pu)w/o, inner core/outer core = 21.139/30.635

Time, Day	Reactor	Breeding ratio excluding ^{235}U destruction				Conversion ratio excluding ^{235}U destruction				Fraction of full control concentration inserted
		Inner Core	Outer Core	Axial Blanket	Radial Blanket	Inner Core	Outer Core	Axial Blanket	Radial Blanket	
0.0	1.097	0.339	0.162	0.219	0.377	0.657	0.412	8.294	5.916	0.2566
68.5	1.104	0.339	0.165	0.220	0.381	0.664	0.418	7.447	5.666	0.1773
137.0	1.118	0.338	0.169	0.223	0.387	0.679	0.431	6.210	5.228	0.1142
205.5	1.129	0.338	0.172	0.226	0.393	0.693	0.444	5.346	4.854	0.0564
274.0	1.140	0.339	0.176	0.228	0.397	0.707	0.457	4.708	4.533	0.0101

TABLE IV-7. Heavy Metal Mass (kg) Inventory in the Equilibrium Cycle of the LWR-Pu-Fueled Clinch River Breeder Reactor

Isotope	Inner core BOEC/EOEC	Outer core BOEC/EOEC	Axial blankets BOEC/EOEC	Radial blanket BOEC/EOEC
1. ^{238}Pu	6.47/5.55	8.21/7.33	0.012/0.032	0.085/0.138
2. ^{239}Pu	472.69/439.39	560.90/509.21	59.62/113.81	250.49/341.73
3. ^{240}Pu	159.35/171.15	185.44/192.99	2.07/5.48	10.15/16.30
4. ^{241}Pu	60.65/48.29	77.69/64.97	0.060/0.218	0.316/0.588
5. ^{242}Pu	19.92/21.17	23.45/24.55	0.001/0.005	0.007/0.014
6. ^{235}U	14.85/11.04	11.94/9.84	10.45/9.24	30.16/28.25
7. ^{238}U	2699.14/2594.42	2012.48/1960.18	5339.72/5270.68	15963.36/15841.80
8. ^{236}U	0.979/1.74	0.503/0.931	0.342/0.647	1.30/1.76
9. ^{237}Np	0.505/0.953	0.310/0.597	0.133/0.262	0.746/1.03
10. ^{241}Am	2.00/3.55	2.70/4.93	0.001/0.005	0.013/0.028
11. ^{243}Am	0.736/1.45	0.547/1.09	--/--	--/--
12. ^{135}Xe	0.0074/0.011	0.0059/0.008	0.001/0.001	0.002/0.002
13. ^{149}Sm	1.02/1.88	0.839/1.57	0.063/0.144	0.338/0.504
14. RSFP ^a	1.09/2.11	0.875/1.70	0.039/0.105	0.220/0.357
15. SSFP ^a	26.61/51.70	21.40/41.48	0.957/2.58	5.38/8.72
16. NSFP ^a	94.57/183.72	76.04/147.39	3.40/9.16	19.11/30.99
17. RSFP ^b	0.056/0.108	0.032/0.063	0.014/0.029	0.074/0.104
18. SSFP ^b	3.41/6.64	1.96/3.87	0.885/1.75	4.56/6.35
19. NSFP ^b	13.29/25.86	7.64/15.08	3.45/6.80	17.76/24.73
20. ^{242}Am	0.217/0.548	0.175/0.454	--/--	0.001/0.002
21. ^{136}Xe	--/--	--/--	--/--	--/--
22. ^{244}Cm	0.054/0.146	0.024/0.067	--/--	--/--
23. ^{135}Cs	5.85/11.38	4.56/8.85	0.354/0.834	1.91/2.91
24. ^{150}Sm	0.154/0.402	0.075/0.200	0.007/0.021	0.040/0.071
Total	3583.62/3583.22	2997.80/2997.32	5421.57/5421.79	16306.00/16306.37

^a ^{239}Pu fission products.

^b ^{235}U fission products.

TABLE IV-8. Comparison with PSAR Calculation of Heavy Metal Mass (kg) Inventory at the Beginning of Equilibrium Cycle for the LWR-Pu-Fueled CRBR

Isotope	Inner core		Outer core		Axial blankets		Radial blanket	
	Present	PSAR	Present	PSAR	Present	PSAR	Present	PSAR
^{238}Pu	6.47	6.6	8.21	8.0	0.012	--	0.085	--
^{239}Pu	472.69	483.2	560.90	586.1	59.62	52.7	250.49	262.4
^{240}Pu	159.35	164.7	185.44	190.8	2.07	1.02	10.15	10.5
^{241}Pu	60.65	61.4	77.69	82.0	0.060	--	0.316	--
^{242}Pu	19.92	20.9	23.45	24.3	0.001	--	0.007	--
^{235}U	14.85	4.55	11.94	3.80	10.45	10.69	30.16	29.95
^{238}U	2699.14	2674.0	2012.48	1993.4	5339.72	5340.0	15963.36	15954.0
Fission products total ^a	146.06	145.3	113.43	96.7	9.17	5.43	49.39	46.0
Other heavy metals ^b	4.49	--	4.26	--	0.476	--	2.06	--
Total	3583.62	3560.6	2997.80	2985.1	5421.57	5409.8	16306.00	16302.85 ^c

^aIncludes ^{135}Xe , ^{149}Sm , all lumped fission products, ^{136}Xe , ^{135}Cs and ^{150}Sm .

^bIncludes ^{236}U , ^{237}Np , ^{241}Am , ^{242}Am , ^{243}Am and ^{244}Cm .

^cPSAR shows an incorrect total of 16310.8.

TABLE IV-9. Plutonium Isotopic Composition (Weight Percent) in the Equilibrium Cycle of the LWR-Pu-Fueled CRBR

Isotope	Inner core		Outer core		Axial blankets		Radial blanket	
	BOEC	EOEC	BOEC	EOEC	BOEC	EOEC	BOEC	EOEC
^{238}Pu	0.900	0.810	0.959	0.917	0.019	0.027	0.033	0.038
^{239}Pu	65.735	64.093	65.550	63.727	96.530	95.203	95.956	95.250
^{240}Pu	22.160	24.965	21.671	24.152	3.352	4.584	3.888	4.543
^{241}Pu	8.434	7.044	9.079	8.131	0.097	0.182	0.121	0.164
^{242}Pu	2.770	3.088	2.741	3.072	0.002	0.004	0.003	0.004

TABLE IV-10. Comparison with PSAR Calculation of Plutonium Buildup (kg)
in the Equilibrium Cycle of the LWR-Pu-Fueled CRBR

Isotope	Inner core Present/PSAR	Outer core Present/PSAR	Axial blankets Present/PSAR	Radial blanket Present/PSAR
^{238}Pu	-0.92/a	-0.88/a	0.020/--	0.053/--
^{239}Pu	-33.30/a	-51.69/a	54.19/48.9	91.24/89.7
^{240}Pu	11.80/a	7.55/a	3.41/2.58	6.15/5.04
^{241}Pu	-12.36/a	-12.72/a	0.158/--	0.272/--
^{242}Pu	1.25/a	1.10/a	0.004/--	0.007/--
Total	-33.53/a	-56.64/a	57.78/51.48	97.72/94.74

^aNot available.

TABLE IV-11. Isotopic Composition and Total Mass of Plutonium in the Discharged Subassemblies
at the End of an Average* Equilibrium Cycle for the LWR-Pu-Fueled CRBR

Isotope	Isotopic composition, w/o				Mass of plutonium discharged, kg			
	Inner Core	Outer Core	Axial Blankets	Radial Blanket	Inner Core	Outer Core	Axial Blankets	Radial Blanket
^{238}Pu	0.730	0.876	0.035	0.054	1.60	2.18	0.020	0.053
^{239}Pu	62.385	61.865	93.784	93.367	136.57	154.37	54.19	91.24
^{240}Pu	27.547	26.580	5.901	6.293	60.31	66.33	3.41	6.15
^{241}Pu	5.995	7.296	0.273	0.278	13.12	18.20	0.158	0.272
^{242}Pu	3.342	3.383	0.007	0.007	7.32	8.44	0.004	0.007
Total	100.	100.	100.	100.	218.92	249.53	57.78	97.72

*The radial blanket is assumed to be refueled precisely in sixths.

TABLE IV-12. Subassembly Burnup in the Equilibrium Cycle of the LWR-Pu-Fueled CRBR

Subassemblies and axial region	Burnup, MWD/kg after the specified number of cycles of residence					
	1	2	3	4	5	6
Rows 2 and 3: A	53.52	101.18	144.55			
	B	34.94	67.15	97.20		
	C	3.103	8.556	15.895		
	D	1.010	2.820	5.332		
Rows 4 and 5: A	49.77	94.38	135.16			
	B	32.42	62.46	90.57		
	C	2.786	7.628	14.144		
	D	0.909	2.519	4.750		
Rows 6 and 7: A	42.29	80.74	116.21			
	B	27.04	52.37	76.29		
	C	2.180	5.821	10.693		
	D	0.694	1.884	3.520		
Rows 8 and 9: A	44.12	83.46	118.93			
	B	27.44	52.89	76.63		
	C	1.359	3.445	6.176		
	D	0.374	0.963	1.752		
Radial blanket: A	1.503	3.733	6.613	10.073	14.050	18.488
	B	0.727	1.735	3.007	4.524	6.228
	C	0.318	0.749	1.287	1.929	2.669
	D	0.100	0.229	0.386	0.570	0.782

A. Average over the axial region $110.225 < Z < 121.730$ cm, an estimate of the axial maximum (Fig. IV-1).

B. Average over the axial region $75.711 < Z < 87.216$ cm.

C. Average over the axial region $57.856 < Z < 75.711$ cm.

D. Average over the axial region $40.000 < Z < 57.856$ cm.

TABLE IV-13. Required Enrichments of the Fresh Charges, and Breeding Ratios Obtained in the Improved Equilibrium Cycle Calculations of the LWR-Pu-Fueled CRBR

Fresh charge enrichment, Pu/(U+Pu)w/o, inner core/outer core = 21.159/30.663

Time, Day	Reactor	Breeding ratio excluding ^{235}U destruction				Conversion ratio excluding ^{235}U destruction				Fraction of full control concentration inserted
		Inner Core	Outer Core	Axial Blankets	Radial Blanket	Inner Core	Outer Core	Axial Blankets	Radial Blanket	
0.0	1.096	0.335	0.165	0.218	0.378	0.655	0.413	8.347	5.904	0.3142
68.5	1.103	0.335	0.166	0.219	0.382	0.663	0.419	7.491	5.611	0.2180
137.0	1.115	0.336	0.170	0.222	0.387	0.678	0.432	6.241	5.109	0.1387
205.5	1.126	0.337	0.173	0.225	0.392	0.692	0.444	5.369	4.697	0.0664
274.0	1.135	0.337	0.175	0.227	0.396	0.706	0.457	4.725	4.352	0.0073

TABLE IV-14. Heavy Metal Mass (kg) Inventory in the Radial Blanket of the LWR-Pu-Fueled CRBR for the Improved* Equilibrium Cycle Calculation

Isotope	Improved calculation BOEC/EOEC	PSAR calculation BOEC
1. ^{238}Pu	0.126/0.184	---
2. ^{239}Pu	295.35/386.0	262.4
3. ^{240}Pu	13.15/19.57	10.5
4. ^{241}Pu	0.424/0.726	---
5. ^{242}Pu	0.009/0.017	---
6. ^{235}U	29.33/27.43	29.95
7. ^{238}U	15900.48/15778.80	15954.
8. ^{236}U	1.47/1.93	
9. ^{237}Np	0.943/1.22	
10. ^{241}Am	0.019/0.039	
11. ^{243}Am	---/---	
12. ^{135}Xe	0.002/0.002	
13. ^{149}Sm	0.440/0.605	
14. RSFP ^a	0.296/0.436	
15. SSFP ^a	7.25/10.66	
16. NSFP ^a	25.75/37.88	
17. RSFP ^b	0.095/0.124	
18. SSFP ^b	5.81/7.62	
19. NSFP ^b	22.64/29.67	
20. ^{242}Am	0.001/0.002	
21. ^{136}Xe	---/---	
22. ^{244}Cm	---/---	
23. ^{135}Cs	2.52/3.53	
24. ^{150}Sm	0.058/0.093	
25. Fission products total	64.86/90.62	46.0
Total	16306.16/16306.54	16302.85

^a ^{239}Pu fission products.

^b ^{235}U fission products.

*Details of shuffling of radial blanket subassemblies modelled.

TABLE IV-15. Isotopic Composition and Total Mass of Plutonium in the Subassemblies Discharged from the Radial Blanket for the Improved Equilibrium Cycle Calculation of the LWR-Pu-Fueled CRBR

Isotope	Improved calculation		Unimproved calculation		PSAR calculation	
	Isotopic composition, w/o	Mass discharged, kg	Isotopic composition, w/o	Mass discharged, kg	Isotopic composition, w/o	Mass discharged, kg
^{238}Pu	0.059	0.058	0.054	0.053	---	---
^{239}Pu	93.034	90.65	93.367	91.24	94.680	89.7
^{240}Pu	6.589	6.42	6.293	6.15	5.320	5.04
^{241}Pu	0.310	0.302	0.278	0.272	---	---
^{242}Pu	0.008	0.008	0.007	0.007	---	---
Total	100.00	97.44	100.00	97.72	100.00	94.74

TABLE IV-16. Axial Maximum Burnup of the Radial Blanket Subassemblies for the Improved Equilibrium Cycle Calculation of the LWR-Pu-Fueled CRBR

Subassembly identification	Burnup, MWD/kg after the specified number of cycles of residence					
	1	2	3	4	5	6
33,34,35,39,40,41	2.447	6.231				
42,43,44,48,49,50			→ 8.790	11.719		
52,53,54,59,60,61					→ 13.965	16.356
37	4.083	10.227	18.061	27.276	37.613	48.860
36,38,51	2.309	5.945	10.716			
45,46,47				→ 13.790	17.167	20.822

TABLE V-1 Radial Structure of the R-Z Model of the Hot Full Power LWR-Pu-Fueled CRBR at
BOEC 14 Used for Power and Reactivity Coefficient Distribution Calculations

Annulus Serial No.	Subassembly Identification	Row	Burnup Stage	Cumulative Number of Subassemblies	Outer Radius of Annulus
1	Central control rod	1	-	1	6.385
2	1	2	1	7	16.894
3	6	3	2	13	23.022
4	2	3	3	19	27.833
5	7	4	1	25	31.926
6	3	4	2	31	35.552
7	6 Control rods of Row 4	4	-	37	38.840
8	10,15	5	3	49	44.697

TABLE V-1 (Contd)

Annulus Serial No.	Subassembly Identification	Row	Burnup Stage	Cumulative Number of Subassemblies	Outer Radius of Annulus
9	8	5	2	55	47.354
10	4	5	1	61	49.870
11	13	6	3	67	52.266
12	16	6	2	73	54.556
13	11,14	6	1	85	58.869
14	3 control rods at flats of row 7	7	-	88	59.899
15	21	7	2	94	61.907
16	5	6	2	100	63.853
17	2 Control rods at corners of row 7	7	-	102	64.488
18	9	7	1	108	66.357
19	12	7	3	114	68.176
20	3 Control rods at flats of row 7	7	-	117	69.067
21	18,24	8	1	129	72.523
22	17	7	3	135	74.190
23	2 Control rods at corners of row 7	7	-	137	74.737
24	22	8	2	143	76.356

TABLE V-1 (Contd)

Annulus Serial No.	Subassembly Identification	Row	Burnup Stage	Cumulative Number of Subassemblies	Outer Radius of Annulus
25	23,32	8,9	3	155	79.496
26	20	8	3	161	81.020
27	2 Control rods at corners of row 7	7	-	163	81.521
28	68	8	1	169	83.008
29	19,25,26	8,9,9	2	187	87.317
30	28,31	9	1	199	90.075
31	30	9	2	205	91.423
32	27,29	9	3	217	94.061
33	34,35,39,40,51; 33,37,41; 36,38	radial blanket	1 2 3	277	106.272
34	43,44,48,49; 42,50	radial blanket	3 4	313	112.967
35	46; 52,53,60,61; 45,47,54,59;	radial blanket	4 5 6	367	122.324
36	20 cm thick radial reflector	radial restraint	-	-	142.324

TABLE V-2 Power by Reactor Region, MWt in the LWR-Pu-Fueled CRBR at the Beginning of Equilibrium Cycle 14 by Different Methods

Case	Inner Core	Outer Core	Lower Blanket	Upper Blanket	Radial Blanket	Total	Comments
1	508.5	376.0	19.4	11.8	59.0	975.0	R-Z model calculation in the normal reactor at 1100°K
2	530.5*	386.9*			57.6	975.0	2-D triangular mesh calculation in the normal reactor at 1100°K

*Includes extrapolation thicknesses at top and bottom.

TABLE V-3. Summary of K-Effective of the LWR-Pu-Fueled CRBR at BOEC 14 Based on the R-Z Model and Version III Cross-Sections

Case	Fuel temperature	Sodium in core and blankets	K-effective
1	1100°K	normal	1.003746
2	2200°K	normal	0.999403
3	4400°K	normal	0.995454
4	1100°K	voided	1.014458
5	2200°K	voided	1.011458
6	4400°K	voided	1.008829

TABLE V-4. Definition of SAS Channels at the Beginning and End of the Equilibrium Cycle

Subassembly identification	Row	Channel Number			
		BOEC		EOEC	
		This Work	PSAR	This Work	PSAR
1	2	1	1	1	1
2	3	3	2	2	2
6	3	2	2	2	2
3	4	2	2	2	3
7	4	1	3	1	3
4	5	5	5	3	5
8	5	4	4	4	4
10	5	3	4	4	4
15	5	3	4	4	4
5	6	4	6	7	6
11	6	5	5	3	5
13	6	6	6	4	6
14	6	5	5	3	5
16	6	4	6	4	6
9	7	5	7	7	7
12	7	6	6	9	7
17	7	6	6	9	7
21	7	10	6	7	7
18	8	8	7	5	8
19	8	7	8	6	9
20	8	9	8	8	9
22	8	7	8	6	9
23	8	9	8	8	9
24	8	8	7	5	8
68	8	8	9	7	10
25	9	10	10	8	9
26	9	10	10	7	10
27	9	10	10	10	10
28	9	8	9	10	10
29	9	10	10	10	10
30	9	10	10	10	10
31	9	8	9	10	10
32	9	9	10	9	10

TABLE V-5. Reactivity Worths Totalled by Channel in the LWR-Pu-Fueled Clinch River Breeder Reactor at BOEC 14

Channel	Sodium ^a void $\frac{\Delta k}{k} \times 10^4$,	Unvoided Doppler coeff. $-T \frac{dk}{dT} \times 10^4$,	Voided Doppler coeff. $-T \frac{dk}{dT} \times 10^4$,	Steel ^b worth $\frac{\Delta k}{k} \times 10^4$		Core fuel worth $\frac{\Delta k}{k} \times 10^3$	
	Case 1	Case 3	Case 3	Case 1	Case 2	Case 1	Case 2
1	17.15	6.667	4.066	-54.65	-50.48	49.34	50.87
2	16.45	6.531	4.012	-53.92	-48.37	37.77	39.99
3	24.36	8.499	5.241	-75.72	-68.09	41.84	45.61
4	21.03	5.513	3.382	-56.21	-49.97	42.12	44.91
5	25.92	6.691	4.140	-66.02	-58.69	65.66	68.78
6	16.59	4.011	2.507	-44.34	-38.18	30.44	33.18
7	1.44	1.547	0.977	-9.97	-5.80	26.06	27.97
8	3.32	3.793	2.424	-21.77	-11.95	76.71	81.68
9	4.18	2.389	1.510	-19.84	-13.24	34.96	37.79
10	-8.50	3.956	2.587	5.08	18.47	57.87	64.29
Total	121.92	49.597	30.846	-397.37	-326.31	462.77	495.07

^aIncludes the void worth of the sodium in the intersubassembly duct wall gap also.

^bIncludes the worth of all the steel in cladding, wrapper wires and subassembly duct.

TABLE V-6. Sodium Void Worth, $\frac{\Delta k}{k} \times 10^3$ by Region in LWR-Pu-Fueled CRBR at BOEC 14 by Different Methods

Case	Inner Core	Outer Core	Lower Blanket	Upper Blanket	Radial Blanket	Total	Comments
1	13.96	-0.034	-1.14	-0.590	-1.13	11.06	Void worth in normal reactor at 1100°K by linearized leakage perturbation.
2						10.71	Void worth in normal reactor at 1100°K by k-effective difference.

TABLE V-7. Unvoided Doppler Coefficient, $-T \frac{dk}{dT} \times 10^4$ by Region Over Different Temperature Ranges in LWR-Pu-Fueled CRBR at BOEC 14

Case	Inner Core	Outer Core	Lower Blanket	Upper Blanket	Radial Blanket	Total	Comments
1	33.73	9.05	6.95	2.13	8.37	60.23	2200-4400°K, perturbation using fluxes at 2200°K.
2	31.27	8.38	5.82	1.85	6.93	54.26	2200-4400°K, perturbation using fluxes at 4400°K.
3*	32.50	8.71	6.39	1.99	7.65	57.25	2200-4400°K, average of cases 1 and 2.
4						56.97	2200-4400°K, by k-effective difference.
5	36.71	10.07	7.33	2.23	9.39	65.73	1100-2200°K, perturbation using fluxes at 1100°K.
6						62.66	1100-2200°K, by k-effective difference.
7*	34.99	9.60	6.99	2.13	8.95	62.66	1100-2200°K, case 5 normalized to case 6.
8						59.81	1100-4400°K, by k-effective difference.

*Recommended values for HCDA analysis.

TABLE V-8. Voided^a Doppler Coefficient, $-T \frac{dk}{dT} \times 10^4$ by Region Over Different Temperature Ranges in LWR-Pu-Fueled CRBR at BOEC 14

Case	Inner Core	Outer Core	Lower Blanket	Upper Blanket	Radial Blanket	Total	Comments
1	19.79	5.54	5.14	1.71	7.35	39.53	2200-4400°K, perturbation using fluxes at 2200°K.
2	18.51	5.15	4.35	1.50	6.20	35.71	2200-4400°K, perturbation using fluxes at 4400°K.
3*	19.15	5.34	4.75	1.60	6.78	37.62	2200-4400°K, average of cases 1 and 2.
4						37.93	2200-4400°K, by k-effective difference.
5	22.46	6.44	5.62	1.87	8.46	44.83	1100-2200°K, perturbation using fluxes at 1100°K.
6						43.28	1100-2200°K, by k-effective difference.
7*	21.68	6.22	5.42	1.80	8.16	43.28	1100-2200°K, case 5 normalized to case 6.
8						40.60	1100-4400°K, by k-effective difference.

*Recommended values for HCDA analysis.

^aCore and blankets completely voided except for control subassemblies.

TABLE V-9. Steel Worth, $\frac{\Delta k}{k} \times 10^3$ by Region in LWR-Pu-Fueled CRBR at BOEC 14 by Different Methods

Case	Inner Core	Outer Core	Lower Blanket	Upper Blanket	Radial Blanket	Total	Comments
1	-39.28	-4.55	2.40	1.70	3.11	-36.63	Worth of all steel in the unvoided reactor at 1100°K by linearized leakage perturbation.
2	-37.20	-2.34	4.00	2.90	4.00	-28.63	Worth of all steel in the core-and-blanket-voided reactor at 1100°K by linearized leakage perturbation.
3	-39.93	-4.63	2.38	1.68	3.10	-37.40	Worth of all steel in the unvoided reactor at 2200°K by linearized leakage perturbation.
4	-37.83	-2.40	3.94	2.87	3.96	-29.45	Worth of all steel in the core-and-blanket-voided reactor at 2200°K by linearized leakage perturbation.

TABLE V-10. Core Fuel* Worth, $\frac{\Delta k}{k} \times 10^3$ by Region in LWR-Pu-Fueled CRBR at BOEC 14 by Different Methods

Case	Inner Core	Outer Core	Lower Blanket	Upper Blanket	Radial Blanket	Total	Comments
1	244.38	165.64	35.82	16.94		462.78	Worth of fuel at 1100°K in the unvoided reactor by perturbation.
2	254.11	176.55	41.55	22.86		495.07	Worth of fuel at 1100°K in the core-and-blanket-voided reactor by perturbation.
3	245.79	166.95	35.17	16.87		464.77	Worth of fuel at 2200°K in the unvoided reactor by perturbation.
4	255.05	177.22	41.03	22.79		496.09	Worth of fuel at 2200°K in the core-and-blanket-voided reactor by perturbation.

*Burnt fuel in the central quarter of the core about the core midplane.

TABLE VI-1. Power Distribution by Region (MW) in the LWR-Pu-Fueled Clinch River Breeder Reactor at EOEC 17 by Different Methods

Case	Inner Core	Outer Core	Lower Blanket	Upper Blanket	Radial Blanket	Total	Comments
1	497.7 ^a	389.3 ^a			88.0	975.0	2-D triangular mesh calculation using unimproved radial blanket compositions and Version III cross-sections.
2	488.1 ^a	386.8 ^a			100.1	975.0	2-D triangular mesh calculation using improved radial blanket compositions and Version III cross-sections.
3	465.8	365.8	26.7	20.2	96.5	975.0	R-Z model calculation using unimproved radial blanket compositions and Version III cross-sections.
4	463.9	365.3	26.8	20.4	98.6	975.0	R-Z model calculation using unimproved radial blanket compositions and Version IV cross-section set 2.
5	448.5	371.5	34.1	12.7	101.4	968.2 ^b	PSAR Table 4.3-7.

^aIncluding extrapolation thicknesses at both ends of the core.

^bThe remaining 6.8 MW is produced by capture in the control and other subassemblies.

TABLE VII-1. Sodium Void Worth, $\frac{\Delta k}{k} \times 10^3$ by Region in LWR-Pu-Fueled CRBR at EOEC 17 by Different Methods

Case	Cross-Section	Inner Core	Outer Core	Lower Blanket	Upper Blanket	Radial Blanket	Total	Comments
1	ENDF/B-III	14.83	0.15	-0.86	-0.87	-1.18	12.07	Void worth in normal reactor with fuel at 1100°K by linearized leakage perturbation.
2	ENDF/B-III						11.56	Void worth in normal reactor with fuel at 1100°K by k-effective difference.
3	ENDF/B-IV ^a	16.99	1.28	-0.61	-0.69	-0.92	16.06	Void worth in normal reactor with fuel at 1100°K by linearized leakage perturbation.
4	ENDF/B-IV ^a						16.43	Void worth in normal reactor with fuel at 1100°K by k-effective difference.

^aVersion IV cross-section set 2 generated using RABANL integral transport theory over the resonance energy interval.

TABLE VII-2. Unvoided Doppler Coefficient, $-\frac{dk}{dT} \times 10^4$ by Region Over Different Temperature Ranges in LWR-Pu-Fueled CRBR at EOEC 17

Case	Cross-Section	Inner Core	Outer Core	Lower Blanket	Upper Blanket	Radial Blanket	Total	Comments
1	ENDF/B-III	36.60	11.86	6.52	3.04	11.24	69.26	2200-4400°K, perturbation using fluxes at 2200°K. Case 3 includes also Doppler effect of steel not included in cases 1 and 2.
2	ENDF/B-IV ^a	37.21	11.97	6.43	3.00	11.49	70.12	
3	ENDF/B-IV	42.02	13.85	6.78	3.15	11.73	77.55	
4	ENDF/B-III	34.02	11.01	5.55	2.68	9.50	62.76	2200-4400°K, perturbation using fluxes at 4400°K. Case 6 includes also Doppler effect of steel not included in cases 4 and 5.
5	ENDF/B-IV	34.24	11.02	5.39	2.60	9.60	62.85	
6	ENDF/B-IV	38.68	12.77	5.68	2.74	9.79	69.66	
7	ENDF/B-III	35.31	11.43	6.03	2.86	10.37	66.00	2200-4400°K, average of cases 1 and 4, cases 2 and 5, and cases 3 and 6.
8	ENDF/B-IV	35.72	11.50	5.91	2.80	10.56	66.48	
9	ENDF/B-IV	40.35	13.31	6.23	2.94	10.76	73.59	
10	ENDF/B-III						65.50	2200-4400°K, by k-effective difference. Case 11 includes Doppler effect of steel not included in case 10.
11	ENDF/B-IV						73.35	
12	ENDF/B-III	39.52	13.12	6.81	3.18	12.46	75.09	1100-2200°K, perturbation using fluxes at 1100°K. Case 14 includes also Doppler effect of steel not included in cases 12 and 13.
13	ENDF/B-IV	41.44	13.77	6.77	3.16	12.84	78.00	
14	ENDF/B-IV	47.71	16.20	7.33	3.42	13.24	87.90	
15	ENDF/B-III						71.66	1100-2200°K, by k-effective difference. Case 16 includes Doppler effect of steel not included in case 15.
16	ENDF/B-IV						83.95	

^a ENDF/B-IV cross-section throughout this table refers to the Version IV cross-section set 2 generated using the RABANL integral transport theory over the resonance energy interval.

TABLE VII-3. Voided Doppler Coefficient, $-T \frac{dk}{dT} \times 10^4$ by Region Over Different Temperature Ranges in LWR-Pu-Fueled CRBR at EOE 17

Case	Cross-Section	Inner Core	Outer Core	Lower Blanket	Upper Blanket	Radial Blanket	Total	Comments
1	ENDF/B-III	22.20	7.22	5.06	2.32	9.65	46.45	2200-4400°K, perturbation using fluxes at 2200°K. Case 3 includes also Doppler effect of steel not included in cases 1 and 2.
2	ENDF/B-IV ^a	23.04	7.39	5.17	2.34	10.05	48.00	
3	ENDF/B-IV	25.58	8.35	5.40	2.43	10.22	51.98	
7	ENDF/B-III	21.48	6.97	4.70	2.19	8.95	44.30	2200-4400°K, average of cases 1 and 4, cases 2 and 5, and cases 3 and 6.
8	ENDF/B-IV	22.22	7.12	4.77	2.20	9.28	45.60	
9	ENDF/B-IV	25.10	8.22	4.94	2.28	9.43	49.98	
4	ENDF/B-III	20.77	6.73	4.34	2.07	8.25	42.16	2200-4400°K, perturbation using fluxes at 4400°K. Case 6 includes also Doppler effect of steel not included in cases 4 and 5.
5	ENDF/B-IV	21.41	6.85	4.38	2.06	8.52	43.21	
6	ENDF/B-IV	24.62	8.09	4.49	2.13	8.64	47.98	
10	ENDF/B-III						44.56	2200-4400°K, by k-effective difference. Case 11 includes Doppler effect of steel not included in case 10.
11	ENDF/B-IV						50.12	
12	ENDF/B-III	24.97	8.32	5.47	2.53	10.96	52.25	1100-2200°K, perturbation using fluxes at 1100°K. Case 14 includes also Doppler effect of steel not included in cases 12 and 13.
13	ENDF/B-IV	26.23	8.63	5.64	2.57	11.48	54.55	
14	ENDF/B-IV	29.53	9.89	6.01	2.71	11.75	59.90	
15	ENDF/B-III						50.49	1100-2200°K, by k-effective difference. Case 16 includes Doppler effect of steel not included in case 15.
16	ENDF/B-IV						58.14	

^aENDF/B-IV cross-section throughout this table refers to the Version IV cross-section set 2 generated using the RABANL integral transport theory over the resonance energy interval.

TABLE VII-4. Steel Worth, $\frac{\Delta k}{k} \times 10^3$ by Region in LWR-Pu-Fueled CRBR at EOEC 17 by Different Methods

Case	Cross-Section	Inner Core	Outer Core	Lower Blanket	Upper Blanket	Radial Blanket	Total	Comments
1	ENDF/B-III	-42.45	-6.23	1.71	2.43	3.05	-41.49	Worth of all steel in the unvoided reactor at 1100°K by linearized leakage perturbation.
2	ENDF/B-IV ^a	-44.41	-6.92	1.74	2.52	3.18	-43.89	
3	ENDF/B-III	-40.81	-3.70	3.22	3.95	4.01	-33.37	Worth of all steel in the core-and-blanket-voided reactor at 1100°K by linearized leakage perturbation.
4	ENDF/B-IV	-42.43	-4.44	3.21	4.00	4.11	-35.55	
5	ENDF/B-III	-43.05	-6.35	1.71	2.40	3.01	-42.28	Worth of all steel in the unvoided reactor with the fuel at 2200°K by linearized leakage perturbation.
6	ENDF/B-IV ^b	-45.15	-7.09	1.73	2.48	3.12	-44.90	
7	ENDF/B-IV ^c	-45.55	-7.24	1.70	2.46	3.09	-45.53	
8	ENDF/B-III	-40.86	-3.76	3.12	3.84	3.89	-33.79	Worth of all steel in the core-and-blanket-voided reactor with the fuel at 2200 °K by linearized leakage perturbation.
9	ENDF/B-IV ^b	-43.22	-4.60	3.14	3.93	4.02	-36.73	
10	ENDF/B-IV ^c	-43.43	-4.68	3.12	3.91	4.00	-37.06	

^aENDF/B-IV cross-section throughout this table refers to the Version IV cross-section set 2 generated using the RABANL integral transport theory over the resonance energy interval.

^bConstituents of steel at 1100°K.

^cConstituents of steel at 2200°K.

TABLE VII-5. Core Fuel^a Worth, $\frac{\Delta k}{k} \times 10^3$ by Region in LWR-Pu-Fueled CRBR at EOE 17 by Different Methods

Case	Cross-Section	Inner Core	Outer Core	Lower Blanket	Upper Blanket	Radial Blanket	Total	Comments
1	ENDF/B-III	196.95	160.54	25.88	20.46		403.83	Worth of fuel at 1100°K in the unvoided reactor by perturbation.
2	ENDF/B-IV ^b	196.40	160.37	25.43	19.96		402.16	
3	ENDF/B-III	209.82	169.10	32.48	26.34		437.74	Worth of fuel at 1100°K in the core-and-blanket-voided reactor by perturbation.
4	ENDF/B-IV	207.49	167.31	31.61	25.47		431.88	
5	ENDF/B-III	198.96	162.04	25.73	20.46		407.21	Worth of fuel at 2200°K in the unvoided reactor by perturbation.
6	ENDF/B-IV	199.01	162.30	25.26	19.97		406.54	
7	ENDF/B-III	211.14	169.98	32.33	26.34		439.79	Worth of fuel at 2200°K in the core-and-blanket-voided reactor by perturbation.
8	ENDF/B-IV	209.18	168.42	31.44	25.46		434.51	

^aBurnt fuel in the central quarter of the core about the core midplane.

^bENDF/B-IV cross-section throughout this table refers to the Version IV cross-section set 2 generated using the RABANL integral transport theory over the resonance energy interval.

TABLE VII-6. Contribution to Differences in Sodium Void Worth for Two Subassemblies in the Inner Core

Subassembly	Void worth based on ENDF/B-IV-Void Worth based on ENDF/B-III data					Total
	R-Leak.	Z-Leak.	Abs.	Net Scat.	Source	
6	0.54	9.24	15.07	77.37	-2.22	100
13	1.94	7.94	14.68	79.36	-3.91	100

TABLE VII-7. Comparison of Peak Reactivity Coefficients by PSAR Channel
($10^{-5} \frac{\Delta k}{k}$ per kg)

PSAR Channel	Sodium Void		Steel Worth		Fuel Worth	
	This Work ^a	PSAR App. F	This Work ^b	PSAR App. F	This Work ^c	PSAR App. F.
1	7.55	7.40	-4.16	-4.20	9.57	11.40
2	8.03	7.35	-4.04	-3.95	6.75	7.85
3	7.24	6.40	-3.66	-3.55	7.95	9.10
4	7.04	6.20	-3.50	-3.40	5.76	6.75
5	5.70	5.40	-2.97	-3.10	7.50	8.90
6	5.62	4.65	-2.91	-2.70	5.90	6.70
7	4.18	4.00	-2.28	-2.40	5.33	6.00
8	3.55	3.10	-2.05	-2.05	10.07	11.15
9	1.59	1.80	-1.05	-1.40	6.48	8.10
10	-0.08	-0.60	-0.22	-0.20	5.88	6.50

^aCase 1 of Table VII-1.^bCase 8 of Table VII-4 (cases 3 and 8 are practically identical).^cCase 7 of Table VII-5.

TABLE VII-8. Effect on the Sodium Voiding Reactivity in the Inner Core of CRBR at EOEC of Changing from ENDF/B-III data to ENDF/B-IV for Selected Materials (One-Dimensional Model)

Isotope Changed	% Change in reactivity from all ENDF/B-III value
^{235}U	0.25
^{238}U	4.91
^{239}Pu	2.23
^{240}Pu	2.85
^{241}Pu	-0.48
^{242}Pu	0.01
^{16}O	-0.16
^{23}Na	-0.13
Fe	0.68
Cr	-0.46
Ni	0.34
Mo	-0.74
Mn	0.39

TABLE VII-9. A More General Fit for the Temperature Dependence of the Doppler Effect in the LWR-Pu-Fueled Clinch River Breeder Reactor at EOEC 17, $\frac{1}{k} \frac{dk}{dT} = -\alpha T^{-\gamma}$

Voiding condition	Number of data points*	α	γ
Unvoided	3 ^a	0.01683	1.1159
Unvoided	4 ^b	0.01751	1.1211
Voided	3 ^a	0.01732	1.1708

^a(1100°, 2200°, 4400°K)

^b(1100°, 2200°, 4400°, 6600°K)

*A data point refers to a pair of values of the fuel temperature and the multiplication constant.

TABLE VII-10. Comparison of Doppler Coefficients with the Preliminary Safety Analysis Report (PSAR) for the LWR-Pu-Fueled Clinch River Breeder Reactor at EOEC 17

Doppler coefficient, $-T \frac{dk}{dT} \times 10^4$

Region	With Sodium		Without Sodium	
	This Work*	PSAR	This Work*	PSAR
Inner Core	35.31	37.0	21.48	19.2
Outer Core	11.43	13.1	6.97	7.7
Lower Axial Blanket	6.03	5.7	4.70	3.9
Upper Axial Blanket	2.86	1.7	2.19	1.5
Radial Blanket	10.37	12.1	8.95	11.9
Total	66.00	69.6	44.30	44.2

*For temperature range from 2200°K to 4400°K, average of Doppler coefficients computed with 2200°K fluxes and 4400°K fluxes (cases 7 of Tables VII-2 and VII-3).

TABLE VII-11. Comparison of Doppler Coefficients by Channel for the LWR-Pu-Fueled CRBR at EOEC 17

Doppler Coefficient ($-T \frac{dk}{dT} \times 10^4$)

PSAR Channel	Sodium In		Sodium Out	
	This Work*	PSAR Table F6.2-7	This Work*	PSAR Table F6.2-7
1	3.27	3.48	2.09	2.18
2	5.39	5.58	3.46	3.44
3	5.95	5.95	3.87	3.82
4	7.48	7.64	4.83	4.85
5	6.83	7.62	4.23	4.59
6	6.32	6.61	3.93	4.14
7	7.05	7.53	4.44	4.81
8	2.88	3.03	1.78	1.91
9	4.82	5.79	3.04	3.64
10	5.71	6.17	3.70	4.35
Total	55.63	59.40	35.35	37.73

*Cases 7 of Tables VII-2 and VII-3

TABLE VIII-1 Comparison of Reactivity Coefficients for Full Core Height, by Channel, for LWR-Pu-Fueled CRBR at BOEC14 as Obtained from 2-D Triangular-Mesh and R-Z Perturbation Calculations, $\Delta k/k^2 \times 10^3$

Channel	Subassembly I.D.	Sodium Void Worth		Steel Removal Worth		Doppler Worth*		Core Fuel Worth	
		Tri.	R-Z	Tri.	R-Z	Tri.	R-Z	Tri.	R-Z
1	1,7	1.758	1.849	5.423	5.748	-0.3917	-0.4400	42.11	42.84
2	3,6	1.684	1.774	5.482	5.656	-0.3886	-0.4257	32.74	32.80
3	2,10,15	2.271	2.636	7.147	7.987	-0.4867	-0.5465	36.70	36.18
4	5,8,16	1.647	2.252	5.221	5.992	-0.3824	-0.3554	37.10	36.74
5	4,9,11,14	1.999	2.765	5.669	7.086	-0.4541	-0.4324	57.82	57.54
6	12,13,17	1.586	1.798	4.307	4.719	-0.2479	-0.2577	26.64	26.64
7	19,22	0.461	0.244	1.825	1.230	-0.1040	-0.1015	24.68	23.40
8	18,24,28,31,68	0.299	0.573	3.080	3.662	-0.2102	-0.2486	61.56	68.89
9	20,23,32	0.274	0.571	1.661	2.338	-0.1386	-0.1552	29.11	31.34
10	21,25,26,27, 29,30	-0.643	-0.585	0.053	0.117	-0.2474	-0.2672	49.93	52.16

*Reactivity for a temperature change of 1100°K to 2200°K in the unvoided reactor corresponding to case 5 or TABLE V-7

TABLE VIII-2 Comparison of the Sodium Void Worth by Channel and Component over full Core Height as Obtained from 2-D Triangular-Mesh and R-Z Perturbation Calculations for LWR-Pu Fueled CRBR at BOEC14 (Normalized to 100 for the total worth from R-Z Calculations)

Channel	R-Leakage	Z-Leakage	Absorption	Fiss Source	Net Scat	Total
1 Tri	-8.03	-38.40	22.52	-2.65	121.68	95.10
R-Z	-8.34	-38.43	24.88	-3.08	124.98	100
2 Tri	-3.92	-40.97	23.67	-2.53	118.67	94.91
R-Z	-6.92	-39.18	24.96	-3.08	124.23	100
3 Tri	-7.84	-37.58	20.66	-2.03	112.92	86.14
R-Z	-3.47	-36.34	22.33	-2.53	120.01	100
4 Tri	-16.57	-34.45	18.82	-1.96	107.28	73.12
R-Z	-10.90	-34.45	17.83	-1.88	129.40	100
5 Tri	-32.77	-34.12	18.25	-2.05	120.40	69.71
R-Z	-19.60	-35.52	18.08	-2.03	139.72	100
6 Tri	-22.15	-35.94	16.96	-1.38	130.76	88.23
R-Z	-15.28	-38.71	17.29	-1.52	138.23	100
7 Tri	-98.30	-130.84	59.28	-2.97	361.67	188.82
R-Z	-176.86	-136.41	55.92	-3.38	360.74	100
8 Tri	-225.46	-108.93	50.51	-2.87	338.90	52.14
R-Z	-225.69	-137.99	58.16	-4.16	409.69	100
9 Tri	-125.27	-75.16	33.78	-1.37	216.06	48.03
R-Z	-89.03	-94.88	37.35	-1.89	248.46	100
10 Tri	412.22	111.28	-54.24	3.08	-362.49	109.85
R-Z	429.44	131.51	-57.35	3.87	-407.48	100

TABLE VIII-3 Comparison of Reactivity Coefficients for a 5.752 cm thick Slice about the Midplane, by Channel, for LWR-Pu-Fueled CRBR with Normal Sodium at EOEC17 as Obtained from 2-D Triangular-Mesh and R-Z Perturbation Calculations, $\Delta k/k^2 \times 10^4$

Channel	Subassembly I.D.	Sodium Void Worth		Steel Removal Worth		Doppler Worth*		Core Fuel Worth	
		Tri	R-Z	Tri	R-Z	Tri	R-Z	Tri	R-Z
1	1,7	2.171	2.317	5.953	6.196	-0.3314	-0.3319	24.25	25.34
2	2,3,6	3.420	3.605	8.938	9.194	-0.4283	-0.4227	26.51	27.38
3	4,11,14	2.631	2.658	7.190	7.218	-0.4040	-0.3814	31.32	31.63
4	8,10,15,13,16	4.816	5.169	12.805	13.423	-0.6063	-0.6205	38.26	39.61
5	18,24	0.788	1.105	2.858	3.455	-0.1598	-0.1661	26.64	28.80
6	19,22	0.438	0.521	1.758	1.930	-0.1151	-0.1144	18.68	19.36
7	5,9,21,26,68	2.283	2.494	7.190	7.659	-0.4280	-0.4397	43.12	44.54
8	20,23,25	0.619	0.714	2.512	2.713	-0.1654	-0.1615	25.29	25.38
9	12,17,32	1.557	1.496	4.652	4.641	-0.2434	-0.2392	20.22	20.76
10	27,28,29,30,31	-0.414	-0.752	0.946	-0.563	-0.1802	-0.1732	34.56	35.39

*Reactivity for a temperature change of 1100°K to 2200°K.

TABLE VIII-4 Comparison of Reactivity Coefficients for a 5.752 cm Thick Slice about the Midplane, by Channel for LWR-Pu-Fueled CRBR with Sodium Voided at FOEC17 As Obtained from 2-D Triangular-Mesh and R-Z Perturbation Calculations, $\Delta k/k^2 \times 10^4$

Channel	Subassembly I.D.	Steel Removal Worth		Doppler Worth*		Core Fuel Worth	
		Tri	R-Z	Tri	R-Z	Tri	R-Z
1	1,7	6.042	6.236	-0.2019	-0.2029	25.65	25.62
2	2,3,6	9.008	9.168	-0.2630	-0.2609	28.96	28.37
3	4,11,14	7.095	7.016	-0.2422	-0.2265	32.71	31.22
4	8,10,13,15,16	12.672	13.165	-0.3650	-0.3760	41.46	40.49
5	18,24	2.765	3.231	-0.0964	-0.0983	27.34	27.92
6	19,22	1.645	1.728	-0.0712	-0.0689	19.77	19.32
7	5,9,21,26,68	6.891	7.244	-0.2607	-0.2654	45.62	44.49
8	20,23,25	2.828	2.401	-0.1026	-0.0981	27.03	25.63
9	12,17,32	4.953	4.291	-0.1493	-0.1453	21.92	21.07
10	27,28,29,30,31	-0.002	-0.476	-0.1173	-0.1108	38.03	37.09

*Reactivity for a temperature change of 1100°K to 2200°K.

TABLE A.1. The ANL-27 and WARD-9 Broad Group Energy Structures

ANL-27						WARD-9	
gp	Upper Energy, eV	gp	Upper Energy, eV	gp	Upper Energy, eV	gp	Upper Energy, eV
1	1.000 + 7	10	1.111 + 5	19	1.234 + 3	1	1.000 + 7
2	6.065 + 6	11	6.738 + 4	20	7.485 + 2	2	2.231 + 6
3	3.679 + 6	12	4.087 + 4	21	4.540 + 2	3	8.209 + 5
4	2.231 + 6	13	2.479 + 4	22	2.754 + 2	4	1.832 + 5
5	1.353 + 6	14	1.503 + 4	23	1.013 + 2	5	4.087 + 4
6	8.209 + 5	15	9.119 + 3	24	3.727 + 1	6	9.119 + 3
7	4.979 + 5	16	5.531 + 3	25	1.371 + 1	7	2.035 + 3
8	3.020 + 5	17	3.355 + 3	26	5.044	8	4.540 + 2
9	1.832 + 5	18	2.035 + 3	27	1.855	9	0.6826

TABLE A.2. Description of Cells Used to Compute Cross Sections Using Integral
Transport Theory Capability of MC²-2 Code

	Inner Core			Outer Core			Radial Blanket		
	pin	clad	coolant	pin	clad	coolant	pin	clad	coolant
radius, cm	0.254	0.3006	0.3924	0.254	0.3006	0.3924	0.6223	0.6616	0.7402
²³⁹ Pu	2.558 - 3			3.722 - 3			1.000 - 10		
²⁴⁰ Pu	7.269 - 4			1.057 - 3			1.000 - 10		
²⁴¹ Pu	3.807 - 4			5.539 - 4			1.000 - 10		
²³⁵ U	1.157 - 4			1.041 - 4			4.917 - 5		
²³⁸ U	1.648 - 2			1.484 - 2			2.232 - 2		
O	4.079 - 2			4.092 - 2			4.474 - 2		
Fe		5.437 - 2			5.437 - 2			5.437 - 2	
Cr		1.578 - 2			1.578 - 2			1.578 - 2	
Ni		1.078 - 2			1.078 - 2			1.078 - 2	
Mo		1.222 - 3			1.222 - 3			1.222 - 3	
⁵⁵ Mn		1.494 - 3			1.494 - 3			1.494 - 3	
²³ Na			2.2066 - 2			2.2066 - 2			2.2066 - 2

TABLE A.3. CRBR Configuration & Compositions Used in
SDX Code to Collapse to 27 Groups

	Inner Core	Outer Core	Rad. Blanket	Rad. Reflector
Outer radius of region, cm	72	94	122	142
Mesh Inter- vals	30	10	10	10
^{238}Pu atoms/ barn-cm	1.599 - 5	2.327 - 5		
^{239}Pu	1.072 - 3	1.559 - 3		
^{240}Pu	3.045 - 4	4.430 - 4		
^{241}Pu	1.595 - 4	2.320 - 4		
^{242}Pu	3.775 - 5	5.491 - 5		
^{235}U	4.846 - 5	4.360 - 5	3.476 - 5	
^{238}U	6.905 - 3	6.216 - 3	1.577 - 2	
O	1.709 - 2	1.714 - 2	3.162 - 2	
Fe	9.132 - 3	9.132 - 3	5.006 - 3	1.220 - 2
Cr	2.650 - 3	2.650 - 3	1.452 - 3	1.250 - 2
Ni	1.811 - 3	1.811 - 3	9.927 - 4	4.810 - 2
Mo	2.051 - 4	2.051 - 4	1.125 - 4	1.710 - 4
^{55}Mn	2.508 - 4	2.508 - 4	1.374 - 4	2.080 - 4
^{23}Na	9.115 - 3	9.115 - 3	4.437 - 3	2.490 - 3

ARGONNE NATIONAL LAB WEST



3 4444 00011119 5